TÉCNICO
LISBOA

UNIVERSIDADE DE LISBOA
INSTITUTO SUPERIOR TÉCNICO

Search for top squarks in the four-body decay mode with single lepton final states in proton-proton collisions at the Large Hadron Collider

Diogo Carlos Chasqueira de Bastos

Supervisor : Doctor Pedrame Bargassa
Co-Supervisor : Doctor João Manuel Coelho dos Santos Varela

Thesis approved in public session to obtain the PhD Degree in Physics

Jury final classification: Pass with Distinction

2023

UNIVERSIDADE DE LISBOA
INSTITUTO SUPERIOR TÉCNICO

Search for top squarks in the four-body decay mode with single lepton final states in proton-proton collisions at the Large Hadron Collider

Diogo Carlos Chasqueira de Bastos

Supervisor : Doctor Pedrame Bargassa
Co-Supervisor : Doctor João Manuel Coelho dos Santos Varela

Thesis approved in public session to obtain the PhD Degree in Physics

Jury final classification: Pass with Distinction

Jury

Chairperson : Doctor Mário João Martins Pimenta, Instituto Superior Técnico, Universidade de Lisboa;

Members of the Committee :

Doctor Jorge Manuel Rodrigues Crispim Romão, Instituto Superior Técnico, Universidade de Lisboa;
Doctor Pablo Martínez Ruiz del Árbol, Instituto de Física de Cantabria, Universidad de Cantabria, Espanha;
Doctor José Ricardo Morais Silva Gonçalo, Faculdadde de Ciências e Tecnologia, Universidade de Coimbra;
Doctor Michele Gallinaro, Instituto Superior Técnico, Universidade de Lisboa;
Doctor Pedrame Bargassa, Ruđer Bošković Institute, Croácia.

Funding Institutions
Fundação para a Ciência e a Tecnologia, Fellowship PD/BD/135424/2017
(IDPASC programme)

2023

Abstract

A search for the pair production of the lightest supersymmetric partner of the top quark, the top squark ($\widetilde{t}_1$), is presented in this thesis. The search targets the four-body decay of the $\widetilde{t}_1$, which is preferred when the mass difference between the top squark and the lightest supersymmetric particle is smaller than the mass of the *W* boson. This decay mode consists of a bottom quark, two other fermions, and the lightest neutralino ($\widetilde{\chi}_1^0$), which is assumed to be the lightest supersymmetric particle. The data correspond to an integrated luminosity of 138 fb^{-1} of proton-proton collisions at a center-of-mass energy of 13 TeV collected by the CMS experiment at the CERN LHC. Events are selected using the presence of a high-momentum jet, an electron or muon with low transverse momentum, and a significant missing transverse momentum. The signal is selected based on a multivariate approach that is optimized for the difference between $m(\widetilde{t}_1)$ and $m(\widetilde{\chi}_1^0)$. The contribution from leading background processes is estimated from data. No significant excess is observed above the expectation from standard model processes. The results of this search exclude top squarks at 95% confidence level for masses up to 480 and 700 GeV for $m(\widetilde{t}_1) - m(\widetilde{\chi}_1^0) = 10$ and 80 GeV, respectively.

Keywords

High energy physics, supersymmetry, supersymmetric top, CMS, LHC.

Resumo

Nesta tese, é apresentada uma pesquisa para a produção de pares do parceiro supersimétrico mais leve do quark top, o squark top ($\widetilde{t}_1$). Esta pesquisa tem como alvo o decaimento em quatro partículas do $\widetilde{t}_1$, que é preferida quando a diferença de massa entre o squark top e a partícula supersimétrica mais leve é menor que a massa do bosão W. Este modo de decaimento consiste em um quark bottom, dois outros fermiões e o neutralino mais leve ($\widetilde{\chi}_1^0$), que é assumido como sendo a partícula supersimétrica mais leve. Os dados correspondem a uma luminosidade integrada de 138 fb^{-1} de colisões protão-protão com energia de centro de massa de 13 TeV coletados pela experiência CMS no LHC do CERN. Os eventos são selecionados usando a presença de um jato de alta energia, um eletrão ou muão com baixo momento transverso e um momento transversal em falta significativo. O sinal é selecionado com base em uma abordagem multivariada que é otimizada para a diferença entre $m(\widetilde{t}_1)$ e $m(\widetilde{\chi}_1^0)$. A contribuição dos principais processos de fundo é estimada a partir dos dados. Nenhum excesso significativo é observado acima da expectativa dos processos do modelo padrão. Os resultados desta pesquisa excluem top squarks com 95% de nível de confiança para massas até 480 e 700 GeV para $m(\widetilde{t}_1) - m(\widetilde{\chi}_1^0) = 10$ e 80 GeV, respetivamente.

Palavras Chave

Física de altas energias, supersimetria, top supersimétrico, CMS, LHC.

Acknowledgments

The research for this doctoral thesis was carried out during the years 2018–2023 at the Compact Muon Solenoid (CMS) group of the Laboratório de Instrumentação e Física Experimental de Partículas (LIP) and at the CMS experiment at European Laboratory for Particle Physics (CERN). The research was funded by the Fundação para a Ciência e Tecnologia (FCT) through the PhD fellowship PD/BD/135424/2017 within the International Doctorate Network in Particle Physics, Astrophysics and Cosmology (IDPASC) program. Travels to various schools, workshops and conferences were funded by LIP and FCT.

I am grateful to my supervisors, Dr. Pedrame Bargassa and Prof. João Varela, for their help, guidance and for the opportunity to contribute to the field of experimental particle physics. I would like to give a special thanks to Dr. Michele Gallinaro for encouraging and supporting me especially during the last stretch of my doctoral work.

A special thank you to my CMS colleagues: Cirstóvão da Cruz e Silva, for consistently being there, Pietro Vischia, for the counseling and mentorship, Carlos Cid, Sergio Cruz, for the stimulating physics discussions and late-night debugging sessions. A special toast goes out to my dear friends from LIP Oleksii, Ksenia, Barrué, Júlia, Marco, Ana Luísa, Glória and Beatriz. You have enriched my life. I cannot overlook the immense support and encouragement I received from my special friends (and flatmates), Lore, Thana, Rebecca and Cris. Your uplifting spirits and positive energy have brightened my days, and I owe you a tremendous debt of gratitude.

Vera, you make me smile everyday. You made the challenging days easy, and the easy days even better. Thank you for being a source of joy and making every moment brighter.

Lastly, but certainly not least, I want to extend my deepest appreciation to my family. First and foremost, I dedicate this thesis to my extraordinary mother. Words cannot adequately express my gratitude for the unwavering love, guidance, and strength you have provided me throughout my life. Your presence has been a constant source of inspiration, and I am forever grateful for the person you are. To my incredible godmother and cousin, I want to express my sincere thanks for the sacrifices you have made on my behalf. Your untiring support and encouragement have propelled me forward, even during the most challenging times. Your belief in me has been a driving force behind my achievements, and I am truly thankful to have you all in my life.

I would also like to express my heartfelt gratitude to my friends, too numerous to all be listed here.

Obrigado.

“It doesn’t matter how beautiful your theory is, it doesn’t matter how smart you are.
If it doesn’t agree with experiment, it’s wrong.”

—Richard P. Feynman

Dedicated to my mother,

for her unwavering and unconditional support,

and for the exemplary role she has consistently played in my life.

Contents

List of Figures

List of Tables

Acronyms

AOD Analysis Object Data. 32

AR Analysis Region. 37, 39, 50, 67, 68, 71, 83

ARC Analysis Review Committee. 4

BDT Boosted Decision Tree. 50, 55–58, 61, 64, 67, 68, 83, 85, 92, 98, 102

BTL Barrel Timing Layer. 29

CDM Cold Dark Matter. 16

CERN European Laboratory for Particle Physics. v, 2, 20, 22

CHS Charged Hadron Subtraction. 40

CMS Compact Muon Solenoid. v, 3, 4, 20, 22, 25–29, 32–35, 37, 40, 44, 48, 85, 98

CR Control Region. 35, 45, 74, 83, 85, 92

CSC Cathode Strip Chamber. 27, 28

DT Drift Tube. 27, 28, 55

ECAL Electromagnetic Calorimeter. 22, 25, 26, 29, 34, 41, 42

EE Electromagnetic Calorimeter Endcap. 34

FCT Fundação para a Ciência e Tecnologia. v

FOM Figure of Merit. 57

HCAL Hadron Calorimeter. 22, 26, 29, 34, 41

HL-LHC High Luminosity LHC. 20, 28, 29

HLT High Level Trigger. 28, 37, 39, 43, 75

IDPASC International Doctorate Network in Particle Physics, Astrophysics and Cosmology. v

ISR Initial-State Radiation. 3, 35, 44, 50, 58, 88, 89, 95

JEC Jet Energy Correction. 88

JER Jet Energy Resolution. 43, 88

JES Jet Energy Scale. 43, 88, 95

JHEP Journal of High Energy Physics. 4

L1 Level 1. 28, 37

LEP Large Electron-Positron Collider. 20

LHC Large Hadron Collider. 2, 4, 20, 22, 25, 27, 32, 34, 57, 108

LIP Laboratório de Instrumentação e Física Experimental de Partículas. v, 4, 29

LO Leading Order. 35, 44

LSP Lightest Supersymmetric Particle. 2, 11, 14, 16, 57

MC Monte Carlo. 34–37, 40, 42–44, 48, 55, 64, 74, 80, 85, 90

MIP Minimum Ionizing Particles. 29

ML Machine Learning. 55

MR Measurement Region. 39, 74, 75

MSSM Minimal Supersymmetric Standard Model. 12–15

MTD MIP Timing Detector. 29

MVA Multivariate Analysis. 32, 54, 55, 57

NLO Next-to-Leading Order. 35, 44, 85

NNLL Next-to-Next-to-Leading logarithmic. 35

NNLO Next-to-Next-to-Leading Order. 35

PD Primary Dataset. 33, 37, 75

PF Particle Flow. 32, 34, 40, 42, 51

pp proton-proton. 32

PS Proton Synchrotron. 20

PU Pileup. 35, 40, 42, 43, 95

PV Primary Vertex. 40–42

QCD Quantum Chromodynamics. 35

RPC Resistive Plate Chamber. 27, 28

SF Scale Factors. 42–45, 48, 88

SM Standard Model. 2, 4, 6–16, 34, 35, 41, 50, 51, 57, 58, 64, 74, 108

SMS Simplified Model Spectra. 15

SPS Super Proton Synchrotron. 20

SR Signal Region. 64, 68, 74, 82, 83, 85, 90, 92, 95, 98, 108

SUSY Supersymmetry. 2, 4, 6, 11–13, 15, 16, 44, 48, 108

TEC Tracker End Cap. 25

TIB Tracker Inner Barrel. 25

TID Tracker Inner Disk. 25

TOB Tracker Outer Barrel. 25

VEV Vacuum Expectation Value. 9, 11, 16

VR Validation Region. 67, 68, 71, 83, 85, 90, 92

VR1 Validation Region 1. 68, 71, 83, 90, 92

VR2 Validation Region 2. 68, 71, 83, 90, 92

1

Introduction

Contents

1.1 Introduction

Supersymmetry (SUSY) [1–6] predicts the existence of a new symmetry that requires that, for each fermion (boson) in the Standard Model (SM), there is also a bosonic (fermionic) superpartner. Searches for SUSY are among the important focal points of the physics program at the CERN Large Hadron Collider (LHC), since SUSY naturally solves the problem of quadratically divergent loop corrections to the mass of the Higgs boson [7–11] and could provide an explanation for dark matter. If the SUSY quantum number R parity [12] is conserved, supersymmetric particles would be produced in pairs, and their decay chains would end with the Lightest Supersymmetric Particle (LSP), often considered to be the lightest neutralino $\widetilde{\chi}^0_1$. Such an LSP, being neutral, weakly interacting, and massive, would have the required characteristics for a dark matter particle, and thus, would offer a solution to an outstanding problem in the cosmological model. When the symmetry is broken, the scalar partners of an SM fermion acquire a mass different from the mass of the SM partner, with the mass splitting between scalar mass eigenstates being proportional to the mass of the SM fermion. Since the top quark is the heaviest fermion of the SM, the splitting between its chiral supersymmetric partners can be the largest among all supersymmetric quarks (squarks). Furthermore, the top Yukawa coupling can be the greatest among all fermions, which affects the masses of the squarks through the renormalization group equations. The lighter supersymmetric scalar partner of the top quark, the top squark ($\widetilde{t}_1$), could therefore be the lightest squark and thus the most accessible experimentally.

If SUSY is realized in nature, cosmological observations imply that for many models the lightest top squark is almost degenerate with the LSP [13]. In this scenario, because the mass difference between the $\widetilde{t}_1$ and the $\widetilde{\chi}^0_1$ is smaller than the mass of the W boson, the two- and three-body decays of the $\widetilde{t}_1$ are kinematically forbidden, while the two-body decay to $c\widetilde{\chi}^0_1$ can be suppressed depending on the parameters of the model. This motivates the search for the four-body decay $\widetilde{t}_1 \rightarrow b\mathrm{f}\bar{\mathrm{f}}'\widetilde{\chi}^0_1$, where b stands for the bottom quark, and the fermions f and $\bar{\mathrm{f}}'$ can be either quarks or leptons. Throughout this thesis, charge conjugation is assumed. Figure 1.1 represents a simplified model [14–19] of the production of $\widetilde{t}_1\bar{\widetilde{t}}_1$ in proton-proton (pp) collisions, where each $\widetilde{t}_1$ and $\bar{\widetilde{t}}_1$ undergoes a four-body decay.

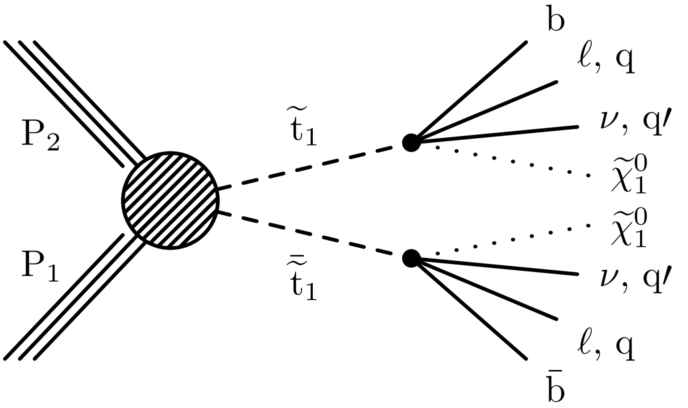

Figure 1.1: Stop pair production at the LHC with four-body decays.

In this thesis, the previous 2016 result of CMS at $\sqrt{s} = 13$ TeV [20] is combined with data recorded in 2017 and 2018. The results of 2016 are directly taken from Ref. [20], except the integrated luminosity and its uncertainty, which are updated to their latest values [21]. The total integrated luminosity for the combined 2016–2018 analysis is 138 fb^{-1}.

In the present search a final state is considered, where the fermions f and $\bar{\mathrm{f}}'$ represent a charged lepton and its neutrino for the decay products of one $\widetilde{t}_1$, and two quarks for the other top squark. A 100% branching fraction is assumed for the four-body decay when interpreting the results [14]. The considered final states contain at least one jet, a large missing transverse momentum, and exactly one charged lepton, which can be either an electron or a muon. The choice of final states where one top squark decays into a lepton is motivated by the decrease of the contributions from the multijet background in this mode, while increasing the selection efficiency with the other top squark decaying hadronically. The selected jet, attributed to the Initial-State Radiation (ISR) of a parton, is required to have high transverse momentum (p_{T}). Both neutralinos and the neutrino escape undetected, leaving high missing transverse momentum. Electrons and muons can be efficiently reconstructed and identified with p_{T} as low as 5.0 and 3.5 GeV, respectively. The signal selection is based on a multivariate analysis, followed by a counting experiment. This approach takes advantage of the different correlations between the discriminating variables for signal and background, and is adapted for different $\Delta m = m(\widetilde{t}_1) - m(\widetilde{\chi}^0_1)$ kinematic regions, thus enhancing the reach of the search across the $(m(\widetilde{t}_1),\ m(\widetilde{\chi}^0_1))$ space. The main contributions to the background events are W+jets, $t\bar{t}$, and Z+jets processes, and are predicted from data. W+jets refers to processes where a W boson is produced and decays into a charged lepton and a neutrino accompanied by jets originating from ISR, $t\bar{t}$ stands for the top quark (t) pair production where one W boson decays leptonically while the other decays hadronically. Processes where a Z boson is produced and decays into a neutrino and a anti-neutrino along with ISR jets are referred as Z+jets, they contribute to the background composition when a jet is misidentified as a lepton. In Figure 1.2, the Feynman diagrams of the main contributions to the background are represented.

A search in the single-lepton final state for the four-body decays of the $\widetilde{t}_1$ has been performed by the ATLAS Collaboration at $\sqrt{s} = 13$ TeV [22], and a comparison of its results to the present search is provided in this thesis.

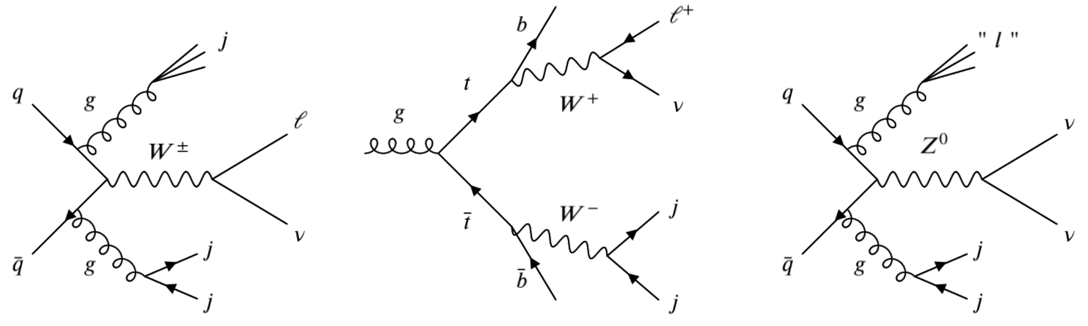

Figure 1.2: Diagrams of W+jets (left), $t\bar{t}$ (middle) and Z+jets (right) in pp collisions.

I am one of the main authors of this search within the CMS collaboration. The publication of the excluded $\widetilde{t}_1$ masses in the compressed scenarios, one of the most difficult regions to probe, passed the collaboration internal review, and I was the contact person at all stages. This process included the development of all the analysis steps, constant reporting within the SUSY group at the end of each step, and subsequent presentations of the analysis for the unblinding of the data, pre-approval and approval within the collaboration, the respective addressing to the answered raised by fellow colleagues during the review, as well as the implementation of the suggestions brought by the Analysis Review Committee (ARC). The results of this work were presented by me on *The XXIX International Conference on Supersymmetry and Unification of Fundamental Interactions* [23] on the 29th of June of 2022 in Ioannina, Greece and featured on the CMS news website [24]. The answers to the questions from the Journal of High Energy Physics (JHEP) referees were also prepared by me and approved by the ARC within the collaboration. The results of this thesis have been published by the JHEP [25]. With the help from the LIP group and the CMS collaboration this research has been carried, to a large extent, by my effort.

This thesis is structured as follows: after the introduction to the thesis (present Chapter 1) the SM and its SUSY extension are reviewed in Chapter 2; the CMS detector at the LHC, i.e. the experimental apparatus, are briefly described in Chapter 3; in Chapter 4 the details about the event reconstruction and selection, and the simulated event samples in the data analysis are provided; the description and validation of the multivariate methods targeting the $\widetilde{t}_1$ signal under study are detailed in Chapter 5; two data-driven methods are used to estimate the contribution of the main background processes, theses methods constitute Chapter 6; Chapter 7 is dedicated to the systematic uncertainties, their effects on the analysis and the combination between the different data-taking years; the results of this thesis are summarized in Chapter 8; and Chapter 9 finishes the thesis following up the search results by conclusions and a discussion of the results obtained.

2

The Standard Model of particle physics and Supersymmetry

Contents

Particle physics is the study of the fundamental building blocks of matter and their interactions. The SM is the most successful theoretical framework that describes the behavior of the matter particles, and the fundamental forces. In the SM, all matter particles are fermions, all force carriers are bosons, and the Higgs boson is responsible for giving particles mass through the mechanism of electroweak symmetry breaking. Despite its success, the SM has some shortcomings, such as: it does not account for the observed baryon asymmetry of the universe, the lack of a candidate for dark matter, and there is no consensus on the mechanism that introduces the neutrino oscillations. SUSY is an extension of the SM that proposes the existence of a new symmetry between fermions and bosons. This symmetry predicts the existence of supersymmetric particles, including the top squark, or stop, which is the supersymmetric partner of the top quark.

In this chapter, an overview of the SM and its particle content, gauge symmetries, and the Higgs mechanism is be provided. The concept of supersymmetry is introduced, with its motivations and implications for particle physics, with a specific focus on the four-body decays of stop. This thesis does not provide a comprehensive coverage of the SM and SUSY. Instead, it focuses on the most critical and relevant elements. For a more comprehensive introduction, interested readers can refer to [26–29].

2.1 The Standard Model of Particle Physics

The SM of particle physics is a theory that provides a description for the electromagnetic, weak and strong interactions of elementary particles. It is founded upon the principles of quantum field theory, which combines special relativity and quantum mechanics. The SM describes particles in terms of three classes, summarized in Figure 2.1 from [30]:

- Fermions, characterized by Fermi–Dirac statistics, have half integer spin, and are the constituents of matter. Fermions are further subdivided into quarks and leptons, each subdivided into three generations that differ only by the masses of their members. There are six types of quarks: up (u), down (d), charm (c), strange (s), top (t), and bottom (b). Quarks are the building blocks of protons and neutrons, which make up the nuclei of atoms. There are also six types of leptons: electron (e), muon (μ), tau (τ), and their corresponding neutrinos (ν_e, ν_μ, ν_τ). Leptons interact only electroweakly, while quarks interact both electroweakly and strongly. They are also distinguished by their electric charge: leptons have charges of either $-1e$ or $0e$, while quarks have charges of either $+\frac{2}{3}e$ or $-\frac{1}{2}e$. The corresponding antiparticles have opposite charges. More details on other quantum numbers can be found in Ref. [31].
- Gauge bosons, characterized by Bose–Einstein statistics, have spin one, and the exchange of bosons between fermions constitutes the interactions between the fermions, hereby serving as force carriers. The photon (γ) is the boson that mediates electromagnetism. The W and Z bosons mediate the weak nuclear force, which is responsible for radioactive decays. The gluon (g) mediates the strong nuclear force that holds quarks together in protons and neutrons.

- The scalar Higgs boson (*H*), which is produced by the quantum excitation of the Higgs field and has spin zero. The Higgs mechanism is the one responsible for giving mass to the other particles in the SM.

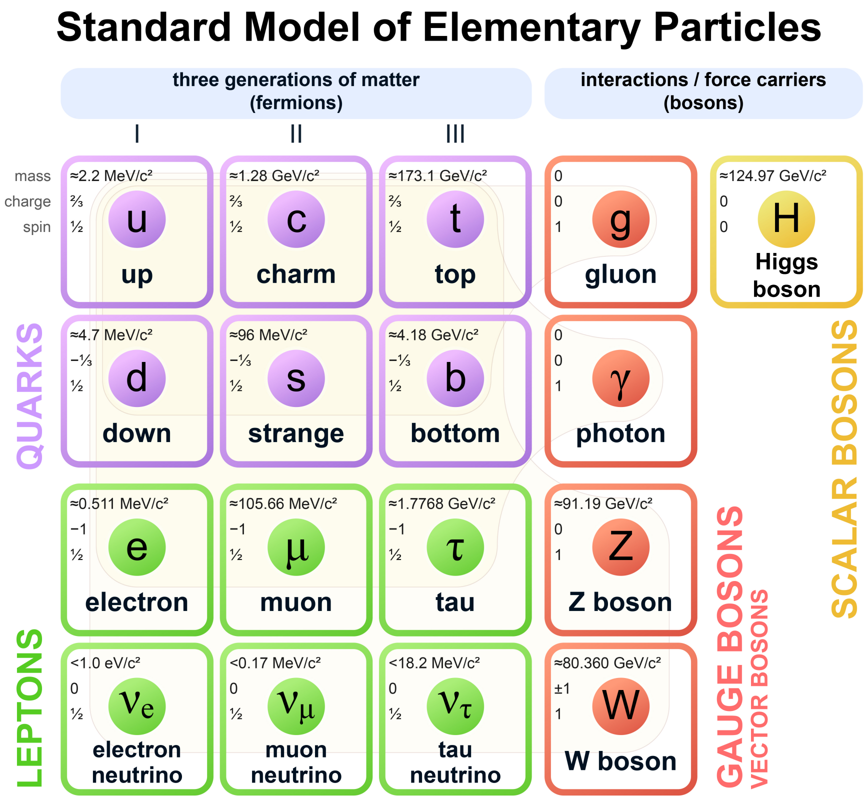

Figure 2.1: Elementary particles of the Standard Model.

Moreover, the SM adheres to the principles of gauge theory, respecting a group of symmetries. The gauge symmetry of the SM is the $SU(3) \times SU(2) \times \mathrm{U}(1)$ gauge group. The $SU(3)$ group describes the strong force, and is associated with three colors for quarks. The $SU(2) \times \mathrm{U}(1)$ group describes the electroweak force, and is associated with the weak isospin, and the weak hypercharge of particles. In the SM, the fields of the elementary particles are assigned to representations of the gauge groups. Thus, the choice of the gauge group determines the structure of the lagrangian. Table 2.1 presents a summary of the field content of the SM and their respective representations. The left–handed antiparticles have been substituted for the fields of the right–handed particles. Additionally, the gauge fields are included for completeness. The most general renormalisable lagrangian, invariant under gauge transformations of $SU(3) \times SU(2) \times \mathrm{U}(1)$, is expressed in 2.1, where each separate contribution will be elaborated on individually.

$$\mathcal{L}_{EW} = \mathcal{L}_{\text{free+interaction}} + \mathcal{L}_{\text{Gauge}} + \mathcal{L}_{\text{Higgs}} + \mathcal{L}_{\text{Yukawa}}. \tag{2.1}$$

The gauge invariant Dirac lagrangian in Equation 2.2, defined as the "free+interaction" term, represents the free fermions and their interaction with the mentioned gauge fields:

$$\begin{aligned}\mathcal{L}_{\text{free+interaction}} = \sum_{i=1}^{3}[&\bar{\Psi}^i_L i\gamma^\mu D_\mu \Psi^i_L + \bar{R}_i i\gamma^\mu D_\mu R_i + \bar{Q}^i_L i\gamma^\mu D_\mu Q^i_L \\ &+ \bar{U}^i_R i\gamma^\mu D_\mu U^i_R + \bar{D}^i_R i\gamma^\mu D_\mu D^i_R],\end{aligned} \tag{2.2}$$

where the covariant derivative D_μ combines the electromagnetic and the weak fields, and is expressed as:

$$D_\mu = \partial_\mu - i\frac{g'}{2}YB_\mu - i\frac{g_w}{2}\sigma_j W^j_\mu, \tag{2.3}$$

where the coupling constant g' is the coupling to the B boson, and the constant g_w represents the coupling to the weak isospin via the three vector bosons W^j (j=1,2,3), whose components are the Pauli matrices σ_j.

Equation 2.4 represents the gauge term, which is fully constrained by the selected gauge group, and represents the kinetic energy terms of the vector fields. Due to the non–Abelian structure of the $SU(2)$ and $SU(3)$ gauge groups, the self–interactions of the W_ν and G_ν fields are accounted for in this term. This allows for the triboson couplings in the SM.

$$\mathcal{L}_{\text{Gauge}} = -\frac{1}{4}B_{\mu\nu}B^{\mu\nu} - \frac{1}{4}\overrightarrow{W}_{\mu\nu} \cdot \overrightarrow{W}^{\mu\nu} - \frac{1}{4}\overrightarrow{G}_{\mu\nu} \cdot \overrightarrow{G}^{\mu\nu}. \tag{2.4}$$

Equation 2.5 represents the Higgs term, where the Higgs field Φ is a complex scalar doublet field.The first term describes the behavior of the Higgs field, its interaction with the gauge bosons and how the bosons get masses. The second term is the Higgs potential.The lagrangian $\mathcal{L}_{\text{Higgs}}$ is expressed as:

$$\mathcal{L}_{\text{Higgs}} = \left|D_\mu \Phi\right|^2 - V(\Phi), \tag{2.5}$$

where the covariant derivative is the same as the one for the fermion fields. Equation 2.6, is the most general Higgs potential that is compatible with the gauge invariant transformations of $SU(2) \times \mathrm{U}(1)$.

$$V(\Phi) = \mu^2\Phi^\dagger\Phi + \lambda(\Phi^\dagger\Phi)^2. \tag{2.6}$$

The final term in the lagrangian $\mathcal{L}_{EW}$ is the Yukawa coupling, which in the absence of right handed neutrinos is the most general term and expressed in Equation 2.7. This term describes the coupling between the fermions and the scalar Φ. Through this term, the fermions are conferred a mass when the $SU(2) \times \mathrm{U}(1)$ symmetry is broken.

$$\begin{aligned}\mathcal{L}_{\text{Yukawa}} = &\sum_{i=1}^{3}\left[G_i(\bar{\Psi}^i_L R_i \Phi + \text{h.c.})\right] + \sum_{i=1}^{3}\left[G^i_u(\bar{Q}^i_L U^i_R \widetilde{\Phi} + \text{h.c.})\right] \\ &+ \sum_{i,j=1}^{3}\left[(\bar{Q}^i_L G^{ij}_d D^j_R + \text{h.c.})\right],\end{aligned} \tag{2.7}$$

where h.c. is the hermitian-conjugate.

In the lagrangian $\mathcal{L}_{EW}$, the gauge bosons B_μ, W_ν and G_ν and all fermions are massless. If the μ^2 parameter of the Higgs potential is negative, a spontaneous symmetry breaking takes place. At a distance of ν from the origin , the Higgs potential reaches its minimum energy state, which is achieved by transforming the Higgs field by a constant, as in Equation 2.8. This transformation from the origin point to a distance of ν generates new terms in the SM lagrangian.

$$\Phi = \frac{1}{\sqrt{2}} \begin{pmatrix} 0 \\ \nu \end{pmatrix} . \tag{2.8}$$

Therefore, the SM comprises a complex scalar Higgs doublet field with an unstable potential. The Higgs field develops a Vacuum Expectation Value (VEV) that spontaneously breaks the electroweak symmetry $SU(2) \times \mathrm{U}(1)$. As a result from the interaction with the Higgs field through the Yukawa lagrangian (see Equation 2.7), the *Z*, and $W^\pm$ bosons acquire masses , while the photon remains massless. From the complex Higgs doublet, only one neutral scalar particle remains, the *H* boson with a mass of 125 GeV. It is from the breaking of this symmetry that the physical states *Z*, W^+, and W^- in Figure 2.1 arise, which are mixtures of the weak isospin and weak hypercharge.

Table 2.1: Field content of the Standard Model, including the gauge fields, fermion fields, and Higgs field, along with their associated charges, groups, couplings, and representations. The transformation of each field under the gauge group is shown in the columns, in the order ($SU(3)$, $SU(2)$, $\mathrm{U}(1)$). The presence of an antiparticle is denoted by the superscript C, and for the $\mathrm{U}(1)$ group, the value of the weak hypercharge is listed instead. The superscript i is the particle generation index.

Gauge Fields - Spin 1

Symbol	Associated Charge	Group	Coupling	Representation
B	Weak hypercharge	$\mathrm{U}(1)$	g'	$(\mathbf{1}, \mathbf{1}, 0)$
W^j	Weak isospin	$SU(2)$	g_w	$(\mathbf{1}, \mathbf{3}, 0)$
G^α	Color	$SU(3)$	g_s	$(\mathbf{8}, \mathbf{3}, 0)$

Fermion Fields - Spin $\frac{1}{2}$

Symbol	Name	Representation
Q_L^i	Left-handed quark	$(\mathbf{3}, \mathbf{2}, \frac{1}{3})$
$U_R^{i\,C}$	Left-handed antiquark (up)	$(\bar{\mathbf{3}}, \mathbf{1}, -\frac{4}{3})$
$D_R^{i\,C}$	Left-handed antiquark (down)	$(\bar{\mathbf{3}}, \mathbf{1}, -\frac{2}{3})$
Ψ_L^i	Left-handed lepton	$(\mathbf{1}, \mathbf{2}, -1)$
$R^{i\,C}$	Left-handed antilepton	$(\mathbf{1}, \mathbf{1}, 2)$

Higgs Fields - Spin 0

Symbol	Name	Representation
Φ	Higgs boson	$(\mathbf{1}, \mathbf{2}, 1)$

2.1.1 Strengths of the Standard Model

The SM was completed in the mid-1970s, and its predictions have been experimentally confirmed with great success. As an example, tests of quantum electrodynamics show experimental results agreeing with theoretical predictions with an accuracy of 10 parts in a billion (10^{-8}). The overall success of the SM can be illustrated through the global electroweak fit of the theory [32]. This fit compares the observed and predicted values of different parameters of the SM. Since the discovery of the Higgs boson, all input parameters are known, allowing for a complete assessment of the SM consistency. Fig. 2.2, extracted from [32] provides the results of the fit, displaying the pull values for each parameter. Importantly, these pull values never exceed 3 standard deviations (3σ), which confirms the overall consistency of the theory. This robust testing has positioned the SM as one of the most rigorously evaluated and validated theories in physics.

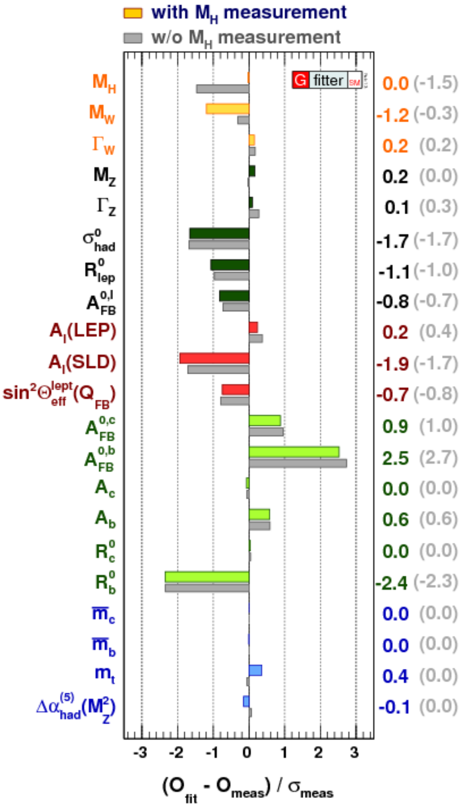

Plot inspired by Eberhardt et al. [arXiv:1209.1101]

Figure 2.2: This figure displays the deviations between the SM prediction and the measured parameter, in units of the uncertainty for the fit with the inclusion of M_H (depicted in color) and without M_H (in grey).

2.1.2 Shortcomings of the Standard Model

Despite the remarkable achievements of the SM, it is not exempt from limitations and shortcomings. For instance, the observed matter–antimatter asymmetry cannot be explained within the SM framework. Another shortcoming of the SM is that it does not offer a candidate for dark matter. The SM can only explain about 5% of the mass–energy content of the Universe, with dark matter accounting for approximately 26% of the mass–energy content, and dark energy for the rest. Another problem of the SM is its lack of explanation for the large discrepancy between the gravity and the three other interactions, where the gravitational interaction is 10^{24} times weaker than the weak interaction. Furthermore, the mass of the Higgs boson is much lighter than what would be expected at the Planck scale, at which gravity becomes as strong as the other fundamental forces. To better understand this problem, consider f as a SM Dirac fermion which acquires the mas m_f by interacting with the Higgs field H. The mass term in the SM lagrangian is spontaneously generated when the Higgs fields develops the VEV.

Fermionic loops in the Higgs field (see Figure 2.3) modify its mass, where a term $-\lambda_f H\bar{f}f$ is added to the bare Higgs mass M^2_{h0}, with λ_f being the coupling of the Higgs field to the fermion f. The correction to the mass of the Higgs is:

$$\Delta m^2_H = \frac{|\lambda_f|^2}{16\pi^2}[-2\Lambda^2_{UV} + 6m^2_f \log(\frac{\Lambda_{UV}}{m_f}) + \text{higher-order terms in } \frac{1}{\lambda^2_f}], \tag{2.9}$$

where Λ_{UV} represents the ultraviolet cutoff in the momentum of the fermion f introduced by the one–loop diagram of Figure 2.3.

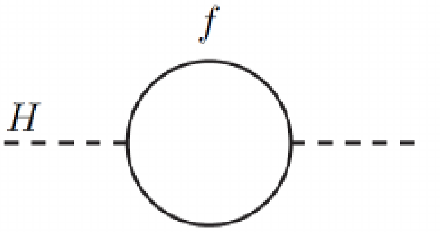

Figure 2.3: One–loop contributions to the Higgs field with a fermion f.

This correction to the Higgs mass is quadratically divergent in Λ_{UV}, which can be as high as the Planck scale: $M_{\text{Planck}} \sim 2.4^{18}$ GeV. This means that within the SM, the corrections of the Higgs mass are many orders of magnitude higher than the measured mass at 125 GeV. This hierarchy problem in turn suggest that either the SM is highly fine–tuned, or it is an incomplete theory of nature. In the latter case, the hierarchy problem suggests the existence of new physics between the electroweak and Planck scales, that introduces a mechanism canceling the quadratic divergence of the Higgs boson mass.

SUSY is one of the possible extensions of the SM that solves the problem of quadratically divergent loop corrections to the mass of the Higgs boson [7–11].

2.2 Supersymmetry

The limitations of the SM suggest that it is an effective theory. SUSY is an extension to the SM that offers a solution to some of these limitations such as the hierarchy problem by introducing new particles that cancel out the divergent corrections; the possibility to unify the electromagnetic, weak and strong forces at high energies; and a candidate for dark matter often considered to be the LSP. SUSY predicts scalar partners for the SM fermions, and fermionic partners for the SM boson, called superpartners. The superpartners have the same characteristics as their SM counterparts, just differing by half a spin. No superpartner has so far been observed. Therefore, if realized in nature, SUSY must be a broken symmetry.

By only generalizing the spin of the SM particles, SUSY offers a solution to the aforementioned hierarchy problem. To understand this, consider a theory with a massive scalar (Φ), a fermion (Ψ) and a Higgs filed (h). The lagrangian can be written as:

$$L \sim -g_f \overline{\Psi} \Psi h - g_S^2 h^2 \Phi. \tag{2.10}$$

In this simplified theory, Fig. 2.4 depicts the one–loop contributions to the mass of Higgs boson, and Eq 2.11 gives the terms that contribute to the Higgs mass.

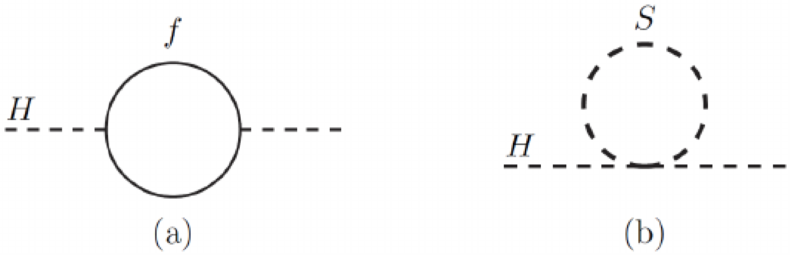

Figure 2.4: One–loop contributions to the Higgs field, with a fermion (a) and scalar (b).

$$M_h^2 \sim M_{h0}^2 + \frac{g_F^2}{4\pi^2}(\Delta^2 + m_F^2) - \frac{g_S^2}{4\pi^2}(\Delta^2 + m_S^2) + \text{logarithmic divergences} + \text{uninteresting terms} \tag{2.11}$$

If the coupling constants of the fermion and scalar contributions, denoted by g_F and g_S respectively, are equal, then the terms that increase with Δ^2 in the Higgs boson mass would cancel each other, resulting in the absence of the quadratic divergence:

$$M_h^2 \sim M_{h0}^2 + \frac{g_F^2}{4\pi^2}(m_F^2 - m_S^2). \tag{2.12}$$

In this scenario, the Higgs boson mass is described by Eq. 2.12 and is well behaved if the masses of the fermion and scalar are comparable. Efforts to quantify "comparable" have determined that the difference between the masses should not surpass 1 TeV [33].

SUSY establishes a symmetry between particles with different spin. As a result, in a supersymmetric theory, such as the Minimal Supersymmetric Standard Model (MSSM), the particle fields that differ by half spin are combined into a superfield. By constructing the superfield in this way, the combined fields have the same coupling, i.e. $g_F = g_S$, reducing the impact of the hierarchy problem.

In the case of the MSSM, only two categories of superfields are considered: Chiral Superfields and Vector Superfields. A Chiral Superfield is composed of a complex scalar field, denoted as S, and a two–component Majorana fermion field, represented as Ψ. A Vector Superfield is comprised of a massless gauge field with strength $F_{\mu\nu}^A$, along with a two-component Majorana fermion field, denoted as λ_A. Being an extension of the SM, which only generalizes spins, the MSSM respects the same gauge symmetry $SU(3) \times SU(2) \times \mathrm{U}(1)$. Therefore, in the MSSM, the same gauge group representations as the ones of the SM are utilized to define superfields which contain the SM fields and their supersymmetric counterparts. Consequently, SUSY increases the particle content of the SM. Furthermore, SUSY contains two complex Higgs doublets, whereas the SM has only one.

The hypothesized superpartners are paired with the original particles in superfields, which are summarized in Table 2.2.

Table 2.2: Field content of the Minimal Supersymmetric Standard Model. The column representation indicates under which representations of the gauge group each field transforms, in the order $SU(3)$, $SU(2)$, $\mathrm{U}(1)$. The presence of an antiparticle is denoted by the superscript C. A tilde over a field is used to denote the corresponding supersymmetric partner field. For the $\mathrm{U}(1)$ group, the value of the weak hypercharge is listed.

Vector Superfields

Superfield	Representation	Field Composition
$\widehat{B}$	$(\mathbf{1}, \mathbf{1}, 0)$	$B, \widetilde{B}$
$\widehat{W^j}$	$(\mathbf{1}, \mathbf{3}, 0)$	$W^j, \widetilde{W^j}$
$\widehat{G^\alpha}$	$(\mathbf{8}, \mathbf{1}, 0)$	$G^\alpha, \widetilde{G^\alpha}$

Chiral Superfields

Superfield	Representation	Field Composition
$\widehat{Q^i_L}$	$(\mathbf{3}, \mathbf{2}, \frac{1}{3})$	$Q^i_L, \widetilde{Q^i_L}$
$\widehat{U^i_R}^C$	$(\bar{\mathbf{3}}, \mathbf{1}, -\frac{4}{3})$	$U^i_R{}^C, \widetilde{U^i_R}^C$
$\widehat{D^i_R}^C$	$(\bar{\mathbf{3}}, \mathbf{1}, \frac{2}{3})$	$D^i_R{}^C, \widetilde{D^i_R}^C$
$\widehat{\Psi^i_L}$	$(\mathbf{1}, \mathbf{2}, -1)$	$\Psi^i_L, \widetilde{\Psi^i_L}$
$\widehat{R_i}^C$	$(\mathbf{1}, \mathbf{1}, 2)$	$R_i{}^C, \widetilde{R_i}^C$
$\widehat{\Phi_1}$	$(\mathbf{1}, \mathbf{2}, 1)$	$\Phi_1, \widetilde{\Phi_1}$
$\widehat{\Phi_2}$	$(\mathbf{1}, \mathbf{2}, -1)$	$\Phi_2, \widetilde{\Phi_2}$

In a supersymmetric theory, the most general renormalisable lagrangian, invariant under gauge transformations of $SU(3) \times SU(2) \times \mathrm{U}(1)$, is written in 2.13, where each separate contribution will be elaborated on individually.

$$\mathcal{L}_{MSSM} = \mathcal{L}_{\text{KE}} + \mathcal{L}_{\text{interaction}} + \mathcal{L}_{\text{W}} + \mathcal{L}_{\text{soft}}. \tag{2.13}$$

Equation 2.14 accounts for the kinetic energy terms of the fields. The summation over the index i refers to the fermion fields in the SM, which are represented as Ψ_i. The supersymmetric scalar partners of these fermion fields, denoted as S_i, as well as the two Higgs doublets, λ_A, and their corresponding fermion superpartners, are also included in this summation. The summation over the index A covers the gauge fields and their respective supersymmetric fermion partners, which are referred to as gauginos. Within this context, the kinetic energy term incorporates the SM equivalent terms from both Equation 2.4 and 2.2.

$$\begin{aligned} \mathcal{L}_{\text{KE}} &= \sum_i \left\{ (D_\mu S_i^*)(D^\mu S_i) + i\bar{\Psi}_i \gamma^\mu D_\mu \Psi_i \right\} \\ &+ \sum_A \left\{ -\frac{1}{4} F_{\mu\nu}{}^A F^{\mu\nu A} + \frac{i}{2} \bar{\lambda}_A \gamma^\mu D_\mu \lambda_A \right\}. \end{aligned} \tag{2.14}$$

The interactions between the gauginos and the chiral superfields, and the quartic interactions of the scalars are determined solely by supersymmetry and the gauge symmetries. Equation 2.15 defines these interaction terms, where the symbol g_A represents the gauge coupling constant.

$$\mathcal{L}_{\text{interaction}} = -\frac{1}{2} \sum_A \left(\sum_i g_A S_i^* T^A S_i \right)^2 - \sqrt{2} \sum_{i,A} g_A \left[S_i^* T^A \bar{\Psi}_i \lambda_A + \text{h.c.} \right]. \tag{2.15}$$

Equation 2.16 gives the most general superpotential W, considering only the first generation of the quark and lepton superfields. Typically, mixing among the 3 generations is allowed because the parameters λ_i can be matrices.

$$\begin{aligned} W = \epsilon_{ij} \mu \widehat{\Phi_1^i} \widehat{\Phi_2^j} &+ \epsilon_{ij} \left[\lambda_L \widehat{\Phi_1^i} \widehat{\Psi_L^j} \widehat{R}^C + \lambda_D \widehat{\Phi_1^i} \widehat{Q_L^j} \widehat{D_R}^C + \lambda_U \widehat{\Phi_2^i} \widehat{Q_L^j} \widehat{U_R}^C \right] \\ &+ \epsilon_{ij} \left[\lambda_1 \widehat{\Psi_L^i} \widehat{\Psi_L^j} \widehat{R}^C + \lambda_2 \widehat{\Psi_L^i} \widehat{Q_L^j} \widehat{D_R}^C \right] + \lambda_3 \widehat{U_R}^C \widehat{D_R}^C \widehat{D_R}^C. \end{aligned} \tag{2.16}$$

From the superpotential W results the term $\mathcal{L}_{\text{W}}$ in the MSSM lagrangian, expressed in Equation 2.17. This term is solely dependent on the chiral superfields, denoted as z_i, and it comprises terms that involve two and three fields. Within this term, the scalar potentials and the Yukawa couplings are included, which are defined by a portion of Equation 2.5 and Equation 2.7 of the SM.

$$\mathcal{L}_{\text{W}} = -\sum_i \left| \frac{\partial W}{\partial z_i} \right|^2 - \frac{1}{2} \sum_{i,j} \left[\bar{\Psi}_i \frac{\partial^2 W}{\partial z_i \partial z_j} \Psi_j + \text{h.c.} \right]. \tag{2.17}$$

In the superpotential W, the mass terms for the Higgs bosons rise from the term $\mu \widehat{\Phi_1^i} \widehat{\Phi_2^j}$. The Yukawa coupling arise from the terms proportional to λ_L, λ_D and λ_U. The terms that are proportional to λ_1, λ_2 and λ_3 pose a challenge as they lead to terms that violate lepton and baryon numbers. A new symmetry, called R parity [12], is introduced to solve this problem. Particles are assigned a new quantum number, where all the SM particles have an R parity value of $+1$, while their corresponding superpartners have a value of -1. The R parity value of a particle is determined as follows:

$$R \equiv (-1)^{3(B-L)+2s}, \tag{2.18}$$

where s is the spin of the particle, B its baryon number, and L its lepton number.

The conservation of this new quantum number would lead to the production of supersymmetric particles in pairs, and their decay chains would terminate in a stable LSP, which is often considered to be the lightest neutralino $\tilde{\chi}_1^0$. Such an LSP would have the required characteristics for a dark matter particle, being weakly interacting, neutral, and massive, thereby providing a solution to another shortcoming of the SM.

The MSSM lagrangian, with $\mathcal{L}_{\text{KE}}$, $\mathcal{L}_{\text{interaction}}$ and $\mathcal{L}_{\text{W}}$, describes the SM particles and their respective supersymmetric partners. Nonetheless, as it stands, supersymmetry is not broken, and all particles would be massless. Since the SM particles have mass, this means that, if SUSY is realized in nature, it must be a broken symmetry. The mechanism behind the breaking of supersymmetry is yet to be fully comprehended. As a result, a set of "soft" mass terms are introduced. For a single quark and lepton superfields generation, Equation 2.19 introduces the mass terms for the scalar members of the chiral superfields and for the gaugino members of the vector superfields. These mass terms are referred to as "soft" as they are selected in a way that prevents the reintroduction of quadratic divergences. In the lagrangian $-\mathcal{L}_{\text{soft}}$ (Equation 2.19), the "soft" operators are constrained to have a dimension of at most 3. This limitation implies that the allowed "soft" operators, which are mass terms, can be bi-linear mixing terms (referred to as B terms), or tri-linear scalar mixing terms (referred to as A terms). The B term introduces mixing between the scalar components of the two Higgs doublets, where the parameter μ is the Higgs mass parameter. The mass terms m_1 and m_2 are associated with the Higgs fields, H_1 and H_2, which are part of the two Higgs doublets. In the presence of non-zero A terms, the scalar counterparts of the left- and right-handed fermions can mix. The mass terms M_3, M_2 and M_1 represent the mass associated with the superfields $\widetilde{G^\alpha}$, $\widetilde{W^j}$ and $\widetilde{B}$ respectively, as well as their conjugates. The masses of physical states are obtained by diagonalizing the mass terms in the lagrangian $-\mathcal{L}_{\text{soft}}$.

$$\begin{aligned}
-\mathcal{L}_{\text{soft}} &= m_1^2 \left|H_1\right|^2 + m_2^2 \left|H_2\right|^2 - B\mu\epsilon_{ij}(H_2^i H_2^j + \text{h.c.}) \\
&+ \tilde{M}_Q^2 \widetilde{Q}_L^* \widetilde{Q}_L + \tilde{M}_U^2 \widetilde{U}_R^* \widetilde{U}_R + \tilde{M}_D^2 \widetilde{D}_R^* \widetilde{D}_R + \tilde{M}_\Psi^2 \widetilde{\Psi}_L^* \widetilde{\Psi}_L + \tilde{M}_R^2 \widetilde{R}^* \widetilde{R} \\
&+ \frac{1}{2}\left[M_3 \widetilde{G^\alpha}^C \widetilde{G^\alpha} + M_2 \widetilde{W^j}^C \widetilde{W^j} + M_1 \widetilde{B}^C \widetilde{B}\right] \\
&+ \frac{g}{\sqrt{2}M_W}\epsilon_{ij}\left[\frac{M_D}{\cos\beta} A_D H_1^i \widetilde{Q_L^j} \widetilde{D_R}^* + \frac{M_U}{\sin\beta} A_U H_2^j \widetilde{Q_L^i} \widetilde{U_R}^* + \frac{M_R}{\cos\beta} A_E H_1^i \widetilde{\Psi_L^j} \widetilde{R}^* + \text{h.c.}\right].
\end{aligned} \tag{2.19}$$

The lagrangian for the MSSM, $\mathcal{L}_{MSSM}$, contains 18 independent parameters that correspond to the SM ones plus 104 which mostly originate from "soft" breaking terms. Since there are more than 100 parameters involved, it is practical to introduce the concept of SUSY Simplified Model Spectra (SMS). A SMS scenario introduces a specific set of superparticles and their decays to SM in order to produce a specific SUSY signature, where the principal free parameters are the masses of the introduced supersymmetric particles and branching ratios of their decays.

2.2.1 The case for the lightest stop

The third generation of supersymmetric particles, such as the stop, are often considered as the most promising candidates for discovering SUSY. Equation 2.20 represents the mass matrix for the top squark of the MSSM. The mass matrices for the quarks of the other families are similar, with the necessary variable substitutions. This mass matrix $M_{\tilde{t}}^2$ is defined as follows:

$$M_{\tilde{t}}^2 = \begin{pmatrix} \tilde{M}_Q^2 + m_t^2 + m_Z^2(\frac{1}{2} - \frac{2}{3}\sin^2\theta_W)\cos 2\beta & m_t(A_T + \mu\cot\beta) \\ m_t(A_T + \mu\cot\beta) & \tilde{M}_U^2 + m_t^2 + \frac{2}{3}m_Z^2\sin^2\theta_W\cos 2\beta \end{pmatrix}, \tag{2.20}$$

where $\tilde{M}_Q^2$ is the left-handed squark mass, $\tilde{M}_U^2$ is the right–handed up–type squark mass, A_T denotes the top quark tri–linear coupling, m_t is the mass of the SM top quark, μ the Higgs bi–linear mixing parameter, and β the Higgs VEV–specific parameter, where $\tan\beta$ is the ratio of the two VEVs. The off-diagonal elements in the mass matrices are proportional to the quark mass and directly contribute to the mass mixing effects mentioned earlier.

When SUSY is broken, the scalar partners of an SM fermion acquire a different mass from their SM partner, with the mass splitting between scalar mass eigenstates being proportional to the mass of the SM fermion. Because the top quark is the heaviest fermion of the SM, the mass splitting between its chiral supersymmetric partners can be the largest among all squarks. As a result, the lighter supersymmetric scalar partner of the top quark, stop ($\tilde{t}_1$), could be the lightest squark. The higher masses of the third generation SM particles can also result in more pronounced mass mixing effects in the SUSY sector. Another motivation for the search of the stop is that it is enough that the stop is of the order of TeV for the hierarchy problem to be more naturally solved [34].

2.2.2 The four-body decays of stop

If SUSY is realized in nature, cosmological observations imply that for many models the lightest top squark is almost degenerate with the LSP [13]. The current measurement of the Cold Dark Matter (CDM) density, denoted by $\Omega_{CDM}h^2$, is 0.1153 ± 0.0019[35]. To explore the potential relationship between the mass difference $\delta m = m_{\tilde{t}1} - m\tilde{\chi}_1^0$, and the mass of the $\tilde{\chi}_1^0$ as a function of $\Omega\tilde{\chi}h^2$, where the $\tilde{\chi}_1^0$ is the CDM particle, Figure2.5 from [36] is presented. Given the observed value of Ω_{CDM}, this figure suggests that the mass difference Δm should not exceed approximately 50 GeV, with a $\tilde{\chi}_1^0$ in the GeV– TeV range.

When Δm is smaller than the mass of the *W* boson (m_W), known as the compressed scenario, the two–body ($\tilde{t}_1 \to t\tilde{\chi}_1^0$, $\tilde{t}_1\tilde{t}_1 \to b\tilde{\chi}_1^+$) and three–body ($\tilde{t}_1 \to bW^+\tilde{\chi}_1^0$) decays of the lightest top squark are kinematically forbidden. In this scenario, the stop may decay via off–shell top quarks denoted as the four-body decay of stop ($\tilde{t}_1 \to b\mathrm{f}\bar{\mathrm{f}}'\tilde{\chi}_1^0$), or via the chargino–mediated decay ($\tilde{t}_1 \to b\tilde{\chi}_1^+ \to b\mathrm{f}\bar{\mathrm{f}}'\tilde{\chi}_1^0$), where in both cases the *W* is off–shell. The chargino–mediated decay of stop is only possible if the mass of the lightest chargino is lower than the top squark mass. Another possible decay mode is the loop-induced flavor changing neutral current process ($\tilde{t}_1 \to c\tilde{\chi}_1^0$), which can be less favorable depending on the parameters of the model compared to the four–body decay of stop [37]. Figure 2.6 represents the simplified models of the production of $\tilde{t}_1\bar{\tilde{t}}_1$ in proton–proton collisions in the compressed scenario. The four–body decays of the stop are one of the most motivated of its decays, because taking place in a kinematic region that is compatible with a scenario of annihilation with the $\tilde{\chi}_1^0$, considered to be the CDM [13, 36]. It is, therefore, the focus of this thesis.

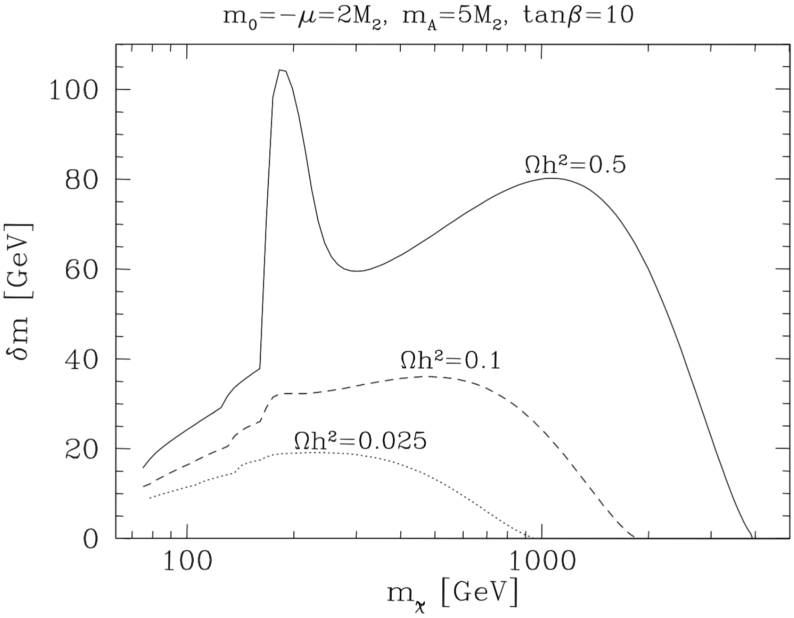

Figure 2.5: Contours of constant $\Omega_{\tilde{\chi}}h^2$ = 0.5 (solid), 0.1 (dashed) and 0.025 (dotted) in the $(m_{\tilde{\chi}_1^0}, \delta m)$ plane, where $\delta m = m_{\tilde{t}_1} - m_{\tilde{\chi}_1^0}$. The parameters μ, m_0 and m_A are fixed to be multiples of $M_2 \simeq 2m_{\tilde{\chi}_1^0}$, as indicated, whereas $\tan\beta$ = 10 is kept fixed. The parameter A_0 varies between about 2.5m_0 and 3.2m_0, with larger A_0 values corresponding to smaller values of δm. In this Figure, m_0 is the mass of a supersymmetric fermion, A_0 a trilinear soft breaking parameter at the Grand Unification scale $M_X = 2 \cdot 10^{16}$, μ the higgsino mass parameter and m_A the mass of the CP-odd Higgs boson.

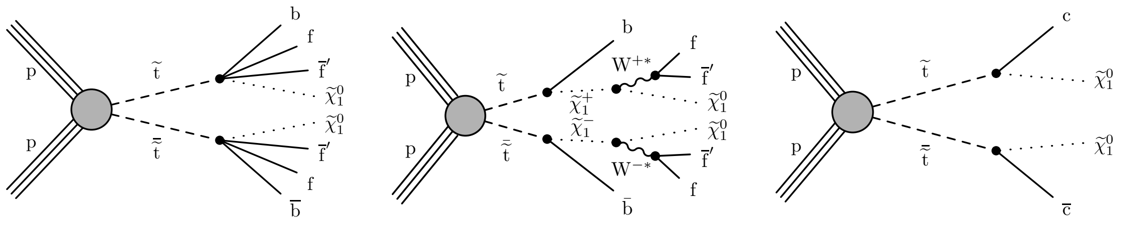

Figure 2.6: Diagrams for the direct top squark production in the compressed scenario with four–body (left), chargino–mediated (middle), and loop-induced flavor changing neutral current (right) decays in simplified models.

3

Experimental apparatus

Contents

3.1 The Large Hadron Collider (LHC)

The LHC located at CERN beneath the border of France and Switzerland near Geneva. As the most massive and energetic particle accelerator worldwide, the LHC is capable of generating three types of collisions: proton-proton, proton-ion, and ion-ion, with its primary purpose being the collision of beams of protons or heavy ions. This thesis examines data from proton-proton collisions.

The LHC is situated in a 26.6 km circumference tunnel, approximately 100 m below the ground level. This tunnel was initially constructed in the CERN's accelerator complex for the Large Electron-Positron Collider (LEP) [38]. Detailed information on the LHC is available in Refs. [39, 40]. Figure 3.1 illustrates the geographic location of the LHC and the layout of the accelerator, including the main detectors' locations. There are four main beam crossing points that host four primary detector experiments, as well as several other access points to the accelerator tunnel. In an underground cavern at point 5 on the accelerator ring, the CMS detector is installed.

The protons used for the collisions originate from ionized hydrogen atoms. Then, they undergo a series of accelerations, increasing their kinematic energy at each stage: Linac2 [41] boosts the energy up to 50 MeV, the Proton Synchrotron (PS) Booster [42] increases it to 1.4 GeV, the PS [43] elevates it further to 25 GeV, and the Super Proton Synchrotron (SPS) [44] brings it to 450 GeV. After these stages, the protons are injected into the LHC. Once in the LHC, the proton beams are accelerated to the operating energy and directed to collide at the interaction points of the accelerator ring. After being injected into the LHC, the proton beams are accelerated to the operating energy and focused to collide at the interaction points along the accelerator ring.

The centre-of-mass energy achieved by the LHC in its proton-proton collisions reaches 13 TeV, which represents the highest energy observed in a laboratory environment for particle collisions. The peak luminosity produced by the LHC is approximately $2 \times 10^{34}\,\mathrm{cm}^{-2}\,\mathrm{s}^{-1}$, resulting in the collection by the detectors at the LHC of around 150 fb^{-1} datasets of 13 TeV proton-proton collisions. However, the large instantaneous luminosity also produces a significant background of pileup events, with an average 50 collisions occurring per bunch crossing.

The LHC machine has the potential for improved performance after suitable upgrade to the machine. The new phase of the accelerator, known as the High Luminosity LHC (HL-LHC), is expected to start in 2027 [45]. The upgrade program aims to achieve $14\,\mathrm{TeV}$ of centre-of-mass energy for proton-proton collisions, increase the instantaneous luminosity by a factor of five, and achieve an order of magnitude increase in the integrated luminosity, corresponding to datasets of approximately $3000\,\mathrm{fb}^{-1}$. The increased instantaneous luminosity will lead to a higher background of pileup events, estimated to be 140–200 events per bunch crossing, which is approximately an order of magnitude greater than the current level.

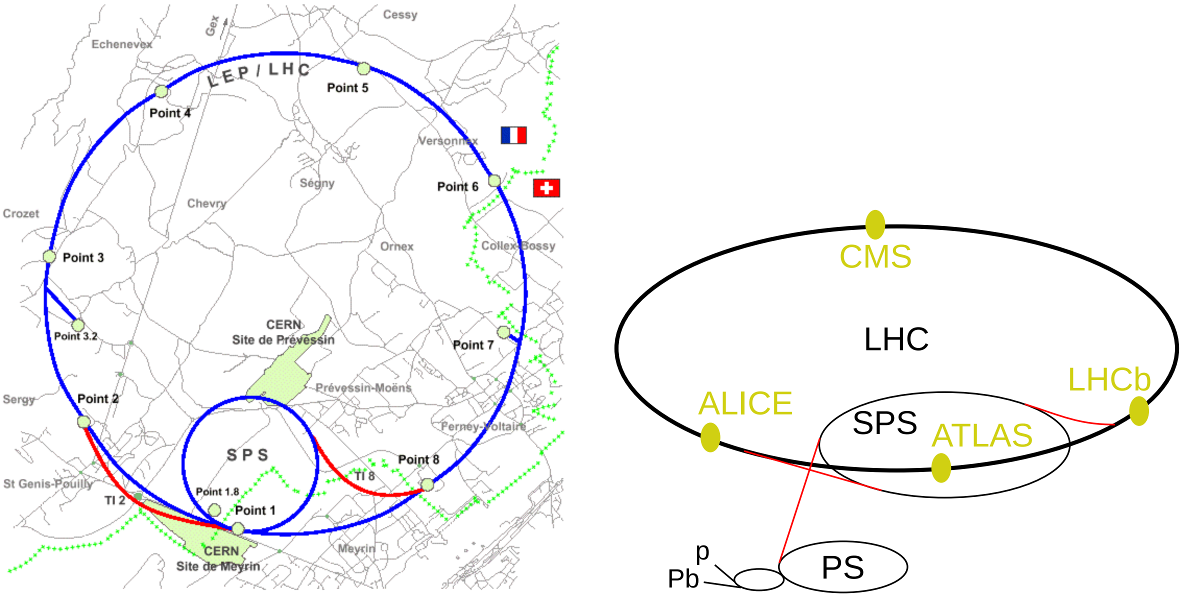

Figure 3.1: The map of the CERN LHC site at Geneva (left), and the scheme of the accelerator with the four main detectors and interaction points (right).

3.2 The Compact Muon Solenoid (CMS) detector

The CMS is general-purpose particle physics detector that operates at the LHC at CERN. Being located at an interaction point of the LHC, the detector has been designed to yield head-on collisions of two proton (ion) beams of 7 TeV (2.75 TeV per nucleon) each, with a design luminosity of $10^{34}\,\mathrm{cm}^{-2}\,\mathrm{s}^{-1}$ ($10^{27}\,\mathrm{cm}^{-2}\,\mathrm{s}^{-1}$). In order to meet the goals of the LHC program, the CMS detector was designed to have radiation-hard front-end electronics and detectors with specific objectives in mind: accurate muon identification and momentum resolution, precise resolution and efficiency in reconstructing charged-particle momentum, reliable electromagnetic energy resolution, and effective resolution for missing-transverse-energy and dijet-mass measurements.

In terms of shape, the CMS detector can be described as a cylindrical structure with a length of 21.6 m, a diameter of 14.6 m. It consists of several distinct layers or sub-detectors, arranged in an "onion-like" structure. The primary distinguishing characteristic of the CMS apparatus, which contributes to its nomenclature, is its superconducting solenoid. This solenoid possesses dimensions of 13 m in length and 6 m in diameter, generating an axial magnetic field measuring 3.8 T. The superconducting solenoid surrounds an all-silicon pixel and strip tracker, a lead-tungstate scintillating-crystals Electromagnetic Calorimeter (ECAL), and a brass-scintillator sampling Hadron Calorimeter (HCAL). Additionally, the iron yoke of the flux-return is equipped with four stations of muon detectors, effectively covering a significant portion of the 4π solid angle. The CMS experiment employs a coordinate system with its origin positioned at the nominal collision point within the experiment. The x–axis extends radially inward, towards the center of the LHC, the y–axis is oriented in an upward vertical direction perpendicular to the LHC plane, and the z–axis aligns with the anti–clockwise beam direction. The polar angle θ is determined from the z–axis, the azimuthal angle ϕ is determined with respect to the x–axis within the x–y plane, and r is used to represent the radial coordinate. Denoted as pseudorapidity, η, is defined as $\eta = -\ln[\tan(\theta/2)]$. Separated by pseudorapidity, the particle detection systems are placed in two regions: the barrel and endcaps, with $|\eta| < 1.4$ and $1.4 < |\eta| < 2.5$, respectively. The pseudorapidity coverage is extended by forward calorimeters that cover $5.2 < |\eta| < 6.6$.

The detector is almost entirely hermetic, allowing for energy balance measurements in the plane transverse to the beam directions. A schematic drawing of the detector is displayed in Figure 3.2. Subsequently, the following paragraphs provide a concise summary of the CMS subdetector systems. For further details about the CMS detector please refer to Ref. [46].

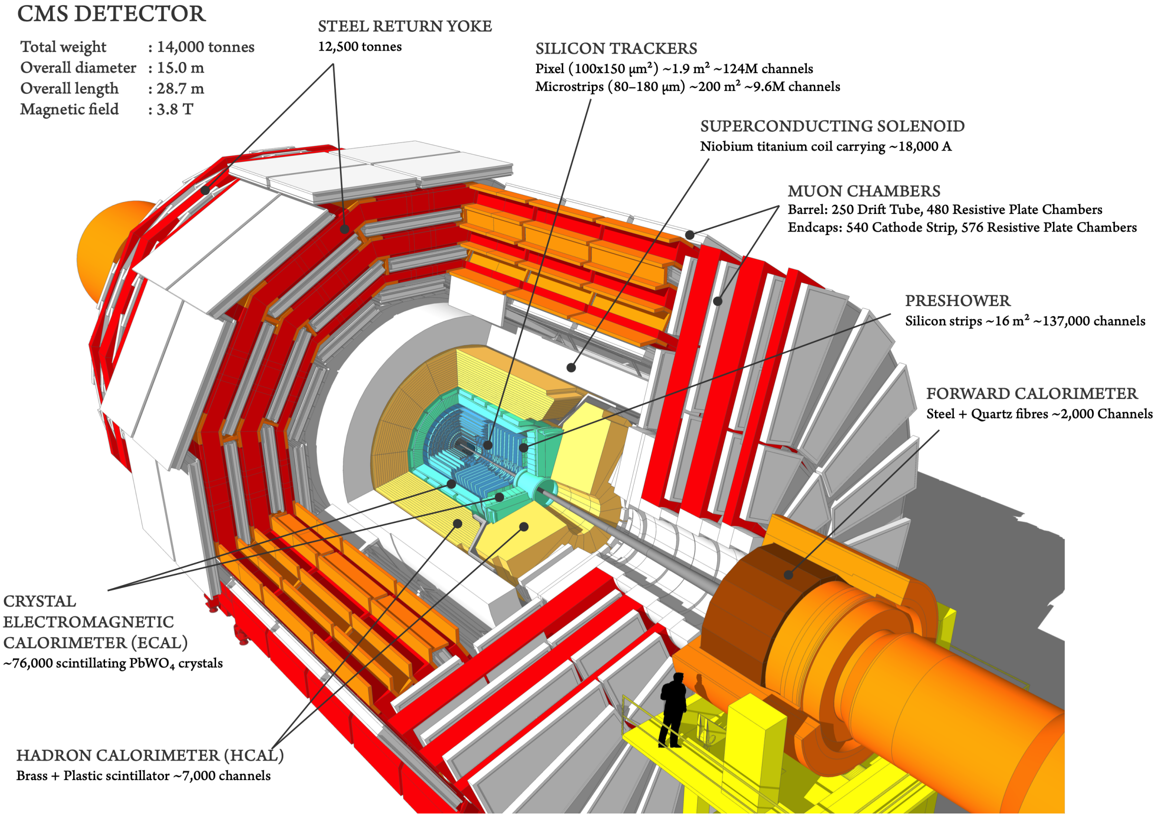

Figure 3.2: A schematic representation of the CMS detector and main subdetector systems.

3.2.1 Inner tracking system

The inner tracking system measures charged particle trajectories and provides a precise reconstruction of secondary vertices. The position of the charge particles is measured by their interaction with the silicon trackers placed within the volume of the inner tracker. Operating at high luminosity, the tracking system was designed to face challenges such as dealing with a large number of overlapping proton–proton interactions and maintaining a balance between detector granularity, speed, radiation hardness, and material minimization. This system is positioned closest to the beamline, covering $|\eta| < 2.5$, and is composed entirely of silicon detectors. Silicon detectors operate based on the principle of a reverse biased diode, which creates a depletion zone with an electric field between the diode contacts. Through ionization, free electrons and holes are generated when a charged particle passes through the depletion zone. Electrons and holes flow in opposite directions towards the diode contacts, producing an electrical pulse that can be detected. Thus, measuring the position a charged particle passed through. By covering a volume with multiple silicon detectors, the trajectory of the charged particles can be measured.

Pixel detectors and silicon strip trackers compose the inner tracking system, and are used in their respective tracker subsystems: the Pixel Detector and the Silicon Strip Tracker. Both subsystems have barrel and endcap layers. Figure 3.3 depicts a schematic representation of the CMS tracker, specifically highlighting the various detector subsystems, in an r–z plane. A comprehensive discussion of the tracker and its performance analysis is available in Refs. [47, 48].

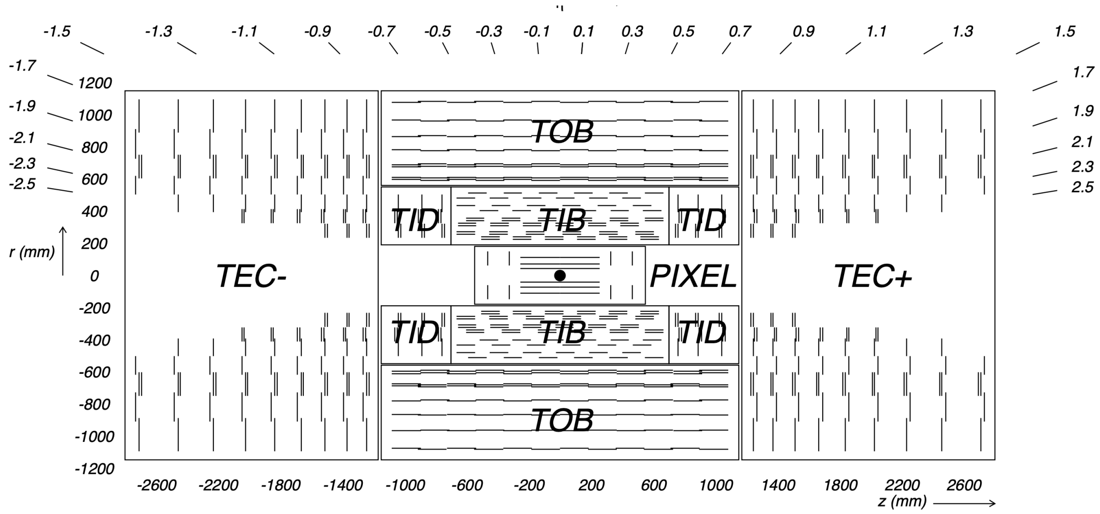

Figure 3.3: Schematic cross section through the CMS tracker. Each line represents a detector module. Double lines indicate back-to-back modules which deliver stereo hits.

Closest to the interaction point is the Pixel Detector subsystem. It measures with precision r-ϕ and z tracking points, achieving a small impact parameter resolution. Therefore, the Pixel Detector is important for the secondary vertex reconstruction. Each pixel cell has a size of 100 × 150 µm^2 in order to achieve a similar track resolution in both r-ϕ and z directions. This subsystem contains 66 million pixels covering an area of 1.06 m^2 and is subdivided in three barrel layers and two endcap disks. This arrangement gives a cover over the range $|\eta| < 2.5$. The low η region, closest to the interaction point, was designed to be radiation tolerant due to the very high track rate and particle fluences. Thus, a n+ pixel on n-substrate detector design was used, which permits partial operation at very high particle rate. The detector exploits the 3.8 T magnetic field and the geometric arrangement to achieve subpixel resolution. This is achieved due to the resulting Lorentz drift that leads to charge spreading over more than one pixel. Thus, a spacial resolution in the range of 15–20 μm is achieved.

The Silicon Strip Tracker uses single sided p–on–p type silicon micro–strip sensors totaling 9.3 million sensors across 198 m^2. This system is subdivided in the Tracker Inner Barrels (TIBs), the Tracker Inner Disks (TIDs), the Tracker Outer Barrels (TOBs), and the Tracker End Caps (TECs) and arranged as shown in Figure 3.3. The size of the strips and the thickness of the sensors differ between the different layers. Depending on the η of the track, the Silicon Strip Tracker offers 8 to 14 high precision measurements of the track position.

3.2.2 Electromagnetic calorimeter

There are three main functions of the ECAL: measuring the energy of electromagnetic radiation, identification of electromagnetic particles (electrons and photons), and enabling triggering capabilities. To perform this functions the ECAL uses lead-tungstate (PbWO_4) crystals, 61200 crystals in the barrel region (EB) with Avalanche photodiodes as photodetectors, and 7324 crystals in each of the endcaps (EEs) with vacuum phototriodes. The barrel and the two endcap sections cover the range $|\eta| < 1.479$ and $1.479 < |\eta| < 3.0$, respectively. In the endcaps, a preshower detector is mounted in front of the crystals to identify neutral pions. The preshower is a double layered sampling calorimeter of lead radiators that start an electromagnetic followed by silicon strip sensors utilized to quantify the energy deposited. The lead-tungstate crystals were chosen given their high density ($8.28\,\mathrm{g\,cm^{-3}}$), their short radiation length ($0.89\,\mathrm{cm}$) and their small Molière radius ($2.2\,\mathrm{cm}$), providing both the detection and absorption media of the calorimeter. Studies on the decays of the *Z* boson and the Higgs boson indicate that the raw energy resolution of the calorimeter is 2–5% for electrons and 1.1–2.6% in the barrel and 2.2–5% in the endcaps for photons. For further reading on the CMS ECAL, please see Ref. [49].

Upon entering the lead-tungstate crystals, electrons and photons initiate an electromagnetic shower. This shower results in a blue–green scintillation light emitted by the crystals that is then measured by the photodetectors at the other end of the crystal. Therefore, the crystals serve their purpose of measuring and absorbing the electromagnetic particles. These crystals have a scintillation decay time that is comparable to the bunch crossing time of the LHC: $\approx$ 80% of the light is emitted in 25 ns. The dimensions of the crystals match their Molière radius, which means that the electromagnetic showers leak into adjoining crystals. Therefore, clusters of crystals are used to measure the energy of the particles. This feature is also used in the particle reconstruction algorithms. An example of a PbWO_4 crystal used in the endcaps of the ECAL is shown in Figure 3.4.

The barrel region of the ECAL uses 360 PbWO_4 crystals in ϕ and 170 crystals in η. To prevent particles from passing through gaps in the detector, the crystals are positioned at a slight angle relative to the direction leading to the nominal interaction point. The PbWO_4 crystals in the barrel

Figure 3.4: An endcap PbWO$_4$ crystal with a phototriode attached.

have a length of 230 mm, the dimensions of the front face are $\approx$ 22×22 mm^2, and at the rear face are 26×26 mm^2. These crystals have $\approx$ 25.8 radiation lengths.

In the end caps regions of the ECAL, the PbWO$_4$ crystals are arranged in a rectangular grid along the x and y–axis. Crystals are also mounted at a slight angle to the interaction point to avoid particles escaping the detector. To do so, the crystals are oriented towards a focal point located 1300 mm beyond the nominal interaction point. The PbWO$_4$ crystals in the endcaps have a length of 220 mm, the dimensions of the front face are $\approx$ 28.62×28.62 mm^2, and at the rear face are 30×30 mm^2. These crystals have $\approx$ 24.7 radiation lengths.

3.2.3 Hadron calorimeter

The HCAL is designed to measure the energy of hadrons that penetrate the ECAL and interact with the brass absorbent material. The triggering capabilities of this subdetector are also used. The HCAL is divided in the barrel detector (HB) and two endcap detectors (HE) that encapsulate the ECAL. The HB and HE cover the range $|\eta| < 3.0$. In addition to the HB and HE detectors, the HCAL is complemented with two subdetectors. Positioned at a distance of 11.15 m from the nominal interaction point in both directions, forward calorimeters (HF) extend the HCAL'cover range to $|\eta| < 5.2$. Located outside the solenoid, the outer hadron calorimeter (HO) ensures adequate sampling depth for the central pseudorapidity region ($|\eta| < 1.3$). This is necessary because the the EB and HB do not provide enough containment for hadron showers. Figure 3.5 shows a schematic of a slice of the HCAL. For further reading on the CMS HCAL, please see Refs. [50, 51].

The HB and HE detectors are sampling calorimeters composed of layers of brass interleaved with tiles of plastic scintillators, which are the absorber and active material respectively. Brass has a radiation length of 1.49 cm and is non–magnetic, for this reasons, it was chosen as the absorber material. The region between the outer boundary of the ECAL (r = 1.77 m) and the inner boundary of the magnet coil (r = 2.95 m) imposes radial constrains to the HCAL barrel. At the same time, CMS was designed to maximize the amount of absorber material before the solenoid. The presence of these two constraints led to the selection of plastic scintillator as the suitable material for the active

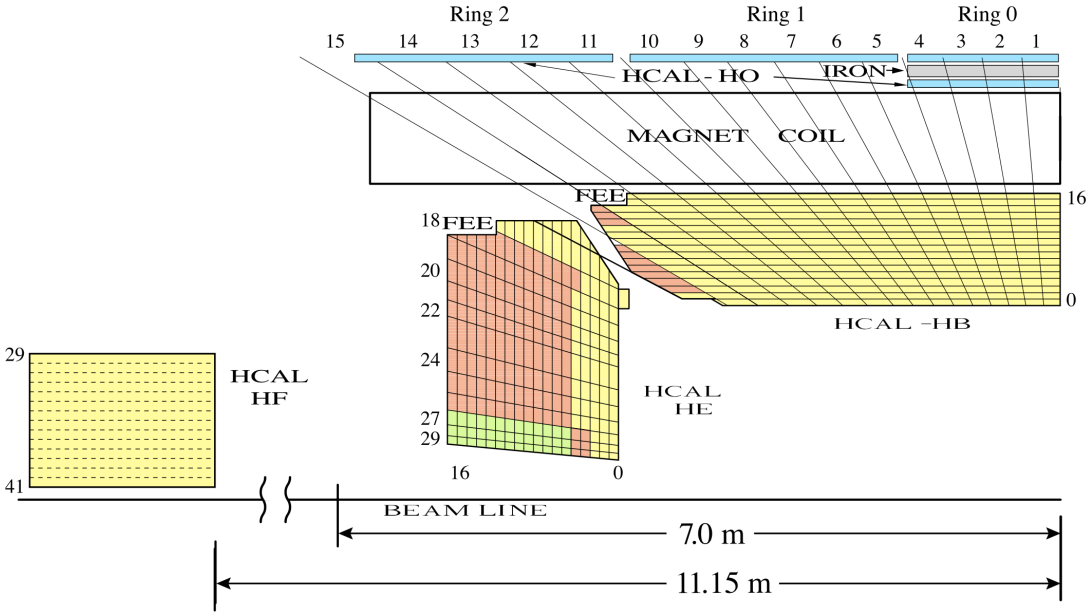

Figure 3.5: Schematic of the CMS HCAL in an r-z slice.

material. Wavelength shifting fibers are used to collect the scintillation light.

The HB detector spans the range of $|\eta| < 1.3$ and is split into two half–barrel section. Each half–barrel section consists of 18 wedges. Each wedge spans an azimuthal angle of 20° and is further equally divided into four azimuthal angle sectors. The plastic scintillator is segmented in 16 η sectors, ensuring a 0.087 × 0.087 segmentation in the $\eta \times \phi$ space. At $\eta = 0$, the thickness of the detector is 5.8 hadronic interaction lengths, which progressively increases to 10 as the absolute value of η reaches 1.2.

The HE detectors encompass the range of $1.3 < |\eta| < 3.0$ and consists of brass disks interleaved with scintillator tiles with no "dead" material. Figure 3.5 illustrates that each HE is divided into 14 towers (16–29) in η. The towers closest to the beam line have a segmentation of 10°, while the ones with the higher η have a segmentation of 5°.

3.2.4 The muon system

Muon detection is essential to pursue the LHC physics program. The muon system of the CMS is of central importance, as it is implied in the name. Similar to the previous subdetectors, the muon system has a cylindrical barrel section located outside of the solenoid and 2 endcap regions. Its three main functions are: the identification of muons, the measuring of muon momentum and triggering. The high magnetic field of the solenoid and its flux-return yoke enable the precise momentum resolution and triggering capability. The flux-return yoke also has the role of hadron absorber for the muons identification. For the muon identification, depending on the radiation environment, the muon system utilizes three distinct types of gaseous particle detectors: Drift Tubes (DTs) stations at $|\eta| < 1.2$, Cathode Strip Chambers (CSCs) at $0.9 < |\eta| < 2.4$, and Resistive Plate Chambers (RPCs) at $|\eta| < 1.9$. The muon rates in the barrel region are the lowest, therefore DTs are used. It is in the encap region where the muon rates are high, hence CSCs are utilized. The RPCs where added as a complementary system to both the barrel and endcaps regions. They offer a faster signal but at the expense of a relatively less precise resolution compared to the DTs and CSCs. The use of RPCs it crucial to address the challenge of the uncertain on background rates. Figure 3.6 illustrates the layout of the detector components in the η plane highlighting the muon detectors. The resolution for muons with momenta up to approximately 100 GeV is 1% in the barrel and 3% in the endcap, as reported in [52].

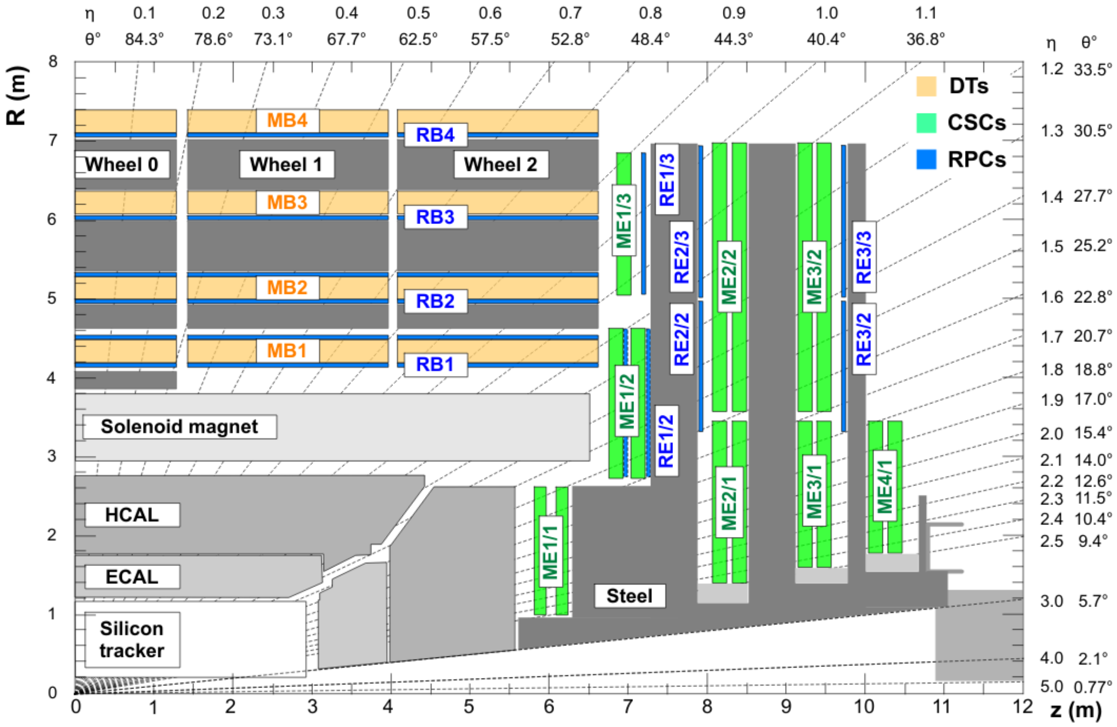

Figure 3.6: A logitudinal representation of the CMS detector showing the position of the subdetectors in the η plane with the muon detectors highlighted.

3.2.5 Trigger

In order to use only the most significant proton-proton collision events for physics analyses, a two-level trigger system is employed [53, 54]. The first level trigger, Level 1 (L1), is designed to handle a collision rate of 1 GHz and reduce the front end readout bandwidth to 100 kHz of 1 MB events. It is implemented in custom hardware that selects detector signals in accordance with streamlined definitions of physical objects such as electrons/photons, muons, and jets. The output of the L1, at a rate of 100 kHz, is further reduced to 1 kHz for offline storage by the High Level Trigger (HLT). The HLT implements more refined reconstruction algorithms in software and runs on a farm of off-the-shelf computers. The HLT's decision on whether to retain an event is considered final in the data acquisition process. The data collected are then processed and analyzed offline.

3.2.6 CMS at the High Luminosity LHC

In order to be prepared for HL-LHC phase and its challenges with respect to the data acquisition speed and the radiation hardness, all CMS subdetectors will undergo an upgrade. The forthcoming upgrades will involve various components, including the pixel tracker upgrades [55], upgrades to the inner and outer tracker [56–58], upgrades to the ECAL [59], implementation of a new high granularity HCAL [60], enhancements to the outer muon detectors [61], and the installation of a new Timing Detector. The new Timing Detector will offer a timing layer to measure Minimum Ionizing Particless (MIPs) with a time resolution of 30–40 ps, denoted as the MIP Timing Detector (MTD) [62], and will be installed between the tracker and the ECAL. The MTD upgrade will provide timing information to the CMS detector, a feature that is not currently present. The main purpose of this upgrade is to reduce the effects of the high levels of pileup expected at the HL-LHC. By exploiting the fact that the individual interactions do not all occur at precisely the same time but over time with a RMS of 180–200 ps, charged tracks will be assigned to the respective interaction vertices. The LIP CMS group has a significant role in the development of the electronics readout for this detector. As part of my Experimental Physics responsibilities within the collaboration I contributed to the testing, characterization and software development for the ASIC that is going to be responsible for the detection of the MIPs in the Barrel Timing Layer (BTL). Figure 3.7 illustrates an overview of the BTL.

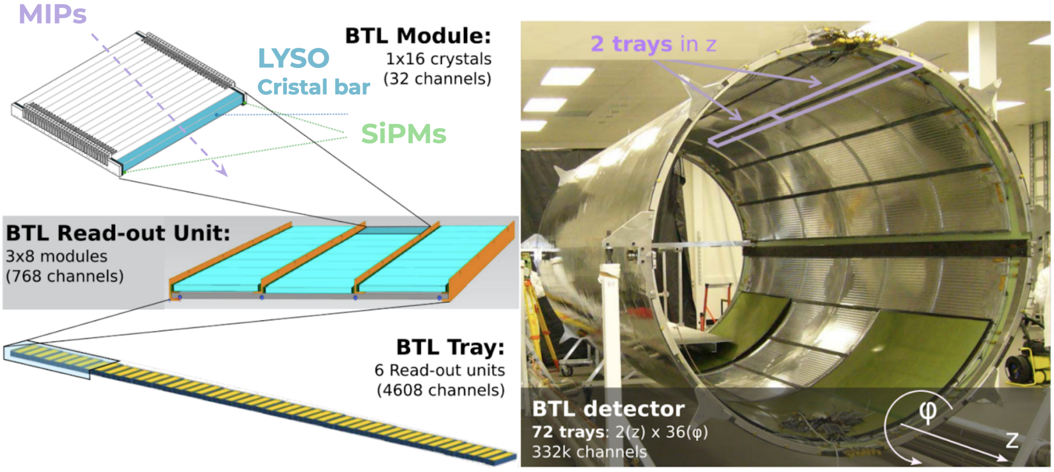

Figure 3.7: An overview of the BTL.

4

Event reconstruction and object selection

Contents

The four-body decay of stop ($\widetilde{t}_1 \rightarrow bff'\widetilde{\chi}^0_1$) signal topology is characterized by the presence of a soft charged lepton from the expected soft decays given the small mass difference between the $\widetilde{t}_1$ and the $\widetilde{\chi}^0_1$, high $E_{\mathrm{T}}^{\text{miss}}$ due to the ν and $\widetilde{\chi}^0_1$ escaping undetected as $E_{\mathrm{T}}^{\text{miss}}$, and by the presence of the jets from quarks. A combination of $E_{\mathrm{T}}^{\text{miss}}$-$H_{\mathrm{T}}^{\text{miss}}$ requirement is used to serve for triggering the events during the data-taking period of the CMS Detector. The collected raw data are then re-processed using the best and most updated algorithms offline in order to reconstruct the physical objects needed for this analysis. The output of the offline reconstruction is stored in the Analysis Object Data (AOD) format which is then stored in the NanoAOD [63] that leaves non-essential information for the analysis, hence providing smaller, faster to produce and more manageable datasets.

The reconstruction and identification of the physical objects use the Particle Flow (PF) algorithm[64, 65]. The PF algorithm combines information from all sub-detectors in order to reconstruct all types of particles in the event such as leptons, photons as well as charged and neutral hadrons, together referred as PF objects. It is from this objects that higher-level objects and observables are reconstructed such as jets and H_{T}, an observable which is defined as the scalar p_{T} sum of all jets. Each object and observable used in this analysis will be described further in this chapter. The process of identifying and reconstructing each type of objects in the analysis is done by a dedicated group within the CMS collaboration that studies the performance of the algorithm for the corresponding object and measures the efficiency and misidentification rate of the algorithm.

The choice of the object reconstruction criteria is based on the analysis of the 2016 data [20] while being updated for the newer CMS algorithms. The updated jet identification efficiency is higher than 99%. The *b*-tagging is performed by the DeepCSV [66] algorithm which outperforms the one used for the 2016 data analysis and is used for the validation of the Multivariate Analysis (MVA) tool. A tighter lepton identification was chosen to reduce nonprompt lepton contamination.

Due to the complexity of both the proton-proton (pp) collisions and the complete CMS detector response, it is impractical to theoretically predict experimentally measured distributions. Instead, theory is represented by simulating the collision events while including the detector response. To account for any particularity on the detector response or beam conditions in specific data-taking periods and reduce differences between the reconstruction of simulated objects and the reconstruction of observed data, the simulation is further calibrated.

Recorded data and simulated samples, online triggers, reconstruction tools, and simulation correction are described in the following sections.

4.1 Data samples

The search described in this thesis is performed using data from pp collisions recorded from 2017 to 2018 by the CMS experiment at the LHC at a centre-of-mass energy of 13 TeV corresponding to a luminosity of 41.5 fb^{-1} and 59.8 fb^{-1} respectively. These results are then combined with the result of the search in the data of 2016 [20] with an integrated luminosity of 36.3 fb^{-1}. The final result of this theses corresponds to a total integrated luminosity of 138 fb^{-1}.

The CMS computing infrastructure identifies each dataset with a logical name defined in three steps: the group of triggers that collected the events (eg. "MET") denoted as Primary Dataset (PD), the data-taking epoch ("Run2018D") and the event reconstruction campaign ("Nano25Oct2019-v1"), and the dataset format ("NANOAOD"). This distinction between data-taking periods is done because each data-taking condition can vary between epochs: pileup profiles, online triggers parameters and other particular details can be different. Every data-taking campaign includes reconstruction calibrations that were cross-checked. All the datasets and exact logical names are listed in Tables 4.1 and 4.2.

Table 4.1: 2017 datasets used in this thesis.

Primary dataset	Logical name
MET	`/MET/Run2017B-Nano25Oct2019-v1/NANOAOD`
	`/MET/Run2017C-Nano25Oct2019-v1/NANOAOD`
	`/MET/Run2017D-Nano25Oct2019-v1/NANOAOD`
	`/MET/Run2017E-Nano25Oct2019-v1/NANOAOD`
	`/MET/Run2017F-Nano25Oct2019-v1/NANOAOD`
Single Electron	`/SingleElectron/Run2017B-Nano25Oct2019-v1/NANOAOD`
	`/SingleElectron/Run2017C-Nano25Oct2019-v1/NANOAOD`
	`/SingleElectron/Run2017D-Nano25Oct2019-v1/NANOAOD`
	`/SingleElectron/Run2017E-Nano25Oct2019-v1/NANOAOD`
	`/SingleElectron/Run2017F-Nano25Oct2019-v1/NANOAOD`
JetHT	`/JetHT/Run2017B-Nano25Oct2019-v1/NANOAOD`
	`/JetHT/Run2017C-Nano25Oct2019-v1/NANOAOD`
	`/JetHT/Run2017D-Nano25Oct2019-v1/NANOAOD`
	`/JetHT/Run2017E-Nano25Oct2019-v1/NANOAOD`
	`/JetHT/Run2017F-Nano25Oct2019-v1/NANOAOD`

Table 4.2: 2018 datasets used in this thesis.

Primary dataset	Logical name
MET	`/MET/Run2018A-Nano25Oct2019-v1/NANOAOD`
	`/MET/Run2018B-Nano25Oct2019-v1/NANOAOD`
	`/MET/Run2018C-Nano25Oct2019-v1/NANOAOD`
	`/MET/Run2018D-Nano25Oct2019_ver2-v1/NANOAOD`
Single Electron	`/EGamma/Run2018A-Nano25Oct2019-v1/NANOAOD`
	`/EGamma/Run2018B-Nano25Oct2019-v1/NANOAOD`
	`/EGamma/Run2018C-Nano25Oct2019-v1/NANOAOD`
	`/EGamma/Run2018D-Nano25Oct2019-v1/NANOAOD`
JetHT	`/JetHT/Run2018A-Nano25Oct2019-v1/NANOAOD`
	`/JetHT/Run2018B-Nano25Oct2019-v1/NANOAOD`
	`/JetHT/Run2018C-Nano25Oct2019-v2/NANOAOD`
	`/JetHT/Run2018D-Nano25Oct2019_ver2-v1/NANOAOD`

This analyses is performed using only events recorded in good data-taking conditions. The quality of data recorded by the CMS experiment is assured by a group dedicated to this effort that guarantees that the sub-detectors, triggers and other systems performed well. Good runs are then encoded in "lumisection certificates" for the analyzers to use. Each year has a "golden json" lumisection certificate that filters all the events from proton-proton collisions collected under the best conditions. This events are certified as good to be used in a physics analysis. Hence, the CMS recommendation. The total data passing the 2017 "golden json" certificate corresponds to a recorded luminosity of 41.5 fb^{-1} whilst the 2018 on corresponds to a recorded luminosity of 59.8 fb^{-1}.

From detector noise, reconstruction inefficiencies or beam related effects, data events with anomalously high values of $E_{\mathrm{T}}^{\text{miss}}$ can be produced. To remove these events, further requirements are applied, commonly referred as "MET filters". The following MET filters are used:

- `goodVertices`: sets quality requirements on the reconstructed vertices serving as a primary vertex filter. This filter is applied to both data and Monte Carlo (MC) simulated events.

- `globalSuperTightHalo2016Filter`: removes the background of machine induced particles flying with the beam produced from the collisions of the beam with residual gas inside the LHC vacuum chamber, interactions with the pipe, ect. This filter is applied to both data and MC simulated events.

- `HBHENoiseFilter` and `HBHENoiseIsoFilter`: HCAL noise filter to tackle electronics noise activity that can cause rare anomalous signals in the HCAL sub-detector. These filters are also applied to data and simulated events.

- `EcalDeadCellTriggerPrimitiveFilter`: certain ECAL channels saturate the energy range of their readout that can wrongfully reconstruct high $p_{\mathrm{T}}^{\text{miss}}$ events. With this filter, such type of events are removed. Both data and MC simulated events are filtered accordingly.

- `BadPFMuonFilter`: events where a muon is good enough quality to become a PF candidate but is still too low quality to pass all PF requirements to be reconstructed as a muon. Particularly, punch through pions mistakenly identified as muons. This filter is applied to data and to MC simulated events.

- `eeBadScFilter` and `ecalBadCalibFilterV2`: in 2012, two Electromagnetic Calorimeter Endcap (EE) 5x5 crystal regions where found to give anomalously high energy. This filter is only applied to data events removing events in this region.

These requirements discard less than 0.1% of the data events and are applied prior to the event selection.

4.2 Background and signal event simulation

This analysis makes use of simulated samples for signal and background processes. The SM background MC samples are used to estimate the relation between the control and signal regions for the main background processes, to validate the background estimation methods based on control samples in data, and finally, to predict the contributions from rare processes.

The W+jets and $Z \to \nu\overline{\nu}$+jets processes are generated at Leading Order (LO) accuracy in Quantum Chromodynamics (QCD) by MADGRAPH5_aMC@NLO 2.4.2 [67]. The $t\bar{t}$ process is generated at Next-to-Leading Order (NLO) accuracy in QCD by MADGRAPH5_aMC@NLO. The POWHEG v2.0 [68–75] generators are used for the NLO simulations of single top and associated tW production. Diboson events are simulated at NLO with MADGRAPH5_aMC@NLO and POWHEG. The LO (NLO) NNPDF3.1LO (NNPDF3.1NNLO) [76] parton distribution functions are used consistently with the order of the matrix element calculation in the generated events. Additional rare backgrounds such as $t\bar{t}$ produced in association with a Z boson, W boson, or photon, referred to as $t\bar{t}X$, are generated with MADGRAPH5_aMC@NLO at NLO [77]. Hadronization and showering of events in all generated samples are simulated using PYTHIA 8.230 [78] with the CP5 tune [79] for the underlying event. All SM MC events are passed through a full simulation of the CMS apparatus, where the response of the detector is modeled using the GEANT4 [80] software. Generated events are processed using the same version of the CMS event reconstruction software used as for data. Additional pp collisions in the same or nearby beam crossings (Pileup (PU)) are simulated and overlaid on the main pp interaction in the MC samples, with distributions that reproduce the conditions observed year-to-year in data. For the pair production of top squarks ($\widetilde{t}_1\bar{\widetilde{t}}_1$), simulated samples are produced for $250 < m(\widetilde{t}_1) < 800$ GeV in steps of 25 GeV, and $10 < \Delta m < 80$ GeV in steps of 10 GeV. The cross section for $\widetilde{t}_1\bar{\widetilde{t}}_1$ production, calculated using PROSPINO v.2 [81–87], is computed at Next-to-Next-to-Leading Order (NNLO) accuracy, and includes Next-to-Next-to-Leading logarithmic (NNLL) corrections. This cross section varies between approximately 25 and 0.03 pb as m($\widetilde{t}_1$) goes from 250 to 800 GeV. The generation of signal events with up to two additional jets, which can originate from ISR, is performed with MADGRAPH5_aMC@NLO and then interfaced with PYTHIA for the decay hadronization and showering. The modeling of the detector response for the signal is done with the CMS fast simulation program [88, 89].

Both signal and background simulated samples are corrected to account for discrepancies from data. Control Regions (CRs) in data are used to measure the reconstruction efficiencies of leptons and jets produced by the hadronization of b quarks, "b jets", as well as the b jet misidentification probabilities for light-quark and gluon jets. The corrections are applied as a function of the p_{T} and η of the objects. Fast simulation signal samples are additionally corrected to take into account any potential difference with respect to the GEANT4 modeling. The latter corrections translate into efficiencies applied to b jets, leptons, and the modeling of the missing transverse momentum. The simulations of W+jets, $t\bar{t}$, and signal processes are corrected for the effect of ISR. The modeling of ISR for these processes is checked in data-based control samples that are highly enriched in $t\bar{t}$ or W+jets events. The simulation of $t\bar{t}$ events is tested by comparing the jet multiplicity observed in a control sample with the simulation, and the $t\bar{t}$ and signal samples are reweighted based on this comparison. The simulation of W+jets events is corrected based on the distribution of the sum of the magnitudes of the lepton ℓ transverse momentum $p_{\mathrm{T}}(\ell)$ and the missing transverse momentum in a control sample. This correction is detailed in Section 4.9

Centrally produced MC samples from the `NanoAODv7` campaign corresponding to `Fall17NanoAODv7` and `Autumn18NanoAODv7` were used. The dataset names of the simulated background samples are listed in Table 4.3.

Table 4.3: Simulated samples of SM background and signal processes used in the 2017 and 2018 analysis. For the background samples, the cross sections used for normalisation are also quoted.

Process	**Dataset**	**σ [pb]**
$t\bar{t}$:		
MC@NLO:	/TTJets_TuneCP5_13TeV-amcatnloFXFX-pythia8/	831.8
W+jets:		
$H_\mathrm{T} \in$ [100,200]	/WJetsToLNu_HT-100To200_TuneCP5_13TeV-madgraphMLM-pythia8/	1632
$H_\mathrm{T} \in$ [200,400]	/WJetsToLNu_HT-200To400_TuneCP5_13TeV-madgraphMLM-pythia8/	478.2
$H_\mathrm{T} \in$ [400,600]	/WJetsToLNu_HT-400To600_TuneCP5_13TeV-madgraphMLM-pythia8/	67.30
$H_\mathrm{T} \in$ [600,800]	/WJetsToLNu_HT-600To800_TuneCP5_13TeV-madgraphMLM-pythia8/	14.95
$H_\mathrm{T} \in$ [800,1200]	/WJetsToLNu_HT-800To1200_TuneCP5_13TeV-madgraphMLM-pythia8/	6.138
$H_\mathrm{T} \in$ [1200,2500]	/WJetsToLNu_HT-1200To2500_TuneCP5_13TeV-madgraphMLM-pythia8/	1.253
$H_\mathrm{T} \in$ [2500,+∞]	/WJetsToLNu_HT-2500ToInf_TuneCP5_13TeV-madgraphMLM-pythia8/	0.009582
Z+jets:		
$H_\mathrm{T} \in$ [100,200]	/ZJetsToNuNu_HT-100To200_13TeV-madgraph/	346.7
$H_\mathrm{T} \in$ [200,400]	/ZJetsToNuNu_HT-200To400_13TeV-madgraph/	96.09
$H_\mathrm{T} \in$ [400,600]	/ZJetsToNuNu_HT-400To600_13TeV-madgraph/	13.56
$H_\mathrm{T} \in$ [600,800]	/ZJetsToNuNu_HT-600To800_13TeV-madgraph/	3.966
$H_\mathrm{T} \in$ [800,1200]	/ZJetsToNuNu_HT-800To1200_13TeV-madgraph/	1.818
$H_\mathrm{T} \in$ [1200,2500]	/ZJetsToNuNu_HT-1200To2500_13TeV-madgraph/	0.4438
$H_\mathrm{T} \in$ [2500,+∞]	/ZJetsToNuNu_HT-2500ToInf_13TeV-madgraph/	0.01012
Multiboson:		
WW	/WW_TuneCP5_13TeV-pythia8/	115
WZ	/WZ_TuneCP5_13TeV-pythia8/	47.13
ZZ	/ZZ_TuneCP5_13TeV-pythia8/	16.52
Z/γ^*, $M(ll) \in$ [5,50]:		
$H_\mathrm{T} \in$ [100,200]	/DYJetsToLL_M-4to50_HT-100to200_TuneCP5_13TeV-madgraphMLM-pythia8/	202.8
$H_\mathrm{T} \in$ [200,400]	/DYJetsToLL_M-4to50_HT-200to400_TuneCP5_13TeV-madgraphMLM-pythia8/	53.7
$H_\mathrm{T} \in$ [400,600]	/DYJetsToLL_M-4to50_HT-400to600_TuneCP5_13TeV-madgraphMLM-pythia8/	5.66
$H_\mathrm{T} \in$ [600,+∞]	/DYJetsToLL_M-4to50_HT-600toInf_TuneCP5_13TeV-madgraphMLM-pythia8/	1.852
Z/γ^*, $M(ll) \in$ [50,+∞]:		
$H_\mathrm{T} \in$ [100,200]	/DYJetsToLL_M-50_HT-100to200_TuneCP5_13TeV-madgraphMLM-pythia8/	174
$H_\mathrm{T} \in$ [200,400]	/DYJetsToLL_M-50_HT-200to400_TuneCP5_13TeV-madgraphMLM-pythia8/	53.27
$H_\mathrm{T} \in$ [400,600]	/DYJetsToLL_M-50_HT-400to600_TuneCP5_13TeV-madgraphMLM-pythia8/	7.583
$H_\mathrm{T} \in$ [600,800]	/DYJetsToLL_M-50_HT-600to800_TuneCP5_13TeV-madgraphMLM-pythia8/	1.882
$H_\mathrm{T} \in$ [800,1200]	/DYJetsToLL_M-50_HT-800to1200_TuneCP5_13TeV-madgraphMLM-pythia8/	0.8729
$H_\mathrm{T} \in$ [1200,2500]	/DYJetsToLL_M-50_HT-1200to2500_TuneCP5_13TeV-madgraphMLM-pythia8/	0.2079
$H_\mathrm{T} \in$ [2500,+∞]	/DYJetsToLL_M-50_HT-2500toInf_TuneCP5_13TeV-madgraphMLM-pythia8/	0.003765
Single t:		
s-channel	/ST_s-channel_4f_leptonDecays_TuneCP5_PSweights_13TeV-amcatnlo-pythia8/	3.681
t-channel	/ST_t-channel_top_4f_inclusiveDecays_TuneCP5_13TeV-powhegV2-madspin-pythia8/	136
W-associated	/ST_tW_top_5f_NoFullyHadronicDecays_TuneCP5_PSweights_13TeV-powheg-pythia8/	19.55
Single $\bar{t}$:		
t-channel	/ST_t-channel_antitop_4f_inclusiveDecays_TuneCP5_13TeV-powhegV2-madspin-pythia8/	80.95
W-associated	/ST_tW_antitop_5f_NoFullyHadronicDecays_TuneCP5_PSweights_13TeV-powheg-pythia8	19.55
$t\bar{t}$ $+X$:		
$t\bar{t}$ +γ+Jets	/TTGJets_TuneCP5_13TeV-amcatnloFXFX-madspin-pythia8/	4.09
$t\bar{t}$ +W to $l\nu$	/TTWJetsToLNu_TuneCP5_PSweights_13TeV-amcatnloFXFX-madspin-pythia8/	0.2043
$t\bar{t}$ +W	/ttWJets_TuneCP5_13TeV_madgraphMLM_pythia8/	0.6105
$t\bar{t}$ +Z to $ll/\nu\nu$, $M > 10$	/TTZToLLNuNu_M-10_TuneCP5_13TeV-amcatnlo-pythia8/	0.2529
$t\bar{t}$ +Z to $ll/\nu\nu$, $M > 10$	/TTZToLLNuNu_M-10_TuneCP5_PSweights_13TeV-amcatnlo-pythia8	0.2529
Multijet:		
$H_\mathrm{T} \in$ [100,200]	/QCD_HT100to200_TuneCP5_13TeV-madgraph-pythia8/	2.785×10^7
$H_\mathrm{T} \in$ [200,300]	/QCD_HT200to300_TuneCP5_13TeV-madgraph-pythia8/	1.717×10^6
$H_\mathrm{T} \in$ [300,500]	/QCD_HT300to500_TuneCP5_13TeV-madgraph-pythia8/	3.513×10^5
$H_\mathrm{T} \in$ [500,700]	/QCD_HT500to700_TuneCP5_13TeV-madgraph-pythia8/	3.163×10^4
$H_\mathrm{T} \in$ [700,1000]	/QCD_HT700to1000_TuneCP5_13TeV-madgraph-pythia8/	6802
$H_\mathrm{T} \in$ [1000,1500]	/QCD_HT1000to1500_TuneCP5_13TeV-madgraph-pythia8/	1206
$H_\mathrm{T} \in$ [1500,2000]	/QCD_HT1500to2000_TuneCP5_13TeV-madgraph-pythia8/	98.71
$H_\mathrm{T} \in$ [2000,Inf]	/QCD_HT2000toInf_TuneCP5_13TeV-madgraph-pythia8/	20.2
Signal:		
	/SMS-T2tt_dM-10to80_genHT-160_genMET-80_mWMin-0p1_TuneCP2_13TeV-madgraphMLM-pythia8/	[75.5,0.0326]

4.3 Trigger

In order to select from the produced collisions interesting physics events, a tow-level trigger system is used in the CMS detector. The first level of triggering, designated as the L1 trigger and implemented in custom-designed electronics, has been designed to select *p p* interactions whose final state includes signatures in the form of high transverse energy charged lepton, jets, or high missing transverse energy. The L1 trigger system processes data at a rate of 40 MHz, has a design latency of 128 bunch crossings and an output rate of 100 KHz. The events pre-selected by L1 are fully reconstructed by the HLT system. The HLT is a streamlined version of the CMS offline reconstruction algorithms that runs in a processor farm, thus being fully parallelized. A software trigger system requires a tradeoff between the complexity of the algorithms running with the available computing power, the sustainable output rate, and the selection efficiency. By optimizing for speed some features are sometimes only partially reconstructed and a limited set of information from the physics objects is retrieved. The HLT selection algorithms are organized in paths, an event is accepted by the HLT if it is accepted by any path.

The online selection for the Analysis Region (AR) is based on $E_{\mathrm{T}}^{\text{miss}}$–$H_{\mathrm{T}}^{\text{miss}}$ (MET-MHT) triggers. Data events collected through these HLT triggers are required to have both $E_{\mathrm{T}}^{\text{miss}}$ and $H_{\mathrm{T}}^{\text{miss}}$ above 120 GeV, where $H_{\mathrm{T}}^{\text{miss}}$ is the missing transverse momentum based only on jets, or to fulfill the same $E_{\mathrm{T}}^{\text{miss}}$–$H_{\mathrm{T}}^{\text{miss}}$ conditions and have $H_{\mathrm{T}} > 60$ GeV.

To measure the trigger efficiency of the $E_{\mathrm{T}}^{\text{miss}}$–$H_{\mathrm{T}}^{\text{miss}}$ based HLT paths, the `Single Electron` PDs, an event sample independent to the one used for the analysis is used with the auxiliary triggers `HLT_EleX_WPTight_Gsf_v* (X=35,32)` . To measure the trigger efficiency, the ratio of the number of events selected by the trigger system to the total number of events iscomputed. However, it is not practical to collect large amounts of data without using the trigger system, as the data rate is too high to store everything. Therefore, a different primary dataset collected with a different trigger configuration designed to collect events that are similar to those of the analysis is used. By measuring the trigger efficiency in a sample of events that is independent of the one used for the physics analysis, possible biases are avoided. Events are required to pass the following selection criteria: leading electron $p_{\mathrm{T}} > 40$ GeV, leading jet $p_{\mathrm{T}} > 100$ GeV and $H_{\mathrm{T}} > 200$ GeV. The measured efficiency is then fitted with a function as illustrated in Figure 4.1, for further trigger efficiency studies see appendix A.1.

The $E_{\mathrm{T}}^{\text{miss}}$–$H_{\mathrm{T}}^{\text{miss}}$ based trigger efficiency reaches a plateau at values of $E_{\mathrm{T}}^{\text{miss}}$ of about 280 GeV. The plateau efficiency is 97% and at 235 GeV it drops to around 90%. The drop in efficiency is due to the fact that the number of events that could pass the trigger criteria is higher than the rate at which the trigger can still perform its function. The efficiency is parameterized with a function. This parametrization is used to correct the MC samples. It should be noted that all signal and control regions in this analysis are safely in the trigger efficiency plateau. The correction for the trigger efficiency is applied in all regions. The absolute value of the plateau depends, slightly, on the initial parameters of the fit. This variance is smaller than 1% but to be conservative a systematic uncertainty of 1% is included to take into account such biases in the measurement method.

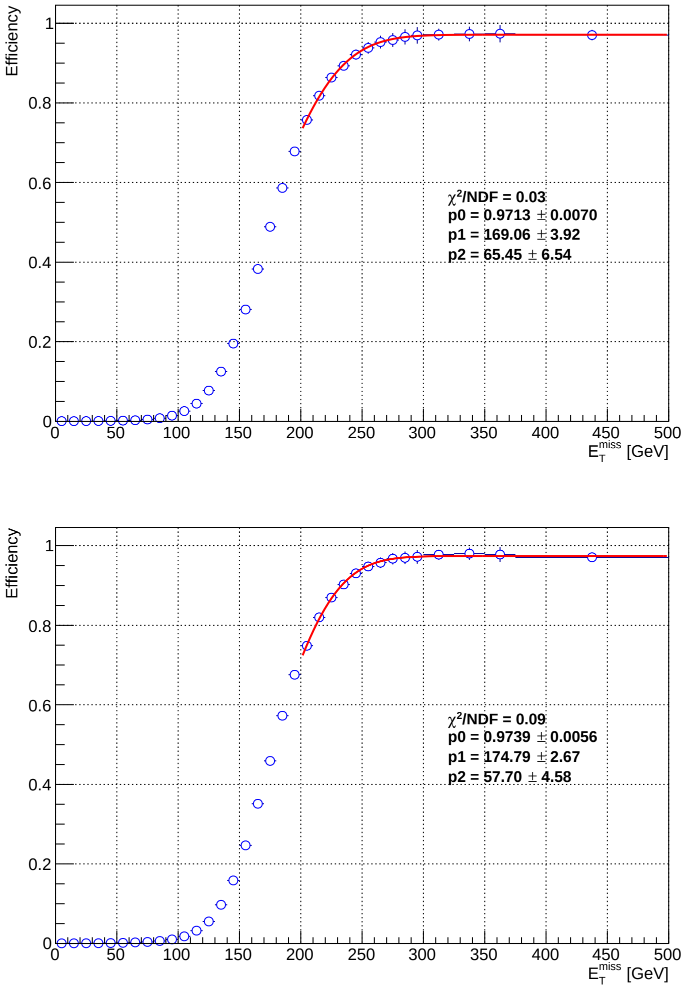

Figure 4.1: Trigger efficiencies as a function of $E_{\mathrm{T}}^{\text{miss}}$ measured in single electron dataset after a requirement on leading electron $p_{\mathrm{T}} > 40$ GeV, jet $p_{\mathrm{T}} > 100$ GeV and $H_{\mathrm{T}} > 200$ GeV fitted with a function. Trigger efficiency measurement for 2017 on the left and for 2018 on the right.

For the Measurement Region (MR), used in the nonprompt lepton background prediction method 6.1, the online selection is based solely on H_{T} in order to enrich the dataset with high jet activity and consequently in nonprompt leptons.

Events passing the HLT paths detailed in Table 4.4 are selected to be analyzed offline.

Table 4.4: HLT trigger paths used in the analyses.

Trigger path	**Kinematic Region**
`HLT_PFMET120_PFMHT120_IDTight_v*`	AR
`HLT_PFMET120_PFMHT120_IDTight_PFHT60_v*`	AR
`HLT_EleX_WPTight_Gsf_v* (X=35,32)`	Trigger efficiency measurement
`HLT_PFHT1050_v*`	MR

4.4 Primary vertex

The Primary Vertex (PV) is taken to be the vertex corresponding to the hardest scattering in the event, evaluated using tracking information alone, as described in Ref. [90]. To identify interaction vertices, tracks consistent with originating from the same collision within the beam interaction region are grouped together. Along the z-coordinate, the reconstructed vertices are required to have a position within the nominal detector center ($|z| < 24$ cm) , and a radial position within the beam spot ($|d_0| < 2$ cm). Because of the presence of additional *pp* interactions, the reconstructed PV of the collision is chosen to be the vertex with the largest value of summed physics object p_{T}^2.

In this context, physics objects are the jets, clustered using a jet finding algorithm with the tracks associated to each vertex as inputs, and the associated missing transverse momentum, taken as the negative vector sum of the p_{T} of those jets.

Due to the high frequency of collisions and other *pp* interactions in the bunch crossing, particles can pollute the currently detected event and clutter the detection environment. In cases of large instantaneous luminosity, these PU collisions are inevitable. Given the high resolution of the CMS detector, the charged particles originating from the PV are distinguishable from the charged particles of PU vertices. From this detection, the neutral activity from the PU vertices can be estimated and removed from the detected event.

4.5 Jets

The final state of this search is expected to contain jet activity and at least one *b* quark flavor jet from each $\widetilde{t}_1$ decay. Jets are obtained by clustering PF candidates using the anti-k_{T} algorithm with the cone parameter value of 0.4 (AK4) [91, 92]. The PU contribution to the jet momentum is partially taken into account by not feeding the charged hadrons originating from a vertex other than the PV to the jet clustering algorithm, this is known as the Charged Hadron Subtraction (CHS) technique. To account for contributions from neutral PU and any inhomogeneity of detector response, the jet p_{T} is further calibrated under the assumption of diffuse noise: PU particles are uniformly distributed on the scale of the jet radius. The jet p_{T} is corrected by subtracting ρA^j, where ρ is the event noise level and A^j is the jet area [93]. In the CMS data, jets reconstructed using the AK4 clustering algorithm from PF physics objects and cleaned from PU using the CHS technique are referred to as "AK4PFchs jets". Furthermore,the reconstructed jet energy is corrected to estimate the genuine jet energy. CMS adopted a factorized solution to the problem of jet energy corrections, where each level of correction is a rescaling of the jet four momentum with a scale factor that depends on various jet parameters (p_{T}, η, area, flavor, etc) and focuses on a different effect such as, the PU contribution, measured in the MC simulation and verified in data; the detector response, $p_{\mathrm{T}}^{\mathrm{reco}}/p_{\mathrm{T}}^{\mathrm{gen}}(p_{\mathrm{T}}, \eta)$, measured in the simulated samples; and the residual data-to-MC correction for the detector response.

Jets are further required to pass the "tight" identification criteria to avoid fake jets which might arise from noise in the calorimeters [94]. Jets with transverse momenta of $p_{\mathrm{T}} > 30$ GeV, $|\eta| < 2.4$ and separated from any isolated light lepton l by $\Delta R(jet, l) > 0.4$ if $p_{\mathrm{T}}(l)/p_{\mathrm{T}}(jet) > 0.5$ are considered in the analysis. They are also used to determine a measure of the hadronic energy in the event: H_{T}, the scalar sum of the transverse momenta of the selected jets.

The tagging of jets produced by the hadronization of *b* quarks (*b* tagging) is performed with the DeepCSV algorithm [66] that uses information from the secondary vertex and is based on a deep neural network. The *b* tagging discriminant is used to tag jets as *b* jets based on a set of working points (loose, medium, tight) and to define further event variables based on the discriminant value or the jet with highest discriminant value. The *b* jet identification working points are defined as the selection values in the discriminator distribution at which the probability of misidentifying a light-flavor jet as a *b* jet is 10%, 1% and 0.1%, respectively, for the loose, medium and tight working points [95].The "loose" and "tight" working points of this algorithm are used to define the *W*+jets and $t\bar{t}$ control regions, respectively.

4.6 Lepton reconstruction

Electron candidates are reconstructed from energy deposits in the ECAL and matched charged particle tracks in the inner tracker obtained using the Gaussian sum filter algorithm [96]. To reduce the number of misidentified electrons, additional constraints on the shape of the electromagnetic shower in the ECAL, the quality of the match between the trajectory of the track, and the ECAL energy deposit around the electron, and the relative HCAL deposit in the electron direction are applied. Electrons are required to have p_{T} above 5 GeV and $|\eta| < 2.5$, with a veto on electron candidates in the ECAL gap region ($1.4442 < |\eta| < 1.5660$). They are identified with requirements on the observables that describe the matching of the measurements in the tracker and the ECAL, the description of energy clusters in the ECAL, and the amount of bremsstrahlung radiation emitted during the propagation through the detector. A loose working point of this algorithm is required for electrons to be selected, which has an average efficiency of 90%.

Muon candidates are reconstructed by combining the information from the silicon tracking systems and the muon spectrometer in a global fit [97] that assigns a quality to the matching between the tracker and muon systems and imposes minimal requirements on the track to reduce the misidentification of muons. The medium working point of this algorithm is required for muons to be selected, which ensures an efficiency above 98%. Muons are required to pass the selection requirements of $p_{\mathrm{T}} > 3.5$ GeV and $|\eta| < 2.4$.

To select electrons or muons originating from the PV, the point of closest approach of the associated track with respect to the PV is required to have a transverse distance $|d_{xy}| < 0.02$ cm, and a longitudinal distance $|d_z| < 0.1$ cm. A lepton is defined as being nonprompt either when it does not originate from the PV, or when a jet is misidentified as a lepton. Background processes with nonprompt leptons are one of the main contributions to the SM background in the signal regions. In this analysis, nonprompt leptons mostly arise from heavy-quark decays in jets produced in association with a *Z* $\rightarrow \nu\bar{\nu}$+jets decay, from multijet production, or from *W*+jets and $t\bar{t}$ events where the prompt lepton was not reconstructed and a different one was accepted. In order to suppress these types of processes, a requirement on the lepton isolation is applied, which uses a combination of an absolute and a relative isolation variable. The absolute isolation variable I_{abs} of the lepton is defined as the scalar sum of the p_{T} of PF candidates within a cone size of $R \equiv \sqrt{(\Delta\phi)^2 + (\Delta\eta)^2} = 0.3$, where ϕ is the azimuthal angle, around the lepton candidate, which is excluded from the sum, as are charged PF candidates not associated with the PV. The contributions from neutral particles originating from PU are estimated according to the method described in Refs. [98, 99], and are subtracted from I_{abs}. The ratio of the lepton I_{abs} to the lepton p_{T} is defined as the lepton relative isolation I_{rel}. A uniform lepton selection efficiency as a function of p_{T} is achieved by requiring leptons to have $I_{\text{abs}} < 5\,$GeV for $p_{\mathrm{T}}(\ell) < 25\,$GeV and $I_{\text{rel}} < 0.2$ for $p_{\mathrm{T}}(\ell) \geq 25\,$GeV.

A summary of the lepton criteria use in this analysis is reported in table 4.5.

Table 4.5: Summary of the lepton criteria.

	Loose	**Tight**
Electron ID	cutID Veto	cutID Loose
Muon ID	Loose	Medium
Lepton Isolation	$I_{abs} < 20\,GeV\,or\,I_{rel} < 0.8$	$I_{abs} < 5\,GeV\,or\,I_{rel} < 0.2$
Impact Parameter	$\lvert d_{xy}\rvert < 0.1\,and\,\lvert d_z\rvert < 0.5$	$\lvert d_{xy}\rvert < 0.02\,and\,\lvert d_z\rvert < 0.1$

4.7 Missing transverse energy

The missing transverse momentum vector, $\vec{p}_{\mathrm{T}}^{\text{miss}}$, is computed as the negative vector-sum of the p_{T} vectors of all objects selected in the event. The calibrations associated with the jet energy estimations are propagated to the missing transverse momentum vector. This is defined as "PF Type-1 MET" in the dedicated performance studies [100]. The magnitude of this vector is denoted as $p_{\mathrm{T}}^{\text{miss}}$ in the following chapters and is defined as follows:

$$\vec{p}_{\mathrm{T}}^{\text{miss}} = -\sum_{PFs} \vec{p}_{T,PF}, \tag{4.1}$$

where PF refers to the PF objects in the event.

Additionally, the $p_{\mathrm{T}}^{\text{miss}}$ reconstruction in 2017 is corrected to address the ECAL transparency loss issue. Due to aging effects, the ECAL transparency loss introduced additional noise in some high η regions of the detector. This noise can have a sizable effect in the tails of $p_{\mathrm{T}}^{\text{miss}}$. To correct for this effect, the 2017 analysis computes the $p_{\mathrm{T}}^{\text{miss}}$ by completely excluding jets with $p_T^{raw} < 50\,$GeV in $|\eta| \in [2.650, 3.139]$ region.

4.8 Calibration of the simulated events

In order to tune and correct simulated detector performance to real data-taking conditions, event weights are applied to all the MC datasets. These weights can serve two purposes: to reshape the simulated kinematic distributions, without affecting the total number of simulated events or to correct the object identification, affecting the number of selected events in the form of Scale Factorss

(SFs). They can be calculated for pre-event parameters, such as PU vertices, or for physics objects specifications, such as the lepton identification. In general, given the different physical nature, it is assumed that there is no correlation between the parameters being corrected. Under this assumption, the product of the weights yields the full event correction weight. In cases where the parameters are correlated, such as jet energy scale and $\vec{p}_{\mathrm{T}}^{\mathrm{miss}}$, the correlations are taken into account by propagating the corrections between them.

The corrections applied to the simulated events are the following:

- **Integrated luminosity ($\mathcal{L}$):** each simulated process is scaled to correspond the the year specific integrated luminosity of the data sample.
- **Cross section (σ):** the theory prediction for the cross section of the respective process.
- **Generated weight (w_e):** event weight within the total number of generated simulation events in the process.
- **PU distribution (w_{PU}):** to include the effect of real PU, minimum bias interactions are superimposed on the simulated events. The number of *pp* interactions per bunch crossing is not well reproduced in simulation. Because there is a discrepancy in the reconstructed simulated events between simulation and observed data, the distribution of the number of primary vertices is reweighed to match the PU interaction multiplicity of the observed data [101].
- **Trigger (ϵ_{trigg}):** HLT trigger efficiency as measured in section 4.3.
- **Lepton identification (SF_{ID}) and isolation (SF_{ISO}) scale factors:** the difference in the performance of the lepton identification, and isolation efficiencies are measured in data and simulation with a tag-and-probe method in $Z \to \ell^+\ell^-$ events [52, 102]. The simulated events are corrected with the corresponding data-to-simulation SFs are reported in section B.2.
- **Jet energy scale (w_{JES}) and resolution (w_{JER}):** following the methodology of Ref. [93], the corrections to the Jet Energy Scale (JES), the Jet Energy Resolution (JER), and $p_{\mathrm{T}}^{\mathrm{miss}}$ scales estimated. A factorized combination of corrections addresses the different effects in the JES: the PU contribution, the detector response in the recorded data, and the residual data-to-simulation disagreement in the detector response.
- ***b*-tagging efficiency (w_{btag}):** to correct the whole DEEPCSV *b*-tagging discriminant (D) distribution in MC to match that in data. SFs that are $(D, p_{\mathrm{T}}, \eta)$-dependent are applied to the event as follows:

$$w_{btag} = \prod_{i}^{N_{jets}} SF(D_i, p_{T,i}, \eta_i) \tag{4.2}$$

- **Renormalization and factorization scales (w_{LHE}):** renormalization and factorization scales for the production cross sections.

- **$t\bar{t}$ ISR reweighting (w_{ISR}):** the p_{T} spectra of top quarks in data was found to be significantly softer than those predicted by various MC simulations based on either LO or NLO matrix elements interfaced with parton showers. A reweighting procedure based on the number of ISR jets is applied to cover the difference between the observed and predicted spectra. This correction is applied to the $t\bar{t}$ and signal samples.
- ***W*+jets S_{T} reweighting ($w_{S_{\mathrm{T}}}$):** The simulation of the *W* p_{T}, especially in boosted regimes, is known to be harder than what was found in data. This particularly affects the p_{T} of the lepton + ν system. Given the Data/MC discrepancies observed in these samples coming from the p_{T} of this system, corrections, derived in *W*+jets enriched control region were derived. For more details, please see section 4.9. This weight is only applied to the *W*+jets samples.
- **Signal generator filter efficiency ($\epsilon_{SMSfilter}$):** the signal sample used in this analysis has been produces with a scan that has been pre–filtered requiring at the generation level $p_{\mathrm{T}}^{\text{miss}} > 80\,$GeV and $H_{\mathrm{T}} > 160\,$GeV. To account for these generator filters, this filter efficiency is measured as explained in section B.3. This efficiency is only applied to the signal sample.
- **weight ($SF_{FullFast}$):** as mentioned in section 4.2, the modeling of the detector response for the signal is done with the CMS fast simulation program, in order to scale the generated sample to the full simulation, lepton flavor, p_{T}, and η SFs are applied. This weight is only applied to the signal sample.

The general formula of the weight applied to the ith simulated event in order to correct it to match the observed data is:

$$\begin{aligned} w_i = \mathcal{L} \times \sigma \times \frac{w_e}{\sum_{e=1}^{N_{gen}}} \times w_{PU} \times \epsilon_{trigg} \times SF_{ID} \times SF_{ISO} \\ \times w_{JES} \times w_{JER} \times w_{btag} \times w_{LHE} \times w_{ISR} \times w_{S_{\mathrm{T}}} \\ \times \epsilon_{SMSfilter} \times SF_{FullFast} \end{aligned} \tag{4.3}$$

4.9 Correcting W+jets samples

One important contribution of this analysis was the methodology developed for the correction of the *W*+jets samples in a kinematic region where $H_{\mathrm{T}} < p_{\mathrm{T}}^{\text{miss}}$, which is probed in this and in other CMS SUSY analysis.

As can be seen in figure 4.2 the MC agreement with data in at preselection (defined in Section 5.1) is poor, particularly in the region of $200 < H_{\mathrm{T}} < 300\,$GeV in both years.

It is known that the $\vec{p}_{\mathrm{T}}$ of the *W* boson is poorly modeled by MC simulation. Within the CMS collaboration, there are methods to correct this known issue, which were not solving the problem for the phase space of this search. Therefore, a novel method to correct the *W*+jets samples was developed by me, presented and accepted by the collaboration. The main idea is: knowing that the $\vec{p}_{\mathrm{T}}$ of the *W* boson is poorly modeled by simulation, one can use the $\vec{p}_{\mathrm{T}}$ of the decaying particles, a

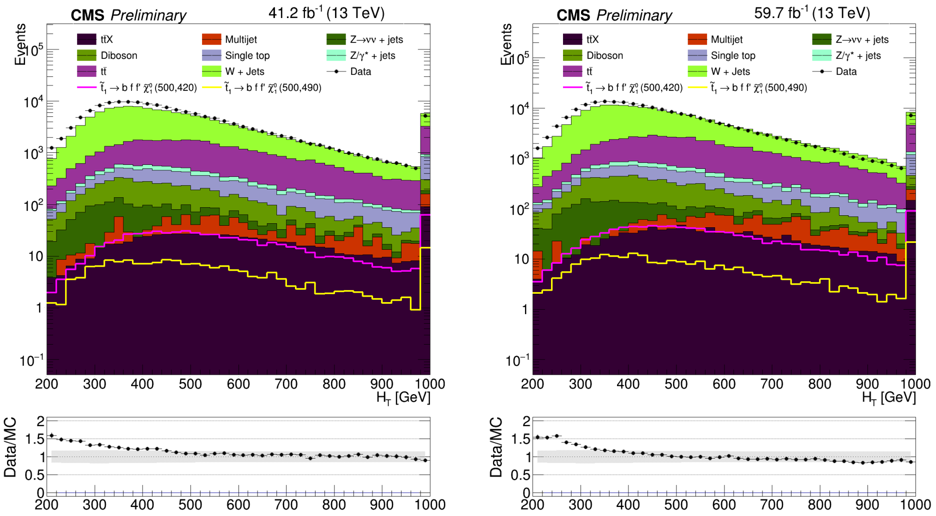

Figure 4.2: Comparison between Data and MC a function of H_{T} for 2017 (left) and 2018 (right) at preselection level before being corrected.

lepton ($\vec{p}_T(l)$) and a neutrino (in the form of $\vec{p}_{\mathrm{T}}^{\,\mathrm{miss}}$), correct these variables simultaneously in a data CR enriched in W+jets. The derived corrections are SFs, which are applied to the W+jets samples.

First, a CR enriched in W+jets is built. This CR is defined by the following kinematic selection: $N_b(loose) == 0$, and $E_{\mathrm{T}}^{\mathrm{miss}} > 200$ GeV, and $p_{\mathrm{T}}(\mathrm{ISR}) > 90$ GeV, and $\Delta\phi(j_1, j_2) <$ 2.5 radians, and exactly one charged lepton. Then, the kinematic variable $\vec{S}_T$ is built as the vector sum of $\vec{p}_T(l)$ and $\vec{p}_{\mathrm{T}}^{\,\mathrm{miss}}$. The magnitude of this vector is denoted as S_{T}. From the $\frac{\mathrm{data}}{\mathrm{MC}}$ ratio in this CR, the correction weights are extracted as a function of the S_{T} and used to correct W+jets samples accordingly. In figure 4.3, the visualization of S_{T} before and after applying this correction in the W+jets control region for both years.

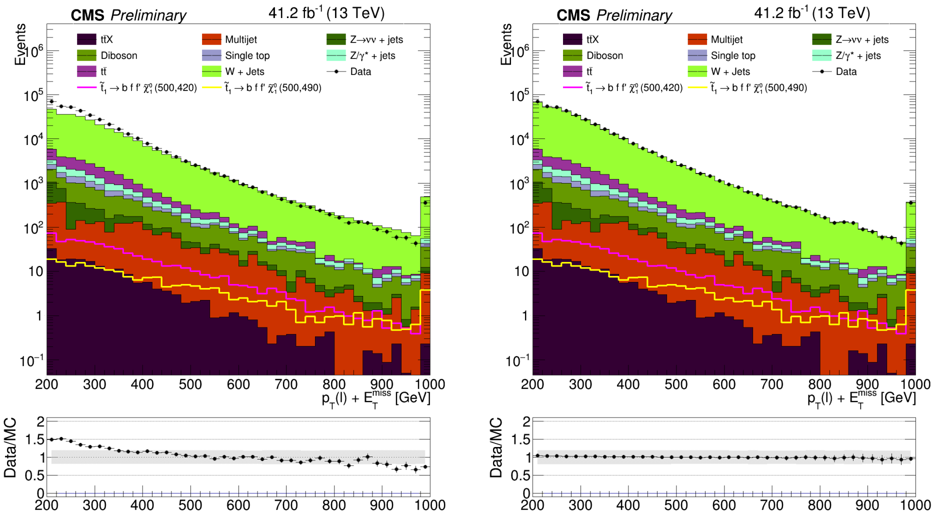

Figure 4.3: 2017 Data/MC agreement as a function of S_{T} in the W+jets enriched CR. Right: non-corrected W+jets samples; left: corrected W+jets samples.

In figure 4.3 the correction for W+jets is derived and cross–checked that the weights are properly implemented. In figures 4.4 & 4.5 the effect of the derived weights at the preselection level for 2017 can be observed.

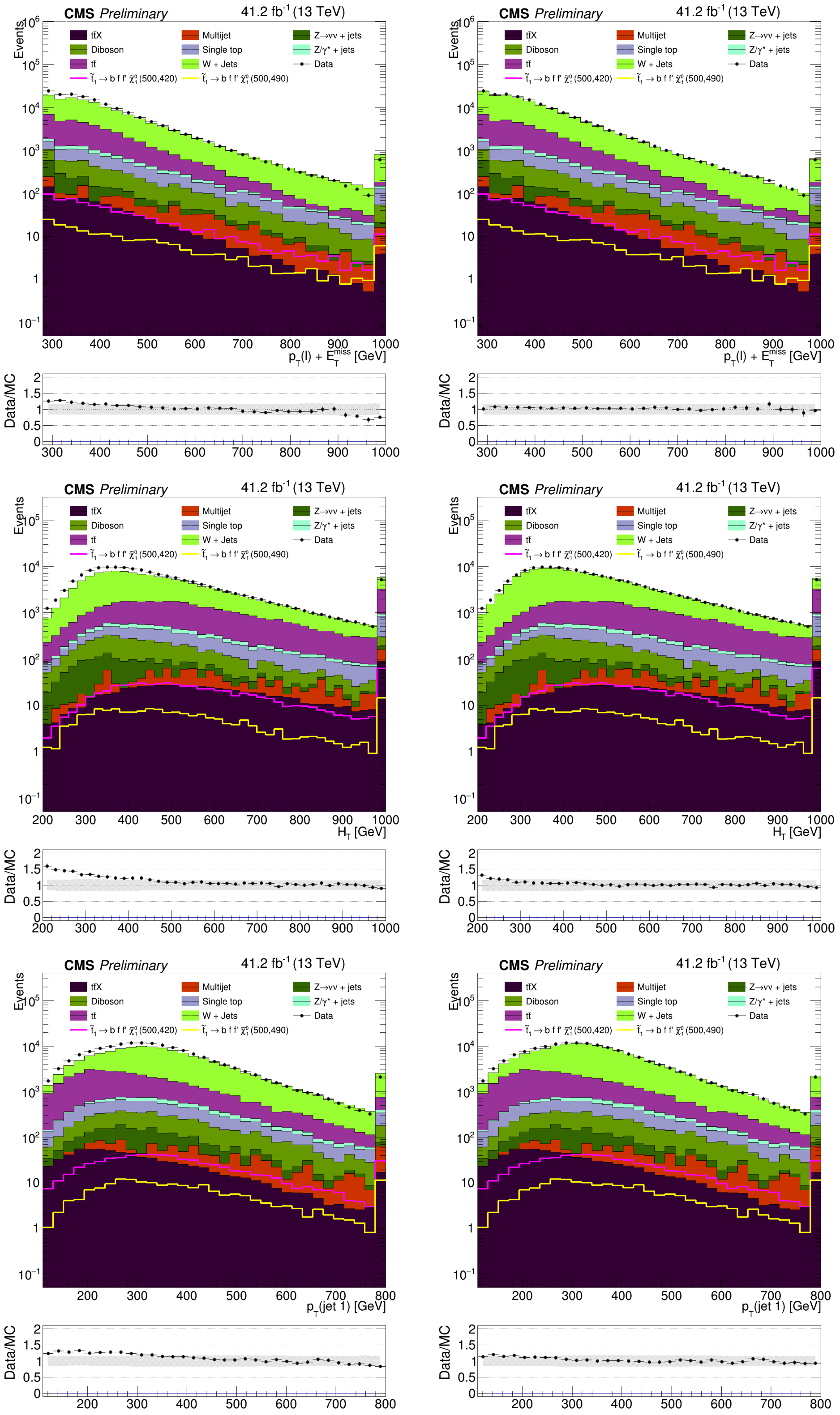

Figure 4.4: 2017 Data/MC agreement at preselection level. Left: non-corrected *W*+jets samples; right: corrected *W*+jets samples. From top to bottom: S_{T}, H_{T} and $p_{\mathrm{T}}(\mathrm{ISR})$.

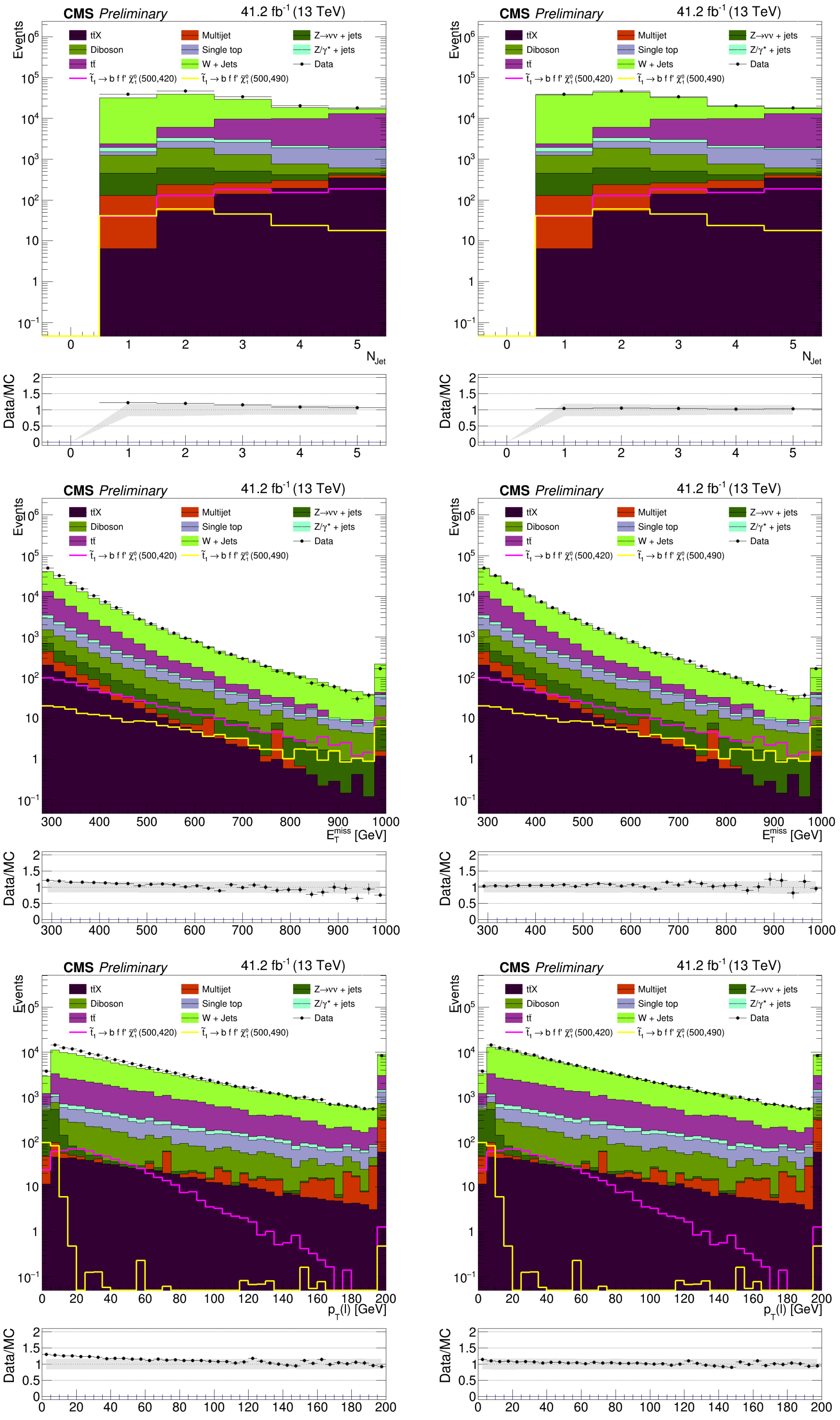

Figure 4.5: 2017 Data/MC agreement at preselection level. Left: non-corrected W+jets samples; right: corrected W+jets samples. From top to bottom: N_{jet}, $p_{\mathrm{T}}^{\text{miss}}$ and $p_{\mathrm{T}}(\ell)$.

In figures 4.4 & 4.5 it can be observed that the overall harshness and the trends in S_{T}, $p_{\mathrm{T}}(\mathrm{ISR})$, $p_{\mathrm{T}}^{\text{miss}}$ and $p_{\mathrm{T}}(\ell)$ have been corrected by the use of the derived weights. The statistical uncertainty of each weight is going to be used to derive the systematic uncertainty introduced by the use of this correction. By applying the weights plus one standard deviation of their uncertainties, it is measured how much it deviates from the central value, this process is repeated in the same manner for the down variation. From the maximum difference between this variations, the relative systematic uncertainty introduced by this SFs is determined.

It is important to note that this method of correcting W+jets samples was conceptualized, implemented and tested by me in the context of this research, and approved by the CMS SUSY MC group. See Section B.1 for the 2018 figures.

5

Event selection

Contents

The selection of events in this search follows two steps. First, a preselection is applied in order to select the final states consisting of a single charged lepton, high $p_{\mathrm{T}}^{\text{miss}}$ and jets, and to reduce the contribution of the main background processes (Section 5.1). Then, Boosted Decision Trees (BDTs) [103, 104] are trained and used to define the signal region (Sections 5.2–5.3). The characteristic of the preselection is to be as inclusive as possible, as to preserve the efficiency for signals of all possible Δm, while leaving the main part of the selection to be performed by the BDTs.

5.1 Preselection and discriminant variables

Without applying any type of selection the SM processes would dominate a possible signal by a factor up to 9 orders of magnitude with SM multijet being the most predominant process, with the highest cross section (see Table 4.3). This motivates the need to perform a selection to diminish background as much as possible, while retaining a maximum number of signal events. As mentioned before, this analysis focus on final states consisting of a soft charged lepton, high $p_{\mathrm{T}}^{\text{miss}}$ and jets. With this in mind, and in order to reduce the background while preserving signal, a kinematic region is based on the online selection and on the reconstructed objects specified in the Chapter 4, called AR. The selection criteria used to create this region is defined as the preselection.

The value of the preselection $p_{\mathrm{T}}^{\text{miss}}$ threshold is set close to the beginning of the maximum efficiency plateau of the combined $p_{\mathrm{T}}^{\text{miss}}$ and $H_{\mathrm{T}}^{\text{miss}}$ trigger, while optimizing the separation between signal and background performed by the BDTs. Events with $p_{\mathrm{T}}^{\text{miss}} > 280\,\text{GeV}$ are selected, favoring the signal where two $\tilde{\chi}_1^0$'s escape detection and where the $p_{\mathrm{T}}^{\text{miss}}$ is therefore larger than for SM processes. For these events, the trigger efficiency is above 98% for both years as shown in Figure 4.1. To account for the small inefficiency, simulated samples are reweighted as a function of $p_{\mathrm{T}}^{\text{miss}}$ to match the efficiency of the triggers in data.

To suppress the contribution of SM processes, additional requirements are imposed on the selected events. In particular, to reduce the W+jets background, $H_{\mathrm{T}} > 200\,\text{GeV}$ is required. To select the single-lepton topology, it is demanded exactly one identified electron or muon in the event, along with at least one jet. This selection reduces the contribution from the dilepton topology of $t\bar{t}$ events. To further improve the selection of signal over SM background events, at least one jet must have $p_{\mathrm{T}} > 110\,\text{GeV}$. These requirements are geared towards signal events in which the $\tilde{t}_1\bar{\tilde{t}}_1$ system recoils against a high-momentum ISR jet, Lorentz boosting the $\tilde{\chi}_1^0$ and increasing the $p_{\mathrm{T}}^{\text{miss}}$. The ISR jet will often be the highest momentum (leading) jet in these events, and the leading-jet p_{T} threshold value is optimized in the same manner as for $p_{\mathrm{T}}^{\text{miss}}$. Lastly, in events with at least two jets, the azimuthal angle between the directions of the leading and second-highest-p_{T} (subleading), defined as $\Delta\phi(j_1, j_2)$ jets must be smaller than 2.5 radians if the subleading jet $p_{\mathrm{T}} > 60\,\text{GeV}$, suppressing the SM multijet background. Table 5.1 summarizes the preselection criteria.

At the preselection stage, the W+jets and $t\bar{t}$ processes are the main SM backgrounds, making up about 70 and 20%, respectively, of the total expected background. Table 5.2 reports the yields at this stage. Both W+jets and $t\bar{t}$ lead to a final state with a real lepton plus jets and a real $p_{\mathrm{T}}^{\text{miss}}$.

Table 5.1: Preselection criteria.

Variable	Selection
$p_{\mathrm{T}}^{\text{miss}}$	> 280 GeV
H_{T}	> 200 GeV
Number of identified leptons ($e^{\pm}$ or $\mu^{\pm}$)	1
$p_{\mathrm{T}}(\mathrm{ISR})$	> 110 GeV
$\Delta\phi(j_1, j_2)$ OR subleading jet p_{T}	< 2.5 OR < 60 GeV

The $Z \to \nu\bar{\nu}$+jets process contributes to the SM background by having jets, genuine $p_{\mathrm{T}}^{\text{miss}}$, and a jet misidentified as a lepton. The remaining background processes are diboson, single top quark, Drell–Yan (DY), multijet, and $t\bar{t}X$ production where X is a vector boson. These processes are a less-important part of the expected background because of having a smaller cross section, a lower acceptance, or both.

Table 5.2: Expected number of simulated background processes, total background and signal events, and total observed data events at preselection lever for 41.5 fb^{-1} (2017) and for 59.8 fb^{-1} (2018).

Year	W+jets	$t\bar{t}$	Z+jets	Other	Total Background	Signal (625,545)
2017	110940	28883	1111	11373	152307 ± 499	237 ± 6.0
2018	155863	44849	1643	16257	218612 ± 752.2	353.4 ± 7.4

Table 5.3: Input variables and their respective definition and symbolic representation.

Definition	Symbol
transverse momentum of the lepton	$p_{\mathrm{T}}(\ell)$
lepton pseudorapidity	$\eta(\ell)$
lepton charge	$Q(\ell)$
negative vector $\vec{p_{\mathrm{T}}}$ sum of all PF candidates in the event	$p_{\mathrm{T}}^{\text{miss}}$
transverse mass of the lepton + $\vec{p}_{\mathrm{T}}^{\text{miss}}$	m_{T}
number of jets in the event satisfying the jet criteria	N_{jet}
p_{T} of the leading jet	$p_{\mathrm{T}}(\mathrm{ISR})$
the scalar p_{T} sum of all jets in the event	H_{T}
number of loosely b tagged jets	$N(b^{\text{loose}})$
highest b tagging discriminant per event	$D(b)$
transverse momentum of the jet with the highest $D(b)$	$p_{\mathrm{T}}(b)$
the distance in (η, ϕ) space between the directions of the lepton and the jet with the highest $D(b)$	$\Delta R(\ell, b)$

Table 5.3 gives the definition of each discriminating variable. The distribution of these variables after the preselection from the 2017 and 2018 data and the simulations are shown in Figure 5.1 and Figure 5.2 respectively. The simulated background distributions for each year are normalized to the corresponding integrated luminosity, to their theoretical cross sections, and reweighed according to Section 4.8. Given the level of agreement with data, the simulated distributions are used in the second step in the event selection.

At this level, the fraction of expected signal events to the total expected events is still smaller than 1%. The distributions of the kinematic variables at preselection of signal and background overlap

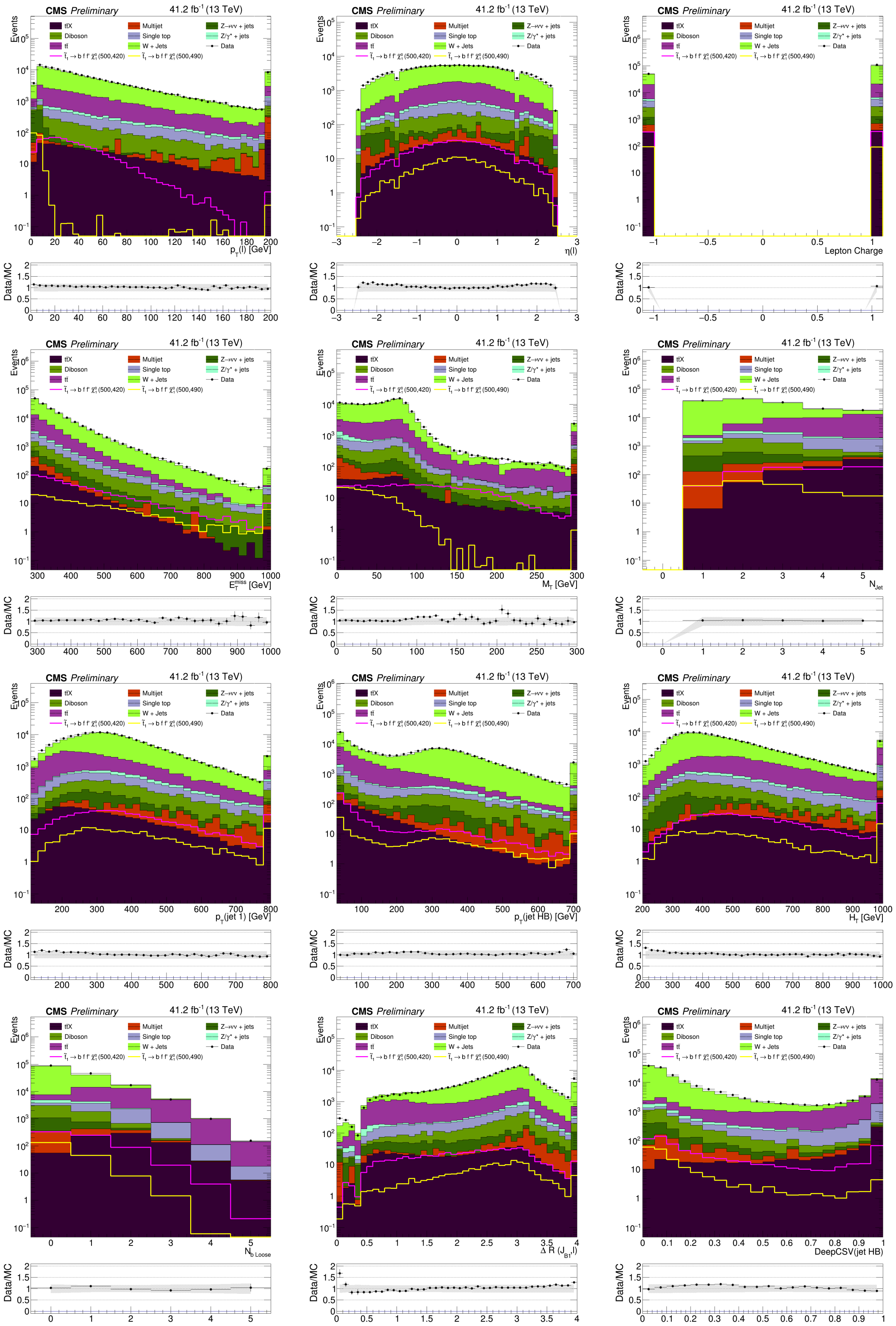

Figure 5.1: From upper left to lower right: Distributions of $p_{\mathrm{T}}(\ell)$, $\eta(\ell)$, $Q(\ell)$, $p_{\mathrm{T}}^{\mathrm{miss}}$, m_{T} , N_{jet}, $p_{\mathrm{T}}(\mathrm{ISR})$, $p_{\mathrm{T}}(b)$, H_{T}, $N(b^{\mathrm{loose}})$, $\Delta R(\ell, b)$, and $D(b)$ for the data of 2017 at the preselection level in data and simulation. The background distributions are obtained directly from simulation, and are normalized to an integrated uminosity of 41.5 fb^{-1}. The distributions of two signal points are represented, while not being added to the background: $(m(\widetilde{t}_1),\ m(\widetilde{\chi}^0_1))$ = (500, 490) and (500, 420) GeV. The last bin in each plot includes the overflow events. The lower panels show the ratio of data to the sum of the SM backgrounds, where the dark shaded bands indicate the statistical uncertainties in the simulated data.

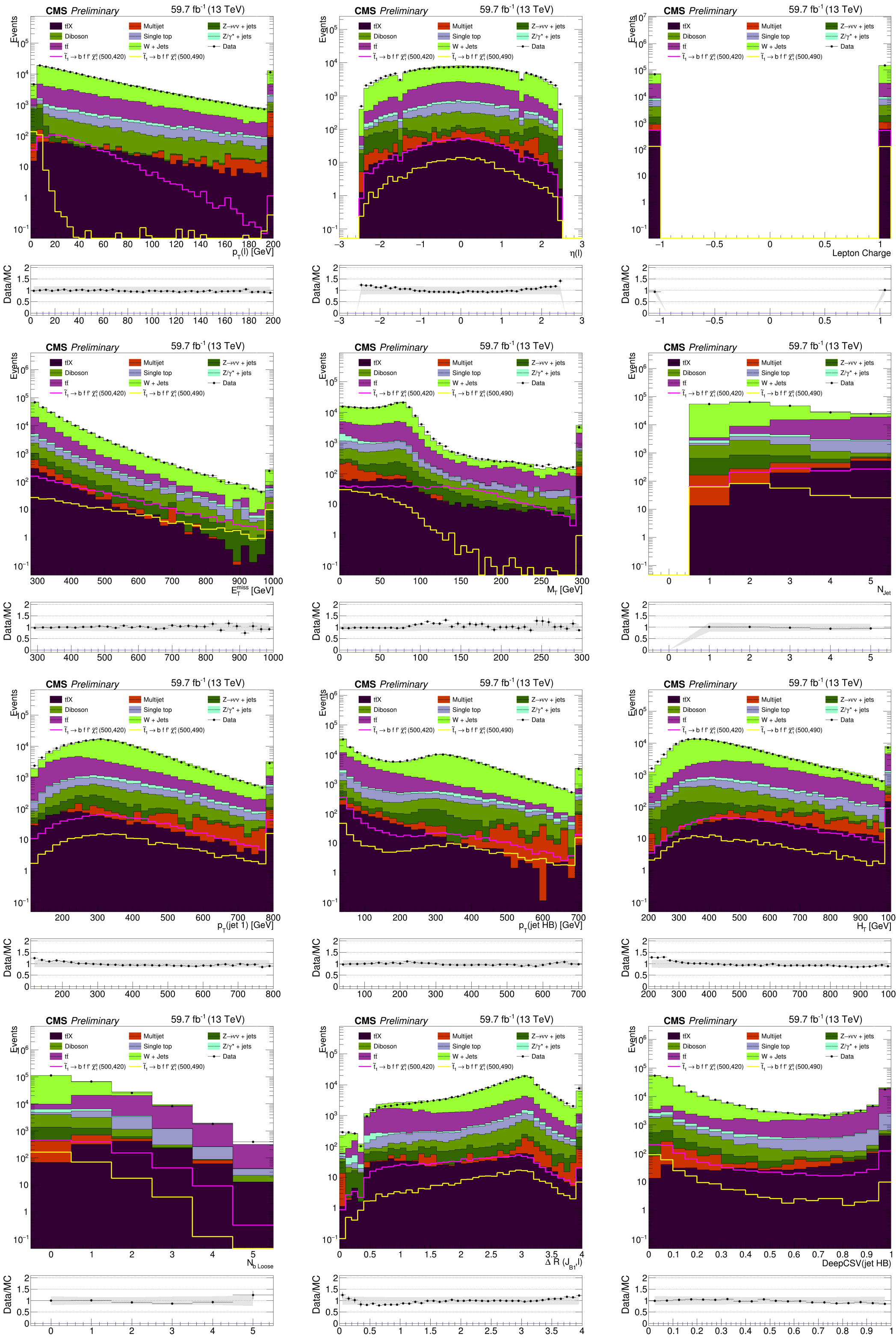

Figure 5.2: From upper left to lower right: Distributions of $p_\mathrm{T}(\ell)$, $\eta(\ell)$, $Q(\ell)$, p_T^miss, m_T , N_jet, $p_\mathrm{T}(\mathrm{ISR})$, $p_\mathrm{T}(b)$, H_T, $N(b^\text{loose})$, $\Delta R(\ell, b)$, and $D(b)$ for the data of 2018 at the preselection level in data and simulation. The background distributions are obtained directly from simulation, and are normalized to an integrated uminosity of 59.8 fb^{-1}. The distributions of two signal points are represented, while not being added to the background: $(m(\widetilde{t}_1),\ m(\widetilde{\chi}^0_1))$ = (500, 490) and (500, 420) GeV. The last bin in each plot includes the overflow events. The lower panels show the ratio of data to the sum of the SM backgrounds, where the dark shaded bands indicate the statistical uncertainties in the simulated data.

are detailed in Figure 5.4. To better separate signal from background and improve the signal to background ratio, a MVA is performed and described in the following Sections.

5.2 Boosted decision trees

For an optimal separation between signal and background, a MVA approach is used that allows to combine several discriminating variables into one final discriminator: $D^n \rightarrow D$ where D is a discriminant variable and n the number of input variables at preselection level, in this case, $n = 12$. The MVA method used is the BDTs with adaptive boosting.

BDTs are a type of supervised Machine Learning (ML) algorithm that are used to create a model that predicts the value of a target variable by learning simple decision rules from data. BDTs are created by combining the predictions of multiple Decision Trees (DTs).

By sequentially applying a series of linear selections on the input variables, a DT divides the initial sample of events in two sub–samples. For each sub-sample, the purity of signal, p, is defined as follows:

$$p = \frac{S}{S+B}, \tag{5.1}$$

where S and B are the signal and background yields respectively. The Gini index, $p(1-p)$, is used as the criterion to decide whether or not to further sub-divide each sub–sample. This process continues until the maximum tree depth is reached, in general defined by the user. The MC events present in the sub–sample with $p > 0.5$ are assigned a value of $+1$, while events in the other sub–sample are assigned to -1. By adjusting the values of the linear selections, a DT is trained in order to maximize the purity of signal of each sub–sample. Merely relying on the output of the DT may lead to misclassification of some events. To overcome this, a technique called boosting is used. Boosting is a ML technique that combines weak learners (DTs) to create a strong learner (BDT). In order to do so, on the same sample, a group of DTs are trained, where a weight a_n is assigned to each DT and updated during the training. By the minimization of the binomial log-likelihood loss function, Equation 5.2, the best weight for each DT is found for the sample of K events. In practice, poor performing DTs are penalized while the best ones see their contribution to the BDT augmented.

$$L(F, y) = \sum_{k=1}^{K} ln(1 + e^{-2Fy}), \tag{5.2}$$

where y is the label: $y = +1$ for a signal event and $y = -1$ for a background event. Considering x as the vector of input variables and b_n as the set of the selection values, each DT is interpreted as a member of a family of functions $f(x; b_n)$. Thus, the BDT output is the weighted average over the individual DTs for N trees:

$$\text{BDT}(x; a, b_n) = \sum_{n=0}^{N} a_n f(x; b_n); a = (a_1, a_2, ..., a_N). \tag{5.3}$$

Each BDT used in this analysis has four hundred trees (400) with a minimum 2.5% of training events required in a leaf node, a maximum depth of 3 layers, and uses adaptive boosting as mentioned prior. To improve the training, the input variables undergo a decorrelation transformation which rotates the input space of the discriminant variables to a space with minimally correlated variables.

Figure 5.3 illustrates a trained tree. The ROOT TMVA [104] library is used to train the BDTs. The BDT output, defined by the ROOT TMVA library, is a real–valued number, that ranges from -1 or $+1$, that represents the classifier's confidence that a given event belongs to either the background or signal class. A perfect classification would classify all the background events as -1 and all the signal events as 1. In a real scenario, typically, background events rank closer to -1 while the signal ones are classified closer to 1.

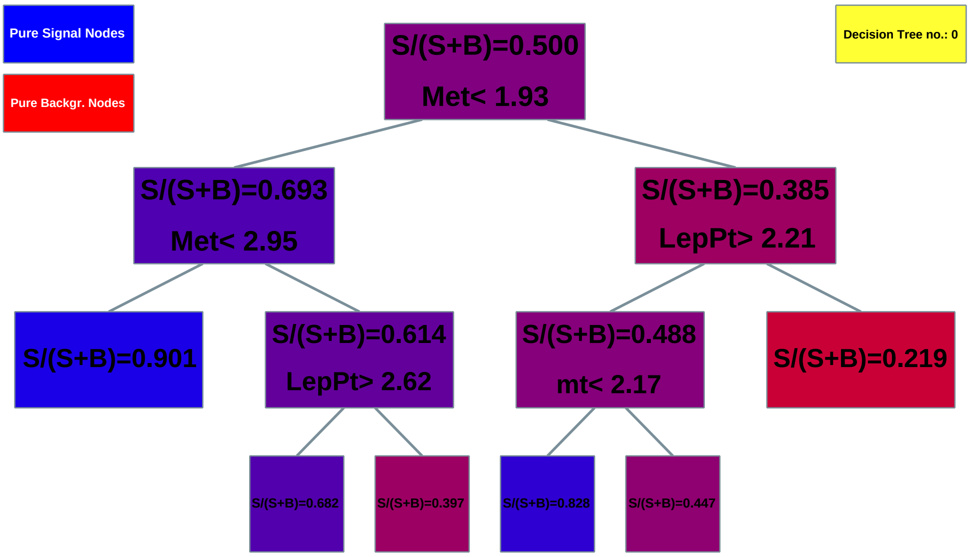

Figure 5.3: Visualization of one of the trees of the $\Delta m = 30$ GeV trained BDT.

5.3 Classification and signal selection

After the Preselection has been applied, the goal is to put in place the best MVA training, by finding the best set of variables that show the most separation between signal and background and explore the subtle differences in kinematics between them and having enough statistics to train the BDTs. For each event passing the preselection, the BDT discriminator value, henceforth referred to as the BDT output, is evaluated. If the discriminator value exceeds the determined threshold, the event is retained. The set of variables used in the BDT training are called discriminant variables and serve as input features. The choice of the discriminating variables is made by maximizing the following Figure of Merit (FOM) [105]:

$$FOM = \sqrt{2\left((S+B)\,ln\left(\frac{(S+B)\cdot\left(B+\sigma_B^2\right)}{B^2+(S+B)\cdot\sigma_B^2}\right)-\frac{B^2}{\sigma_B^2}ln\left(1+\frac{\sigma_B^2\cdot S}{B\cdot\left(B+\sigma_B^2\right)}\right)\right)}, \tag{5.4}$$

where S and B stand for the expected signal and background yields. The term $\sigma_B = (f \cdot B)$ represents the expected systematic uncertainty in the background, with f being the relative uncertainty of the background yield, taken to be $f = 20\%$. This FOM is chosen because it accounts for both the signal and background yields, the statistical uncertainties of both, and systematic uncertainty of the background. Therefore, it allows to capture, in a single number, a rather complete picture of the performance of a given selection.

Various BDTs are trained with different sets of discriminating variables, and a variable is included in the final set only if it significantly increases the FOM obtained for any selection using the BDT output. The discriminant variables used for the analysis of the 2017 and 2018 data are same as of the 2016 published results. The list of the twelve retained input variables and a short description of their signal and background distributions is as follows:

- Variables related to $p_{\mathrm{T}}^{\text{miss}}$: $p_{\mathrm{T}}^{\text{miss}}$ and m_{T} , where m_{T} is the transverse invariant mass of the lepton + $\vec{p}_{\mathrm{T}}^{\text{miss}}$ system, defined as: $m_{\mathrm{T}} = \sqrt{2p_{\mathrm{T}}^{\ell}p_{\mathrm{T}}^{\text{miss}}[1-\cos(\Delta\phi_{\ell,\vec{p}_{\mathrm{T}}^{\text{miss}}})]}$, where $\Delta\phi$ is the azimuthal angular difference between the lepton $\vec{p}_{\mathrm{T}}$ and $\vec{p}_{\mathrm{T}}^{\text{miss}}$. The $p_{\mathrm{T}}^{\text{miss}}$ distribution extends to higher values for the signal than for the backgrounds due to the two undetected LSPs in the signal decays. The m_{T} spectrum peaks around 80 GeV for the SM background where a *W* boson is produced, and is a broad distribution for the signal.

- Lepton-related variables: $p_{\mathrm{T}}(\ell)$, $\eta(\ell)$, and $Q(\ell)$. The correlation between $p_{\mathrm{T}}^{\text{miss}}$ and $p_{\mathrm{T}}(\ell)$ is different for the signal, where $p_{\mathrm{T}}^{\text{miss}}$ comes from three undetected particles (two $\tilde{\chi}_1^0$ and a ν), than for *W*+jets and $t\bar{t}$ backgrounds, where $p_{\mathrm{T}}^{\text{miss}}$ is the result of a single undetected particle (ν). Because the decay products of the signal are more centrally produced than those of the *W*+jets process, the lepton pseudorapidity $\eta(\ell)$ distribution is populated at more central values for the signal than this background. The lepton charge $Q(\ell)$ is a discriminating variable because W^+ and W^- bosons are not produced equally at the LHC, while the signal events contain equal numbers of positively and negatively charged leptons.

- Jet-related variables: $p_{\mathrm{T}}(\mathrm{ISR})$, $p_{\mathrm{T}}(b)$, N_{jet}, and H_{T}. The variable $p_{\mathrm{T}}(\mathrm{ISR})$ is defined as the p_{T} of the leading jet, and selects the high-momentum ISR jet in signal events. The $p_{\mathrm{T}}(b)$ variable is the transverse momentum of the jet with the highest b tagging discriminant value. Both the $p_{\mathrm{T}}(\mathrm{ISR})$ and $p_{\mathrm{T}}(b)$ variables are sensitive to the available phase space, which depends on $m(\widetilde{t}_1) - m(\widetilde{\chi}^0_1)$ for the signal, and $m(t) - m(W)$ for the $t\bar{t}$ background. The N_{jet} variable is sensitive to the mass difference Δm, while the H_{T} variable provides discrimination between signal and both the W+jets and $t\bar{t}$ backgrounds.

- b jet-related variables: $N(b^{\text{loose}})$, $\Delta R(\ell, b)$, and $D(b)$. The number of loosely b tagged jets $N(b^{\text{loose}})$, the distance in (η, ϕ) space between the directions of the lepton and the jet with the highest b tagging discriminant $\Delta R(\ell, b)$, and the highest b tagging discriminant per event $D(b)$ are included as input variables. While the preselection has no requirement on b tagging, information related to it is passed to the BDT to help discriminate between the signal and mainly the W+jets background.

The five most discriminating variables, in decreasing power, are $p_{\mathrm{T}}(\ell)$, $p_{\mathrm{T}}^{\text{miss}}$, $p_{\mathrm{T}}(\mathrm{ISR})$, H_{T}, and m_{T} .

The discrimination power of the input variables varies as a function of Δm, as illustrated in Figure 5.4. An important feature of this search is the adaptation of the selection tool to the evolving kinematic variables of the signal over the $(m(\widetilde{t}_1),\ m(\widetilde{\chi}^0_1))$ plane. Therefore, this plane is divided into eight Δm regions (from 10 to 80 GeV, in steps of 10), and a separate BDT is trained for each Δm region. The W+jets and $t\bar{t}$ processes, which constitute a large fraction of the total background after preselection, are included in the training of the BDT. This is done using both simulated signal and background events. The SM background samples are normalized to their theoretical cross sections in the training. As seen in Fig. 5.5, different signal points with the same Δm have similar input variable distributions. This is expected since with the same Δm they have the same available phase space. Because of this, all the signal points with the same Δm are grouped together when training the BDT, thus increasing the number of signal events for each training. Because of the large variation of the $p_{\mathrm{T}}(\ell)$ spectrum across the $(m(\widetilde{t}_1),\ m(\widetilde{\chi}^0_1))$ plane, it is required that $p_{\mathrm{T}}(\ell) < 30$ GeV for signal points with $\Delta m < 70$ GeV before training the respective BDTs, while imposing no restriction on $p_{\mathrm{T}}(\ell)$ for signal points with higher Δm. This improves the ability of the BDT to separate the low Δm signal from the $t\bar{t}$ background.

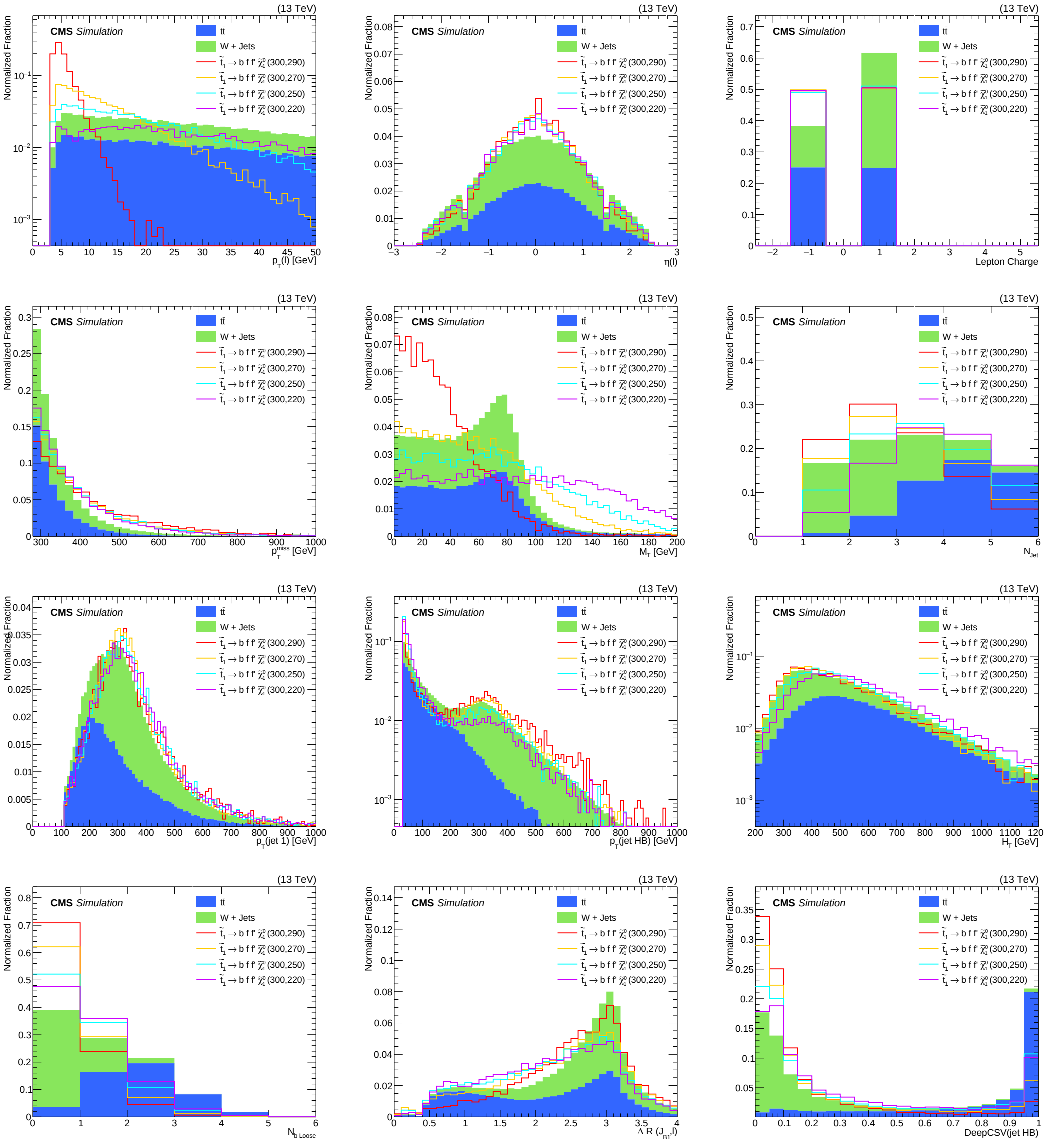

Figure 5.4: Variation of discriminant variables versus different Δm for signal and for W+jets and $t\bar{t}$. Starting from top-left to bottom-right: $p_{\mathrm{T}}(\ell)$, $\eta(\ell)$, $Q(\ell)$, $p_{\mathrm{T}}^{\mathrm{miss}}$, m_{T} , N_{jet}, $p_{\mathrm{T}}(\mathrm{ISR})$, $p_{\mathrm{T}}(b)$, H_{T}, $N(b^{\mathrm{loose}})$, $\Delta R(\ell, b)$ and $D(b)$. Distributions are normalized to the same area and shown at preselection. We choose to represent here a comparison between signal and the background process where the shape difference of the discriminant variable is more notable in order to understand why a specific variable is a good discriminator, hence, used as an input variable for the BDT.

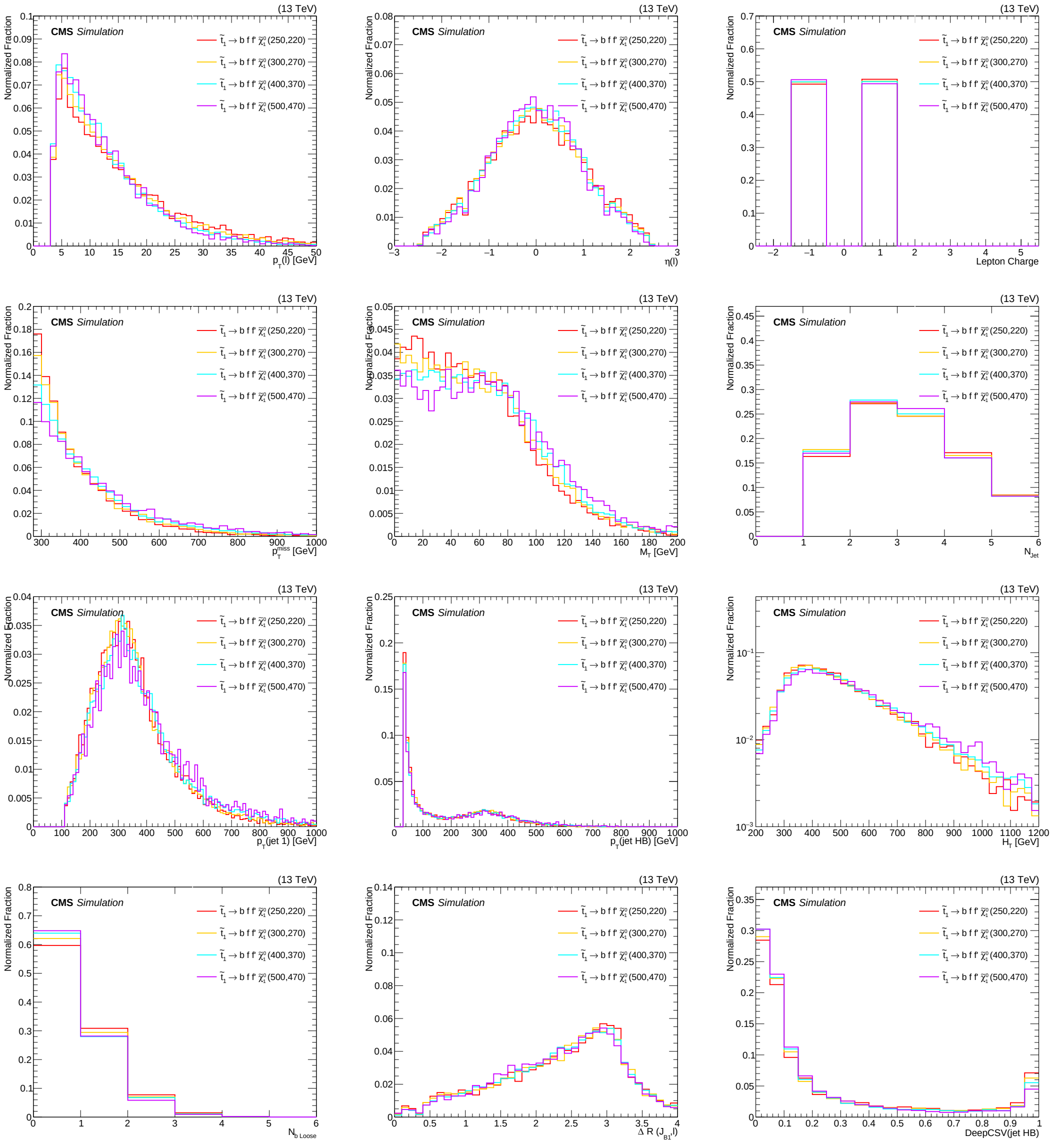

Figure 5.5: Discriminant variables for different signal points with Δm = 30 GeV. Starting from top-left to bottom-right: $p_{\mathrm{T}}(\ell)$, $\eta(\ell)$, $Q(\ell)$, $p_{\mathrm{T}}^{\text{miss}}$, m_{T} , N_{jet}, $p_{\mathrm{T}}(\mathrm{ISR})$, $p_{\mathrm{T}}(b)$, H_{T}, $N(b^{\text{loose}})$, $\Delta R(\ell, b)$ and $D(b)$. Distributions are normalized to the same area and shown at preselection.

Before the training of the BDTs, the signal and background datasets are split in half in order to separate the training and the testing samples to avoid bias. After the BDT training is completed using the training datasets, it is applied to the testing datasets where the BDT output distribution attributes a classification to each event according to Equation 5.3. According to this equation, background events are classified at low values of the BDT output, while signal events are classified towards the higher values.

The BDT output distributions for data and simulated SM background are shown in Figs. 5.6 and 5.7 for the 2017 and 2018 data, respectively. In each case a $(m(\widetilde{t}_1),\ m(\widetilde{\chi}_1^0))$ signal point belonging to the Δm value for which the training has been done is also reported. The BDT output is found to be different for various values of Δm, which is to be expected because of the changing mix of signal and background and the varying correlations across the $(m(\widetilde{t}_1),\ m(\widetilde{\chi}_1^0))$ plane, resulting in different BDTs outputs for different Δm values. A good agreement between the data and simulation is observed for the BDT output distributions over their entire range, for all trainings; the region at small BDT output values (e.g., <0.3) is dominated by background events.

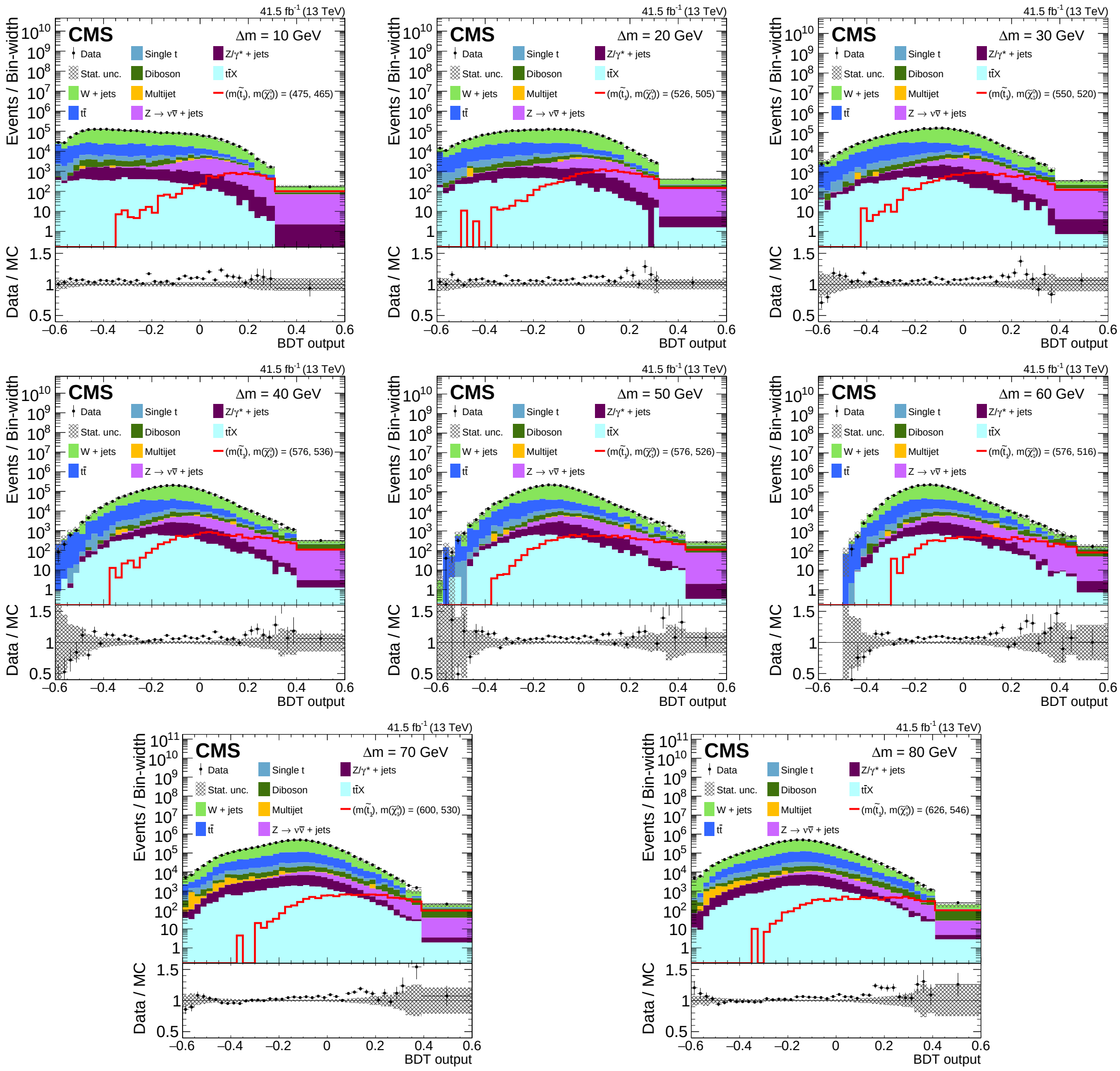

Figure 5.6: Distributions of the BDT output at the preselection level in data and simulation in 10 GeV steps of Δm from 10 (upper left) to 80 (lower right) GeV for the data of 2017. The last bin represents the SR. For each BDT training, a representative $(m(\widetilde{t}_1),\ m(\widetilde{\chi}^0_1))$ signal point is also presented, while not added to the SM background. The shaded area on the Data/MC ratio represents the statistical uncertainty of the simulated background.

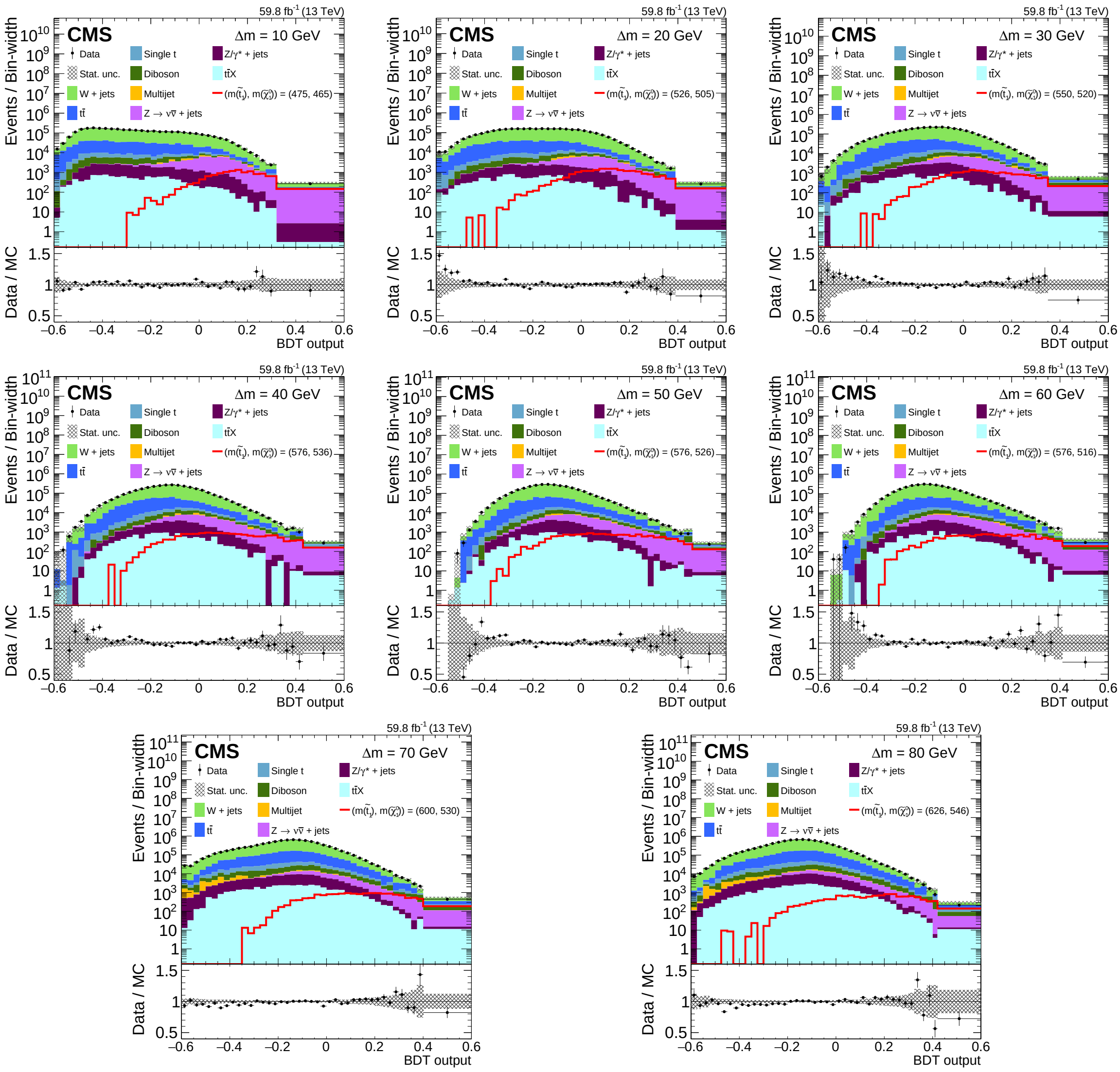

Figure 5.7: Distributions of the BDT output at the preselection level in data and simulation in 10 GeV steps of Δm from 10 (upper left) to 80 (lower right) GeV for the data of 2018. The last bin represents the SR. For each BDT training, a representative $(m(\widetilde{t}_1),\ m(\widetilde{\chi}^0_1))$ signal point is also presented, while not added to the SM background. The shaded area on the Data/MC ratio represents the statistical uncertainty of the simulated background.

By requiring a lower limit on each BDT output, a Signal Region (SR) is defined. To determine this value, a benchmark $(m(\widetilde{t}_1),\ m(\widetilde{\chi}^0_1))$ signal point at the exclusion limit of the 2016 search is chosen. For each one of these points, the BDT trained for its Δm is considered. The expected upper limit on the signal cross section of each benchmark $(m(\widetilde{t}_1),\ m(\widetilde{\chi}^0_1))$ signal point is computed as a function of the lower limit of the BDT output using the asymptotic CL_s method [105, 106]. The value that minimizes this curve is chosen to define the SR. This value, $BDT^{SR}_{\Delta m}$, is cross-checked with the efficiency curves of signal and background to avoid regions affected by statistical fluctuations. As an example of this process, Figure 5.8 illustrates this for $\Delta m = 30$ GeV for the year of 2017. The complete exercise is shown in appendix C.1. In summary, the SR for a given Δm region is defined as Preselection $\bigoplus$ BDT output $\geq BDT^{SR}_{\Delta m}$. The benchmark signal points and the exact values of the cuts of $\geq BDT^{\Delta m}_{SR}$ are reported in Table 5.4.

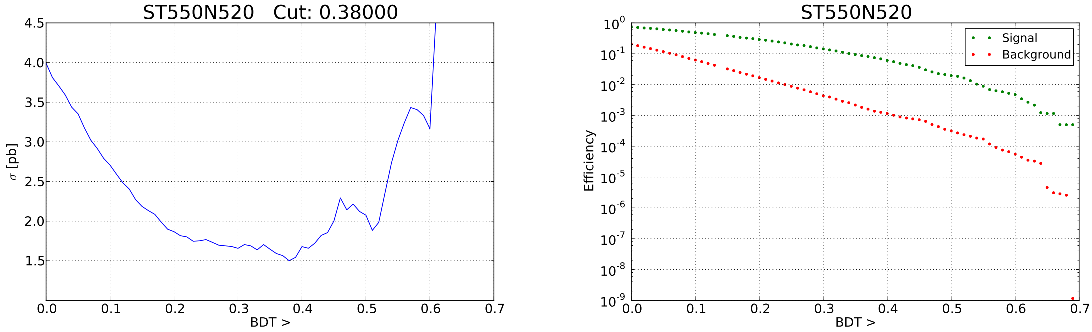

Figure 5.8: Minimization of the expected upper limit cross section at 95 % Confidence Limit for the year of 2017 for $\Delta m = 30$ GeV. The signal region is defined when the selection criteria of $BDT > 0.38$ is satisfied.

Table 5.4: Δm regions and corresponding benchmark (m($\widetilde{t}_1$),m($\widetilde{\chi}^0_1$)) points. For each region, the SR is determined as a cut on the output of the corresponding BDT training.

$\boldsymbol{\Delta m}$ (GeV)	Benchmark point	2017 $BDT^{SR}_{\Delta m}$	2018 $BDT^{SR}_{\Delta m}$
10	(475,465)	0.31	0.32
20	(525,505)	0.32	0.39
30	(550,520)	0.38	0.35
40	(575,535)	0.40	0.43
50	(575,525)	0.43	0.46
60	(575,515)	0.47	0.41
70	(600,530)	0.39	0.40
80	(625,545)	0.41	0.42

In Tables 5.5–5.12 the yields of the simulated MC background and the benchmark signal point at both preselection and signal selection level are provided. As an illustration of the selection power of the BDTs, in the case of $\Delta m = 80$ GeV, the SM background is suppressed by a factor of $\approx 3.7 \times 10^3$ compared to the preselection, while the signal is only reduced by a factor of ≈13.

Table 5.5: 2017 expected number of simulated background processes, total background and signal events, and total observed data events at various levels of the selection for 41.5 fb^{-1}. The BDT used is the one for Δm = 10 and the benchmark signal point is (m($\widetilde{t}_1$),m($\widetilde{\chi}_1^0$))=(475,465). Uncertainties are statistical.

Selection level	***W*+jets**	***t t̄***	***Z*+jets**	**Other**	**Total Background**	**Signal (475,465)**
Preselection	43580	9946	1005	3380	57911 ± 317	241 ± 6.1
$BDT \geq 0.31$	22.8	4.5	19.6	5.4	52.3 ± 5.1	29.1 ± 2.1

Table 5.6: 2017 expected number of simulated background processes, total background and signal events, and total observed data events at various levels of the selection for 41.5 fb^{-1}. The BDT used is the one for Δm = 30 and the benchmark signal point is (m($\widetilde{t}_1$),m($\widetilde{\chi}_1^0$))=(550,520). Uncertainties are statistical.

Selection level	***W*+jets**	***t t̄***	***Z*+jets**	**Other**	**Total Background**	**Signal (550,520)**
Preselection	43580	9946	1005	3380	57911 ± 317	369 ± 7.2
$BDT \geq 0.38$	26.5	6.3	31.1	3.8	67.7 ± 8.3	27.5 ± 2.0

Table 5.7: 2017 expected number of simulated background processes, total background and signal events, and total observed data events at various levels of the selection for 41.5 fb^{-1}. The BDT used is the one for Δm = 60 and the benchmark signal point is (m($\widetilde{t}_1$),m($\widetilde{\chi}_1^0$))=(575,515). Uncertainties are statistical.

Selection level	***W*+jets**	***t t̄***	***Z*+jets**	**Other**	**Total Background**	**Signal (575,515)**
Preselection	43580	9946	1005	3380	57911 ± 317	249 ± 6.0
$BDT \geq 0.47$	4.6	2.2	6.1	1.9	14.8 ± 5.8	10.3 ± 1.2

Table 5.8: 2017 expected number of simulated background processes, total background and signal events, and total observed data events at various levels of the selection for 41.5 fb^{-1}. The BDT used is the one for Δm = 80 and the benchmark signal point is (m($\widetilde{t}_1$),m($\widetilde{\chi}_1^0$))=(625,545). Uncertainties are statistical.

Selection level	***W*+jets**	***t t̄***	***Z*+jets**	**Other**	**Total Background**	**Signal (625,545)**
Preselection	110940	28883	1111	11373	152307 ± 499	237 ± 6.0
$BDT \geq 0.41$	15.6	20.4	4.2	1.6	41.8 ± 8.9	18.2 ± 1.7

Table 5.9: 2018 expected number of simulated background processes, total background and signal events, and total observed data events at various levels of the selection for 59.8 fb^{-1}. The BDT used is the one for Δm = 10 and the benchmark signal point is (m($\widetilde{t}_1$),m($\widetilde{\chi}_1^0$))=(475,465). Uncertainties are statistical.

Selection level	***W*+jets**	***t t̄***	***Z*+jets**	**Other**	**Total Background**	**Signal (475,465)**
Preselection	61696	14680	1499	4680	82555 ± 465.3	352.2 ± 7.1
$BDT \geq 0.32$	29.3	3.6	40.3	6.9	80.1 ± 7.0	40.9 ± 2.3

Table 5.10: 2018 expected number of simulated background processes, total background and signal events, and total observed data events at various levels of the selection for 59.8 fb^{-1}. The BDT used is the one for Δm = 30 and the benchmark signal point is (m($\widetilde{t}_1$),m($\widetilde{\chi}_1^0$))=(550,520). Uncertainties are statistical.

Selection level	***W*+jets**	***t t̄***	***Z*+jets**	**Other**	**Total Background**	**Signal (550,520)**
Preselection	61696	14680	1499	4680	82555 ± 465.3	530.0 ± 8.7
$BDT \geq 0.35$	50.6	20.8	56.1	32.3	159.8 ± 13.4	54.0 ± 2.7

Table 5.11: 2018 expected number of simulated background processes, total background and signal events, and total observed data events at various levels of the selection for 59.8 fb^{-1}. The BDT used is the one for Δm = 60 and the benchmark signal point is (m($\widetilde{t}_1$),m($\widetilde{\chi}^0_1$))=(575,515). Uncertainties are statistical.

Selection level	**W+jets**	**$t\bar{t}$**	**Z+jets**	**Other**	**Total Background**	**Signal (575,515)**
Preselection	61696	14680	1499	4680	82555 ± 465.3	401.1 ± 8.7
$BDT \geq 0.41$	17.7	18.2	21.9	21.5	79.3 ± 10.8	36.0 ± 2.5

Table 5.12: 2018 expected number of simulated background processes, total background and signal events, and total observed data events at various levels of the selection for 59.8 fb^{-1}. The BDT used is the one for Δm = 80 and the benchmark signal point is (m($\widetilde{t}_1$),m($\widetilde{\chi}^0_1$))=(625,545). Uncertainties are statistical.

Selection level	**W+jets**	**$t\bar{t}$**	**Z+jets**	**Other**	**Total Background**	**Signal (625,545)**
Preselection	155863	44849	1643	16257	218612 ± 752.2	353.4 ± 7.4
$BDT \geq 0.42$	14.3	11.8	7.7	18.9	52.7 ± 9.9	25.5 ± 2.0

5.4 Validation of the MVA

The process of the BDTs validation are done via two procedures. First, each BDT is checked for overtraining. This check is described in Section 5.4.1. In the second procedure, the BDT output distribution is evaluated in Validation Regions (VRs) that are orthogonal but kinematically close to the AR and reported in Section 5.4.2.

5.4.1 Checking for overtraining

In order to trust the BDTs classification results, they are checked for overtraining. If there is no overtraining of the model, the BDT response of the test sample, which by definition has not been exposed to the training, should be similar to the one of the training sample. In order to measure this similarity, a Kolmogorov-Smirnov test is applied to all BDTs. Figure 5.9 illustrate that these two distributions are similar and pass the Kolmogorov-Smirnov test. For all the cases, see appendix C.2. In conclusion, because all BDTs pass the Kolmogorov-Smirnov test, there is no overtraining.

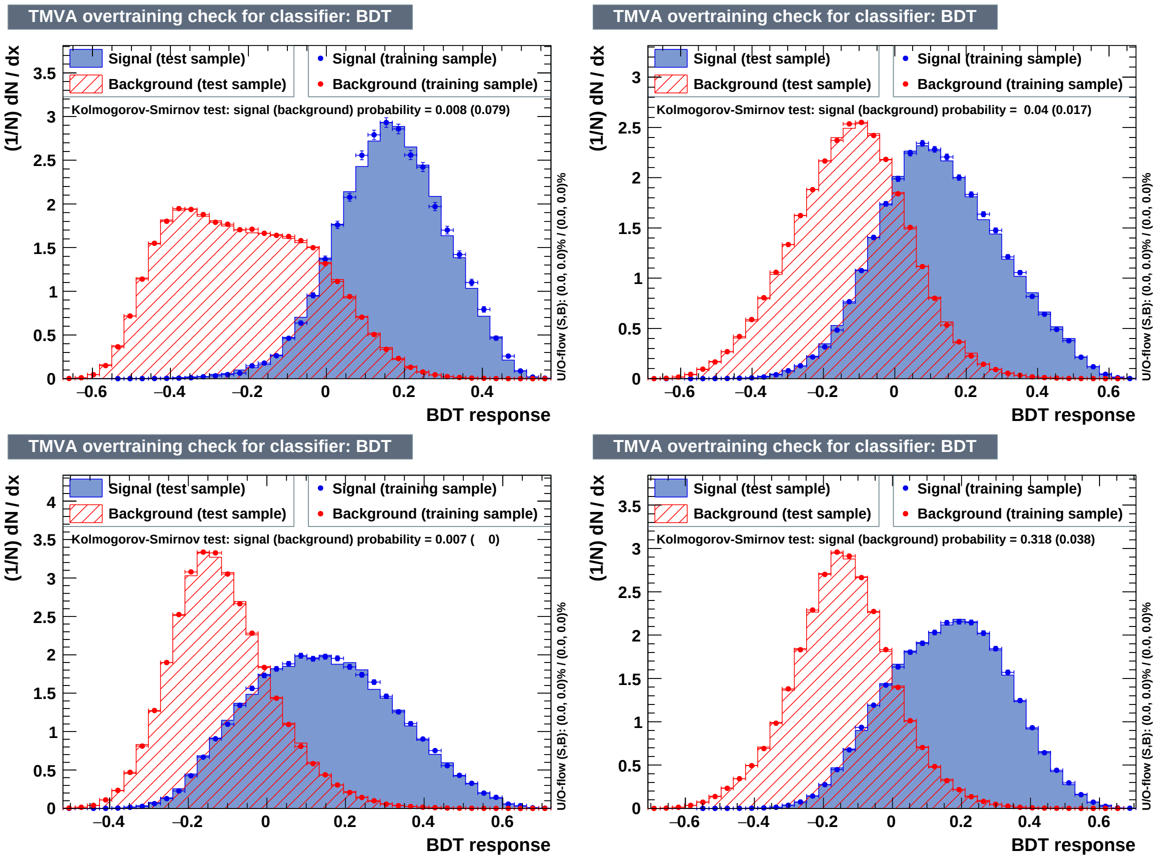

Figure 5.9: 2017: Distribution of the output of the BDT for signal (blue) and background (red) across test- (full histogram) and train-samples (dot). The four illustrated cases are the BDT for Δm = 10 GeV (upper left), 30 GeV (upper right), 60 GeV (lower left) and 80 GeV (lower right).

5.4.2 Validation regions

The final step to validate the BDTs is to ensure that the output of the BDT in data is well reproduced by the simulation over its entire range, including a signal-type region. For this purpose, the VRs are orthogonal but kinematically close to the AR and are defined as follows:

- **Validation Region 1 (VR1):** invert only the $p_{\mathrm{T}}^{\text{miss}}$ selection to be: $200 < p_{\mathrm{T}}^{\text{miss}} < 280$. The other preselection criteria, are the kept the same.
- **Validation Region 2 (VR2)::** In a similar approach to VR1 but in a complementary phase-space to this latter, invert only the $p_{\mathrm{T}}(\ell)$ selection to be: $30 < p_{\mathrm{T}}(\ell)$ while keeping the remaining preselection criteria. This region is only defined for $\Delta m \leq 60$ GeV.

A graphical representation of these VRs is provided in Figure 5.10.

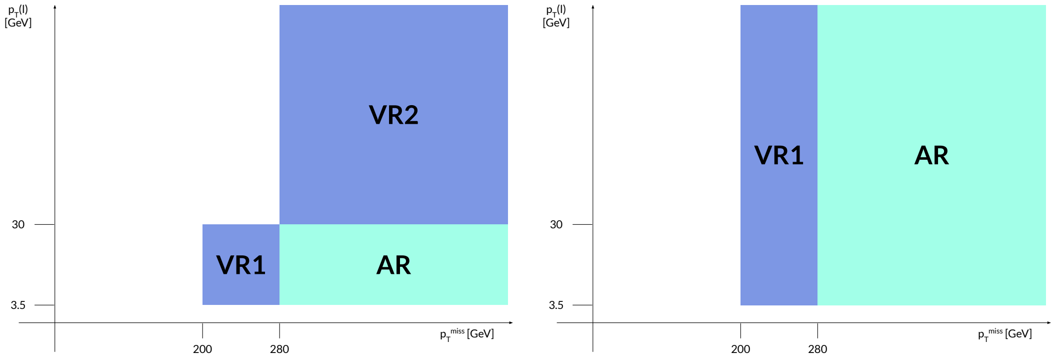

Figure 5.10: Definition of VR1 and VR2 as function of $p_{\mathrm{T}}^{\text{miss}}$ and $p_{\mathrm{T}}(\ell)$. for $\Delta m \leq 60$ GeV (left) and for $\Delta m = 70$ GeV and 80 GeV (right).

The distributions of the BDT output for VR1 for the cases of Δm = 10 & 80 GeV and for VR2 for the case of Δm = 10 GeV are shown in Figs. 5.11-5.12 for the data taking years of 2017 and 2018 respectively. As can be observed, the shape of the distributions in simulation is compatible with data over the entire range of the BDT output , covering a SR type region at the higher values of the distributions. The BDT outputs for all the VRs of all Δm regions as well as the distribution of the discriminant variables in the same regions are reported in appendices C.3 and C.4. Differences in the shape of the BDT distributions between data and simulation are taken into account as sources of systematic uncertainties and are further developed in Section 7.

To note that the VRs as defined above are orthogonal to the AR and can therefore be used as a data-based region where the method used to predict the W+jets and $t\bar{t}$ backgrounds can be tested; this is presented, along with the method of the prediction, in Section 6.2. Not only are VR1 & VR2 kinematically close to AR, they are “complementary” to it in terms of both $p_{\mathrm{T}}^{\text{miss}}$ and $p_{\mathrm{T}}(\ell)$.

Finally, it is important to measure the contamination of VR1 & VR2 by the signal with the highest cross section, (m($\widetilde{t}_1$),m($\widetilde{\chi}_1^0$))=(250,220). The signal contamination of the VRs has to be kept negligible, otherwise, possible disagreements between observed data and predicated background can

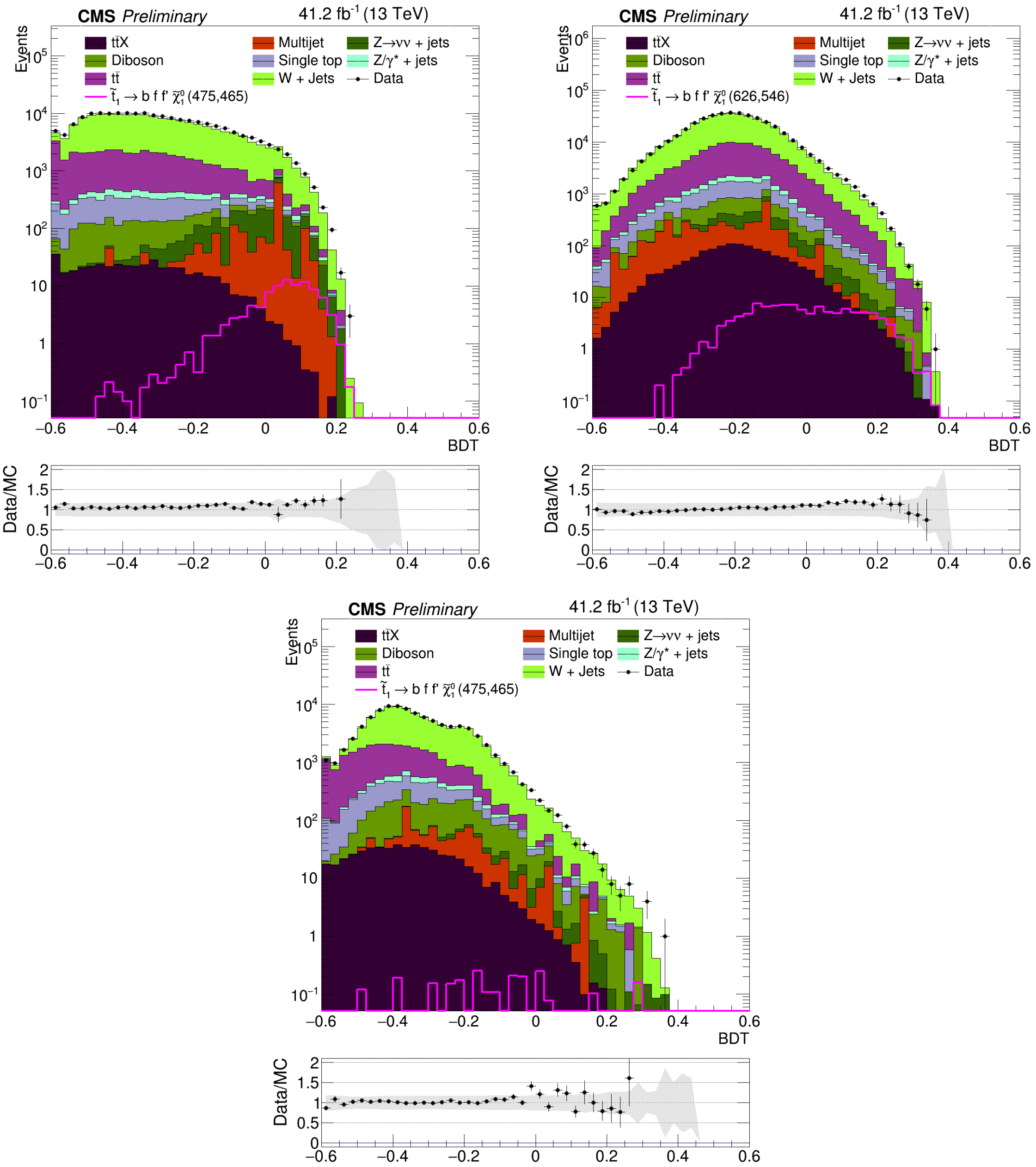

Figure 5.11: 2017 Data and expected MC contributions for the BDT output for L=41.5 fb^{-1} at VR1 for Δm =10 GeV (upper left), VR1 for Δm =80 GeV (upper right) and VR2 for Δm =10 GeV (bottom).

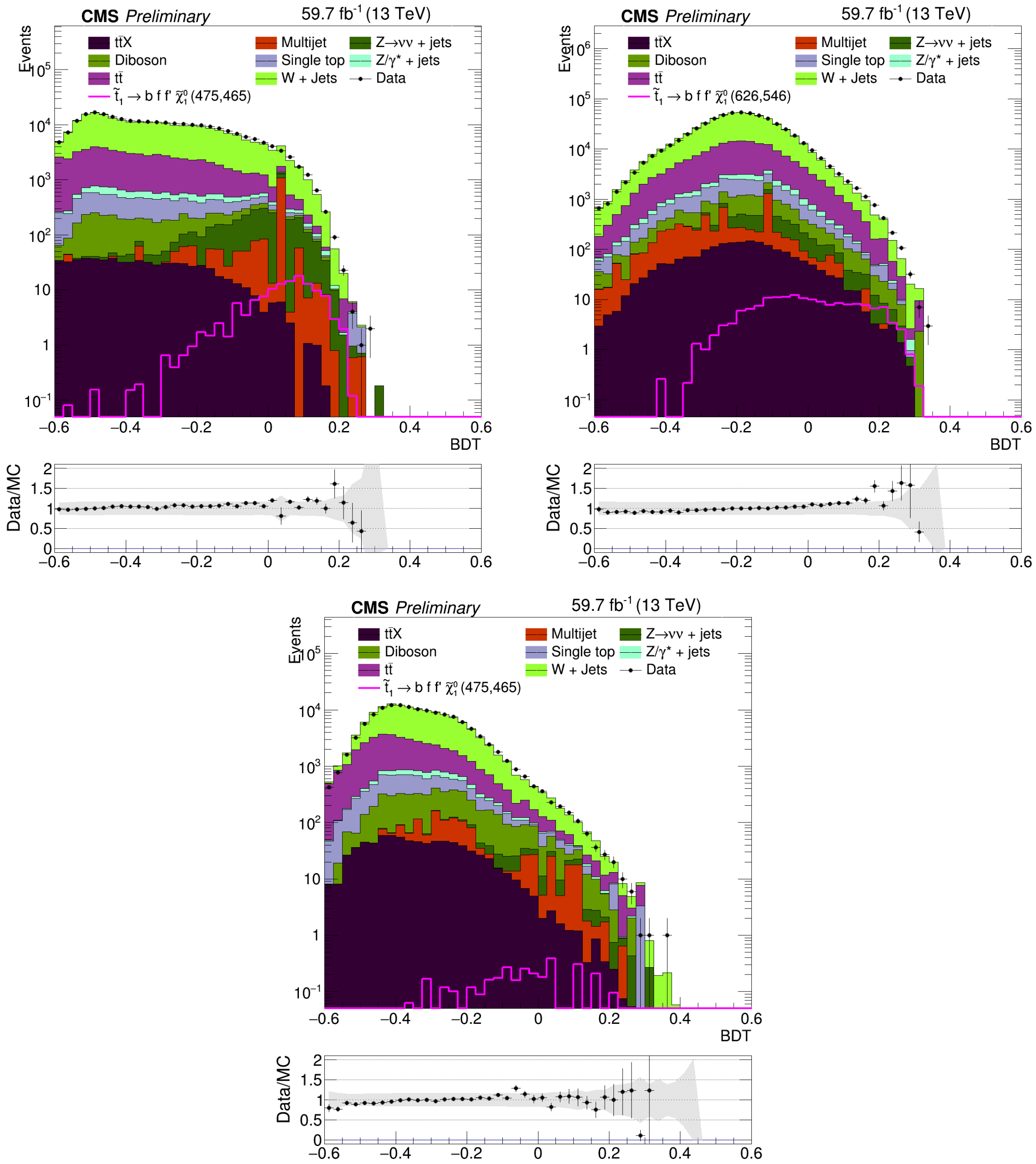

Figure 5.12: 2018 Data and expected MC contributions for the BDT output for L=59.8 fb^{-1} at VR1 for Δm =10 GeV (upper left), VR1 for Δm =80 GeV (upper right) and VR2 for Δm =10 GeV (bottom).

falsely indicate the presence of signal. To avoid this, the choice of the VRs is purposefully chosen to be orthogonal to the AR. The maximum signal contamination for VR1 & VR2 is $\sim$3.8% and $\sim$1.0% respectively. The contamination of a high Δm signal in VR2 is also measured to be below 5%.

6

Background estimation

Contents

The main background processes in this search are W+jets and $t\bar{t}$ with a prompt lepton, and events having a nonprompt lepton that passes the lepton criteria, mainly $Z \to \nu\bar{\nu}$+jets process. The latter category is labeled as nonprompt background. These three main sources of background are estimated using data, as described in Sections 6.1 and 6.2. The background from rare SM processes, such as single top quark, diboson, DY, and $t\bar{t}X$ production, are estimated from simulation.

6.1 Nonprompt background

Nonprompt leptons mostly arise from the decay of heavy-flavor quarks and from misidentified hadrons. The processes contributing to the nonprompt background are mainly $Z \to \nu\bar{\nu}$+jets, and to a lesser extent, W+jets and $t\bar{t}$, where a jet is misidentified as a lepton. Furthermore, there can also be events in which a genuine lepton (mainly from W+jets or $t\bar{t}$) escapes detection, while a nonprompt lepton is selected.

The nonprompt background is predicted from data using the "tight-to-loose" method [107]. The loose selection is defined by relaxing the requirement on the lepton isolation to $I_{\text{abs}} < 20$ GeV for $p_{\mathrm{T}}(\ell) < 25$ GeV and $I_{\text{rel}} < 0.8$ for $p_{\mathrm{T}}(\ell) > 25$ GeV, as well as relaxing the impact parameter conditions to $|d_{xy}| < 0.1\,$cm and $|d_z| < 0.5\,$cm. The tight criteria correspond to the selection of the lepton as described in Section 4.6. The probability ϵ_{TL} for a loose lepton to pass the tight criteria is measured as a function of its p_{T} and η in a data CR that is largely dominated by multijet events, and is enriched in nonprompt leptons defined as the MR. For each SR, a side-band region is defined with the same requirements, but where the lepton is required to pass the loose criteria while failing the tight ones ("L!T"). The number of such events is denoted as $N^{L!T}$(Data). From the loose-not-tight data sample, events where vector boson or a top quark produce a prompt lepton are subtracted, $N_p^{L!T}$(MC). The predicted nonprompt yield $Y_{\mathrm{np}}^{\mathrm{SR}}$ in each SR is obtained by weighting the resulting events by the transfer factor $\epsilon_{\mathrm{TL}}/(1-\epsilon_{\mathrm{TL}})$:

$$Y_{\mathrm{np}}^{\mathrm{SR}} = \frac{\epsilon_{\mathrm{TL}}}{1-\epsilon_{\mathrm{TL}}} \cdot [N^{\mathrm{L!T}}(\text{Data}) - N_{\mathrm{p}}^{\mathrm{L!T}}(\text{MC})]. \tag{6.1}$$

The estimate is data-driven where the MC events with prompt leptons are subtracted from data in the measurement and "L!T" regions. This requires the separation of events with leptons into prompt and nonprompt categories. The tagging of prompt and nonprompt events is performed using MC generated leptons matched to the reconstructed leptons. Furthermore, studies have shown that there is a non-negligible contribution of nonprompt leptons arising from the mis-identification of hadronically-decaying taus, which are not estimated well with this method, due to their differing isolation shapes. These events have been tagged using the matching between the reconstructed nonprompt lepton and generated taus coming from W, Z or γ bosons. They are placed into the prompt category and thus estimated via the method for prompt W+jets and $t\bar{t}$, essentially separating them from the nonprompt rate method. Their contribution relative to prompt backgrounds (and hence total background) is very small.

The MR is constructed to be enriched in nonprompt leptons, where the "tight-to-loose" ratio ϵ_{TL}

is determined as a function of the lepton p_{T} and η. The MR is enriched in multijet events, where events are extracted from the JetHT PD, and are required to have passed the lowest un-prescaled H_{T} HLT `HLT_PFHT1050`. Apart from an H_{T} selection of $H_{\mathrm{T}} > 1200$ GeV, allowing the events to be on the trigger plateau, selection on $p_{\mathrm{T}}^{\text{miss}} < 40$ GeV and $m_{\mathrm{T}} < 30$ GeV are applied to reduce the prompt contamination. The lepton with the leading p_{T} is considered for the measurement.

The lepton p_{T} distributions for both tight and loose leptons in the MR are presented in Figures 6.1 and 6.2 for 2017 and in Figures 6.3 and 6.4 for 2018. The measured ϵ_{TL} ratios as a function of lepton p_{T} in data for both years are shown in Figures 6.5 and 6.6. These measurements are further split into two $|\eta|$ bins at $|\eta| = 1.5$.

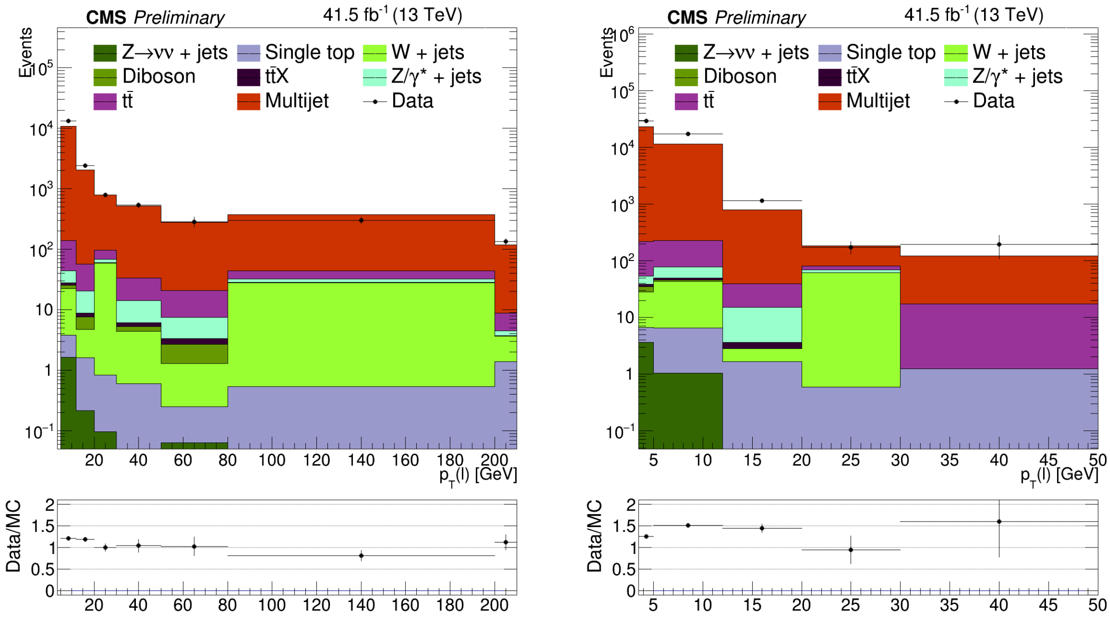

Figure 6.1: 2017 Loose lepton p_{T} distributions in the MR for electrons (left) and muons (right).

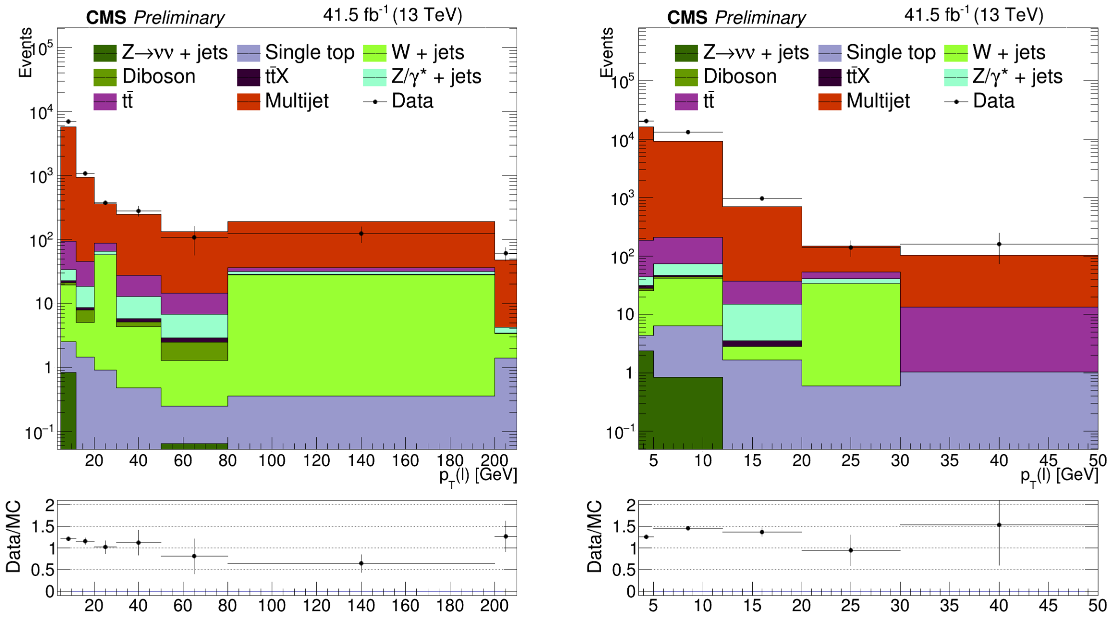

Figure 6.2: 2017 Tight lepton p_{T} distributions in the MR for electrons (left) and muons (right).

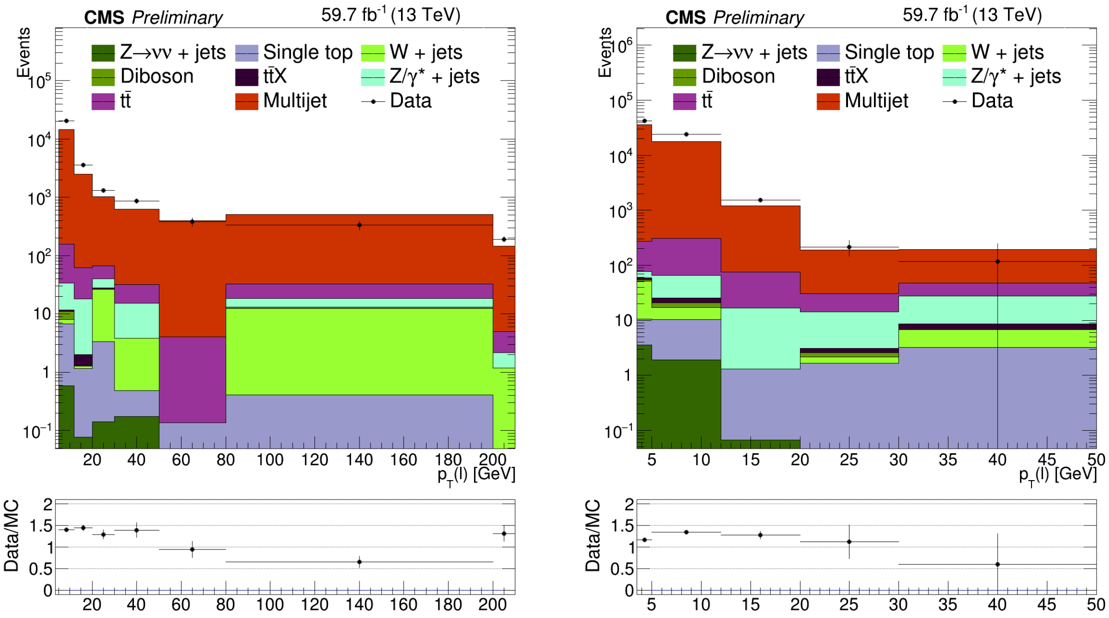

Figure 6.3: 2018 Loose lepton p_T distributions in the MR for electrons (left) and muons (right).

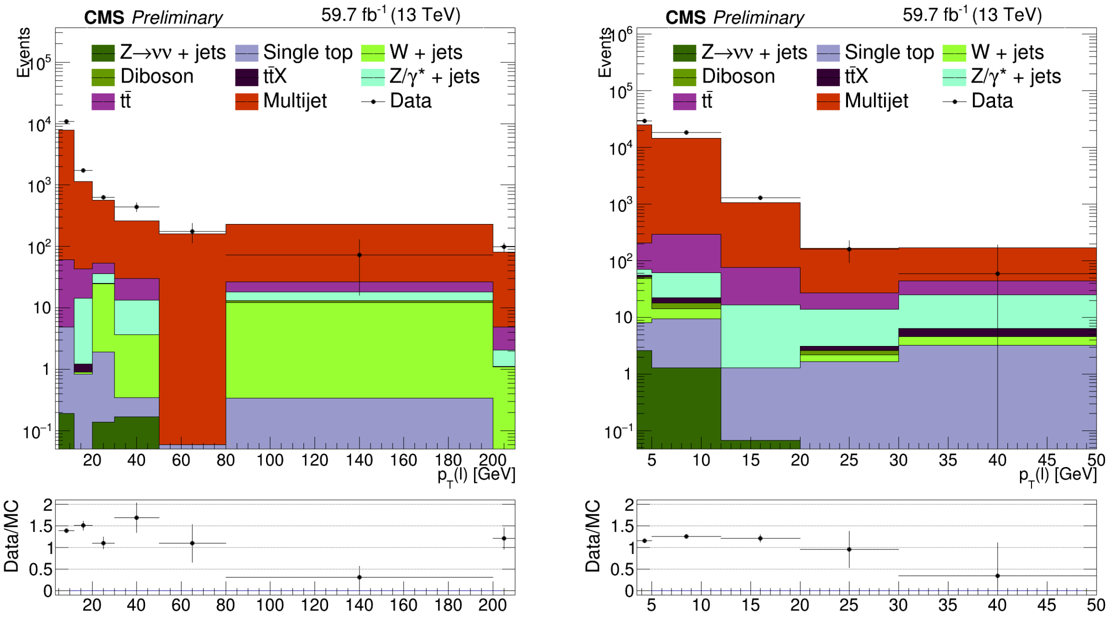

Figure 6.4: 2018 Tight lepton p_T distributions in the MR for electrons (left) and muons (right).

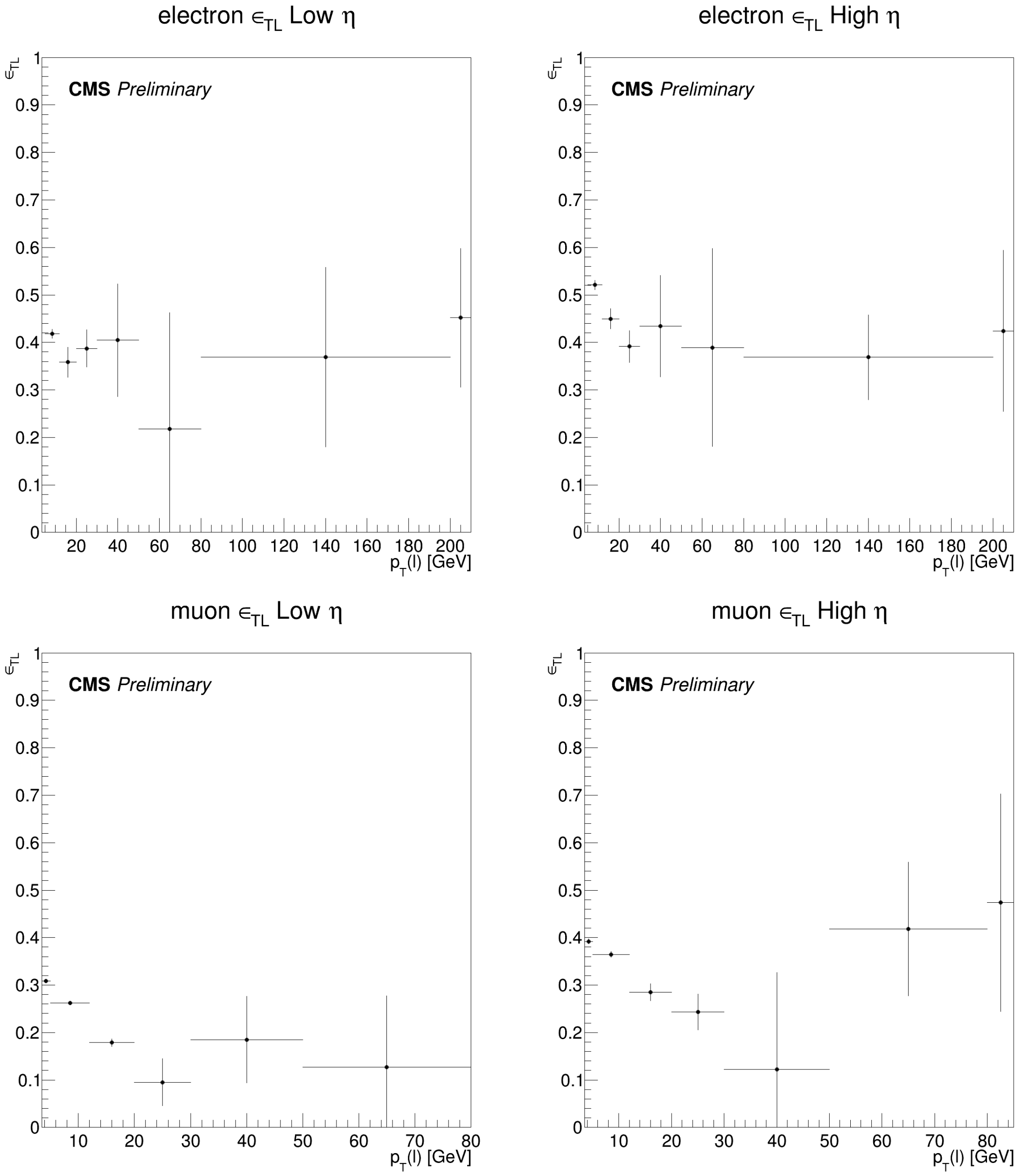

Figure 6.5: 2017 “Tight-to-loose” ratios ϵ_{TL}, see eq. 6.1, in data for electrons (top) and muons (bottom). The Low η region, where $|\eta| < 1.5$, is on the left for both lepton flavors while the High η region, where $|\eta| > 1.5$, is shown on the right.

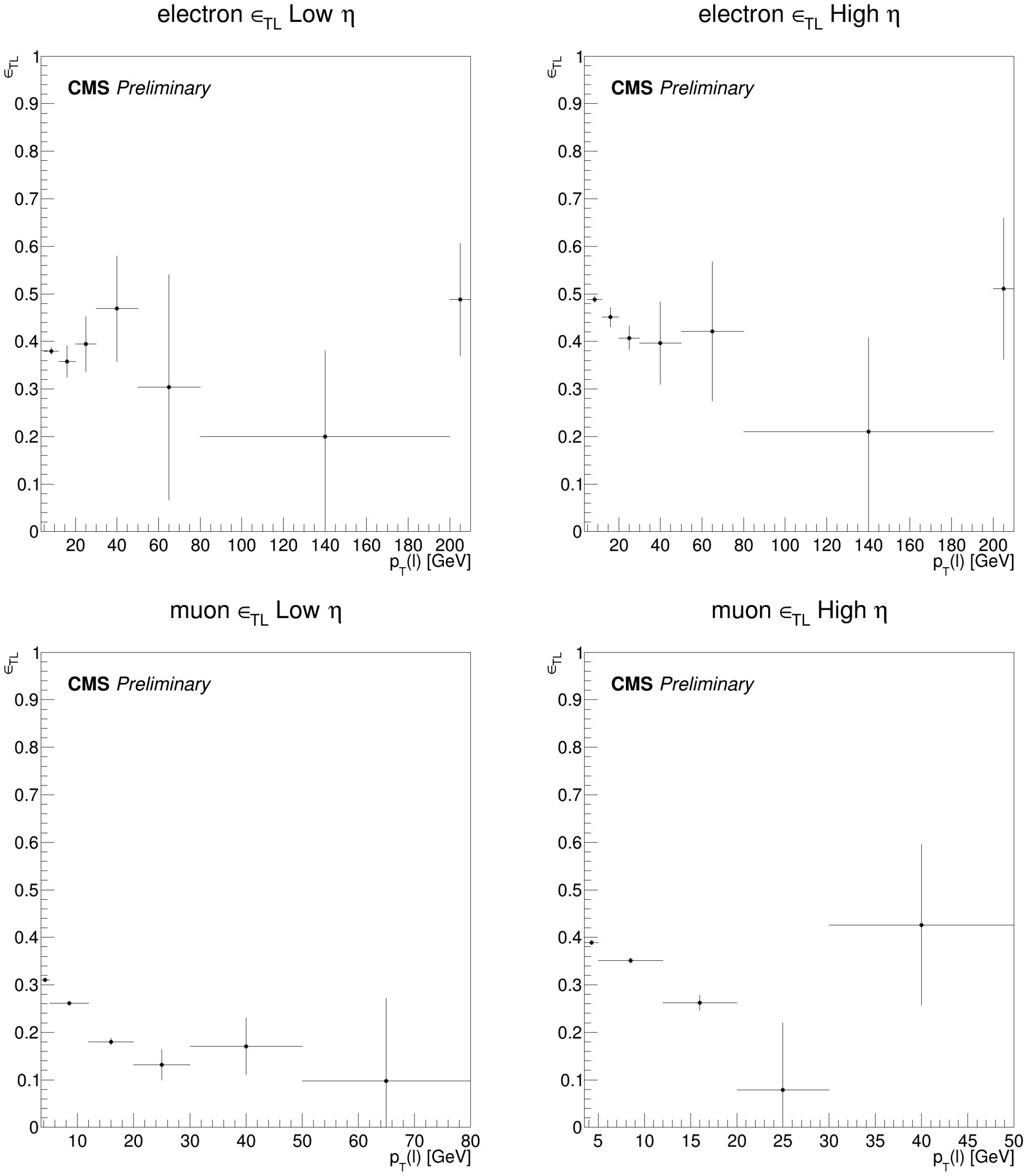

Figure 6.6: 2018 "Tight-to-loose" ratios ϵ_{TL}, see eq. 6.1, in data for electrons (top) and muons (bottom). The Low η region, where $|\eta| < 1.5$, is on the left for both lepton flavors while the High η region, where $|\eta| > 1.5$, is shown on the right.

One of the main contributions to the systematic uncertainty of this measurement is the non-universality of the ϵ_{TL} due to the dependence on the flavour and the p_{T} of mother parton jets from which the nonprompt leptons originate. In order to evaluate this systematic effect, the measurement was additionally performed when enriching or depleting the sample with *b* tagged jets, by requiring at least one *b* tagged jet, or by applying a *b* veto. These variations are presented in Figures 6.7 and 6.8. The systematic uncertainty in the "tight-to-loose" ratio is based on these *b* tagged variations, and their values are shown in Table 6.1. Furthermore, the MC statistical uncertainty affecting the prompt contribution which is subtracted from both the measurement and "L!T" regions is taken into account in the total systematic uncertainty. Finally, the systematic uncertainty related to the *W*+jets reweighing of the prompt samples is propagated to the estimate.

Table 6.1: Systematic uncertainties in the "tight-to-loose" ratio non-universality, based on measurements with *b* tag variations.

$p_{\mathbf{T}}(\ell)$ (GeV)	2017 Sys. unc. (%)	2018 Sys. unc. (%)
$[3.5, 5[$	3	3
$[5, 12[$	5	5
$[12, 20[$	15	10
$[20, 30[$	50	70
$[30, Inf.[$	70	90

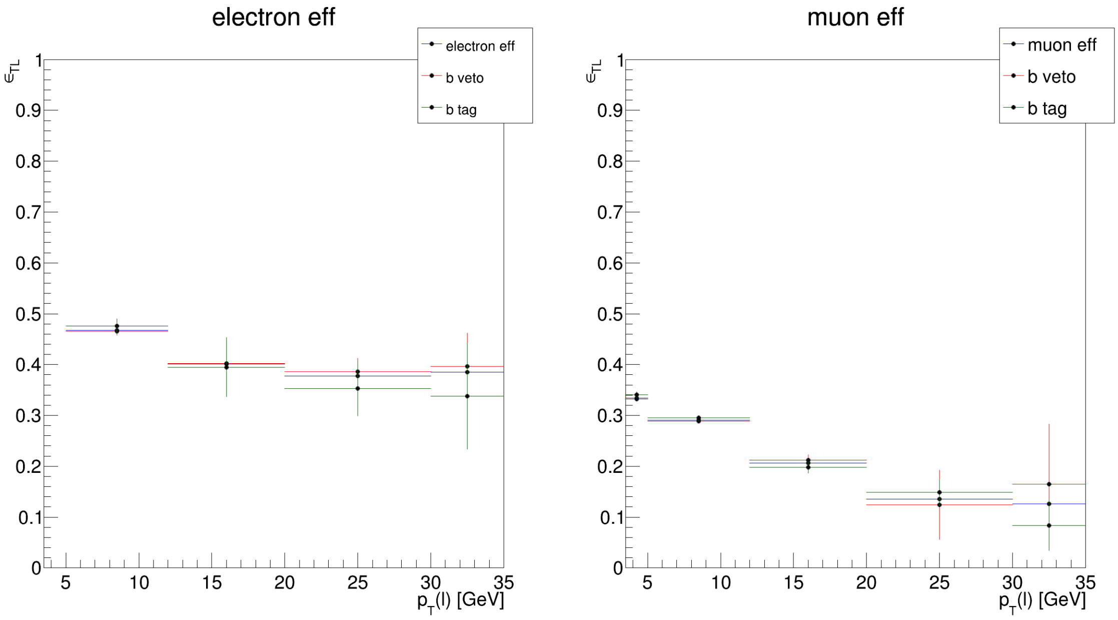

Figure 6.7: 2017 “Tight-to-loose” ratios ϵ_{TL}, see eq. 6.1, in data for electrons (left) and muons (right). ϵ_{TL} measured as a function of heavy-flavour criteria.

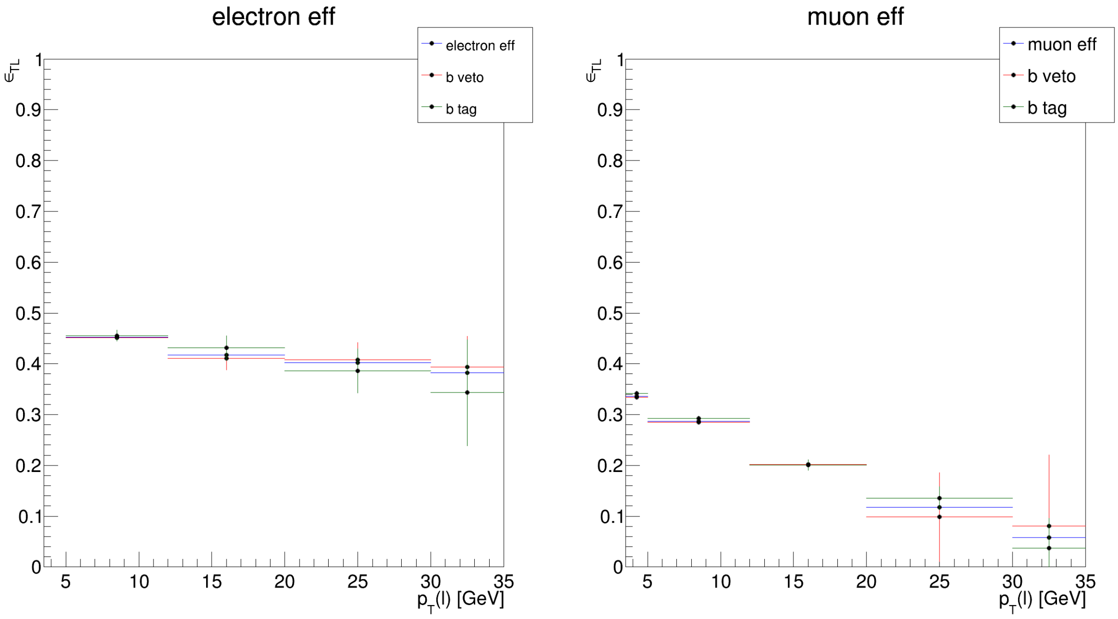

Figure 6.8: 2018 “Tight-to-loose” ratios ϵ_{TL}, see eq. 6.1, in data for electrons (left) and muons (right). ϵ_{TL} measured as a function of heavy-flavour criteria.

The nonprompt background prediction for the SRs as defined in Table 5.4 is reported in Tables 6.2 and 6.3 for the years of 2017 and 2018 respectively. The values of $N^{L!T}(Data)$ and $N_{\mathrm{p}}^{L!T}$ in Equation 6.1 is also reported.

Table 6.2: 2017 Estimate of the background with a nonprompt lepton for the eight SRs. The reported uncertainties are statistical.

Δm **(GeV)**	$N^{L!T}(Data)$	$N_{\mathbf{p}}^{L!T}$	$Y_{\mathbf{np}}^{\mathbf{SR}}$
10	21 ± 3	1.11 ± 0.34	20.08 ± 3.31
20	53 ± 5	3.58 ± 0.61	49.55 ± 3.35
30	43 ± 5	1.72 ± 0.36	41.70 ± 4.79
40	34 ± 4	0.91 ± 0.23	32.59 ± 4.10
50	23 ± 3	0.61 ± 0.21	22.31 ± 3.34
60	8 ± 2	0.13 ± 0.04	7.60 ± 1.97
70	14 ± 3	1.03 ± 0.59	12.86 ± 2.64
80	9 ± 2	0.27 ± 0.10	8.32 ± 1.86

Table 6.3: 2018 Estimate of the background with a nonprompt lepton for the eight SRs. The reported uncertainties are statistical.

Δm **(GeV)**	$N^{L!T}(Data)$	$N_{\mathbf{p}}^{L!T}$	$Y_{\mathbf{np}}^{\mathbf{SR}}$
10	18 ± 3	1.36 ± 0.43	16.71 ± 3.22
20	17 ± 3	2.21 ± 0.86	14.45 ± 3.09
30	29 ± 4	6.27 ± 1.86	22.52 ± 4.38
40	12 ± 3	0.71 ± 0.17	11.66 ± 2.67
50	11 ± 3	0.48 ± 0.14	10.46 ± 2.59
60	19 ± 4	1.70 ± 1.00	17.32 ± 3.40
70	19 ± 3	2.04 ± 1.03	16.94 ± 3.63
80	11 ± 3	0.21 ± 1.63	10.86 ± 2.69

6.2 Dominant prompt backgrounds

To estimate the prompt contributions from the *W*+jets and $t\bar{t}$ processes, a method based on the number of these background events observed in data CRs is used. The method uses the output of the BDT, and a transfer factor between the CR and the SR, obtained from simulation. This factor, of the order 10^{-3} for both backgrounds and for both years, is the ratio of the number of predicted events in the SR, N_{p}^{SR}, to the one in the CR, N_{p}^{CR}. The estimated yield Y_{p}^{SR} of the dominant prompt background in the SR, estimated independently per process and per year, is then determined using:

$$Y_{\text{p}}^{\text{SR}}(X) = \frac{N_{\text{p}}^{\text{SR}}(X)}{N_{\text{p}}^{\text{CR}}(X)} \left[N^{\text{CR}}(\text{Data}) - N_{\text{p}}^{\text{CR}}(\text{non-}X) - Y_{\text{np}}^{\text{CR}}\right], \tag{6.2}$$

where X refers to the background process being estimated, either *W*+jets or $t\bar{t}$, and where the terms prompt and nonprompt refer to their definition as given at the beginning of the present section. To obtain a data sample enriched in the backgrounds being estimated, a CR is defined by applying the preselection criteria, with the additional requirement $\text{BDT} < 0$. The number of such events is denoted as $N^{\text{CR}}(\text{Data})$. The number $N_{\text{p}}^{\text{CR}}(\text{non-}X)$ is the number of prompt background events other than the process being estimated in the CR, estimated from simulation and subtracted from the number of data events; e.g.: if $X =$ *W*+jets, this term includes $t\bar{t}$, and vice versa. The yield $Y_{\text{np}}^{\text{CR}}$, which is the predicted number of nonprompt background in the CR, is also subtracted. To enrich the CR in *W*+jets or $t\bar{t}$ events, it is required that the number of loosely *b* tagged jets to be zero, or the number of tightly tagged *b* jets to be at least one, respectively. Thus, these CRs are defined as follows:

Table 6.4: *W*+jets and $t\bar{t}$ CRs selection criteria.

CR(*W*+jets)	**CR($t\bar{t}$)**
Preselection	Preselection
BDT $<$ 0.0	BDT $<$ 0.0
$N_b(loose) = 0$	$N_b(tight) > 0$

Tables 6.5 and 6.7 show the composition of CR(*W*+jets) and CR($t\bar{t}$), which are summarized in Tables 6.6 and 6.8 respectively in terms of the percentage of *W*+jets & $t\bar{t}$ processes to the total background, as well as the level of signal contamination in each CR. The BDTs trainings for Δm = 10 and 80 GeV for both years are considered. The signals with the highest cross section, (m($\widetilde{t}_1$),m($\widetilde{\chi}_1^0$))=(250,240) GeV for the lowest Δm signal and (m($\widetilde{t}_1$),m($\widetilde{\chi}_1^0$))=(250,170) GeV for the highest one, are considered in order to measure the highest possible signal contamination.

The purity of *W*+jets and $t\bar{t}$ in the corresponding CRs is approximately 93% and 78%, respectively. It is observed that the level of signal contamination is well below 5%.

In order to test the method for predicting the *W*+jets and $t\bar{t}$ backgrounds independently of the AR, the validation regions VR1 and VR2, as defined in Section5.4.2, are further enriched in the specific process in which the method is being tested. These VRs are chosen because they are orthogonal to the AR while at the same time being kinematically close to it, and kinematically complementary with each other versus the AR. Thus, VR1 and VR2 are used as data regions where this method is tested. To gain events in the SR of these VRs, the selection on BDT is loosen to be BDT $>$ 0.0; the

Table 6.5: 2017 and 2018 expected number of simulated background processes, total background and signal events in the control regions CR(W+jets) and CR($t\bar{t}$) for 41.5 fb^{-1} and 59.8 fb^{-1} respectively. The BDT used is the one for Δm = 10 GeV and the benchmark signal point is (m($\widetilde{t}_1$),m($\widetilde{\chi}^0_1$))=(250,240). Uncertainties are statistical.

Selection level	**W+jets**	**$t\bar{t}$**	**Z+jets**	**Other**	**Total Background**	**Signal (250,240)**
2017						
CR(W+jets)	27960	801	192	1075	30028 ± 200	360.5 ± 19.5
CR($t\bar{t}$)	797	5628	46	790	7261 ± 157	77.1 ± 9.6
2018						
CR(W+jets)	36682	1015	223	1330	39250 ± 268	417.2 ± 19.3
CR($t\bar{t}$)	1221	8356	60	1114	10751 ± 241	120.9 ± 15.3

Table 6.6: Percentage of the W+jets & $t\bar{t}$ processes to the total background, as well as the level of signal contamination in each of the control regions CR(W+jets) and CR($t\bar{t}$). The BDT training considered is for Δm = 10 GeV with the benchmark signal point (m($\widetilde{t}_1$),m($\widetilde{\chi}^0_1$))=(250,240).

	2017			**2018**		
Process	**W+jets**	**$t\bar{t}$**	**Signal (250,240)**	**W+jets**	**$t\bar{t}$**	**Signal (250,240)**
CR(W+jets)	93.1 %	2.7 %	1.2 %	93.5 %	2.6 %	1.1 %
CR($t\bar{t}$)	11.0 %	77.5 %	1.1 %	11.4 %	77.7 %	1.1 %

Table 6.7: 2017 and 2018 expected number of simulated background processes, total background and signal events in the control regions CR(W+jets) and CR($t\bar{t}$) for 41.5 fb^{-1} and 59.8 fb^{-1} respectively. The BDT used is the one for Δm = 80 GeV and the benchmark signal point is (m($\widetilde{t}_1$),m($\widetilde{\chi}^0_1$))=(250,170). Uncertainties are statistical.

Selection level	**W+jets**	**$t\bar{t}$**	**Z+jets**	**Other**	**Total Background**	**Signal (250,170)**
2017						
CR(W+jets)	71446	1937	441	3443	77267 ± 295	1227.1 ± 35.2
CR($t\bar{t}$)	2107	15292	54	2643	20096 ± 262	728.1 ± 30.1
2018						
CR(W+jets)	92664	2582	601	4394	100240 ± 402	1614.4 ± 36.7
CR($t\bar{t}$)	3126	23606	68	3807	30607 ± 406	1284.8 ± 45.3

Table 6.8: Percentage of the W+jets & $t\bar{t}$ processes to the total background, as well as the level of signal contamination in each of the control regions CR(W+jets) and CR($t\bar{t}$). The BDT training considered is for Δm = 80 GeV with the benchmark signal point (m($\widetilde{t}_1$),m($\widetilde{\chi}^0_1$))=(250,170).

	2017			**2018**		
Process	**W+jets**	**$t\bar{t}$**	**Signal (250,170)**	**W+jets**	**$t\bar{t}$**	**Signal (250,170)**
CR(W+jets)	92.5 %	2.5 %	1.6 %	92.4 %	2.6 %	1.6 %
CR($t\bar{t}$)	10.5 %	76.1 %	3.6 %	10.2 %	77.1 %	4.2 %

CRs are defined by inverting this criteria on the BDT output values to be BDT < 0.0. This value was chosen taking into account the level of signal present as well as the statistics available in the SR of the VRs. In these VRs the predicted yield from Equation 6.2 is compared to the observed number of data events in the SR of the VRs. These tests are presented in the Appendix C.6 and are the basis for systematic uncertainty methods presented in Section 7.3.

Tables 6.9 to 6.12 provide the necessary yields to calculate the predicted background $Y_{\mathrm{p}}^{\mathrm{SR}}$ from Equation 6.2 within the SR, for the SRs as defined in Table 5.4. In these tables, the number of background events other than *W*+jets, $t\bar{t}$ and nonprompt lepton are taken from simulation. To note that, due to the selection power of the BDTs, in some cases very few $t\bar{t}$ MC events ($\sim$15) populate the SR. Since the $t\bar{t}$ samples used in this analysis are simulated to NLO, in some Δm cases, $N_p^{SR}(t\bar{t})$ is negative. To deal with such cases, $N_p^{SR}(t\bar{t})$ is set to zero and the uncertainty to equal the uncertainty of the negative value of $N_p^{SR}(t\bar{t})$ before the correction. This approach was recommended by the CMS Statistics Committee).

Table 6.9: 2017 estimate of *W*+jets background for all Δm cases. Number of observed data events and simulated events in the control region CR(*W*+jets). Here, $N_p^{CR}(Rare)$ designates the number of $t\bar{t}$ events in the CR. Number of simulated events and number of estimated *W*+jets events in the signal region. The uncertainty in the estimated yield is statistical only.

Δm (GeV)	$N_p^{SR}(W+jets)$	$N_p^{CR}(W+jets)$	$N^{CR}(Data)$	$Y_{\mathrm{np}}^{\mathrm{CR}}$	$N_p^{CR}(Rare)$	$Y_{\mathrm{p}}^{\mathrm{SR}}(W+jets)$
10	7.81 ± 0.64	23222 ± 169	36125 ± 190	1440 ± 63	1945 ± 58	11.01 ± 0.91
20	26.50 ± 1.40	23077 ± 169	35841 ± 189	1404 ± 62	1892 ± 58	37.37 ± 2.01
30	16.89 ± 1.52	23011 ± 169	35742 ± 189	1387 ± 61	1873 ± 58	23.84 ± 2.16
40	11.28 ± 1.38	23057 ± 169	35867 ± 189	1381 ± 61	1899 ± 58	15.94 ± 1.95
50	7.74 ± 1.07	23086 ± 169	35907 ± 189	1364 ± 61	1905 ± 58	10.94 ± 1.51
60	2.74 ± 0.48	23111 ± 169	35981 ± 190	1369 ± 61	1918 ± 58	3.88 ± 0.68
70	8.38 ± 0.92	62188 ± 234	89485 ± 299	4535 ± 116	2546 ± 66	11.10 ± 1.22
80	11.75 ± 2.57	62043 ± 234	89188 ± 299	4477 ± 115	2538 ± 66	15.56 ± 3.40

Table 6.10: 2017 estimate of $t\bar{t}$ background for all Δm cases. Number of observed data events and simulated events in the control region CR($t\bar{t}$). Here, $N_p^{CR}(Rare)$ designates the number of *W*+jets events in the CR. Number of simulated events and number of estimated $t\bar{t}$ events in the signal region. The uncertainty in the estimated yield is statistical only.

Δm (GeV)	$N_p^{SR}(t\bar{t})$	$N_p^{CR}(t\bar{t})$	$N^{CR}(Data)$	$Y_{\mathrm{np}}^{\mathrm{CR}}$	$N_p^{CR}(Rare)$	$Y_{\mathrm{p}}^{\mathrm{SR}}(t\bar{t})$
10	1.53 ± 1.55	4121 ± 131	7846 ± 89	1157 ± 31	661 ± 36	2.25 ± 2.26
20	2.26 ± 3.21	4119 ± 131	7828 ± 88	1153 ± 31	659 ± 36	3.30 ± 4.70
30	0 ± 4.95	4121 ± 131	7811 ± 88	1148 ± 31	652 ± 36	0 ± 7.23
40	0 ± 5.14	4104 ± 131	7784 ± 88	1144 ± 30	650 ± 36	0 ± 7.50
50	0 ± 4.40	4102 ± 131	7766 ± 88	1139 ± 30	641 ± 36	0 ± 6.41
60	0 ± 4.21	4100 ± 131	7765 ± 88	1136 ± 30	640 ± 36	0 ± 6.15
70	7.51 ± 6.42	13819 ± 244	21209 ± 146	4099 ± 50	790 ± 43	8.87 ± 7.58
80	8.73 ± 8.15	13810 ± 244	21239 ± 146	4103 ± 50	787 ± 43	10.34 ± 9.65

Table 6.11: 2018 estimate of *W*+jets background for all Δm cases. Number of observed data events and simulated events in the control region CR(*W*+jets). Number of simulated events and number of estimated *W*+jets events in the signal region. The uncertainty in the estimated yield is statistical only.

Δm (GeV)	$N_p^{SR}(W + jets)$	$N_p^{CR}(W + jets)$	$N^{CR}(Data)$	$Y_{\mathrm{np}}^{\mathrm{CR}}$	$N_p^{CR}(Rare)$	$Y_{\mathrm{p}}^{\mathrm{SR}}(W + jets)$
10	12.48 ± 1.49	30460 ± 228	45582 ± 213	1759 ± 84	1589 ± 67	17.30 ± 2.08
20	13.30 ± 1.50	30242 ± 228	45221 ± 213	1730 ± 84	1569 ± 67	18.43 ± 2.08
30	34.96 ± 4.00	30231 ± 227	45236 ± 213	1703 ± 83	1560 ± 67	48.54 ± 5.57
40	7.70 ± 1.58	30263 ± 227	45326 ± 213	1709 ± 83	1569 ± 67	10.70 ± 2.20
50	6.28 ± 1.68	30267 ± 227	45366 ± 213	1685 ± 82	1558 ± 67	8.74 ± 2.34
60	11.85 ± 2.03	30301 ± 227	45402 ± 213	1672 ± 82	1562 ± 67	16.48 ± 2.83
70	27.20 ± 4.85	80685 ± 333	113774 ± 337	5879 ± 153	2153 ± 77	35.65 ± 6.37
80	12.41 ± 1.81	80669 ± 332	113731 ± 337	5810 ± 152	2158 ± 77	16.27 ± 2.38

Table 6.12: 2018 estimate of $t\bar{t}$ background for all Δm cases. Number of observed data events and simulated events in the control region CR($t\bar{t}$). Number of simulated events and number of estimated $t\bar{t}$ events in the signal region. The uncertainty in the estimated yield is statistical only.

Δm (GeV)	$N_p^{SR}(t\bar{t})$	$N_p^{CR}(t\bar{t})$	$N^{CR}(Data)$	$Y_{\mathrm{np}}^{\mathrm{CR}}$	$N_p^{CR}(Rare)$	$Y_{\mathrm{p}}^{\mathrm{SR}}(t\bar{t})$
10	0 ± 1.53	5862 ± 198	11316 ± 106	1728 ± 51	476 ± 47	0 ± 2.38
20	0.16 ± 1.96	5848 ± 198	11297 ± 106	1724 ± 51	474 ± 47	0.25 ± 3.05
30	5.88 ± 5.38	5834 ± 198	11241 ± 106	1711 ± 51	471 ± 47	9.13 ± 8.37
40	2.19 ± 2.82	5803 ± 197	11197 ± 106	1713 ± 51	470 ± 47	3.40 ± 4.38
50	2.19 ± 2.82	5769 ± 197	11164 ± 106	1696 ± 51	468 ± 46	3.42 ± 4.40
60	10.36 ± 5.14	5750 ± 197	11135 ± 106	1693 ± 51	460 ± 46	16.19 ± 8.05
70	12.97 ± 7.18	20800 ± 374	31120 ± 176	6124 ± 97	605 ± 58	15.21 ± 8.42
80	9.29 ± 6.57	20819 ± 374	31175 ± 177	6138 ± 97	610 ± 58	10.90 ± 7.71

7

Systematic uncertainties

Contents

7.1 Systematic uncertainties in the MC estimated backgrounds

Processes for which the absolute yield is predicted by simulation are subject to systematic uncertainties in the determination of the integrated luminosity, which is estimated year-by-year with uncertainties in the 1.2–2.5% range [108, 109]. An uncertainty of 50% is assigned to the cross sections of all backgrounds whose yields are predicted from simulation. The uncertainty due to the simulation of pileup for simulated background processes is estimated by varying the inelastic *pp* cross section by 4.6% [101].

The systematic uncertainties in the scale factors applied to the simulated samples for trigger, and lepton efficiencies are taken into account. The source of uncertainties for this efficiencies correspond to the precision with which these SFs are known.

All simulated samples are subject to experimental uncertainties in the JES and JER. JES uncertainties are primarily due to the imperfect calibration of the detector response to jet energy, which can be affected by uncertainties in the energy measurement of individual particles within the jet, as well as by the presence of additional particles in the jet environment. JER uncertainties, on the other hand, are mainly caused by fluctuations in the energy measurements of individual particles within the jet, which can be affected by factors such as detector noise, pileup, and the intrinsic properties of the jet fragmentation and hadronization processes. The uncertainties arising from miscalibration of the JES are estimated by varying the Jet Energy Correction (JEC) up and down by one standard deviation of their uncertainties, and propagating the effect to the calculation of $p_{\mathrm{T}}^{\text{miss}}$. Differences in the JER between data and simulation are accounted by smearing the momenta of jets in simulation according to a Gaussian with a width that is given as a function of p_{T} and η of the jet, in order to match the measured resolution in data. The smearing parameters are varied up and down within their uncertainties and the effect is propagated to $p_{\mathrm{T}}^{\text{miss}}$ and all jet–related variables [93].

Variations in the efficiency of the *b* jet identification would move events between the *b* tagged bins, and change the fractions of *W*+jets and $t\bar{t}$ events in each bin, therefore affecting the prediction of these two backgrounds (see Table 6.4). This also affects the event-by-event weight via the Equation 4.2 (see Section 4.8). Each jet is assigned a *b* tagging efficiency which is the product of the simulated *b* tagging efficiency and the data-to-simulation scale factor. Both depend on the parton associated to the jet (*b* quark, *c* quark or light quark), and the p_{T} and η of the jet. Variations are done independently for light–flavor and for *c*- or *b*-quark jets. These variations are propagated to the event level by calculating for every simulated event the probability to yield 0, 1 or ≥ 2 *b* tagged jets ("combinatorial weights").

Uncertainties from unknown higher-order terms in the perturbative expansion are estimated through uncorrelated variations of the renormalization and factorization scales by factors of 0.5, 1, and 2 [110].

The estimations of the *W*+jets and $t\bar{t}$ backgrounds rely partially on the simulation and are therefore sensitive to theoretical uncertainties in the modeling of ISR. For the $t\bar{t}$ process, half of the ISR correction is assigned as the systematic uncertainty, which also applies to the simulated signal samples. For the *W*+jets process, the difference between the ISR-corrected and uncorrected simulation is taken as the systematic uncertainty.

7.2 Systematic uncertainties in the nonprompt background estimation

The systematic uncertainty in the prediction of the nonprompt lepton background has three components:

- The uncertainty related to the reweighing of the prompt processes, which is the reweighing of the W+jets process versus S_{T} (see Section 4.9), and the ISR correction of $t\bar{t}$ samples, both of which are propagated to the estimate.
- The systematic uncertainty of the non-universality of the ϵ_{TL} due to the dependence on flavor and p_{T} of the mother parton of the jets from which the nonprompt leptons originate (see Section 6.1).
- A systematic uncertainty which is the measure of how well the method closes (see Appendix C.5).

These three components are reported in Table 7.1 for 2017 and in Table 7.2 for 2018. The total systematic uncertainty in the prediction of the nonprompt background, per Δm region, is reported in Section 7.5.

Table 7.1: 2017: Relative systematic uncertainties affecting the data-driven nonprompt lepton prediction, this per Δm region.

Δm (GeV)	S_{T} & ISR	Lepton non- -universality	Closure
10	0.8 %	6.2 %	0.0 %
20	0.9 %	9.1 %	0.0 %
30	0.5 %	9.0 %	0.0 %
40	0.3 %	9.4 %	6.3 %
50	0.3 %	9.7 %	0.0 %
60	0.2 %	10.1 %	0.0 %
70	0.3 %	9.7 %	0.0 %
80	0.2 %	14.8 %	0.0 %

Table 7.2: 2018: Relative systematic uncertainties affecting the data-driven nonprompt lepton prediction, this per Δm region.

Δm (GeV)	S_{T} & ISR	Lepton non- -universality	Closure
10	1.2 %	7.2 %	5.8 %
20	1.5 %	9.3 %	0.0 %
30	1.5 %	8.3 %	0.0 %
40	0.7 %	8.7 %	0.0 %
50	0.3 %	9.7 %	0.0 %
60	0.3 %	9.3 %	0.8 %
70	0.6 %	14.9 %	0.0 %
80	0.4 %	26.9 %	0.0 %

7.3 Systematic uncertainties in the prompt background estimation

To determine the inherent systematic uncertainty in the data-driven method for predicting the W+jets and $t\bar{t}$ backgrounds, the predicted yield from Equation 6.2 is compared to the observed number of data events in the SR, this in a given VR. For each of these background processes, $S_{DD}(X)$ measures how well the predicted number of background events $Y^{\mathrm{SR}}_{\mathsf{pred}}(X) = Y^{\mathrm{SR}}_{\mathsf{p}}(X) + N^{SR}(\text{non-}X)$ matches the number of observed data events $N^{SR}(Data)$ in the SR:

$$S_{DD}(X) = \quad [N^{SR}(Data) - Y^{\mathrm{SR}}_{\mathsf{pred}}(X)]^{VR} \tag{7.1}$$

The quantity $S_{DD}(X)$ is taken as the absolute systematic uncertainty inherent to the data-driven method. However this uncertainty cannot be known with a precision higher than on $N^{SR}(Data) - N^{SR}(Other)$ where $Other$ refers to processes determined from simulation in this very calculation (i.e. rare processes, Z+jets, either W+jets or $t\bar{t}$). To estimate this precision, $\delta_{S_{DD}}(X)$, the statistical uncertainty in data, the uncertainty in rare MC processes as 50% of the yield of each rare and Z+jets processes, and the uncertainty of the cross contaminating MC process (e.g. the $t\bar{t}$ contribution when evaluating the W+jets uncertainty) as 20% of its yield, are quadratically added. All this in the SR of the appropriate VR. Consequently, it is considered the absolute systematic uncertainty inherent to the data-driven method to be the maximum between $S^2_{DD}(X)$ and $\delta^2_{S_{DD}}(X)$, once again, in the appropriate VR:

$$\delta^2_{DD}(X) = Max(S^2_{DD}(X), \delta^2_{S_{DD}}(X)) \tag{7.2}$$

Therefore the relative systematic uncertainty Sys_{DD} inherent to the data-driven prediction is defined as follows:

$$Sys_{DD}(X) = \frac{\delta_{DD}(X)}{[Y^{\mathrm{SR}}_{\mathsf{p}}(X)]^{VR}} \tag{7.3}$$

By applying the method described above to VR1 (Tables C.3 to C.10) and VR2 (Tables C.19 to C.24) for the prediction of W+jets, the relative systematic uncertainty $Sys_{DD}(W + jets)$ for data-driven estimation of this background process according to two different VRs is reported in Table 7.3 for the year of 2017. This process is repeated for the year of 2018, in VR1 (Tables C.31 to C.38) and VR2 (Tables C.47 to C.52). The relative systematic uncertainty for W+jets in 2018 due to this method is reported in Table 7.4. Similarly, the method described above is applied to VR1 (Tables C.11 to C.18) and VR2 (Tables C.25 to C.30) for the prediction of $t\bar{t}$ in 2017. For the application of the method in the prediction of $t\bar{t}$ in 2018 in VR1 (Tables C.39 to C.46) and VR2 (Tables C.53 to C.58). The relative systematic uncertainty $Sys_{DD}(t\bar{t})$ for data-driven prediction of $t\bar{t}$ is obtained according to two different VRs in Table 7.3 and 7.4 for 2017 and 2018 respectively. To be conservative, per year, largest uncertainty per Δm is taken.

Table 7.3: 2017 Relative systematic uncertainties $Sys_{DD}(W + jets)$ and $Sys_{DD}(t\bar{t})$ affecting the data-driven prediction of W+jets and $t\bar{t}$ per Δm region in the two validation regions VR1 & VR2. The uncertainties are calculated according to Equation 7.3. NA stands for not-applicable.

Δm	$Sys_{DD}(W + jets)$		$Sys_{DD}(t\bar{t})$	
(GeV)	**vr1**	**vr2**	**vr1**	**vr2**
10	18.3 %	20.0 %	77.9 %	68.7 %
20	8.9 %	11.1 %	26.5 %	69.8 %
30	13.0 %	7.4 %	26.4 %	37.0 %
40	10.8 %	6.2 %	41.0 %	25.5 %
50	12.6 %	6.8 %	15.2 %	21.3 %
60	11.5 %	6.8 %	19.0 %	20.5 %
70	14.1 %	NA	8.0 %	NA
80	17.1 %	NA	9.2 %	NA

Table 7.4: 2018 Relative systematic uncertainties $Sys_{DD}(W + jets)$ and $Sys_{DD}(t\bar{t})$ affecting the data-driven prediction of W+jets and $t\bar{t}$ per Δm region in the two validation regions VR1 & VR2. The uncertainties are calculated according to Equation 7.3. NA stands for not-applicable.

Δm	$Sys_{DD}(W + jets)$		$Sys_{DD}(t\bar{t})$	
(GeV)	**vr1**	**vr2**	**vr1**	**vr2**
10	14.6 %	21.6 %	66.9 %	61.2 %
20	5.8 %	10.4 %	35.4 %	81.5 %
30	12.0 %	7.7 %	45.8 %	43.1 %
40	20.7 %	7.7 %	31.3 %	25.0 %
50	20.8 %	6.9 %	25.5 %	17.9 %
60	23.1 %	7.1 %	21.8 %	16.0 %
70	16.5 %	NA	11.2 %	NA
80	17.7 %	NA	8.1 %	NA

The next studies address the modeling of BDT output. To cross-check the accuracy of the data-driven prompt background prediction method, $R(X)$ is defined for both the CR and SR of each VR as the data to simulation ratio:

$$R^{CR,SR}(X) = \left[\frac{N(Data) - N(Other)}{N(X)}\right]^{CR,SR} \tag{7.4}$$

A visualization of the difference between $R^{CR}(X)$ and $R^{SR}(X)$ in both VRs is reported in Section C.7. If there is a difference in the shape of the distribution of the output of the BDT between data and simulation, $R^{CR}(X)$ and $R^{SR}(X)$ would differ. The difference D, defined as $D = R^{CR} - R^{SR}$, is an estimator of the percentual bias inherent to the data-driven method because of a shape difference affecting the prediction of the prompt background. The relative systematic uncertainty of the data-driven prediction due to shape differences, δ'_{DD}, is defined as:

$$\delta'^{2}_{DD} = Max(D^2 - \delta^2_D, \left[\left(\frac{\delta_{sta}(DD)}{N^{SR}_{DD}(X)}\right)^2\right]^{VR}), \tag{7.5}$$

where δ_D is the statistical uncertainty in D and $\delta_{sta}(DD)$ the statistical uncertainty of the data-driven prediction of the prompt background in the SR of VR.

Tables 7.5 and 7.7 provide the values of the ratios $R^{CR}(X)$ and $R^{SR}(X)$, the difference D, and the final relative systematic uncertainty δ'_{DD} due to shape difference, all this in two sub-regions of VR1 for *W*+jets and for $t\bar{t}$ and across the eight Δm regions for both 2017 and 2018 respectively. It is observed that within the available statistics, there is a slight difference in the variation of the shape of the BDT output between data and simulation for *W*+jets, this across control- & signal-regions. This shape comparison in the CR and SR of VRs between data and simulation accounts for observed trends which ultimately translate into a systematic uncertainty of the data driven estimation of the prompt backgrounds. In Tables 7.6 and 7.8 the same analysis is provided for VR2.

In order to be conservative, the final relative systematic uncertainty in the estimation of the prompt backgrounds, in their respective year, is the largest percentual uncertainty across Tables 7.3 to 7.8. The final systematic uncertainties are reported in Section 7.5.

Table 7.5: 2017 Relative systematic uncertainty Sys'_{DD} affecting the data-driven prediction of *W*+jets (upper table) & $t\bar{t}$ (bottom table) per Δm region, in the VR1 region. The uncertainties are calculated according to Equation 7.5.

$\boldsymbol{\Delta m}$	**VR1: *W*+jets**					
(GeV)	$\boldsymbol{R^{CR}(W+jets)}$	$\boldsymbol{R^{SR}(W+jets)}$	$\boldsymbol{D}$	$\boldsymbol{D^2-\delta_D^2}$	$\boldsymbol{\left(\frac{\delta_{sta}(DD)}{N_{DD}^{SR}(X)}\right)^2}$	$\boldsymbol{Sys'_{DD}}$
10	1.04 ± 0.01	0.94 ± 0.21	-0.10 ± 0.21	-0.0343	0.0004	2.0 %
20	1.03 ± 0.01	1.12 ± 0.03	0.09 ± 0.03	0.0073	0.0005	8.6 %
30	1.03 ± 0.01	1.17 ± 0.04	0.13 ± 0.04	0.0164	0.0006	12.8 %
40	1.03 ± 0.01	1.14 ± 0.04	0.11 ± 0.04	0.0105	0.0008	10.3 %
50	1.03 ± 0.01	1.16 ± 0.04	0.13 ± 0.04	0.0152	0.0008	12.3 %
60	1.03 ± 0.01	1.15 ± 0.04	0.12 ± 0.04	0.0125	0.0007	11.2 %
70	1.01 ± 0.01	1.15 ± 0.03	0.14 ± 0.03	0.0198	0.0003	14.1 %
80	1.01 ± 0.01	1.18 ± 0.02	0.17 ± 0.02	0.0293	0.0002	17.1 %

$\boldsymbol{\Delta m}$	**VR1: $\boldsymbol{t\bar{t}}$**					
(GeV)	$\boldsymbol{R^{CR}(t\bar{t})}$	$\boldsymbol{R^{SR}(t\bar{t})}$	$\boldsymbol{D}$	$\boldsymbol{D^2-\delta_D^2}$	$\boldsymbol{\left(\frac{\delta_{sta}(DD)}{N_{DD}^{SR}(X)}\right)^2}$	$\boldsymbol{Sys'_{DD}}$
10	1.09 ± 0.03	0.24 ± 0.77	-0.85 ± 0.77	0.1238	0.3342	57.8 %
20	1.09 ± 0.03	1.04 ± 0.26	-0.04 ± 0.26	-0.0667	0.0298	17.3 %
30	1.09 ± 0.03	0.80 ± 0.23	-0.29 ± 0.23	0.0297	0.0357	18.9 %
40	1.09 ± 0.03	0.64 ± 0.12	-0.45 ± 0.13	0.1835	0.0158	42.8 %
50	1.09 ± 0.03	0.92 ± 0.13	-0.17 ± 0.13	0.0105	0.0119	10.9 %
60	1.09 ± 0.03	0.88 ± 0.10	-0.21 ± 0.10	0.0321	0.0083	17.9 %
70	1.00 ± 0.01	1.08 ± 0.06	0.08 ± 0.06	0.0019	0.0026	5.1 %
80	1.00 ± 0.01	1.09 ± 0.06	0.09 ± 0.06	0.0050	0.0023	7.1 %

Table 7.6: 2017 Relative systematic uncertainty Sys'_{DD} affecting the data-driven prediction of *W*+jets (upper table) & $t\bar{t}$ (bottom table) per Δm region, in the VR2 region. The uncertainties are calculated according to Equation 7.5.

$\boldsymbol{\Delta m}$	**VR2: *W*+jets**					
(GeV)	$\boldsymbol{R^{CR}(W+jets)}$	$\boldsymbol{R^{SR}(W+jets)}$	$\boldsymbol{D}$	$\boldsymbol{D^2-\delta_D^2}$	$\boldsymbol{\left(\frac{\delta_{sta}(DD)}{N_{DD}^{SR}(X)}\right)^2}$	$\boldsymbol{Sys'_{DD}}$
10	1.01 ± 0.01	1.21 ± 0.08	0.20 ± 0.0765	0.0350	0.0006	18.7 %
20	1.01 ± 0.01	1.12 ± 0.04	0.11 ± 0.0384	0.0111	0.0002	10.5 %
30	1.01 ± 0.01	1.07 ± 0.02	0.06 ± 0.0249	0.0030	0.0001	5.5 %
40	1.02 ± 0.01	1.00 ± 0.02	-0.01 ± 0.0174	-0.0001	0.0001	1.0 %
50	1.01 ± 0.01	1.01 ± 0.02	0.00 ± 0.0182	-0.0003	0.0001	1.0 %
60	1.01 ± 0.01	1.01 ± 0.02	0.00 ± 0.0173	-0.0003	0.0001	1.0 %

$\boldsymbol{\Delta m}$	**VR2: $\boldsymbol{t\bar{t}}$**					
(GeV)	$\boldsymbol{R^{CR}(t\bar{t})}$	$\boldsymbol{R^{SR}(t\bar{t})}$	$\boldsymbol{D}$	$\boldsymbol{D^2-\delta_D^2}$	$\boldsymbol{\left(\frac{\delta_{sta}(DD)}{N_{DD}^{SR}(X)}\right)^2}$	$\boldsymbol{Sys'_{DD}}$
10	0.84 ± 0.02	0.56 ± 0.47	-0.29 ± 0.47	-0.1428	0.2649	51.5 %
20	0.84 ± 0.02	0.25 ± 0.37	-0.59 ± 0.37	0.2097	0.2384	48.8 %
30	0.84 ± 0.02	0.71 ± 0.17	-0.13 ± 0.17	-0.0104	0.0331	18.2 %
40	0.85 ± 0.02	0.79 ± 0.09	-0.05 ± 0.09	-0.0057	0.0085	9.2 %
50	0.84 ± 0.02	0.89 ± 0.08	0.05 ± 0.08	-0.0033	0.0057	7.6 %
60	0.83 ± 0.02	0.96 ± 0.07	0.13 ± 0.08	0.0107	0.0048	10.4 %

Table 7.7: 2018 Relative systematic uncertainty Sys'_{DD} affecting the data-driven prediction of W+jets (upper table) & $t\bar{t}$ (bottom table) per Δm region, in the VR1 region. The uncertainties are calculated according to Equation 7.5.

Δm	**VR1: W+jets**					
(GeV)	$R^{CR}(W+jets)$	$R^{SR}(W+jets)$	D	$D^2-\delta_D^2$	$\left(\frac{\delta_{sta}(DD)}{N_{DD}^{SR}(X)}\right)^2$	Sys'_{DD}
10	1.02 ± 0.01	0.95 ± 0.15	-0.07 ± 0.15	-0.0172	0.0004	1.9 %
20	1.02 ± 0.01	1.05 ± 0.02	0.04 ± 0.02	0.0007	0.0003	2.7 %
30	1.01 ± 0.01	1.14 ± 0.03	0.12 ± 0.03	0.0138	0.0005	11.7 %
40	1.01 ± 0.01	1.22 ± 0.03	0.21 ± 0.03	0.0427	0.0006	20.7 %
50	1.01 ± 0.01	1.22 ± 0.04	0.21 ± 0.04	0.0428	0.0007	20.7 %
60	1.01 ± 0.01	1.24 ± 0.03	0.23 ± 0.03	0.0534	0.0005	23.1 %
70	0.99 ± 0.01	1.15 ± 0.02	0.16 ± 0.02	0.0261	0.0002	16.2 %
80	0.99 ± 0.01	1.16 ± 0.02	0.17 ± 0.02	0.0301	0.0002	17.3 %

Δm	**VR1: $t\bar{t}$**					
(GeV)	$R^{CR}(t\bar{t})$	$R^{SR}(t\bar{t})$	D	$D^2-\delta_D^2$	$\left(\frac{\delta_{sta}(DD)}{N_{DD}^{SR}(X)}\right)^2$	Sys'_{DD}
10	1.06 ± 0.02	1.76 ± 0.24	0.71 ± 0.24	0.4397	0.0159	66.3 %
20	1.06 ± 0.02	1.44 ± 0.27	0.38 ± 0.27	0.0695	0.0245	26.4 %
30	1.06 ± 0.02	1.55 ± 0.25	0.49 ± 0.25	0.1752	0.0193	41.9 %
40	1.06 ± 0.02	1.39 ± 0.16	0.33 ± 0.16	0.0851	0.0097	29.2 %
50	1.06 ± 0.02	1.33 ± 0.13	0.27 ± 0.13	0.0557	0.0074	23.6 %
60	1.05 ± 0.02	1.28 ± 0.09	0.23 ± 0.09	0.0448	0.0039	21.2 %
70	0.95 ± 0.01	0.93 ± 0.12	-0.02 ± 0.12	-0.0136	0.0111	10.6 %
80	0.95 ± 0.01	0.93 ± 0.12	-0.02 ± 0.12	-0.0135	0.0117	10.8 %

Table 7.8: 2018 Relative systematic uncertainty Sys'_{DD} affecting the data-driven prediction of W+jets (upper table) & $t\bar{t}$ (bottom table) per Δm region, in the VR2 region. The uncertainties are calculated according to Equation 7.5.

Δm	**VR2: W+jets**					
(GeV)	$R^{CR}(W+jets)$	$R^{SR}(W+jets)$	D	$D^2-\delta_D^2$	$\left(\frac{\delta_{sta}(DD)}{N_{DD}^{SR}(X)}\right)^2$	Sys'_{DD}
10	1.01 ± 0.01	1.23 ± 0.17	0.22 ± 0.17	0.0180	0.0043	13.4 %
20	1.01 ± 0.01	1.04 ± 0.04	0.03 ± 0.04	-0.0009	0.0005	2.3 %
30	1.01 ± 0.01	1.08 ± 0.03	0.08 ± 0.03	0.0050	0.0002	7.0 %
40	1.00 ± 0.01	1.07 ± 0.02	0.07 ± 0.02	0.0041	0.0002	6.4 %
50	1.01 ± 0.01	1.05 ± 0.02	0.04 ± 0.02	0.0013	0.0001	3.6 %
60	1.01 ± 0.01	1.04 ± 0.02	0.03 ± 0.02	0.0007	0.0001	2.7 %

Δm	**VR2: $t\bar{t}$**					
(GeV)	$R^{CR}(t\bar{t})$	$R^{SR}(t\bar{t})$	D	$D^2-\delta_D^2$	$\left(\frac{\delta_{sta}(DD)}{N_{DD}^{SR}(X)}\right)^2$	Sys'_{DD}
10	0.77 ± 0.02	0.30 ± 0.31	-0.47 ± 0.32	0.1251	0.2034	45.1 %
20	0.78 ± 0.02	0.14 ± 0.10	-0.64 ± 0.10	0.3927	0.0239	62.7 %
30	0.78 ± 0.02	0.45 ± 0.08	-0.34 ± 0.08	0.1081	0.0111	32.9 %
40	0.79 ± 0.02	0.59 ± 0.05	-0.20 ± 0.06	0.0357	0.0051	18.9 %
50	0.78 ± 0.02	0.69 ± 0.05	-0.09 ± 0.05	0.0064	0.0035	8.0 %
60	0.78 ± 0.02	0.75 ± 0.04	-0.02 ± 0.04	-0.0017	0.0029	5.4 %

7.4 Systematic uncertainties in signal

A relative uncertainty is taken into account for the limited statistical size of signal samples. This uncertainty varies from 3 to 20% in 2017 and from 3 to 15% in 2018 signal samples, depending on the signal mass point and on the corresponding selection. Signal samples are also subject to the limitations of the generator to properly simulate the ISR jet. The effect of this systematic uncertainty ranges from <1 to 5 %, depending on the signal mass point and on the corresponding selection as well. Signal samples which are generated with the fast simulation program are subject to the uncertainty affecting the data-to-full-simulation and the full-to-fast simulation corrections. These latter are determined by the collaboration [111], and are applied to the signal as function of the p_{T} and η of the leptons. A systematic uncertainty of 1% is added in order to take into account biases in the measurement of the trigger efficiency, as described in Section 4.3. The systematic uncertainties affecting the signal points are summarized in table 7.10.

7.5 Summary of systematic uncertainties

The inherent relative systematic uncertainties attributed to the data-driven estimation of the nonprompt and prompt backgrounds are summarized in Table 7.9.

Table 7.9: Inherent relative systematic uncertainty affecting the data-driven prediction of fake lepton, W+jets, and $t\bar{t}$, this per Δm region.

Δm		**2017**			**2018**	
(GeV)	**W+jets**	**$t\bar{t}$**	**nonprompt**	**W+jets**	**$t\bar{t}$**	**nonprompt**
10	20.0 %	77.9 %	6.3 %	21.6 %	66.9 %	9.3 %
20	11.1 %	69.8 %	9.1 %	10.4 %	81.5 %	9.4 %
30	13.0 %	37.0 %	9.0 %	12.0 %	45.8 %	8.4 %
40	10.8 %	42.8 %	11.3 %	20.7 %	31.3 %	8.7 %
50	12.6 %	21.3 %	9.7 %	20.8 %	25.5 %	9.7 %
60	11.5 %	20.5 %	10.1 %	23.1 %	21.8 %	9.3 %
70	14.1 %	8.0 %	9.7 %	16.5 %	11.2 %	14.9 %
80	17.1 %	9.2 %	14.8 %	17.7 %	10.8 %	26.9 %

Table 7.10 provides a complete summary of all the systematic uncertainties affecting this analysis. It has to be noted that in cases where the relative uncertainty is very high, the data driven background estimated processes have a small yield,close to zero or one event, in the SR. In such cases, the statistical uncertainty dominates. In order to combine the results of different years, a systematic uncertainty whose source is exactly the same across the years is considered as fully correlated, namely the uncertainty in the cross section, PU, JES, the reweighting of the W+jets sample, the renormalization and factorization scales, and the prediction of the W+jets, $t\bar{t}$ and nonprompt backgrounds. The systematic uncertainty in the integrated luminosity has multiple components and is thus considered as partially correlated between the years [21, 108, 109]. Similarly, the systematic uncertainty in b tagging is considered as partially correlated across the different years.

The overall relative systematic uncertainties in the total background arising from the contribution of W+jets, $t\bar{t}$, and nonprompt lepton backgrounds, as well as the relative systematic uncertainties

Table 7.10: Summary of input relative uncertainties separated by year and the correlation scheme across years used. Numbers are measured in percentages over the total yields of the associated process they have an effect on. Systematic uncertainty on the data-driven estimated processes include the statistical uncertainty added in quadrature.

Source of Systematic unc.	**Affects**	**Correlation Scheme**	**2017**		**2018**	
			Background Amplitude	**Signal Amplitude**	**Background Amplitude**	**Signal Amplitude**
Int. luminosity	Signal, Diboson, single-top Drell-Yan & $t\bar{t}$ $+X$	partially correlated	2.3 %	2.3 %	2.5 %	2.5 %
Cross section	W+jets, $t\bar{t}$, Diboson, single-top Drell-Yan & $t\bar{t}$ $+X$	fully correlated	<1 %	-	<3 %	-
PU	Signal, Diboson, single-top Drell-Yan & $t\bar{t}$ $+X$	fully correlated	[1,8] %	<3 %	[1,6] %	<1 %
Trigger	Signal, Diboson, single-top Drell-Yan & $t\bar{t}$ $+X$	uncorrelated	1 %	1 %	1 %	1 %
Lepton ID	Signal, Diboson, single-top Drell-Yan & $t\bar{t}$ $+X$.	uncorrelated	[0,9] %	<1 %	[0,8] %	<1 %
Lepton ISO	Signal, Diboson, single-top Drell-Yan & $t\bar{t}$ $+X$	uncorrelated	<1 %	<1 %	<1 %	<1 %
JES	Signal, Diboson, single-top Drell-Yan & $t\bar{t}$ $+X$	fully correlated	[1,20]%	[3,9]%	[2,20]%	[5,10]%
JER	Signal, Diboson, single-top Drell-Yan & $t\bar{t}$ $+X$	uncorrelated	<2 %	<1 %	<3 %	<1 %
b-tag	Signal, Diboson, single-top Drell-Yan & $t\bar{t}$ $+X$.	partially correlated	[0,9] %	[0,6] %	[0,8] %	<1 %
Ren. & fact. scales	Signal, Diboson, single-top Drell-Yan & $t\bar{t}$ $+X$	fully correlated	[5,30]%	<1 %	[1,30] %	<1 %
ISR	Signal & $t\bar{t}$	uncorrelated	1 %	<5 %	1 %	<5 %
W+jets reweighing	W+jets & $t\bar{t}$	fully correlated	[1,6] %	-	[1,6] %	-
FastSim	Signal	uncorrelated	-	<2 %	-	<2 %
W+jets and $t\bar{t}$ pred.	W+jets & $t\bar{t}$	fully correlated	[8,70] %	-	[10,81] %	-
Fake-lepton pred.	Fake-lepton	fully correlated	[6,15] %	-	[8,27] %	-

in the signal, are provided in Table 7.11. Pulls and impacts on the signal strength of each source of uncertainty are shown in Appendix A.2. The systematic uncertainties of the data driven background prediction methods are the major contributors to the total uncertainty.

Table 7.11: Relative systematic uncertainties (in %) in the total background, and signal prediction for the 2017 (left) and 2018 (right) data analysis. The "—" symbol means that a given source of uncertainty is not applicable. In the case of the background, the uncertainties are in the total background. The range of each systematic uncertainty is provided across the eight SRs.

	2017		**2018**	
Systematic uncertainty	**Background**	**Signal**	**Background**	**Signal**
Integrated luminosity	—	2.3	—	2.5
Pileup	1–5	0–3	1–4	0–1
Trigger	0–1	1	0–1	1
Lepton efficiency	0–1	0–1	0–1	0–1
JES	0–2	3–9	0–2	5–10
JER	0–1	0–1	0–1	0–1
b tagging	0–1	0–6	0–1	0–1
Renormalization & factorization scales	0–7	0–1	0–10	0–1
ISR ($t\bar{t}$ and signal)	0–1	0–5	0–1	0–5
ISR (W+jets)	0–4	—	0–4	—
$p_{\mathrm{T}}^{\mathrm{miss}}$ modeling (FASTSIM)	—	0–2	—	0–2
Prediction of W+jets	2–6	—	4–9	—
Prediction of $t\bar{t}$	1–5	—	2–7	—
Prediction of nonprompt bkg.	2–5	—	2–4	—

8

Results and interpretation

In this chapter, the results of the search for top squarks in the four-body decay mode with single lepton final states in $p\,p$ collisions at $\sqrt{s} = 13$ TeV, recorded with the CMS detector during the years of 2016, 2017, and 2018, and corresponding to an integrated luminosity of 138 fb^{-1} are presented. The observed and expected numbers of signal and background events at the final selection level, as well as their uncertainties, from the 2017-18 data analysis for the eight values of Δm are given in Table 8.1 and shown in Figs. 8.1 and 8.2. The selected events require exactly one charged lepton (electron or muon), at least one high-momentum jet, and high missing transverse momentum. One BDT is trained for each Δm region, for each year. By doing so, the signal selection is adapted to the difference in the kinematics through the $(m(\widetilde{t}_1),\ m(\widetilde{\chi}_1^0))$ plane. In general, from Table 8.1, the W+jets contribution to the total background across the different SRs does not vary and is approximately 25%. The BDTs are rather efficient at rejecting $t\bar{t}$ events, which tend to contribute more to the total background composition at higher values of Δm. The nonprompt background is the main contributor to the total background for the lowest Δm regions ($\approx 40\%$), which is expected given that these regions are characterized by the low p_{T} of the lepton, while for the high Δm regions, the contribution is approximately 20%.

Table 8.1: The predicted number of W+jets, $t\bar{t}$, nonprompt, and other (N^{SR}(Other)) background events and their sum (N^{SR}(Total)), in the eight SRs for the 2017 and 2018 data analysis. The first 3 predicted yields are derived from data, while the yields of the other background processes come from simulation. The uncertainties shown are the quadratic sum of the statistical and systematic uncertainties given in Table 7.11 for all the background processes. The corresponding Δm and BDT output threshold values for each SR are displayed in the first and second columns, respectively, and the observed number of events in data is shown in the last column.

Year	Δm (GeV)	BDT $>$	$Y_{\mathrm{p}}^{\mathrm{SR}}$($W$+jets)	$Y_{\mathrm{p}}^{\mathrm{SR}}$($t\bar{t}$)	$Y_{\mathrm{np}}^{\mathrm{SR}}$	N^{SR}(Other)	N^{SR}(Total)	N^{SR}(Observed)
2017	10	0.31	11.0 ± 2.4	2.2 ± 2.9	20.1 ± 3.5	5.4 ± 3.7	38.8 ± 6.3	49
	20	0.32	37.4 ± 4.6	3.3 ± 5.2	49.6 ± 7.0	18.4 ± 9.3	109 ± 14	116
	30	0.38	23.8 ± 3.8	0.0 ± 7.2	41.7 ± 6.1	19.4 ± 9.9	85 ± 14	86
	40	0.40	15.9 ± 2.6	0.0 ± 8.1	32.6 ± 5.5	20 ± 10	69 ± 15	66
	50	0.43	10.9 ± 2.0	0.0 ± 6.7	22.3 ± 4.0	17.9 ± 9.2	51 ± 12	48
	60	0.47	3.9 ± 0.8	0.0 ± 6.2	7.6 ± 2.2	10.3 ± 5.4	21.8 ± 8.5	23
	70	0.39	11.1 ± 2.0	8.9 ± 7.6	12.9 ± 2.9	19.7 ± 9.8	53 ± 13	50
	80	0.41	15.6 ± 4.3	10.3 ± 9.7	8.3 ± 2.2	17.1 ± 8.2	51 ± 14	51
2018	10	0.32	17.3 ± 4.3	0.0 ± 2.4	16.7 ± 3.6	7.1 ± 4.5	41.1 ± 7.6	77
	20	0.39	18.4 ± 2.8	0.3 ± 3.1	14.5 ± 3.4	6.3 ± 3.5	39.4 ± 6.4	57
	30	0.35	48.5 ± 8.1	9.1 ± 9.4	22.5 ± 4.8	33 ± 14	114 ± 19	127
	40	0.43	10.7 ± 3.1	3.4 ± 4.5	11.7 ± 2.9	12.3 ± 6.7	38.1 ± 9.1	49
	50	0.46	8.7 ± 3.0	3.4 ± 4.5	10.5 ± 2.8	10.3 ± 5.2	32.9 ± 8.0	36
	60	0.41	16.5 ± 4.7	16.2 ± 8.8	17.3 ± 3.8	22 ± 10	72 ± 15	61
	70	0.40	35.6 ± 8.7	15.2 ± 8.6	16.9 ± 5.2	30 ± 12	97 ± 18	96
	80	0.42	16.3 ± 3.7	10.9 ± 7.8	10.7 ± 4.3	21.5 ± 9.8	59 ± 14	41

The predictions and the associated uncertainties in Figs. 8.1 and 8.2 are given before a profiled likelihood fit [106, 112, 113] is performed. The post-fit uncertainties do not get reduced because of the lack of constraints from a single bin. It should be noted that the background composition varies for the same Δm region for different years. This is because an independent BDT is trained per Δm and per year, with a different selection on its output. There is good agreement between the observed and predicted numbers of events for most of the SRs. The largest difference is for $\Delta m = 10$ GeV, where there are 1.1 and 2.9 standard deviations (local significance) excesses of signal events over the predicted background for the 2017 and 2018 data, respectively. The 2016 analysis had a similar excess for the same Δm value, corresponding to 0.7 standard deviations. Studies of this excess for the 2017 and 2018 data are reported in Appendix D, which do not point to a problem in the background estimation methods. None of these excesses is statistically significant, so it is concluded that there is no evidence for direct top squark production in this decay mode.

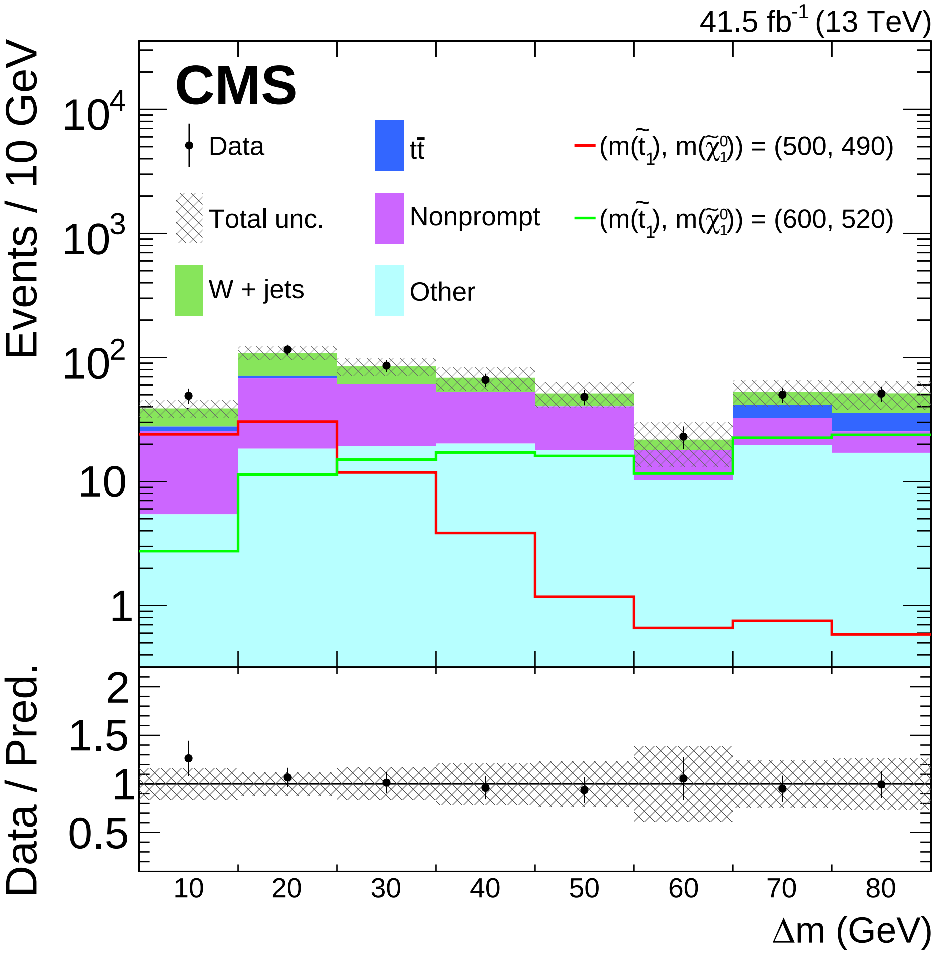

Figure 8.1: The observed yields in data (points) and the predicted background components (colored histograms) in the eight SRs for the 2017 data. The vertical bars on the points give the statistical uncertainty in the data. The hatched area shows the total uncertainty in the sum of the backgrounds. The expected yields for two signal points with $(m(\tilde{t}_1),\ m(\tilde{\chi}_1^0))$ = (500, 490) and (600, 520) GeV are also given by the lines, unstacked from the histograms. The lower panel shows the ratio of the number of observed events to the predicted total background. The vertical bars on the points give the statistical uncertainty in the ratio and the hatched area the total uncertainty.

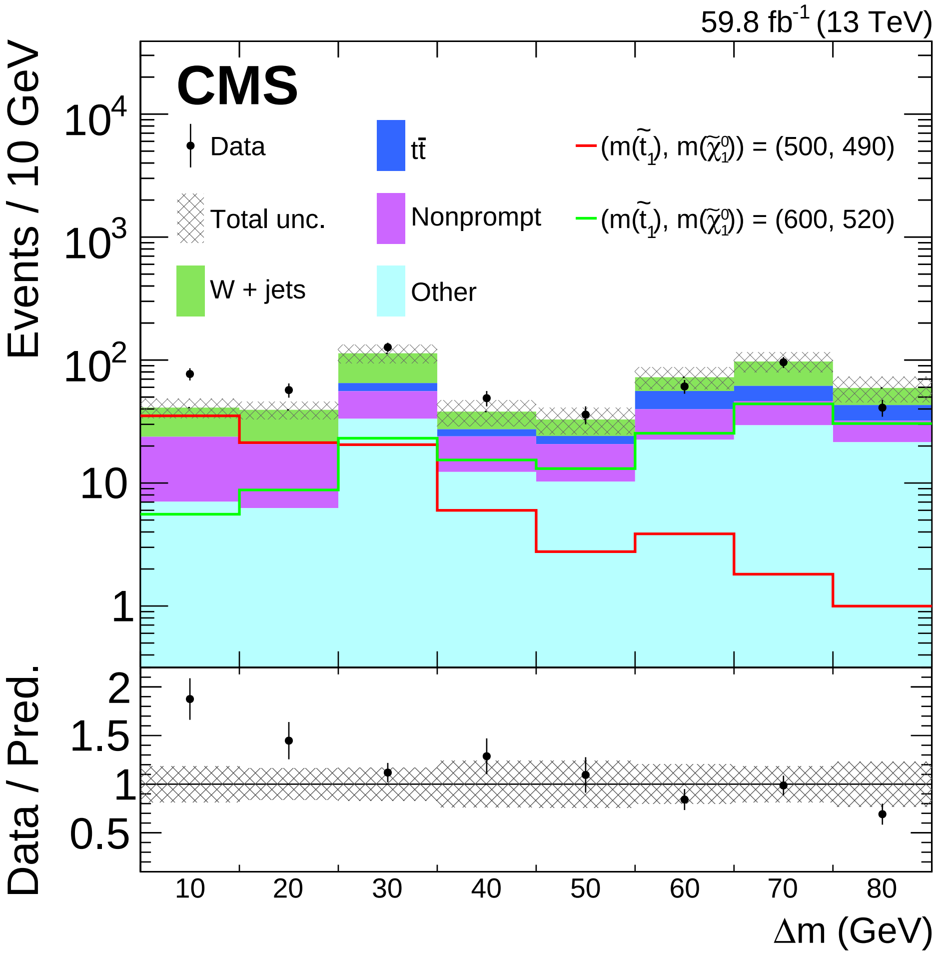

Figure 8.2: The observed yields in data (points) and the predicted background components (colored histograms) in the eight SRs for the 2018 data. The vertical bars on the points give the statistical uncertainty in the data. The hatched area shows the total uncertainty in the sum of the backgrounds. The expected yields for two signal points with $(m(\tilde{t}_1),\ m(\tilde{\chi}_1^0))$ = (500, 490) and (600, 520) GeV are also given by the lines, unstacked from the histograms. The lower panel shows the ratio of the number of observed events to the predicted total background. The vertical bars on the points give the statistical uncertainty in the ratio and the hatched area the total uncertainty.

The observed and expected number of events for each signal mass point and their corresponding uncertainties are converted into 95% confidence level (CL) upper limits on the $\widetilde{t}_1\bar{\widetilde{t}}_1$ production cross section in the $(m(\widetilde{t}_1),\ m(\widetilde{\chi}^0_1))$ plane. These are shown by the colored regions as a function of $m(\widetilde{t}_1)$ and Δm, where the color scale gives the corresponding upper limit values, in Figures 8.3, 8.4, and 8.5 for data collected in 2017, 2018 and the combined results of the data collected during the years of 2016, 2017, and 2018, respectively. The limits are calculated according to the modified frequentist $\mathrm{CL_s}$ criterion [106, 112, 113]. A test statistic is defined as the likelihood ratio between the background-only and signal-plus-background hypotheses, and is used to set exclusion limits on the top squark pair production. The distributions of the test statistic are built using simulated experiments, where statistical uncertainties are modeled with Poisson distributions, and where all systematic uncertainties are modeled with a log-normal distribution. When interpreting the results, a branching fraction of 100% is assumed for the four-body decay scenario. For the combined results of the three years, the largest excess in the data corresponds to 2.5 standard deviations (local significance) for the $\Delta m = 10$ GeV SR.

Using the measured upper limits on the top squark pair cross section and the theoretical predictions for the cross section, it is determined the 95% CL lower limits on $m(\widetilde{t}_1)$ versus Δm. The solid black line and thick dotted red line in Fig. 8.5 give the resulting 95% CL observed and expected exclusion contours, respectively, on $m(\widetilde{t}_1)$ as a function of Δm, obtained from combining the 2016, 2017, and 2018 data. The corresponding thin black lines in Fig. 8.5 represent the ±1 standard deviation (σ_{theory}) variations in the limits due to the theoretical uncertainties in the case of the observed limits. The thin dashed red lines give the ±1 and ±2 standard deviation ($\sigma_{\text{experiment}}$) variations in the case of the expected limits, coming from the experimental uncertainties. The maximum sensitivity is reached for the highest Δm ($\Delta m \approx m(W)$), where top squark masses up to 700 GeV are excluded. At the lowest Δm value of 10 GeV covered by the search, the corresponding value is 480 GeV. The reduced sensitivity at lower Δm is explained by the lower transverse momentum spectrum of the decay products, as shown in Figures 5.1 and 5.2, which results in a loss of acceptance.

The limits of the previous analysis are improved. At low Δm the top squark mass limit is 60 GeV higher, thus improving the sensitivity at low mass splittings beyond simple luminosity scaling, while at high Δm the top squark mass limit is extended by 140 GeV. Compared to the results of a similar analysis by the ATLAS Collaboration for the same decay mode and final state [22], the search presented here has comparable limits at intermediate and high Δm values. However, at low Δm, the excluded top squark mass is 120 GeV higher than the ATLAS limit. This is attributed to a more inclusive preselection criteria, where *b* tagging is not used, and where the discrimination between the signal and the dominating *W*+jets background is done by a multivariate analysis tool, whose performance is further enhanced by a BDT specifically trained for each Δm.

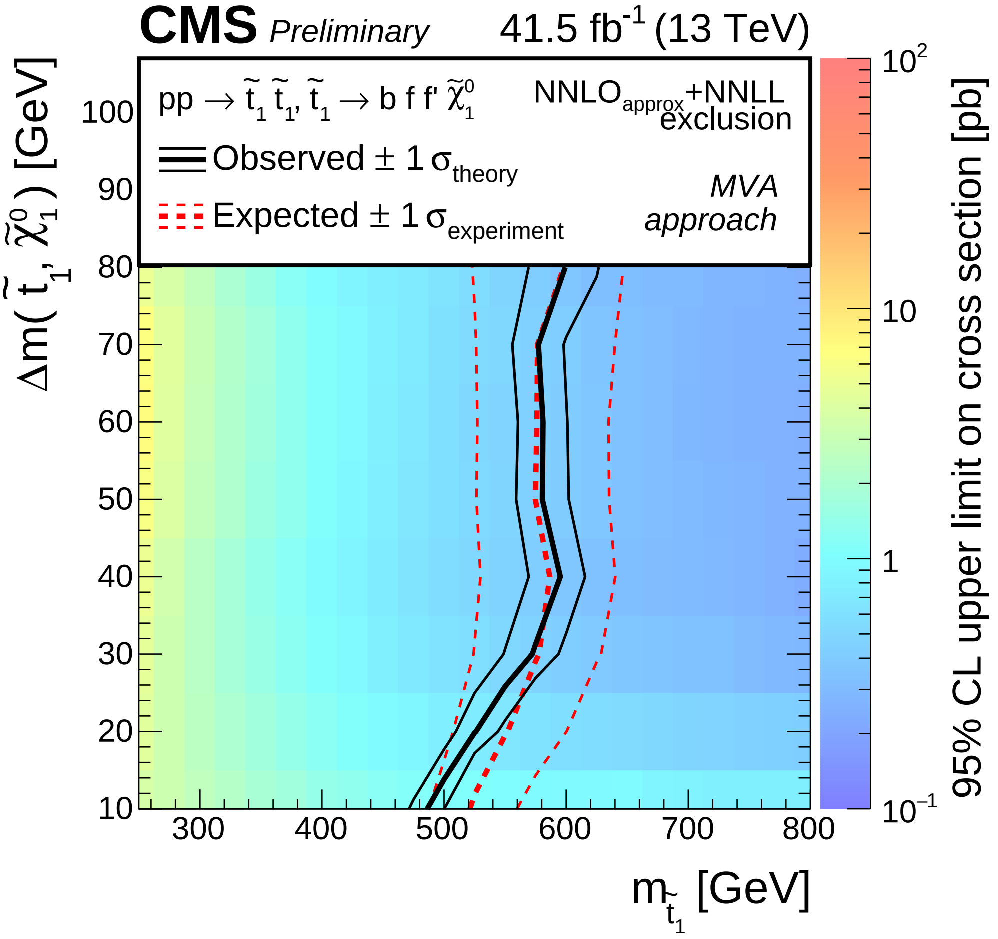

Figure 8.3: Exclusion limit at 95% CL for the four-body decay of the top squark as a function of $m(\widetilde{t}_1)$ and Δm for the data of the year of 2017. The color shading represents the observed limit on the cross section for a given signal point. The solid black and dashed red lines represent the observed and expected limits, respectively. These limits are derived using the expected top squark pair production cross section. The thick lines represent the central values, and the thin lines the variations due to the theoretical or experimental uncertainties.

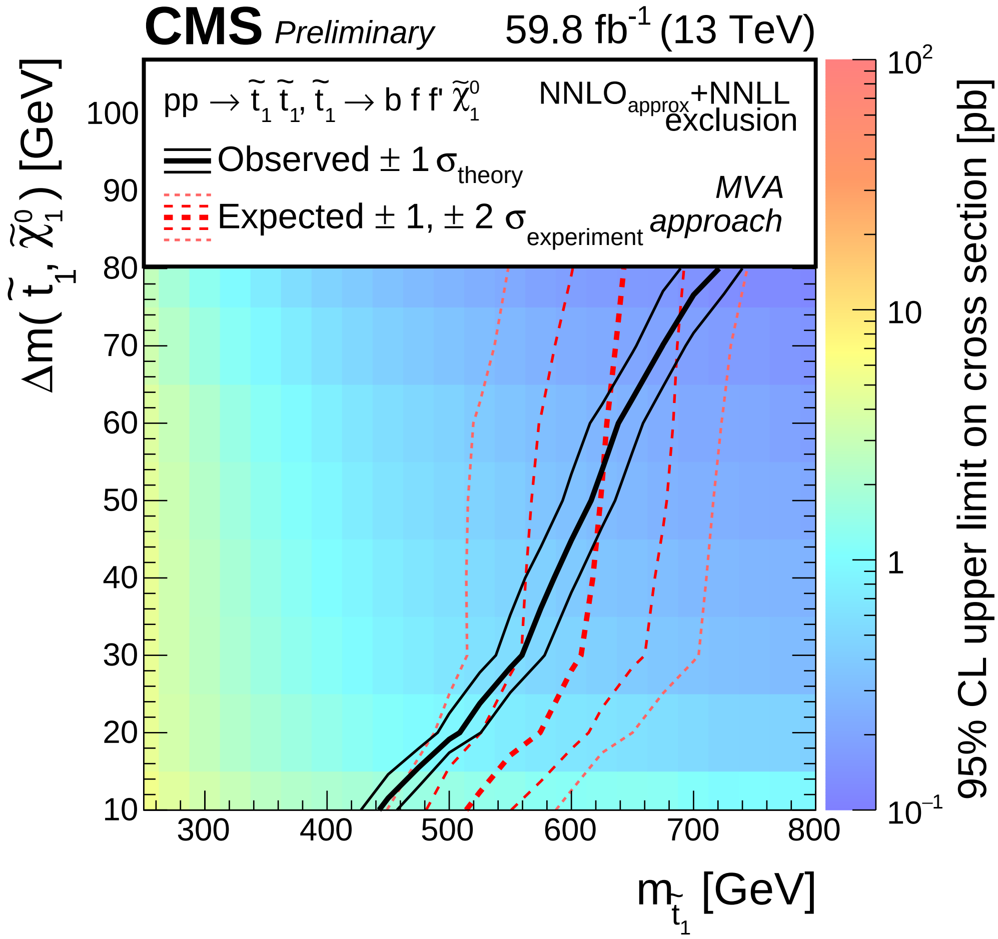

Figure 8.4: Exclusion limit at 95% CL for the four-body decay of the top squark as a function of $m(\widetilde{t}_1)$ and Δm for the data of the year of 2018. The color shading represents the observed limit on the cross section for a given signal point. The solid black and dashed red lines represent the observed and expected limits, respectively. These limits are derived using the expected top squark pair production cross section. The thick lines represent the central values, and the thin lines the variations due to the theoretical or experimental uncertainties.

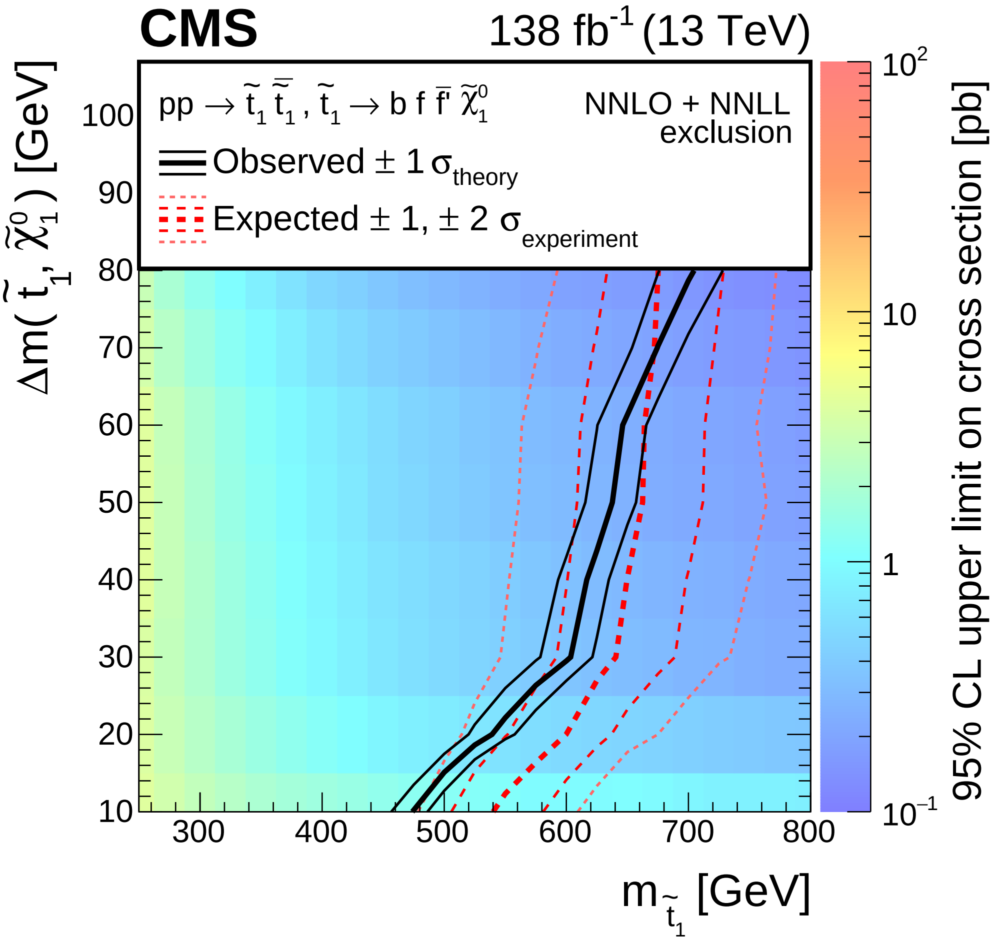

Figure 8.5: The 95% CL upper limits in the (m($\widetilde{t}_1$), Δm) plane on the cross section for the production and four-body decay of the top squark using the combined 2016, 2017, and 2018 data. The color shading represents the observed upper limit for a given point in the plane, using the color scale to the right of the figure. The solid black and dashed red lines show the observed and expected 95% CL lower limits, respectively, on m($\widetilde{t}_1$) as a function of Δm. The thick lines give the central values of the limits. The corresponding thin lines represent the ± 1 standard deviation (σ_{theory}) variations in the limits due to the theoretical uncertainties in the case of the observed limits, and ± 1 and 2 standard deviation ($\sigma_{\text{experiment}}$) variations due to the experimental uncertainties in the case of the expected limits.

9

Conclusion

The results of a search for the direct pair production of top squarks in single-lepton final states are presented within a compressed scenario where R parity is conserved, and the mass difference $\Delta m = m(\widetilde{t}_1) - m(\widetilde{\chi}^0_1)$ between the lightest top squark ($\widetilde{t}_1$) and the lightest supersymmetric particle, taken to be the lightest neutralino $\widetilde{\chi}^0_1$, does not exceed the W boson mass. The considered decay mode of the top squark is the prompt four-body decay to $b\mathrm{f}\bar{\mathrm{f}}'\widetilde{\chi}^0_1$, where the fermions in the final state f and $\bar{\mathrm{f}}'$ represent a charged lepton and its neutrino for the decay products of one $\widetilde{t}_1$, and two quarks for the other top squark. The search is based on data collected from proton-proton collisions at $\sqrt{s} = 13$ TeV, recorded with the CMS detector during the years 2016, 2017, and 2018, corresponding to an integrated luminosity of 138 fb^{-1}. Events are selected containing a single lepton (electron or muon), at least one high-momentum jet, and significant missing transverse momentum. The analysis is based on a multivariate tool specifically trained for different Δm regions, thus adapting the signal selection to the evolution of the kinematical variables as a function of $(m(\widetilde{t}_1),\ m(\widetilde{\chi}^0_1))$. The dominant background processes are W+jets, $t\bar{t}$, and events with nonprompt leptons, which are estimated using control regions in the data.

The observed number of events is consistent with the predicted standard model backgrounds in all signal regions. Upper limits are set at the 95% confidence level on the $\widetilde{t}_1\bar{\widetilde{t}}_1$ production cross section as a function of the $\widetilde{t}_1$ and $\widetilde{\chi}^0_1$ masses, within the context of a simplified model. Assuming a 100% branching fraction in the four-body decay mode, the search excludes top squark masses up to 480 and 700 GeV at $\Delta m = 10$ and 80 GeV, respectively. The results summarized in this thesis are among the best limits to date on the top squark pair production cross section, where the top squark decays via the four-body mode, and currently correspond to the most stringent limits for $\Delta m < 30$ GeV.

In the SR where the data exceeds the expected SM background, the significance of the excess is approximately 2.5 standard deviations, meaning that such a result is expected to be seen with a probability of 1/160 even in the absence of SUSY, pointing to the possibility of statistical fluctuations. As far as investigated, this excess is not due to problems in methods to predict the SM background. This excess can possibly be due to another signal whose kinematics is close to the four-body decay of stop, such as the chargino–mediated one, which can co–exist in the same kinematic region. Finally, this can be due to the signal of stop decaying in four bodies, and whose presence has not been observed with enough significance. It will therefore be interesting to carry a similar search during the Run–3, which is the next period of data-taking of the LHC. The higher amount of collected data and improved search methods will hopefully allow to see if this excess disappears or is further confirmed.

Bibliography

[1] S. P. Martin, “A supersymmetry primer,” *Adv. Ser. Direct. High Energy Phys.*, vol. 18, p. 1, 1998.

[2] J. Wess and B. Zumino, “Supergauge transformations in four dimensions,” *Nucl. Phys. B*, vol. 70, p. 39, 1974.

[3] H. P. Nilles, “Supersymmetry, supergravity and particle physics,” *Phys. Reports*, vol. 110, p. 1, 1984.

[4] H. E. Haber and G. L. Kane, “The search for supersymmetry: Probing physics beyond the standard model,” *Phys. Reports*, vol. 117, p. 75, 1985.

[5] R. Barbieri, S. Ferrara, and C. A. Savoy, “Gauge models with spontaneously broken local supersymmetry,” *Phys. Lett. B*, vol. 119, p. 343, 1982.

[6] S. Dawson, E. Eichten, and C. Quigg, “Search for supersymmetric particles in hadron-hadron collisions,” *Phys. Rev. D*, vol. 31, p. 1581, 1985.

[7] E. Witten, “Dynamical breaking of supersymmetry,” *Nucl. Phys. B*, vol. 188, p. 513, 1981.

[8] S. Dimopoulos and H. Georgi, “Softly broken supersymmetry and SU(5),” *Nucl. Phys. B*, vol. 193, p. 150, 1981.

[9] Aad, Georges and others, “Observation of a new particle in the search for the standard model Higgs boson with the ATLAS detector at the LHC,” *Phys. Lett. B*, vol. 716, p. 1, 2012.

[10] Chatrchyan, Serguei and others, “Observation of a new boson at a mass of 125 GeV with the CMS experiment at the LHC,” *Phys. Lett. B*, vol. 716, p. 30, 2012.

[11] S. Chatrchyan *et al.*, “Observation of a new boson with mass near 125 GeV in pp collisions at $\sqrt{s}$ = 7 and 8 TeV,” *JHEP*, vol. 06, p. 081, 2013.

[12] G. R. Farrar and P. Fayet, “Phenomenology of the production, decay, and detection of new hadronic states associated with supersymmetry,” *Phys. Lett. B*, vol. 76, p. 575, 1978.

[13] C. Balázs, M. Carena, and C. E. M. Wagner, “Dark matter, light stops and electroweak baryogenesis,” *Phys. Rev. D*, vol. 70, p. 015007, 2004.

[14] T. Cohen, T. Golling, M. Hance, A. Henrichs, K. Howe, J. Loyal, S. Padhi, and J. G. Wacker, “SUSY simplified models at 14, 33, and 100 TeV proton colliders,” *JHEP*, vol. 04, p. 117, 2014.

[15] N. Arkani-Hamed, P. Schuster, N. Toro, J. Thaler, L.-T. Wang, B. Knuteson, and S. Mrenna, "MARMOSET: the path from LHC data to the new standard model via on-shell effective theories," 2007, .

[16] J. Alwall, P. C. Schuster, and N. Toro, "Simplified models for a first characterization of new physics at the LHC," *Phys. Rev. D*, vol. 79, p. 075020, 2009.

[17] J. Alwall, M.-P. Le, M. Lisanti, and J. G. Wacker, "Model-independent jets plus missing energy searches," *Phys. Rev. D*, vol. 79, p. 015005, 2009.

[18] D. Alves *et al.*, "Simplified models for LHC new physics searches," *J. Phys. G*, vol. 39, p. 105005, 2012.

[19] S. Chatrchyan *et al.*, "Interpretation of searches for supersymmetry with simplified models," *Phys. Rev. D*, vol. 88, p. 052017, 2013.

[20] ——, "Search for top squarks decaying via four-body or chargino-mediated modes in single-lepton final states in proton-proton collisions at $\sqrt{s}$ = 13 TeV," *JHEP*, vol. 09, p. 065, 2018.

[21] A. M. Sirunyan *et al.*, "Precision luminosity measurement in proton-proton collisions at $\sqrt{s} = 13\ \mathrm{TeV}$ in 2015 and 2016 at CMS," *Eur. Phys. J. C*, vol. 81, p. 800, 2021.

[22] G. Aad *et al.*, "Search for new phenomena with top quark pairs in final states with one lepton, jets, and missing transverse momentum in *pp* collisions at $\sqrt{s}$ = 13 TeV with the ATLAS detector," *JHEP*, vol. 04, p. 174, 2021.

[23] https://indico.cern.ch/event/1083758/.

[24] C. Collaboration, "How to write a Latex Article," https://cms.cern/news/searching-top-squarks-cms-data, October 2022.

[25] ——, "Search for top squarks in the four-body decay mode with single lepton final states in proton-proton collisions at $$ \sqrt{s} $$= 13 tev," *Journal of High Energy Physics*, vol. 2023, no. 6, p. 60, 2023. [Online]. Available: https://doi.org/10.1007/JHEP06(2023)060

[26] S. F. Novaes, "Standard model: An introduction," 2000.

[27] P. Langacker, "Introduction to the Standard Model and Electroweak Physics," in *Theoretical Advanced Study Institute in Elementary Particle Physics: The Dawn of the LHC Era*, 2010, pp. 3–48.

[28] S. Dawson, *Susy and Such*. Boston, MA: Springer US, 1997, pp. 33–80. [Online]. Available: https://doi.org/10.1007/978-1-4615-5963-4_2

[29] H. E. Haber and M. Schmitt, "Supersymmetry," *The European Physical Journal C - Particles and Fields*, vol. 15, no. 1, pp. 817–844, 2000.

[30] "Standard model," https://en.wikipedia.org/wiki/Standard_Model, 2023.

[31] Particle Data Group, M. Tanabashi *et al.*, “Review of particle physics,” *Phys. Rev. D*, vol. 98, p. 030001, 2018.

[32] M. Baak and R. Kogler, *The global electroweak Standard Model fit after the Higgs discovery*, 2013, pp. 349–358.

[33] H. Murayama and M. E. Peskin, “PHYSICS OPPORTUNITIES OF ee LINEAR COLLIDERS,” *Annual Review of Nuclear and Particle Science*, vol. 46, no. 1, pp. 533–608, dec 1996. [Online]. Available: https://doi.org/10.1146%2Fannurev.nucl.46.1.533

[34] J. L. Feng, “Naturalness and the status of supersymmetry,” *Annual Review of Nuclear and Particle Science*, vol. 63, no. 1, pp. 351–382, oct 2013. [Online]. Available: https://doi.org/10.1146%2Fannurev-nucl-102010-130447

[35] C. L. Bennett, D. Larson, J. L. Weiland, N. Jarosik, G. Hinshaw, N. Odegard, K. M. Smith, R. S. Hill, B. Gold, M. Halpern, E. Komatsu, M. R. Nolta, L. Page, D. N. Spergel, E. Wollack, J. Dunkley, A. Kogut, M. Limon, S. S. Meyer, G. S. Tucker, and E. L. Wright, “Nine-year wilkinson microwave anisotropy probe (wmap) observations: Final maps and results,” *The Astrophysical Journal Supplement Series*, vol. 208, no. 2, p. 20, sep 2013. [Online]. Available: https://dx.doi.org/10.1088/0067-0049/208/2/20

[36] C. Boehm, A. Djouadi, and M. Drees, “Light scalar top quarks and supersymmetric dark matter,” *Phys. Rev. D*, vol. 62, p. 035012, Jul 2000. [Online]. Available: https://link.aps.org/doi/10.1103/PhysRevD.62.035012

[37] C. Boehm, A. Djouadi, and Y. Mambrini, “Decays of the lightest top squark,” *Phys. Rev. D*, vol. 61, p. 095006, Apr 2000. [Online]. Available: https://link.aps.org/doi/10.1103/PhysRevD.61.095006

[38] *LEP design report*. Geneva: CERN, 1984, copies shelved as reports in LEP, PS and SPS libraries. [Online]. Available: https://cds.cern.ch/record/102083

[39] Brüning, Oliver Sim and Collier, Paul and Lebrun, P and Myers, Stephen and Ostojic, Ranko and Poole, John and Proudlock, Paul, *LHC Design Report*, ser. CERN Yellow Reports: Monographs. Geneva: CERN, 2004. [Online]. Available: https://cds.cern.ch/record/782076

[40] L. Evans and P. Bryant, “LHC machine,” *Journal of Instrumentation*, vol. 3, no. 08, pp. S08 001–S08 001, aug 2008. [Online]. Available: https://doi.org/10.1088%2F1748-0221%2F3%2F08%2Fs08001

[41] “Linear accelerator 2,” Sep 2012. [Online]. Available: https://cds.cern.ch/record/1997427

[42] “The Proton Synchrotron Booster,” Jul 2012. [Online]. Available: https://cds.cern.ch/record/1997372

[43] “Proton Synchrotron,” 1959. [Online]. Available: https://cds.cern.ch/record/1479637

[44] “The Super Proton Synchrotron,” Jan 2012. [Online]. Available: http://cds.cern.ch/record/1997188

[45] “High-Luminosity Large Hadron Collider (HL-LHC): Technical Design Report V. 0.1,” *CERN Yellow Rep. Monogr.*, vol. 4, p. 1, 2017.

[46] S. Chatrchyan *et al.*, “The CMS experiment at the CERN LHC,” *JINST*, vol. 3, p. S08004, 2008.

[47] ——, “Description and performance of track and primary-vertex reconstruction with the CMS tracker,” *JINST*, vol. 9, no. 10, p. P10009, 2014.

[48] V. Khachatryan *et al.*, “CMS Tracking Performance Results from Early LHC Operation,” *Eur. Phys. J. C*, vol. 70, p. 1165, 2010.

[49] S. Chatrchyan *et al.*, “Energy Calibration and Resolution of the CMS Electromagnetic Calorimeter in pp Collisions at $\sqrt{s} = 7$ TeV,” *JINST*, vol. 8, p. P09009, 2013, [JINST8,9009(2013)].

[50] C. Collaboration, “Performance of the cms hadron calorimeter with cosmic ray muons and lhc beam data,” *Journal of Instrumentation*, vol. 5, no. 03, p. T03012, mar 2010. [Online]. Available: https://dx.doi.org/10.1088/1748-0221/5/03/T03012

[51] S. Abdullin *et al.*, “Design, performance, and calibration of CMS hadron-barrel calorimeter wedges,” *Eur. Phys. J.*, vol. C55, no. 1, pp. 159–171, 2008.

[52] A. M. Sirunyan *et al.*, “Performance of the CMS muon detector and muon reconstruction with proton-proton collisions at $\sqrt{s} = 13$ TeV,” *JINST*, vol. 13, p. P06015, 2018.

[53] V. Khachatryan *et al.*, “The CMS trigger system,” *JINST*, vol. 12, p. P01020, 2017.

[54] G. Bauer, B. Beccati, U. Behrens, K. Biery, O. Bouffet, J. Branson, S. Bukowiec, E. Cano, H. Cheung, M. Ciganek, S. Cittolin, J. A. Coarasa, C. Deldicque, A. Dupont, S. Erhan, D. Gigi, F. Glege, R. Gomez-Reino, D. Hatton, A. Holzner, Y. L. Hwong, L. Masetti, F. Meijers, E. Meschi, R. K. Mommsen, R. Moser, V. O'Dell, L. Orsini, C. Paus, A. Petrucci, M. Pieri, A. Racz, O. Raginel, H. Sakulin, M. Sani, P. Schieferdecker, C. Schwick, D. Shpakov, M. Simon, and K. Sumorok, “The data-acquisition system of the CMS experiment at the LHC,” *Journal of Physics: Conference Series*, vol. 331, no. 2, p. 022021, dec 2011. [Online]. Available: https://doi.org/10.1088%2F1742-6596%2F331%2F2%2F022021

[55] E. Migliore, “CMS pixel detector design for HL-LHC,” *Journal of Instrumentation*, vol. 11, no. 12, pp. C12 061–C12 061, dec 2016. [Online]. Available: https://doi.org/10.1088%2F1748-0221%2F11%2F12%2Fc12061

[56] ——, “The CMS Tracker Upgrade for the High-Luminosity LHC,” in *Connecting the Dots and Workshop on Intelligent Trackers*, 11 2019.

[57] M. Backhaus, “The Upgrade of the CMS Inner Tracker for HL-LHC,” CERN, Geneva, Tech. Rep. CMS-CR-2019-011, Feb 2019. [Online]. Available: https://cds.cern.ch/record/2683265

[58] J. Luetić, “The CMS Outer Tracker Upgrade for the High Luminosity LHC,” *PoS*, vol. Vertex 2017, p. 003, 2018.

[59] F. Ferri, “The CMS ECAL Phase-2 upgrade for high precision energy and timing measurements,” *Nucl. Instrum. Meth. A*, vol. 958, p. 162159, 2020.

[60] A. Martelli, “The CMS HGCAL detector for HL-LHC upgrade,” in *5th Large Hadron Collider Physics Conference*, 8 2017.

[61] C. Collaboration, “The Phase-2 Upgrade of the CMS Muon Detectors,” CERN, Geneva, Tech. Rep. CERN-LHCC-2017-012. CMS-TDR-016, Sep 2017, this is the final version, approved by the LHCC. [Online]. Available: https://cds.cern.ch/record/2283189

[62] C. H. Peña and on behalf of the CMS Collaboration, “Precision timing with the cms mip timing detector,” *Journal of Physics: Conference Series*, vol. 1162, no. 1, p. 012035, jan 2019. [Online]. Available: https://dx.doi.org/10.1088/1742-6596/1162/1/012035

[63] M. Peruzzi, G. Petrucciani, and A. Rizzi, “The NanoAOD event data format in CMS,” *Journal of Physics: Conference Series*, vol. 1525, no. 1, p. 012038, apr 2020. [Online]. Available: https://doi.org/10.1088/1742-6596/1525/1/012038

[64] “Particle-flow event reconstruction in cms and performance for jets, taus, and missing e_t,” *CMS Physics Analysis Summary*, vol. PFT-09-001, 2009.

[65] “Commissioning of the particle-flow reconstruction in minimum-bias and jet events from pp collisions at 7 tev,” *CMS Physics Analysis Summary*, vol. PFT-10-002, 2010.

[66] A. M. Sirunyan *et al.*, “Identification of heavy-flavour jets with the CMS detector in pp collisions at 13 TeV,” *JINST*, vol. 13, p. P05011, 2018.

[67] J. Alwall, R. Frederix, S. Frixione, V. Hirschi, F. Maltoni, O. Mattelaer, H. S. Shao, T. Stelzer, P. Torrielli, and M. Zaro, “The automated computation of tree-level and next-to-leading order differential cross sections, and their matching to parton shower simulations,” *JHEP*, vol. 07, p. 079, 2014.

[68] P. Nason, “A new method for combining NLO QCD with shower Monte Carlo algorithms,” *JHEP*, vol. 11, p. 040, 2004.

[69] S. Frixione, P. Nason, and C. Oleari, “Matching NLO QCD computations with parton shower simulations: the POWHEG method,” *JHEP*, vol. 11, p. 070, 2007.

[70] S. Alioli, P. Nason, C. Oleari, and E. Re, “A general framework for implementing NLO calculations in shower Monte Carlo programs: the POWHEG BOX,” *JHEP*, vol. 06, p. 043, 2010.

[71] ——, “NLO single-top production matched with shower in POWHEG: s- and t-channel contributions,” *JHEP*, vol. 09, p. 111, 2009.

[72] E. Re, “Single-top Wt-channel production matched with parton showers using the POWHEG method,” *Eur. Phys. J. C*, vol. 71, p. 1547, 2011.

[73] T. Melia, P. Nason, R. Röntsch, and G. Zanderighi, “W^+W^-, WZ and ZZ production in the POWHEG BOX,” *JHEP*, vol. 11, p. 078, 2011.

[74] P. Nason and G. Zanderighi, “W^+W^-, WZ and ZZ production in the POWHEG-BOX-V2,” *Eur. Phys. J. C*, vol. 74, p. 2702, 2014.

[75] H. B. Hartanto, B. Jäger, L. Reina, and D. Wackeroth, “Higgs boson production in association with top quarks in the POWHEG BOX,” *Phys. Rev. D*, vol. 91, p. 094003, 2015.

[76] R. D. Ball, V. Bertone, S. Carrazza, L. D. Debbio, S. Forte, P. Groth-Merrild, A. Guffanti, N. P. Hartland, Z. Kassabov, J. I. Latorre, E. R. Nocera, J. Rojo, L. Rottoli, E. Slade, and M. Ubiali, “Parton distributions from high-precision collider data,” *Eur. Phys. J. C*, vol. 77, p. 663, 2017.

[77] R. Frederix and S. Frixione, “Merging meets matching in MC@NLO,” *JHEP*, vol. 12, p. 061, 2012.

[78] T. Sjöstrand, S. Ask, J. R. Christiansen, R. Corke, N. Desai, P. Ilten, S. Mrenna, S. Prestel, C. O. Rasmussen, and P. Z. Skands, “An introduction to PYTHIA 8.2,” *Comput. Phys. Commun.*, vol. 191, p. 159, 2015.

[79] A. M. Sirunyan *et al.*, “Extraction and validation of a new set of CMS PYTHIA 8 tunes from underlying-event measurements,” *Eur. Phys. J. C*, vol. 80, p. 4, 2020.

[80] S. Agostinelli *et al.*, “GEANT4—a simulation toolkit,” *Nucl. Instrum. Meth. A*, vol. 506, p. 250, 2003.

[81] W. Beenakker, R. Höpker, and M. Spira, “PROSPINO: A program for the production of supersymmetric particles in next-to-leading order QCD,” 1996.

[82] C. Borschensky, M. Krämer, A. Kulesza, M. Mangano, S. Padhi, T. Plehn, and X. Portell, “Squark and gluino production cross sections in pp collisions at $\sqrt{s}$ = 13, 14, 33 and 100 TeV,” *Eur. Phys. J. C*, vol. 74, p. 3174, 2014.

[83] W. Beenakker, R. Höpker, M. Spira, and P. M. Zerwas, “Squark and gluino production at hadron colliders,” *Nucl. Phys. B*, vol. 492, p. 51, 1997.

[84] A. Kulesza and L. Motyka, “Threshold resummation for squark-antisquark and gluino-pair production at the LHC,” *Phys. Rev. Lett.*, vol. 102, p. 111802, 2009.

[85] ——, “Soft gluon resummation for the production of gluino-gluino and squark-antisquark pairs at the LHC,” *Phys. Rev. D*, vol. 80, p. 095004, 2009.

[86] W. Beenakker, S. Brensing, M. Krämer, A. Kulesza, E. Laenen, and I. Niessen, “Soft-gluon resummation for squark and gluino hadroproduction,” *JHEP*, vol. 12, p. 41, 2009.

[87] W. Beenakker, S. Brensing, M. Krämer, A. Kulesza, E. Laenen, L. Motyka, and I. Niessen, "Squark and gluino production," *Int. J. Mod. Phys. A*, vol. 26, p. 2637, 2011.

[88] S. Abdullin, P. Azzi, F. Beaudette, P. Janot, and A. Perrotta, "The fast simulation of the CMS detector at LHC," *J. Phys. Conf. Ser.*, vol. 331, p. 032049, 2011.

[89] A. Giammanco, "The fast simulation of the CMS experiment," *J. Phys. Conf. Ser.*, vol. 513, p. 022012, 2014.

[90] CMS Collaboration, "Technical proposal for the Phase-II upgrade of the Compact Muon Solenoid," CMS Technical Proposal CERN-LHCC-2015-010, CMS-TDR-15-02, 2015. [Online]. Available: http://cds.cern.ch/record/2020886

[91] M. Cacciari, G. P. Salam, and G. Soyez, "The anti-k_t jet clustering algorithm," *JHEP*, vol. 04, p. 063, 2008.

[92] ——, "FastJet user manual," *Eur. Phys. J. C*, vol. 72, p. 1896, 2012.

[93] V. Khachatryan *et al.*, "Jet energy scale and resolution in the CMS experiment in pp collisions at 8 TeV," *JINST*, vol. 12, p. P02014, 2017.

[94] "Jet algorithms performance in 13 TeV data," CERN, Geneva, Tech. Rep. CMS-PAS-JME-16-003, 2017. [Online]. Available: http://cds.cern.ch/record/2256875

[95] "Performance of the DeepJet b tagging algorithm using 41.9/fb of data from proton-proton collisions at 13TeV with Phase 1 CMS detector," Nov 2018. [Online]. Available: https://cds.cern.ch/record/2646773

[96] A. M. Sirunyan *et al.*, "Electron and photon reconstruction and identification with the CMS experiment at the CERN LHC," *JINST*, vol. 16, p. P05014, 2021.

[97] ——, "Performance of the CMS muon detector and muon reconstruction with proton-proton collisions at $\sqrt{s} = 13$ TeV," *JINST*, vol. 13, p. P06015, 2018.

[98] V. Khachatryan *et al.*, "Search for supersymmetry in pp collisions at $\sqrt{s} = 13$ TeV in the single-lepton final state using the sum of masses of large-radius jets," *JHEP*, vol. 08, p. 122, 2016.

[99] K. Rehermann and B. Tweedie, "Efficient identification of boosted semileptonic top quarks at the LHC," *JHEP*, vol. 03, p. 059, 2011.

[100] "Performance of missing energy reconstruction in 13 TeV pp collision data using the CMS detector," CERN, Geneva, Tech. Rep. CMS-PAS-JME-16-004, 2016. [Online]. Available: http://cds.cern.ch/record/2205284

[101] CMS Collaboration, "Measurement of the inelastic proton-proton cross section at $\sqrt{s} =$ 13 TeV," 2018, submitted to JHEP.

[102] V. Khachatryan *et al.*, “Performance of electron reconstruction and selection with the CMS detector in proton-proton collisions at $\sqrt{s} = 8\,$TeV,” *JINST*, vol. 10, p. P06005, 2015.

[103] L. Rokach and O. Maimon, *Data mining with decision trees: theory and applications*. World Scientific Pub Co Inc., 2008.

[104] A. Hoecker, P. Speckmayer, J. Stelzer, J. Therhaag, E. von Toerne, and H. Voss, “TMVA: Toolkit for multivariate data analysis,” *PoS*, vol. ACAT, p. 040, 2007.

[105] G. Cowan, K. Cranmer, E. Gross, and O. Vitells, “Asymptotic formulae for likelihood-based tests of new physics,” *Eur. Phys. J. C*, vol. 71, p. 1554, 2011.

[106] A. L. Read, “Presentation of search results: the CL_s technique,” *J. Phys. G*, vol. 28, p. 2693, 2002.

[107] V. Khachatryan *et al.*, “Search for new physics in same-sign dilepton events in proton-proton collisions at $\sqrt{s} = 13\,$TeV,” *Eur. Phys. J. C*, vol. 76, p. 439, 2016.

[108] “CMS luminosity measurement for the 2017 data-taking period at $\sqrt{s} = 13$ TeV,” CMS Physics Analysis Summary CMS-PAS-LUM-17-004, 2018. [Online]. Available: http://cds.cern.ch/record/2621960

[109] “CMS luminosity measurement for the 2018 data-taking period at $\sqrt{s} = 13$ TeV,” CMS Physics Analysis Summary CMS-PAS-LUM-18-002, 2019. [Online]. Available: http://cds.cern.ch/record/2676164

[110] A. Kalogeropoulos and J. Alwall, “The SysCalc code: A tool to derive theoretical systematic uncertainties,” 2018.

[111] https://twiki.cern.ch/twiki/bin/view/CMS/SUSLeptonSF.

[112] T. Junk, “Confidence level computation for combining searches with small statistics,” *Nucl. Instrum. Meth. A*, vol. 434, p. 435, 1999.

[113] ATLAS and CMS Collaborations, LHC Higgs Combination Group, “Procedure for the LHC Higgs boson search combination in summer 2011,” CERN, Tech. Rep. ATL-PHYS-PUB/2011-11, CMS NOTE 2011/005, 2011. [Online]. Available: http://cdsweb.cern.ch/record/1379837

[114] T. A. collaboration, “Search for the $b\bar{b}$ decay of the standard model higgs boson in associated (w/z)h production with the ATLAS detector,” *Journal of High Energy Physics*, vol. 2015, no. 1, p. 69, 2015. [Online]. Available: https://doi.org/10.1007/JHEP01(2015)069

A

Data quality

Contents

A.1 Supporting material for the Trigger studies

Since this analysis uses $E_{\mathrm{T}}^{\text{miss}}$-$H_{\mathrm{T}}^{\text{miss}}$ based triggers, the measurement of figure 4.1 is repeated as a function of $H_{\mathrm{T}}^{\text{miss}}$ at preselection.

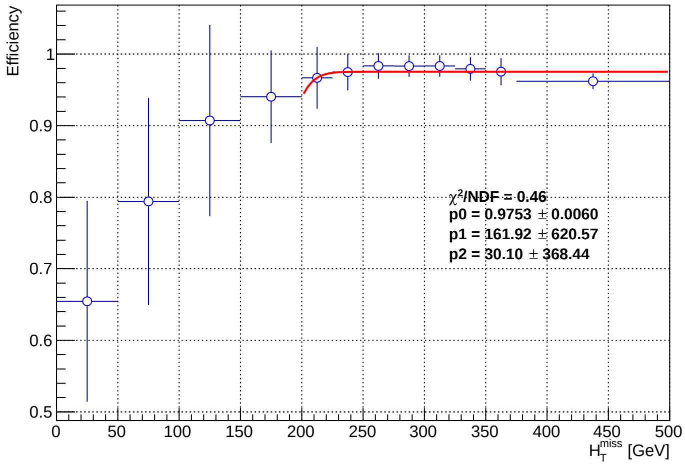

Figure A.1: Trigger efficiency as a function of $H_{\mathrm{T}}^{\text{miss}}$ measured in single electron dataset after a requirement on leading electron $p_{\mathrm{T}} > 40\,\text{GeV}$, jet $p_{\mathrm{T}} > 100\,\text{GeV}$, $H_{\mathrm{T}} > 200\,\text{GeV}$ and $E_{\mathrm{T}}^{\text{miss}} > 280\,\text{GeV}$ fitted with an error function.

As one can observe in figure A.1, the trigger efficiency plateaus at $H_{\mathrm{T}}^{\text{miss}} \sim 200\,\text{GeV}$. The value of this plateau is approximately 97%, which is the same value than the plateau of the trigger efficiency versus $E_{\mathrm{T}}^{\text{miss}}$, and used throughout the analysis. There is a small fraction of events with $H_{\mathrm{T}}^{\text{miss}} < 200\,\text{GeV}$. To assess if these events have an impact in the analysis, we visualize $H_{\mathrm{T}}^{\text{miss}}$ at preselection for different signal points in figure A.2. As it can be seen the fraction of signal events with $H_{\mathrm{T}}^{\text{miss}} < 200\,\text{GeV}$ is negligible.

Secondly, the fraction of the signal yield at preselection that permeates the region of $H_{\mathrm{T}}^{\text{miss}} < 200\,\text{GeV}$ is measured and reported in table A.1.

Table A.1: Signal yields at preselection and at preselection $\bigoplus H_{\mathrm{T}}^{\text{miss}} < 200\,\text{GeV}$ as well as the ratio between the two yields for multiple signal points.

Signal point	Preselection	Preselection $\bigoplus H_{\mathrm{T}}^{\text{miss}} < 200$ GeV	Ratio (%)
(250,170)	11025 ± 79	51 ± 5	0.5
(600,520)	408 ± 6	1.9 ± 0.4	0.5
(550,520)	511 ± 6	1.8 ± 0.4	0.4
(600,590)	83.6 ± 2.3	0.47 ± 0.18	0.6
(800,790)	15.0 ± 0.5	0.024 ± 0.017	0.2

As one can observe, the fraction of signal events with $H_{\mathrm{T}}^{\text{miss}} < 200\,\text{GeV}$ is negligible, below 0.7% for all the points in table A.1. Therefore, this has no impact on the analysis, particularly that the systematic uncertainties due to trigger correction is of the order of 1%. In conclusion, the events with $H_{\mathrm{T}}^{\text{miss}} < 200\,\text{GeV}$ are negligible in this analysis and the trigger efficiency curve measured as a function of $E_{\mathrm{T}}^{\text{miss}}$ can be used.

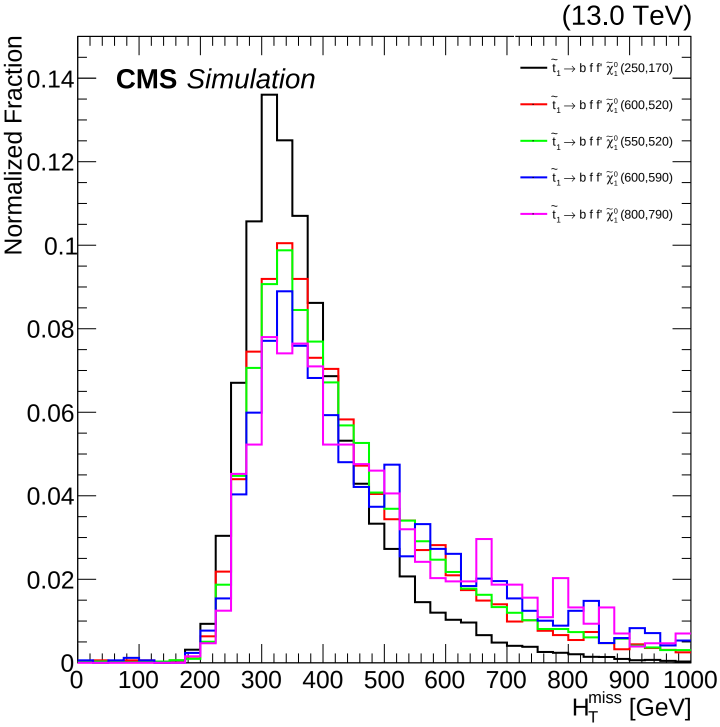

Figure A.2: Distribution of $H_{\mathrm{T}}^{\text{miss}}$ for various signal points.

A.2 Pulls and impacts on the signal strength of each source of uncertainty

The impact of a Nuisance Parameter (NP), θ, on the signal strength, r, is defined as the shift Δr that is induced as θ is fixed and varied up and down by one standard deviation of their uncertainties, with all other parameters profiled as normal (see [114] for a description of this method). This is effectively a measure of the correlation between the NP and the signal strength, and is useful for determining which NPs have the largest effect on the signal strength uncertainty. The effects from the variations of the NPs on the signal strength are shown in Figures A.3 to A.5 . As can be seen, there are several NPs of almost exactly 0 and with uncertainty 1, which is the desired situation, where the fit does not shift its value, nor squeezes its uncertainty. The pulls that are not zero are the result of a spurious constraint coming from the data that pulls the nuisance parameter, nonetheless, the effect is negligible and the pulls on the signal strength of all NPs have been considered to be good by the collaboration. The systematic uncertainties of the background prediction methods are the major contributors to the total uncertainty.

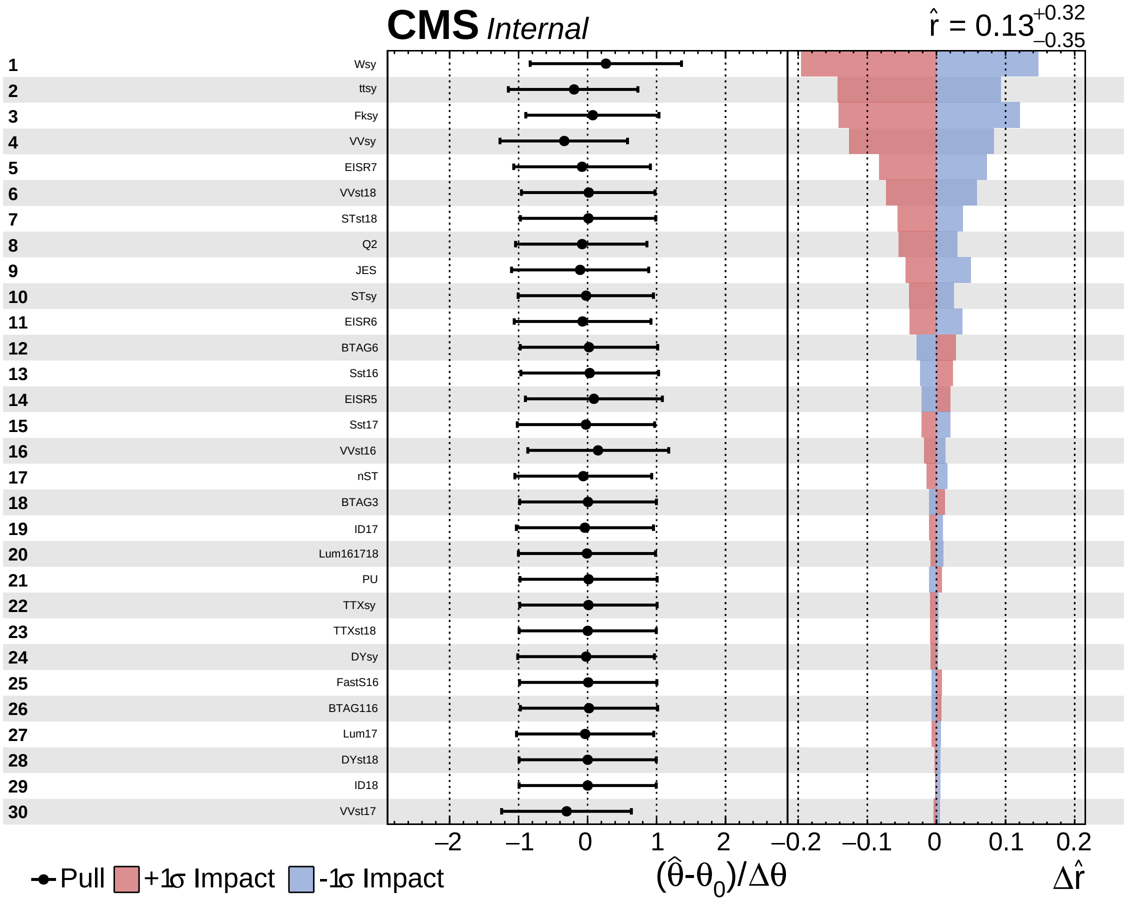

Figure A.3: Pulls and impacts on the signal strength of each of the NPs representing the different sources of uncertainty for the combination of all years using data. The uncertainties are listed in decreasing order of their impact on r. Statistical and systematic uncertainties are denoted as st and sys respectively. The numbers 16, 17 and 18 stand for the year that the uncertainty has been considered, 2016, 2017 and 2018 respectively. W, tt, and Fk represent the data–driven predicted backgrounds, W+jets, $t\bar{t}$ and nonprompt backgrounds. VV, ST, TTX, and DY represent the backgrounds predicted from simulation, diboson, single top quark, $t\bar{t}X$, and DY respectively. EISR and ISR are used for the uncertainties arising from ISR corrections for the W+jets and $t\bar{t}$ processes respectively. JES and JER refer to the JEC corrections. BTAG, ID and ISO are uncertainties that correspond to the SFs used to correct for the b tagging efficiencies, and lepton identification and isolation. The luminosity, trigger, pile–up, and renormalization and factorization corrections uncertainties are represented by LUM, Trg, PU, and Q2 respectively.

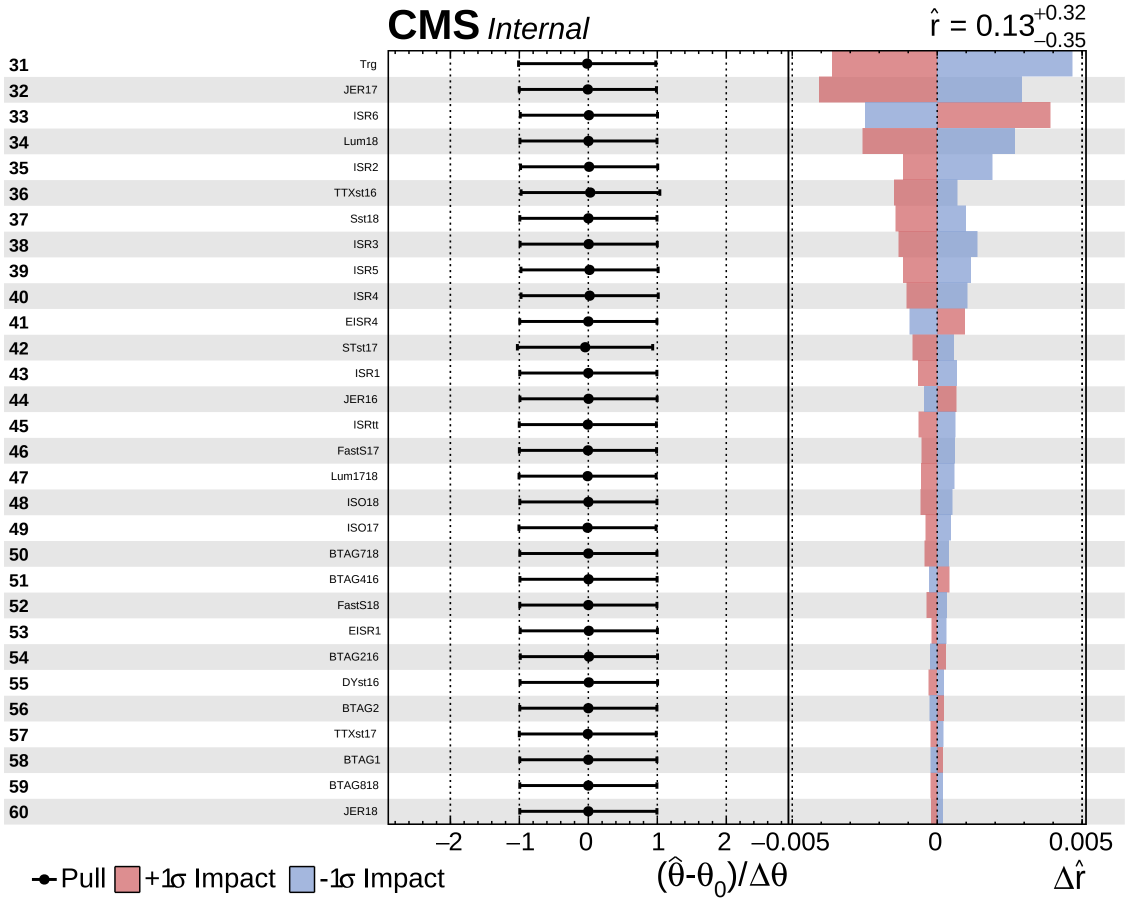

Figure A.4: Pulls and impacts on the signal strength of each of the NPs representing the different sources of uncertainty for the combination of all years using data. The uncertainties are listed in decreasing order of their impact on r. Statistical and systematic uncertainties are denoted as st and sys respectively. The numbers 16, 17 and 18 stand for the year that the uncertainty has been considered, 2016, 2017 and 2018 respectively. W, tt, and Fk represent the data–driven predicted backgrounds, W+jets, $t\bar{t}$ and nonprompt backgrounds. VV, ST, TTX, and DY represent the backgrounds predicted from simulation, diboson, single top quark, $t\bar{t}X$, and DY respectively. EISR and ISR are used for the uncertainties arising from ISR corrections for the W+jets and $t\bar{t}$ processes respectively. JES and JER refer to the JEC corrections. BTAG, ID and ISO are uncertainties that correspond to the SFs used to correct for the b tagging efficiencies, and lepton identification and isolation. The luminosity, trigger, pile–up, and renormalization and factorization corrections uncertainties are represented by LUM, Trg, PU, and Q2 respectively.

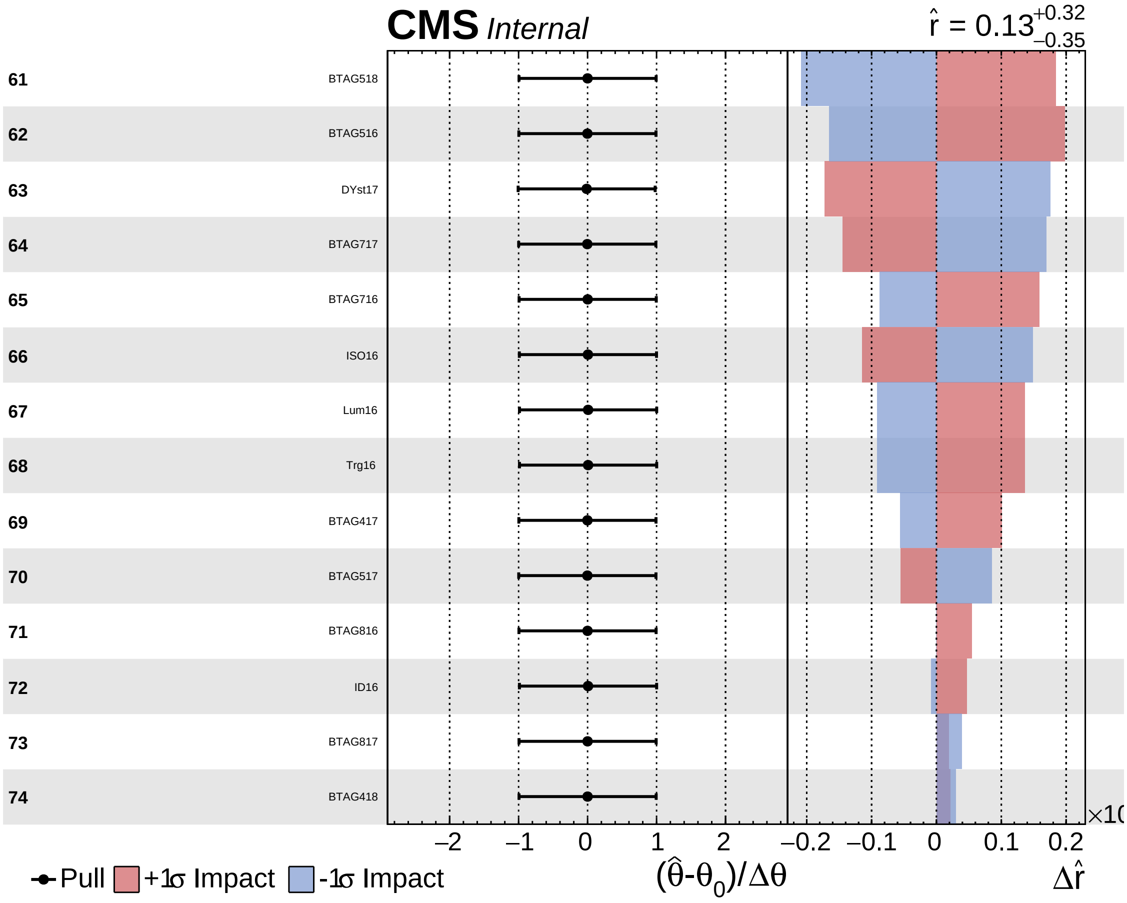

Figure A.5: Pulls and impacts on the signal strength of each of the NPs representing the different sources of uncertainty for the combination of all years using data. The uncertainties are listed in decreasing order of their impact on r. Statistical and systematic uncertainties are denoted as st and sys respectively. The numbers 16, 17 and 18 stand for the year that the uncertainty has been considered, 2016, 2017 and 2018 respectively. W, tt, and Fk represent the data–driven predicted backgrounds, W+jets, $t\bar{t}$ and nonprompt backgrounds. VV, ST, TTX, and DY represent the backgrounds predicted from simulation, diboson, single top quark, $t\bar{t}X$, and DY respectively. EISR and ISR are used for the uncertainties arising from ISR corrections for the W+jets and $t\bar{t}$ processes respectively. JES and JER refer to the JEC corrections. BTAG, ID and ISO are uncertainties that correspond to the SFs used to correct for the b tagging efficiencies, and lepton identification and isolation. The luminosity, trigger, pile–up, and renormalization and factorization corrections uncertainties are represented by LUM, Trg, PU, and Q2 respectively.

B

Monte Carlo Simulation quality

Contents

B.1 Correcting W+jets samples

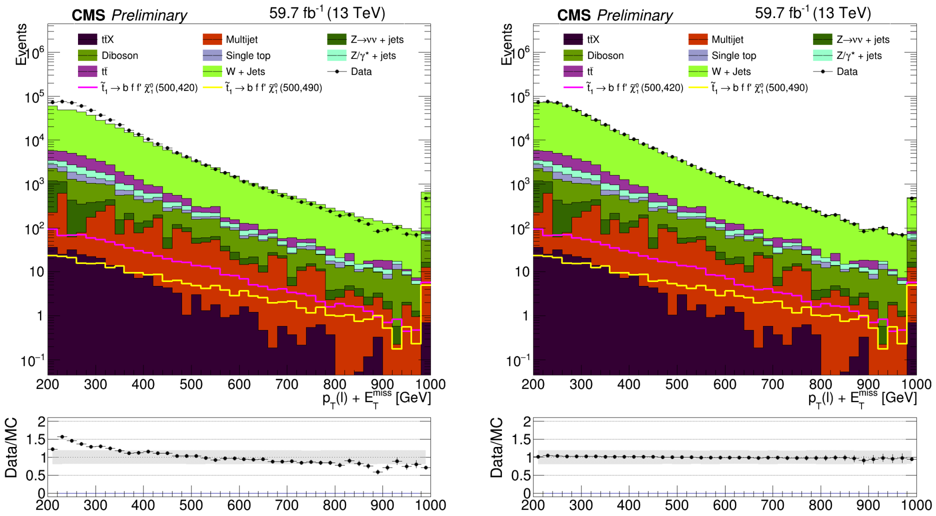

Figure B.1: 2018 Data/MC agreement as a function of S_{T} in the W+jets enriched Control Region. Right: non-corrected W+jets samples; left: corrected W+jets samples.

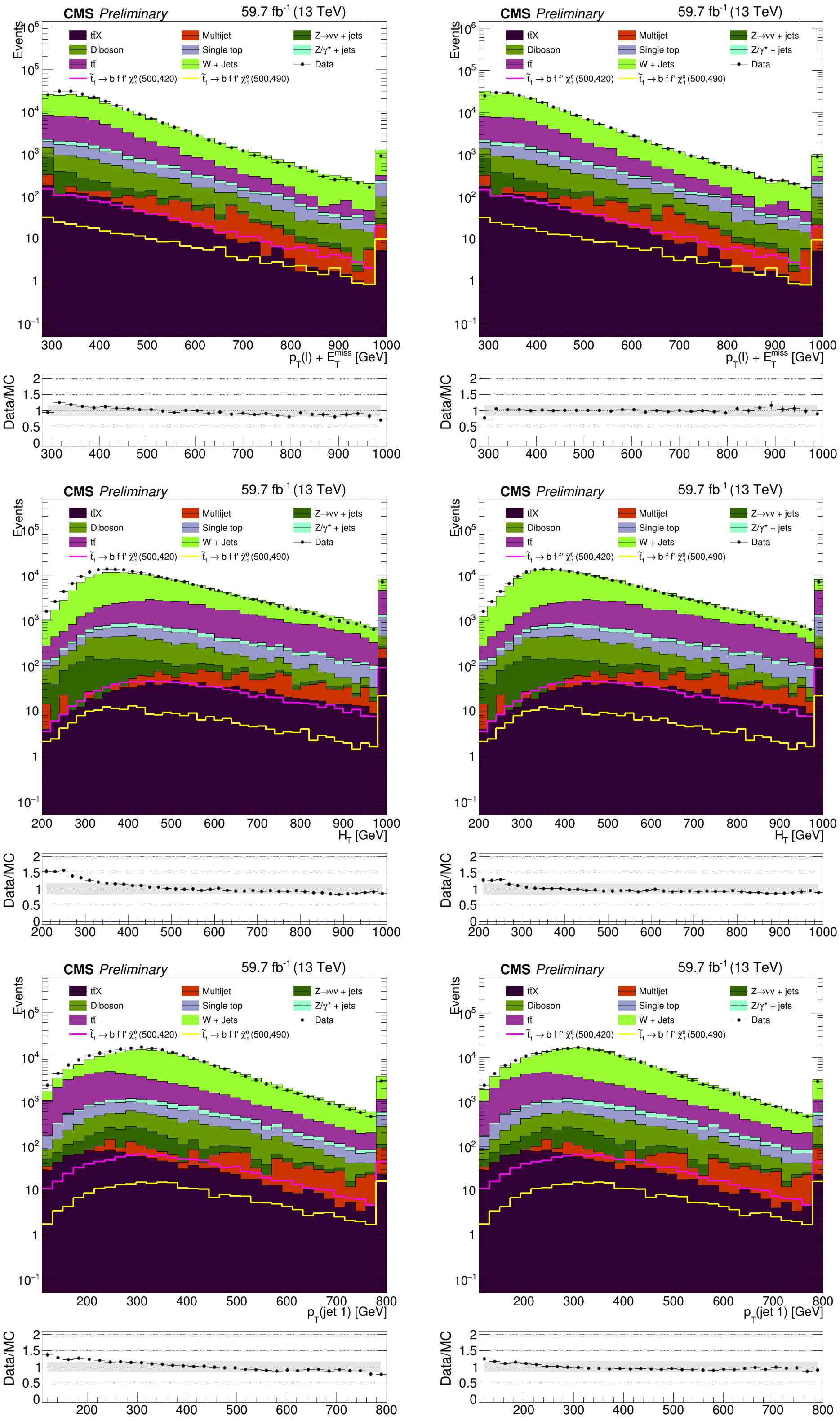

Figure B.2: 2018 Data/MC agreement at Preselection level. Left: non-corrected *W*+jets samples; right: corrected *W*+jets samples. From top to bottom: S_T, H_T and $p_\mathrm{T}(\mathrm{ISR})$.

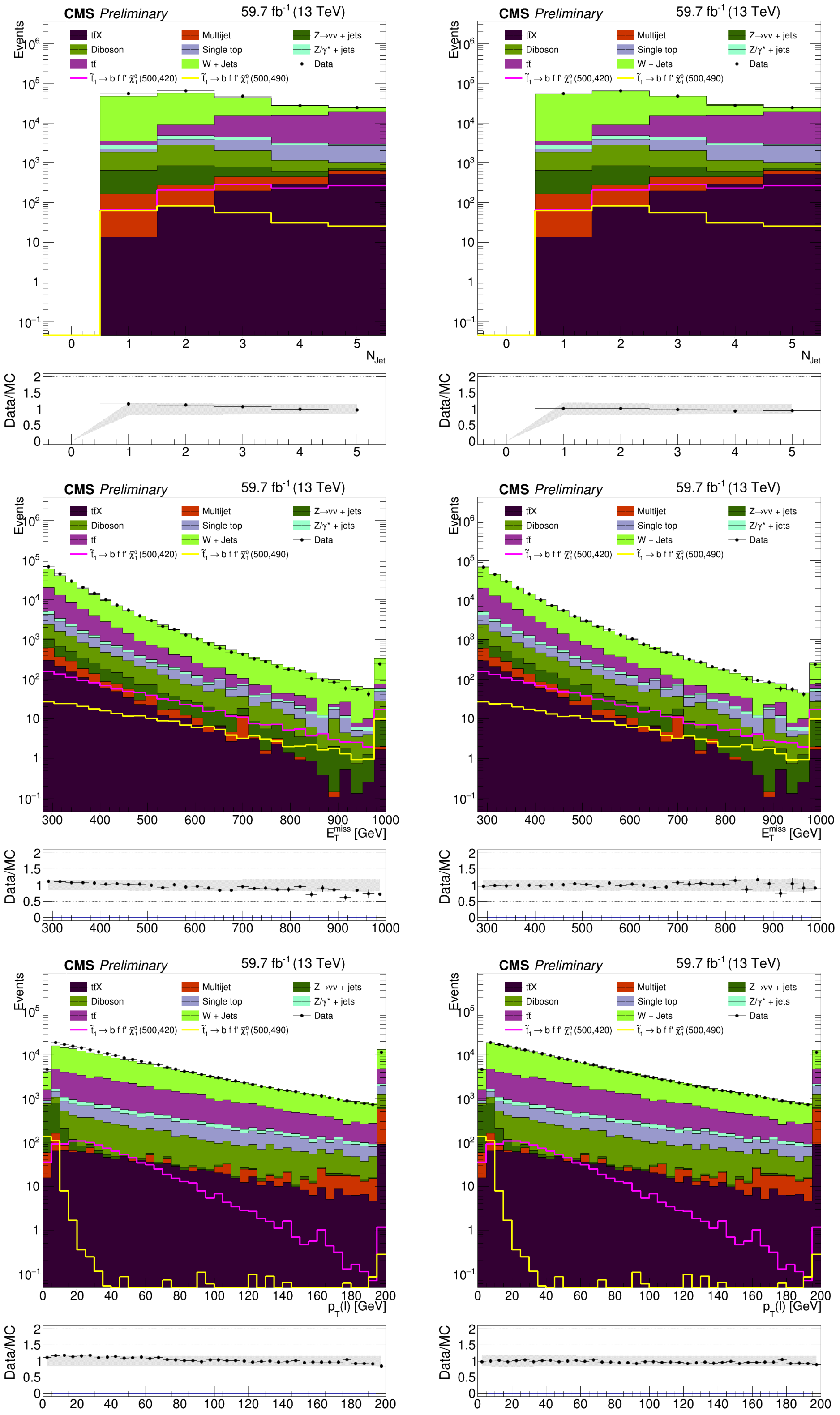

Figure B.3: 2018 Data/MC agreement at Preselection level. Left: non-corrected W+jets samples; right: corrected W+jets samples. From top to bottom: N_{jet}, $p_{\mathrm{T}}^{\text{miss}}$ and $p_{\mathrm{T}}(\ell)$.

B.2 Lepton identification and isolation scale factors

The electron low–p_{T} identification, and lepton isolation scale factors where derived by author, and approved by the respective Particle Object Groups within the CMS collaboration. These SFs are derived as function of lepton–p_{T} and lepton–η, because the efficiency of the reconstruction algorithms depends on these same variables. The method used is the "tag-and-probe". The tag and probe method is a data–driven technique for measuring particle detection efficiencies, ϵ. It is based on the decays of known resonances (e.g. *J*/ψ, γ and *W*) to pairs of leptons being studied. In this method, a "tag" lepton with a known and well-measured momentum is used to select the event. Then, a "probe" lepton is selected and its momentum is measured. The tag and probe leptons are required to have opposite electrical charges, and to have an invariant mass in a window around the mass of the resonance. The efficiency is given by the fraction of probe leptons that pass a given set of criteria X, where X can be identification, isolation or impact parameter criteria:

$$\epsilon = \frac{N(\text{probe leptons passing criteria } X)}{N(\text{probe leptons})}, \tag{B.1}$$

where, the denominator corresponds to the number of resonance candidates ("tag"+"probe" pairs) reconstructed in the dataset, and the numerator corresponds to the subset for which the probe passes the criteria X. The determination of the detector efficiency is a critical ingredient in any physics measurement. It accounts for the particles that were produced in the collision but escaped detection. The "tag-and-probe" method provides a useful approach for extracting efficiencies directly from data.

For high–p_{T} electrons and muon identification, the centrally produced ones were used. Figures B.4 and B.5 represent the low–p_{T} electron identification efficiencies, and figures B.6 and B.7 illustrate the electron isolation scale factors. In figures B.8 and B.9 the muon isolation efficiencies are reported.

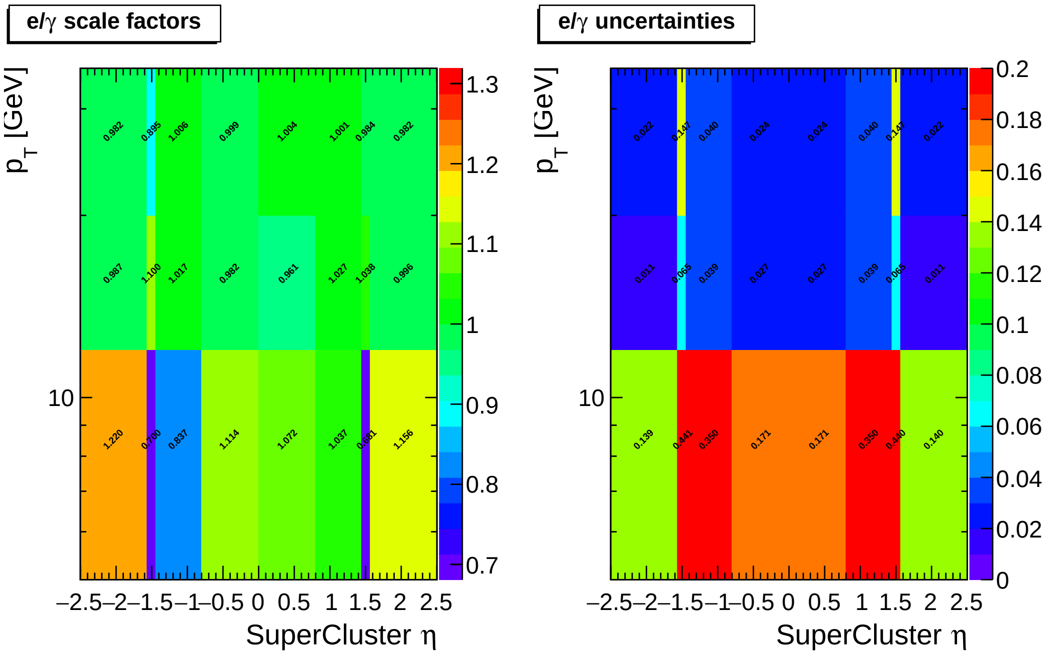

Figure B.4: 2017 electron identification scale factor for $p_{\mathrm{T}} < 10\,\mathrm{GeV}$ derived from central tag-and-probe trees at the *Z* peaks with respective uncertainties (statistical and systematic).

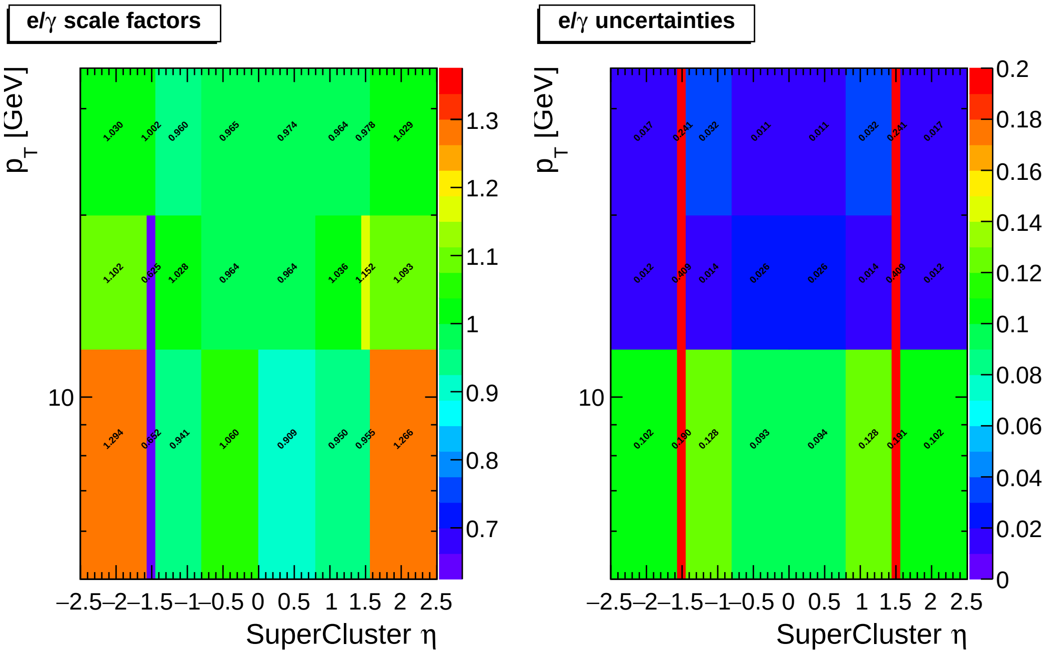

Figure B.5: 2018 electron identification scale factor for $p_{\mathrm{T}} < 10\,\mathrm{GeV}$ derived from central tag-and-probe trees at the *Z* peak with respective uncertainties (statistical and systematic).

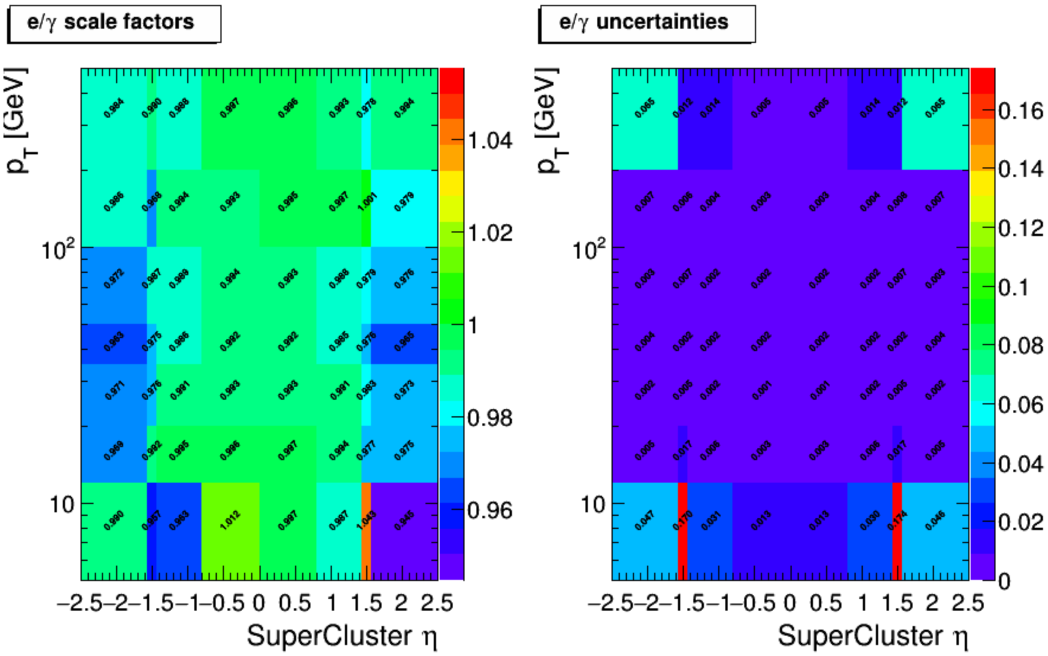

Figure B.6: 2017 electron Impact Parameter and Isolation scale factors with respect to cutID Loose identification derived from central tag-and-probe trees at the Z peaks with respective uncertainties (statistical and systematic).

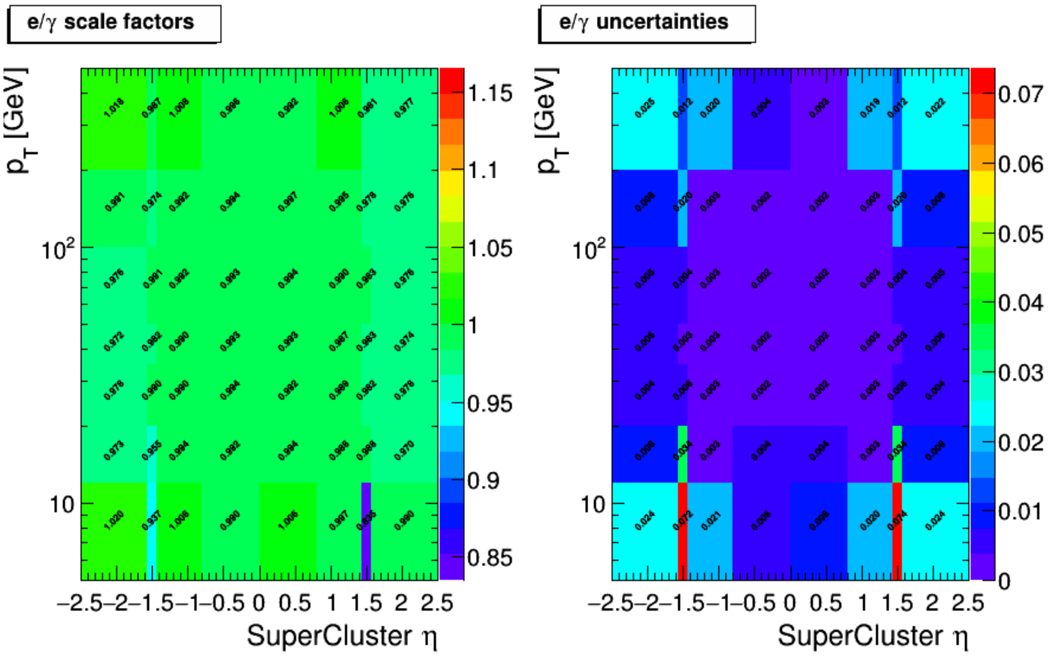

Figure B.7: 2018 electron Impact Parameter and Isolation scale factors with respect to cutID Loose identification derived from central tag-and-probe trees at the Z peak with respective uncertainties (statistical and systematic).

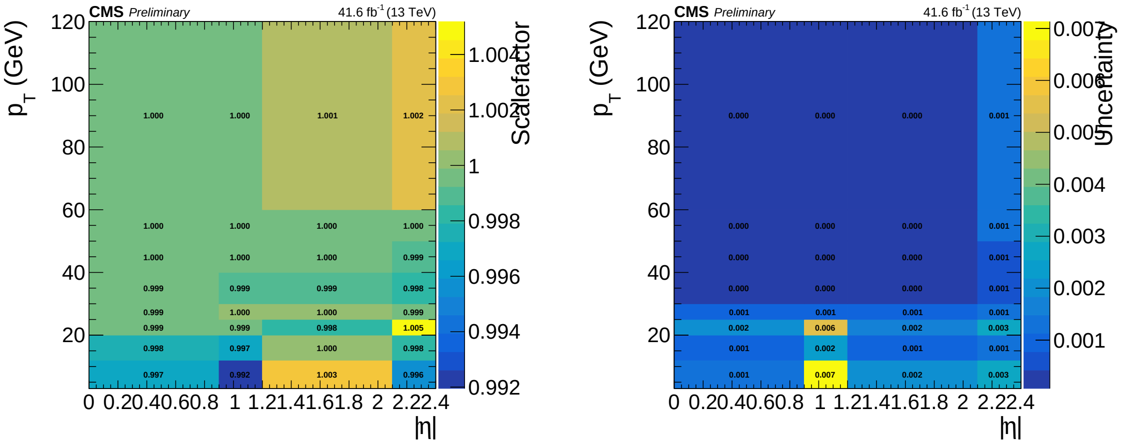

Figure B.8: 2017 muon Impact Parameter and Isolation scale factors with respect to Medium ID derived from central tag-and-probe trees at the Z peaks with respective uncertainties (statistical and systematic).

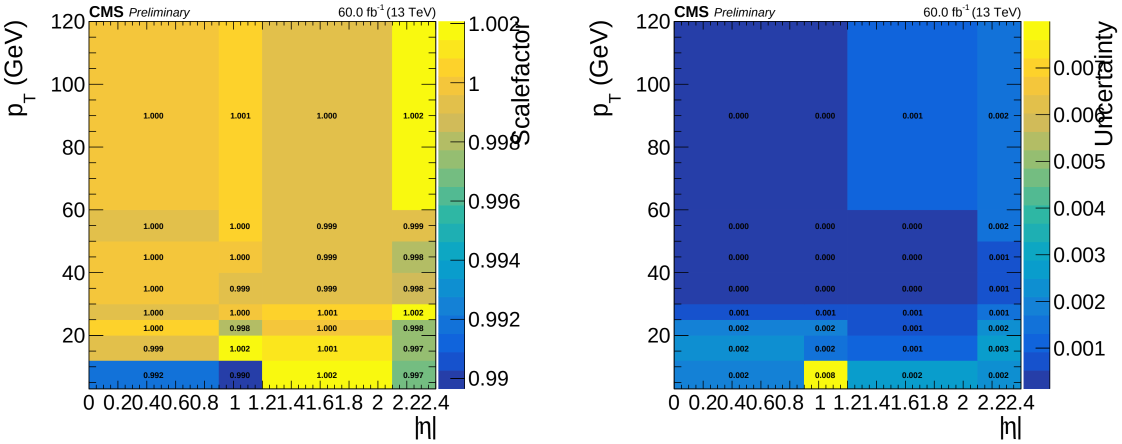

Figure B.9: 2018 muon Impact Parameter and Isolation scale factors with respect to Medium ID derived from central tag-and-probe trees at the Z peak with respective uncertainties (statistical and systematic).

B.3 Efficiency of the signal generator filters

As mentioned in section 4.8, this signal scan has been pre-filtered requiring at the generation level $E_{\mathrm{T}}^{\mathrm{miss}} > 80\,$GeV and $H_{\mathrm{T}} > 160\,$GeV. Per year, the generator filter efficiency $\epsilon_{SMSfilter}$ is computed as a function of the masses of $\widetilde{t}_1$ and $\widetilde{\chi}_1^0$ as:

$$\epsilon_{SMSfilter} = \frac{N_{passSMSfilter}}{N_{total}}(m_{\tilde{t}_1}, m_{\tilde{\chi}_1^0}) \tag{B.2}$$

In figure B.10, the $\epsilon_{SMSfilter}$ for different $(m(\widetilde{t}_1),\ m(\widetilde{\chi}_1^0))$ signal points is reported per year. One can observe the variation of the filter efficiency versus mass of the $\widetilde{\chi}_1^0$ and versus Δm.

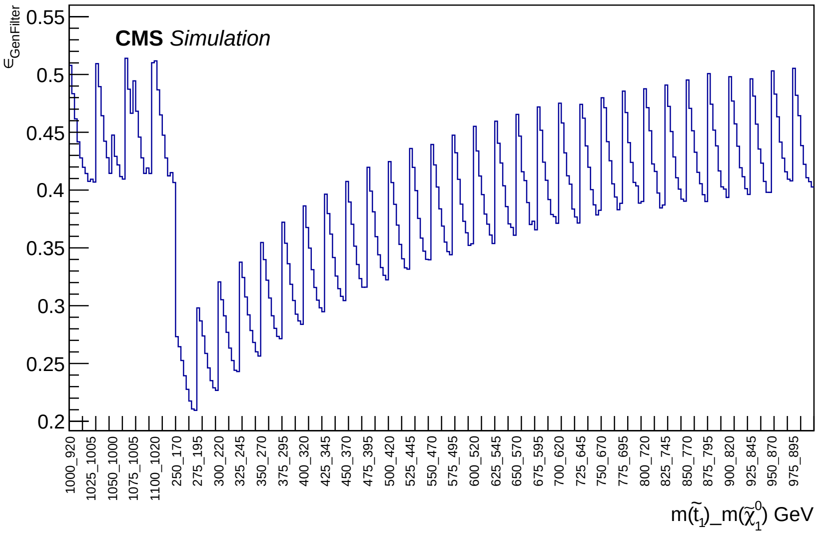

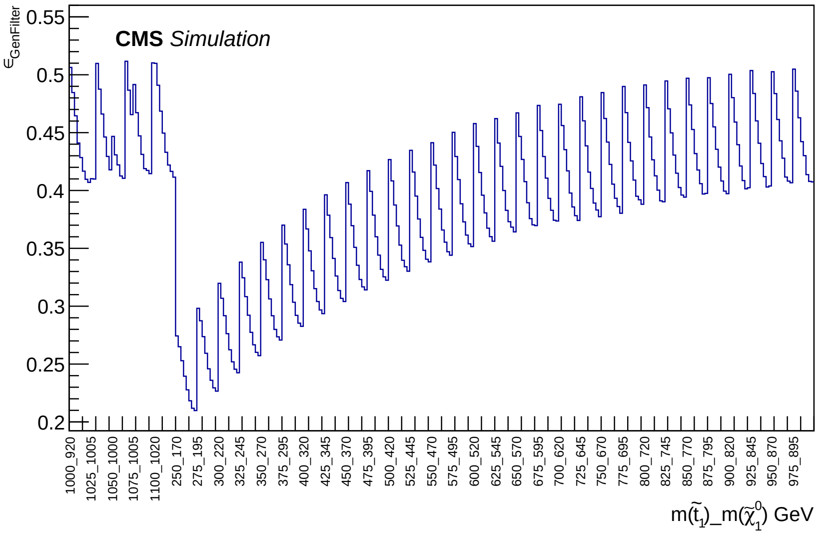

Figure B.10: Signal generator filter efficiency as a function of the masses of $\widetilde{t}_1$ and $\widetilde{\chi}_1^0$. On the top, $\epsilon_{SMSfilter}$ for 2017 signal samples, 2018 is reported on the bottom plot.

The measured $\epsilon_{SMSfilter}$ for 2017 and 2018 signal samples are compared to the published results of 2016 to show that the measured values for $\epsilon_{SMSfilter}$ are very compatible across different years.

Table B.1 gives an illustration of this, where one can also observe the effect of the mass of the $\tilde{\chi}_1^0$ and Δm on the filter efficiency.

Table B.1: Full RunII comparison of signal $\epsilon_{SMSfilter}$ for 6 signal points

Signal Point	**2016 $\epsilon_{SMSfilter}$**	**2017 $\epsilon_{SMSfilter}$**	**2018 $\epsilon_{SMSfilter}$**
(250,170)	0.27	0.27	0.27
(250,240)	0.20	0.21	0.21
(550,520)	0.35	0.36	0.36
(600,520)	0.45	0.46	0.46
(800,720)	0.49	0.49	0.49
(800,790)	0.39	0.39	0.39

In order to complete this measurement, it has to be confirmed that there are no events in the signal region that could possibly be affected by the generator selection of $GenE_{\mathrm{T}}^{\text{miss}} > 80\,$GeV and $GenH_{\mathrm{T}} > 160\,$GeV. As can be seen in figure B.11 there are no events in the SR close enough to the region selected by the generator filters.

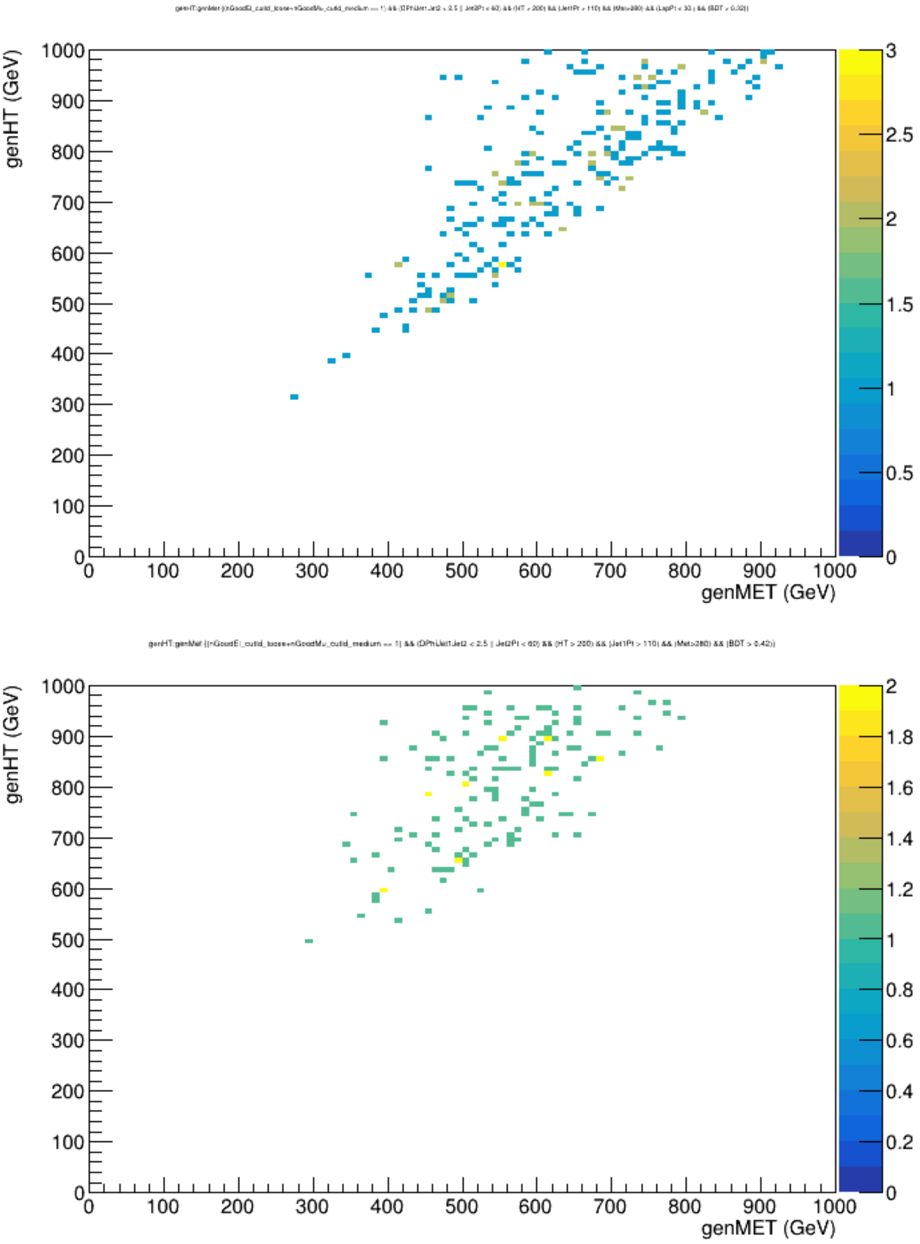

Figure B.11: $GenE_{\mathrm{T}}^{\text{miss}}$ as a function of $GenH_{\mathrm{T}}$ for the benchmark signal points for Δm =10 GeV (top) and Δm =80 GeV (bottom) of events in the signal region.

C

Supporting Material for the BDT approach

Contents

C.1 BDT cut setting

The expected upper limit on the signal cross section of each benchmark $(m(\widetilde{t}_1),\ m(\widetilde{\chi}_1^0))$ signal point is computed as a function of the lower limit imposed on the BDT output, using the asymptotic CL$_s$ method [105, 106]. The value that minimizes this curve is chosen to define the SR. This value, $BDT^{SR}_{\Delta m}$, is cross-checked with the efficiency curves of signal and background to avoid choosing the selection on the BDT output in regions affected by statistical fluctuations.

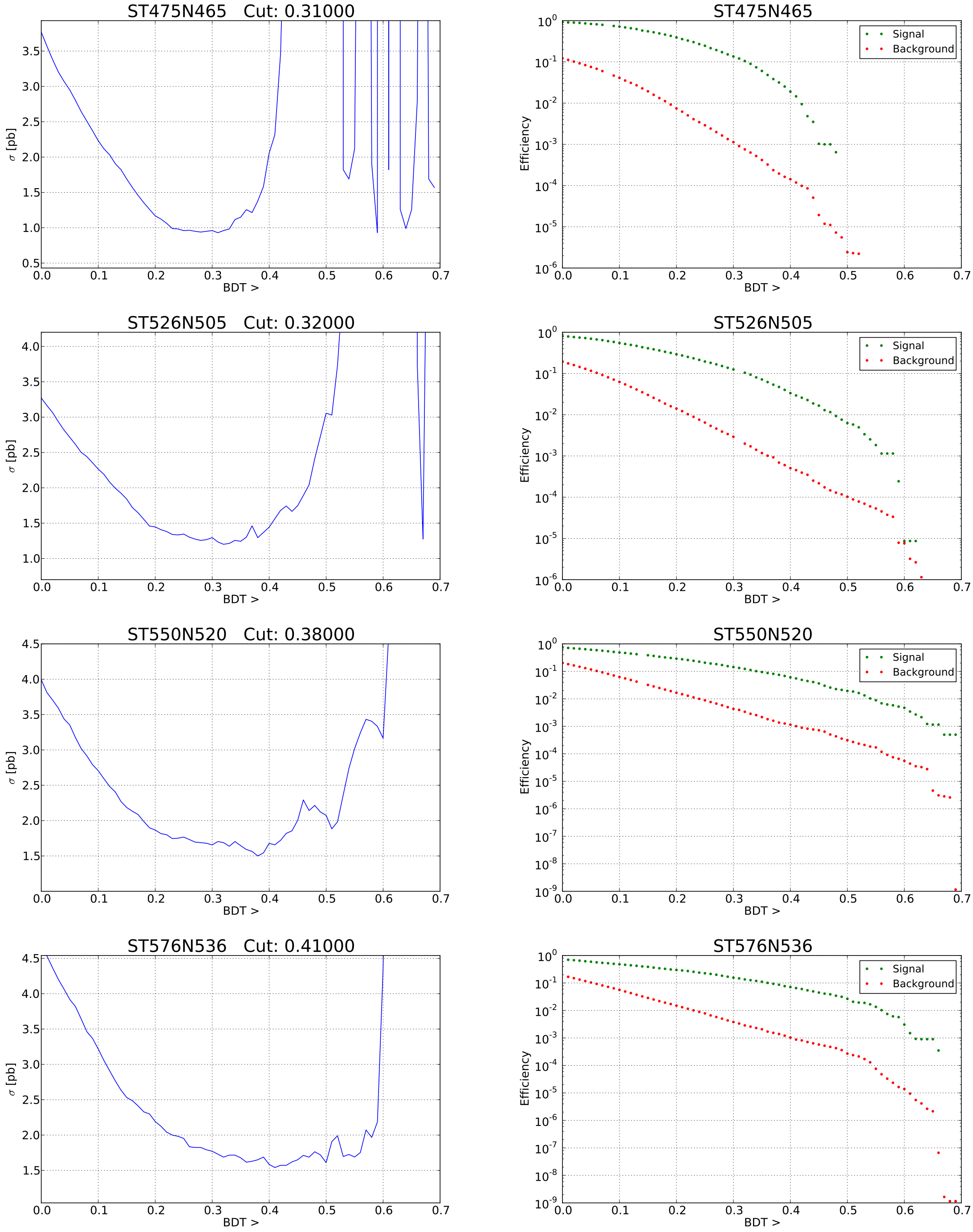

Figure C.1: Minimization of the expected upper limit cross section at 95 % Confidence Limit for the year of 2017 for $\Delta m = 10, 20, 30,$ and 40 GeV.

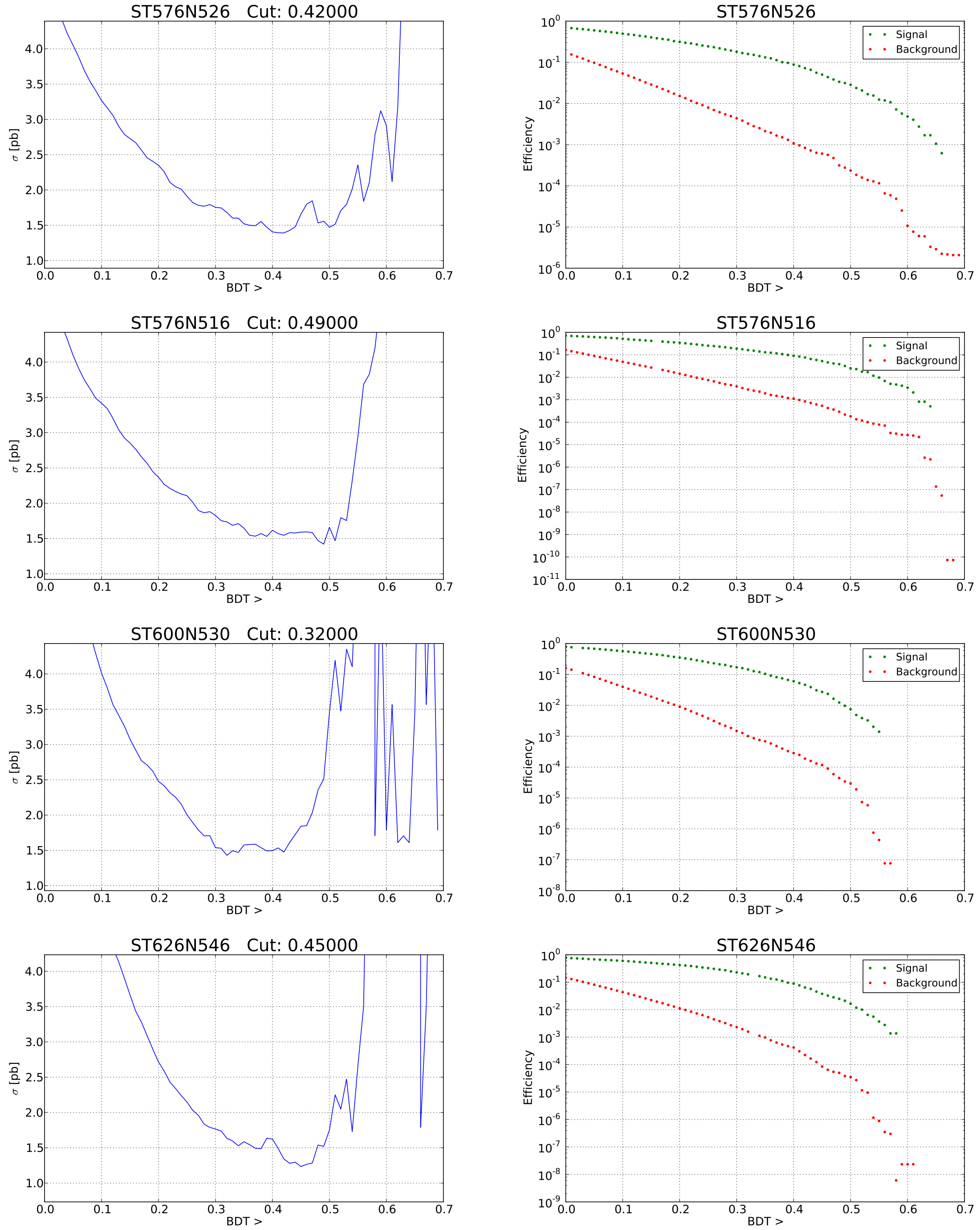

ST576N526 Cut: 0.42000

ST576N526

ST576N516 Cut: 0.49000

ST576N516

ST600N530 Cut: 0.32000

ST600N530

ST626N546 Cut: 0.45000

ST626N546

Figure C.2: Minimization of the expected upper limit cross section at 95 % Confidence Limit for the year of 2017 for $\Delta m = 50, 60, 70,$ and 80 GeV.

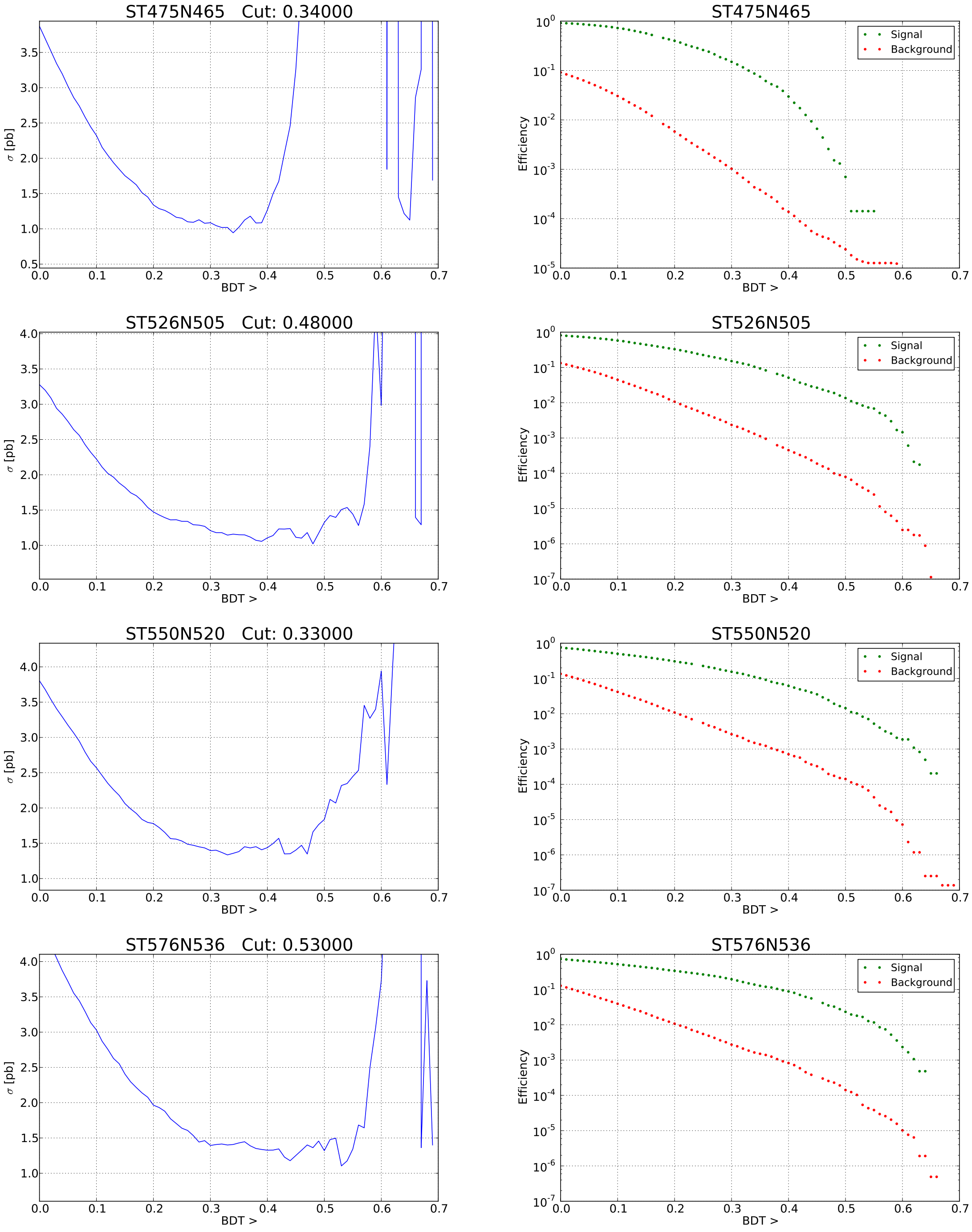

Figure C.3: Minimization of the expected upper limit cross section at 95 % Confidence Limit for the year of 2018 for $\Delta m = 10, 20, 30,$ and $40\,$GeV.

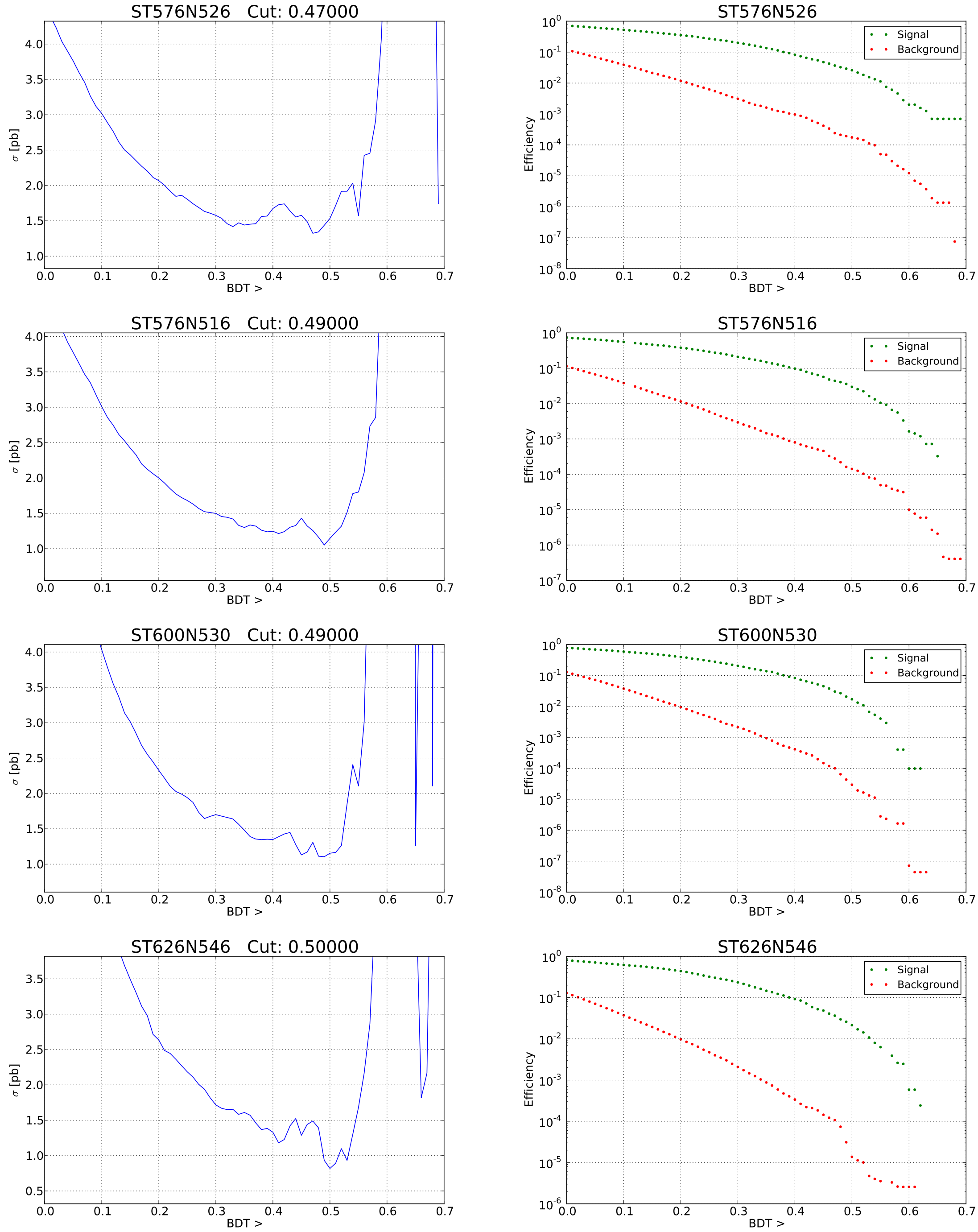

Figure C.4: Minimization of the expected upper limit cross section at 95 % Confidence Limit for the year of 2018 for $\Delta m = 50, 60, 70$, and 80 GeV.

C.2 BDT overtraining plots for different Δm

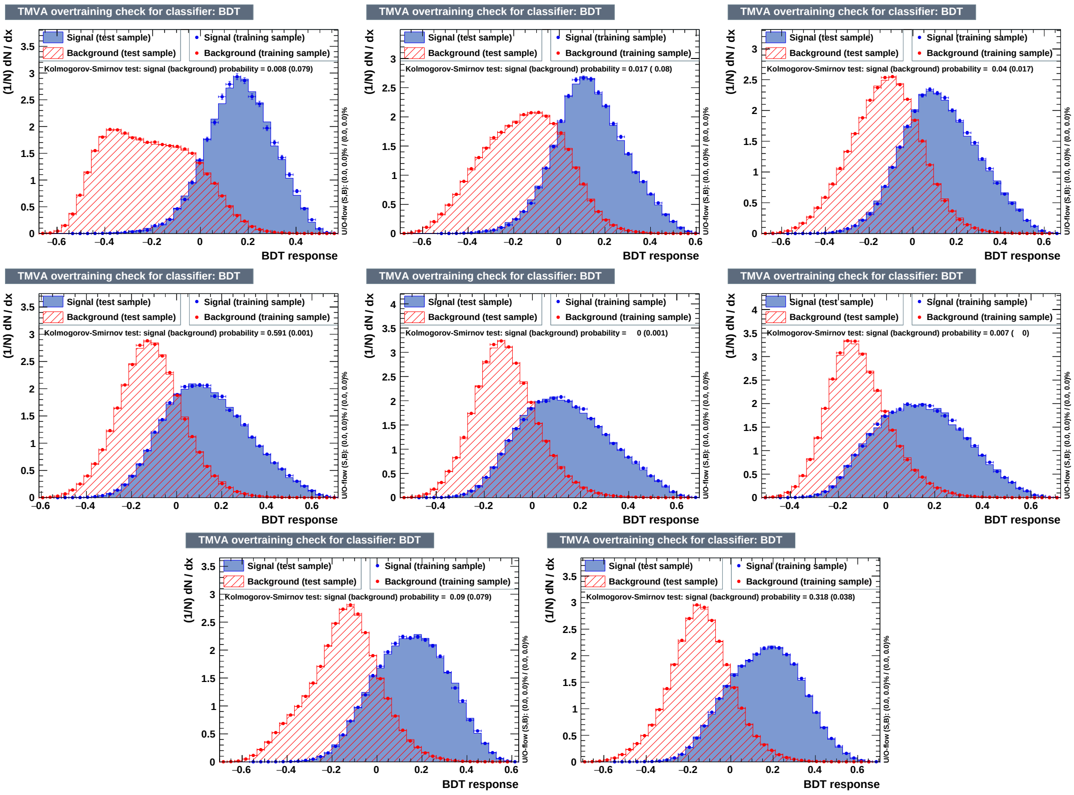

Figure C.5: 2017: Distribution of the output of the BDT for signal (blue) and background (red) across test- (full histogram) and train-samples (dot). The illustrated cases are the BDT for Δm = 10 GeV (upper left) to 80 GeV (lower right).

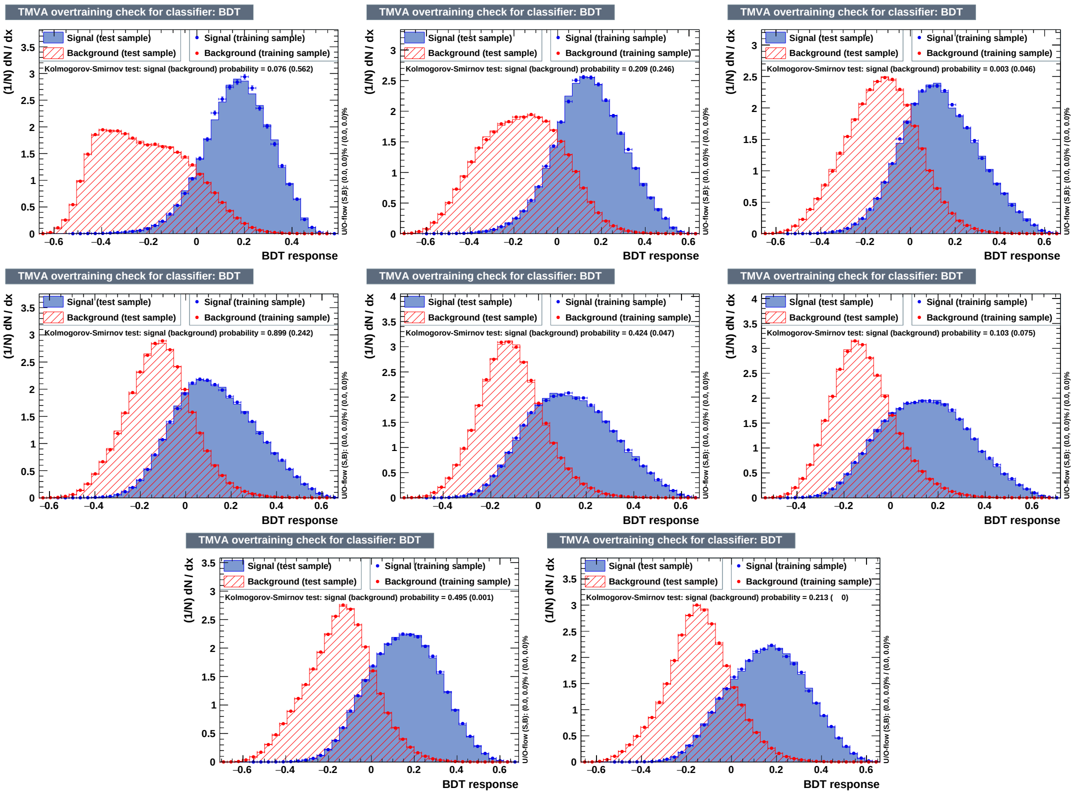

Figure C.6: 2018: Distribution of the output of the BDT for signal (blue) and background (red) across test- (full histogram) and train-samples (dot). The illustrated cases are the BDT for Δm = 10 GeV (upper left) to 80 GeV (lower right).

C.3 Discriminant variables in the validation regions

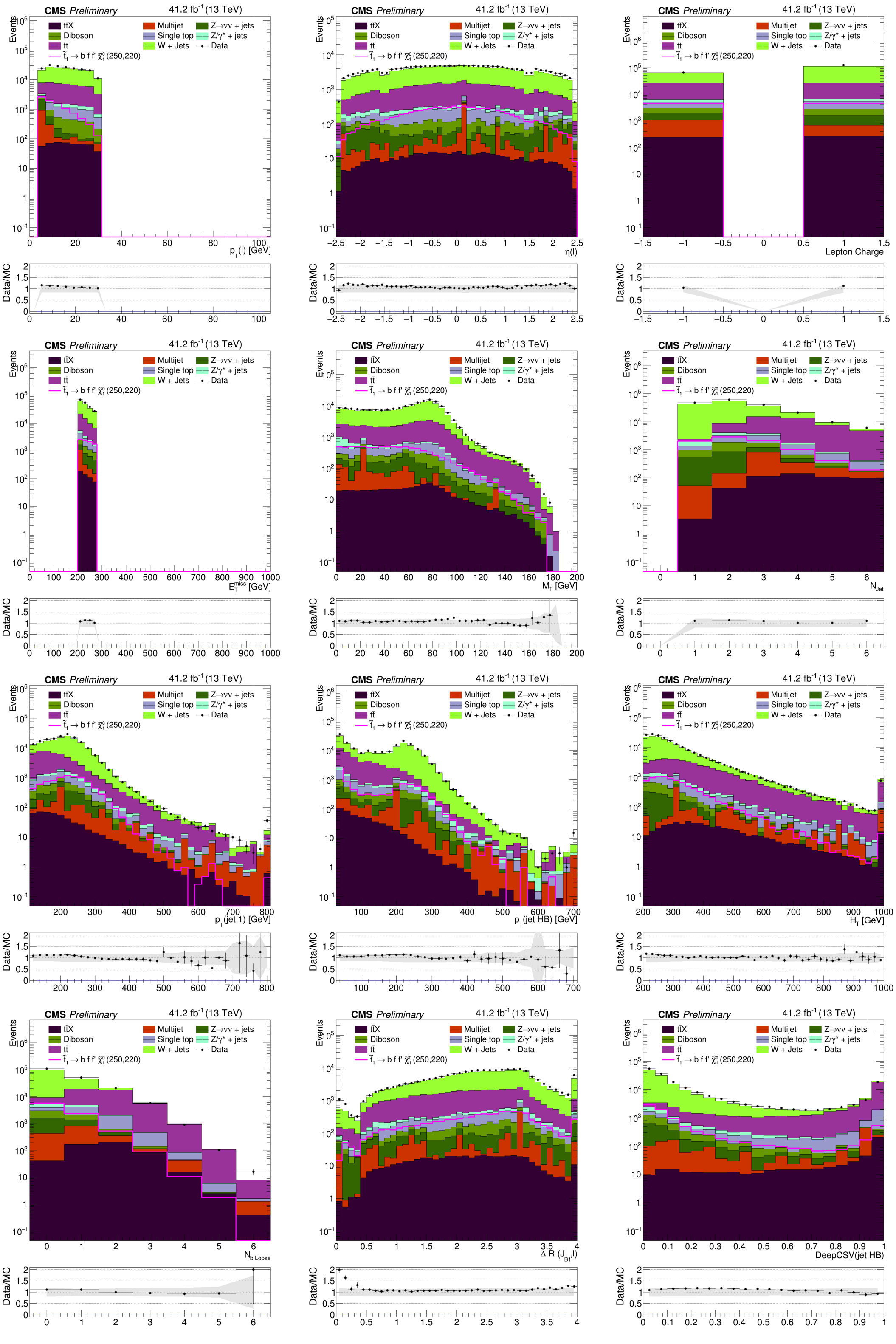

Figure C.7: Data and expected MC contributions for different variables in both final states and for L=41.2 fb^{-1} in the VR2 region. Starting from top-left to bottom-right: $p_{\mathrm{T}}(\ell)$, $\eta(\ell)$, $Q(\ell)$, $p_{\mathrm{T}}^{\mathrm{miss}}$, m_{T} , N_{jet}, $p_{\mathrm{T}}(\mathrm{ISR})$, $p_{\mathrm{T}}(b)$, H_{T}, $N(b^{\mathrm{loose}})$, $\Delta R(\ell, b)$, $D(b)$. The systematic uncertainties in the background are quadratically added to the statistical uncertainty when calculating the Data/MC ratio.

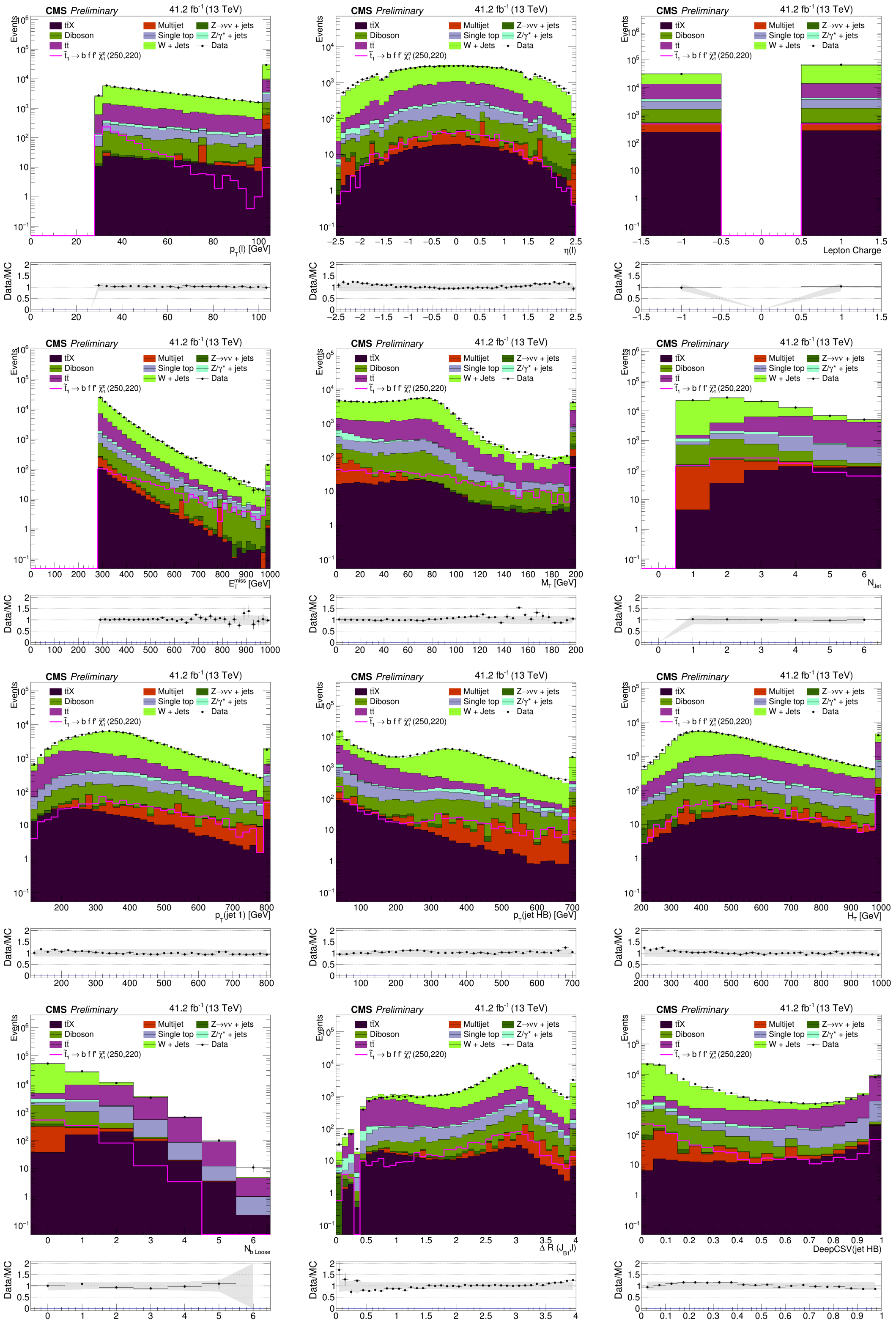

Figure C.8: Data and expected MC contributions for different variables in both final states and for L=41.2 fb^{-1} in the VR3 region. Starting from top-left to bottom-right: $p_{\mathrm{T}}(\ell)$, $\eta(\ell)$, $Q(\ell)$, $p_{\mathrm{T}}^{\text{miss}}$, m_{T} , N_{jet}, $p_{\mathrm{T}}(\text{ISR})$, $p_{\mathrm{T}}(b)$, H_{T}, $N(b^{\text{loose}})$, $\Delta R(\ell, b)$, $D(b)$. The systematic uncertainties in the background are quadratically added to the statistical uncertainty when calculating the Data/MC ratio.

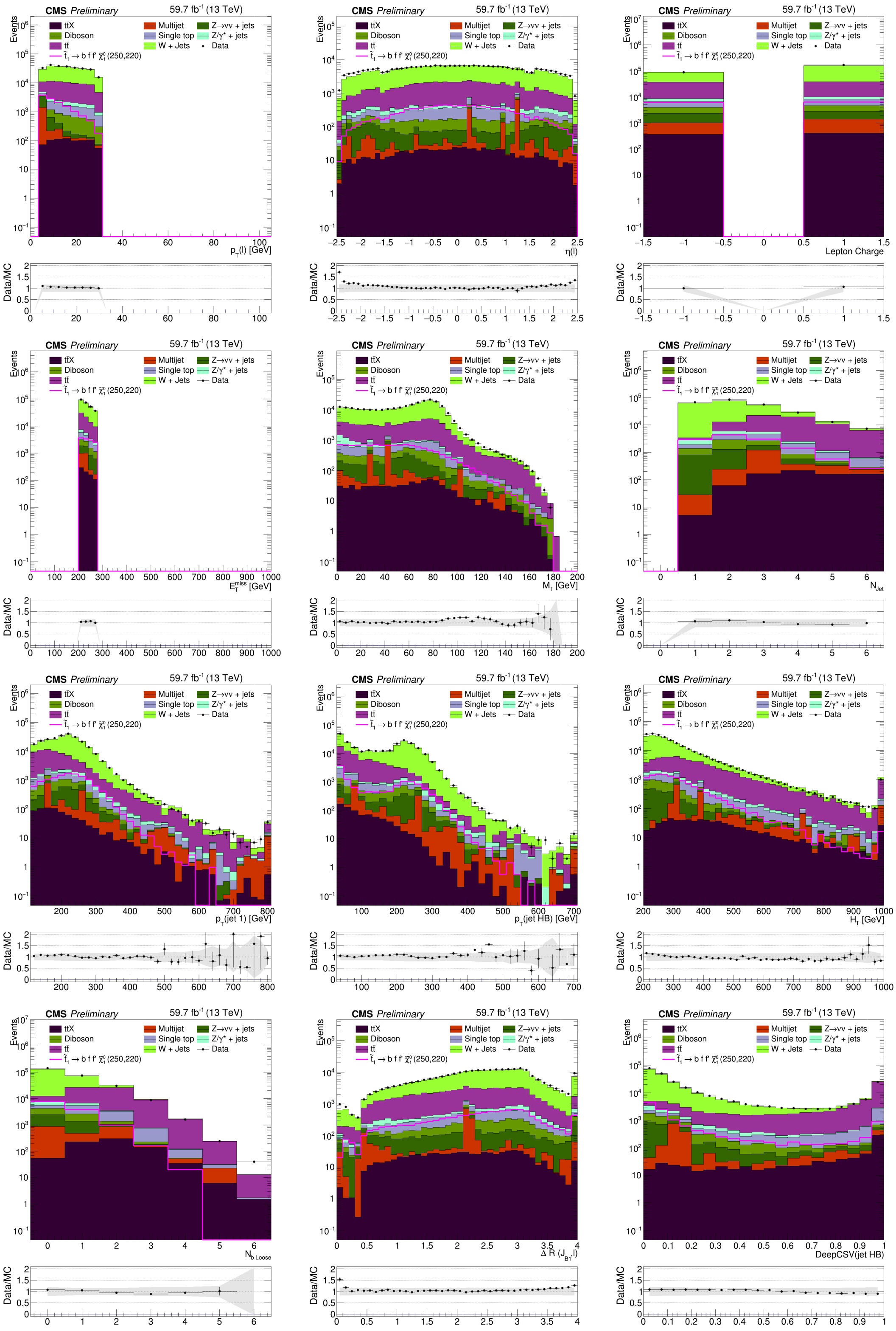

Figure C.9: Data and expected MC contributions for different variables in both final states and for L=59.7 fb^{-1} in the VR2 region. Starting from top-left to bottom-right: $p_{\mathrm{T}}(\ell)$, $\eta(\ell)$, $Q(\ell)$, $p_{\mathrm{T}}^{\mathrm{miss}}$, m_{T} , N_{jet}, $p_{\mathrm{T}}(\mathrm{ISR})$, $p_{\mathrm{T}}(b)$, H_{T}, $N(b^{\text{loose}})$, $\Delta R(\ell, b)$, $D(b)$. The systematic uncertainties in the background are quadratically added to the statistical uncertainty when calculating the Data/MC ratio.

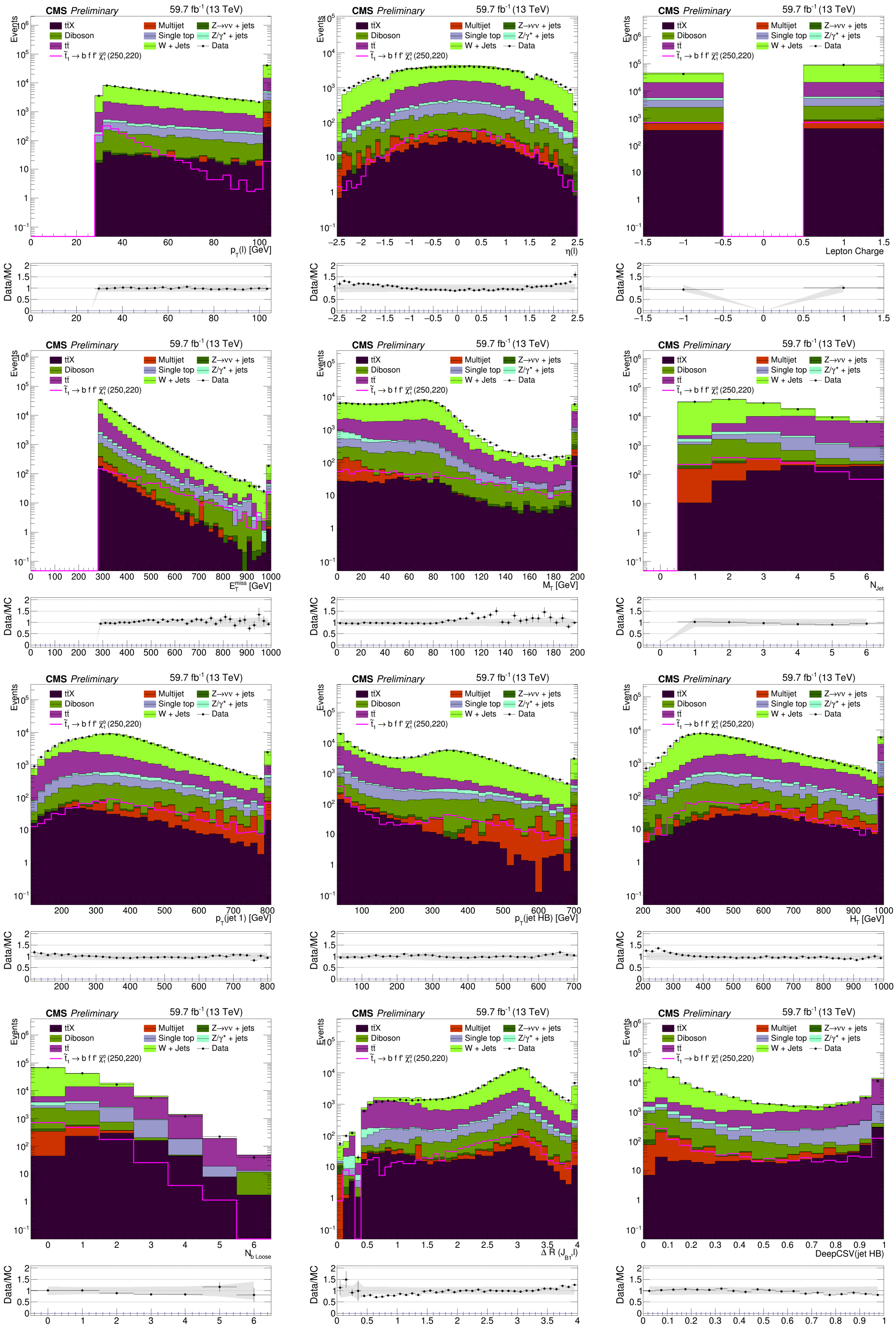

Figure C.10: Data and expected MC contributions for different variables in both final states and for L=59.7 fb^{-1} in the VR3 region. Starting from top-left to bottom-right: $p_{\mathrm{T}}(\ell)$, $\eta(\ell)$, $Q(\ell)$, $p_{\mathrm{T}}^{\mathrm{miss}}$, m_{T} , N_{jet}, $p_{\mathrm{T}}(\mathrm{ISR})$, $p_{\mathrm{T}}(b)$, H_{T}, $N(b^{\text{loose}})$, $\Delta R(\ell, b)$, $D(b)$. The systematic uncertainties in the background are quadratically added to the statistical uncertainty when calculating the Data/MC ratio.

C.4 BDT output for different Δm for validation

Figures C.11– C.14 show the BDTs output for all the VRs of all Δm regions.

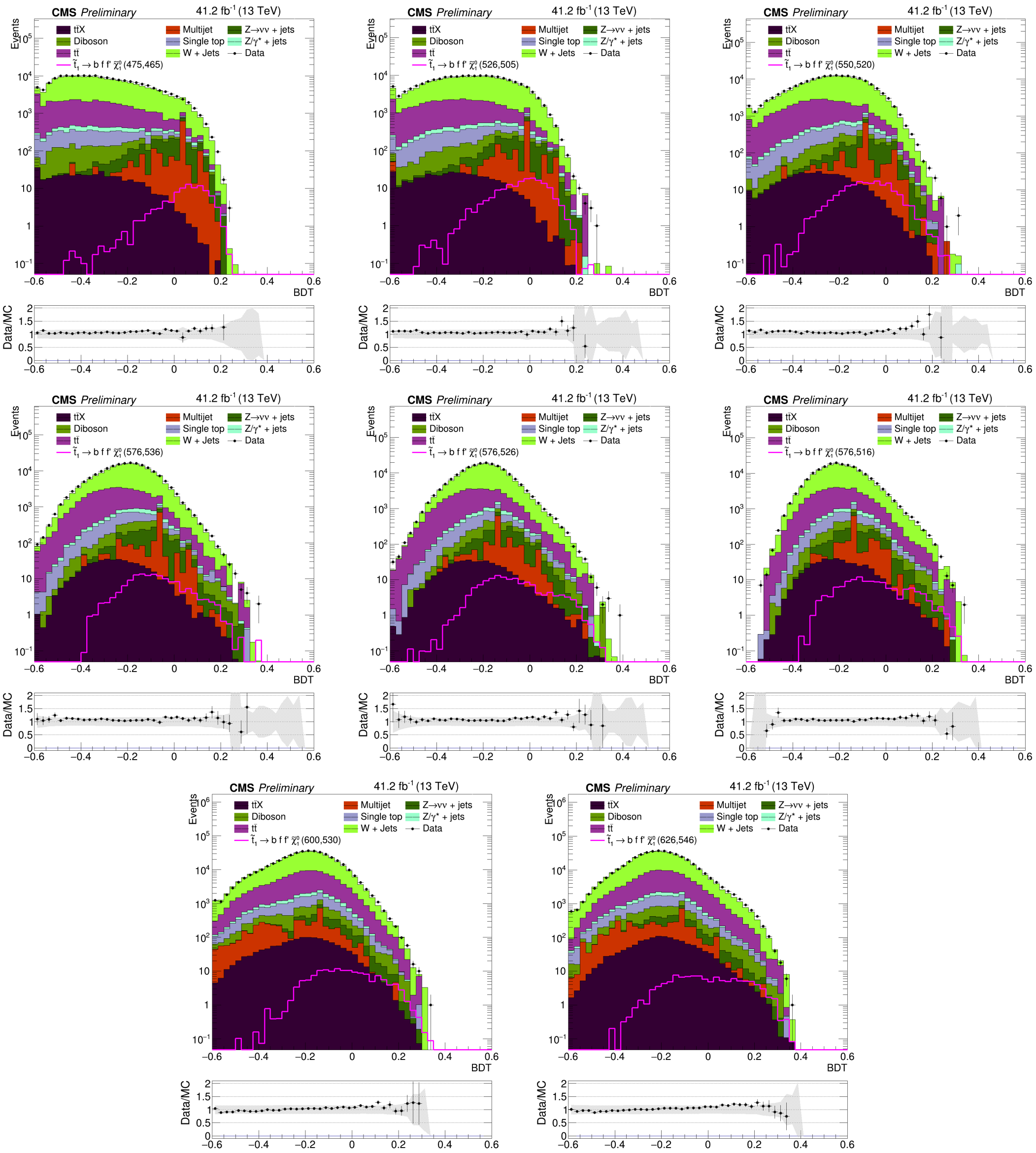

Figure C.11: 2017 Data and expected MC contributions for the BDT output for L=41.2 fb^{-1} at the preselection level, in the VR2 region. From top-left to bottom-right, plots show the BDT output for Δm = 10, 20, 30, 40, 50, 60, 70 and 80 GeV.

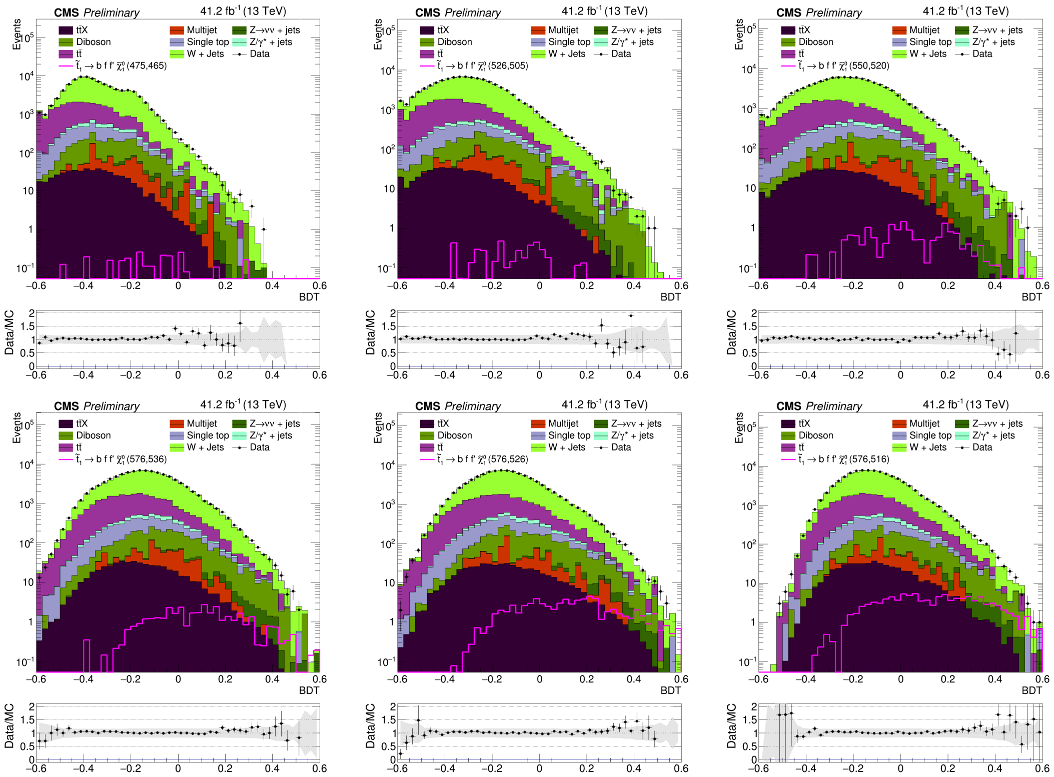

Figure C.12: 2017 Data and expected MC contributions for the BDT output for L=41.2 fb^{-1} at the preselection level, in the VR3 region. From top-left to bottom-right, plots show the BDT output for Δm = 10, 20, 30, 40, 50 and 60 GeV.

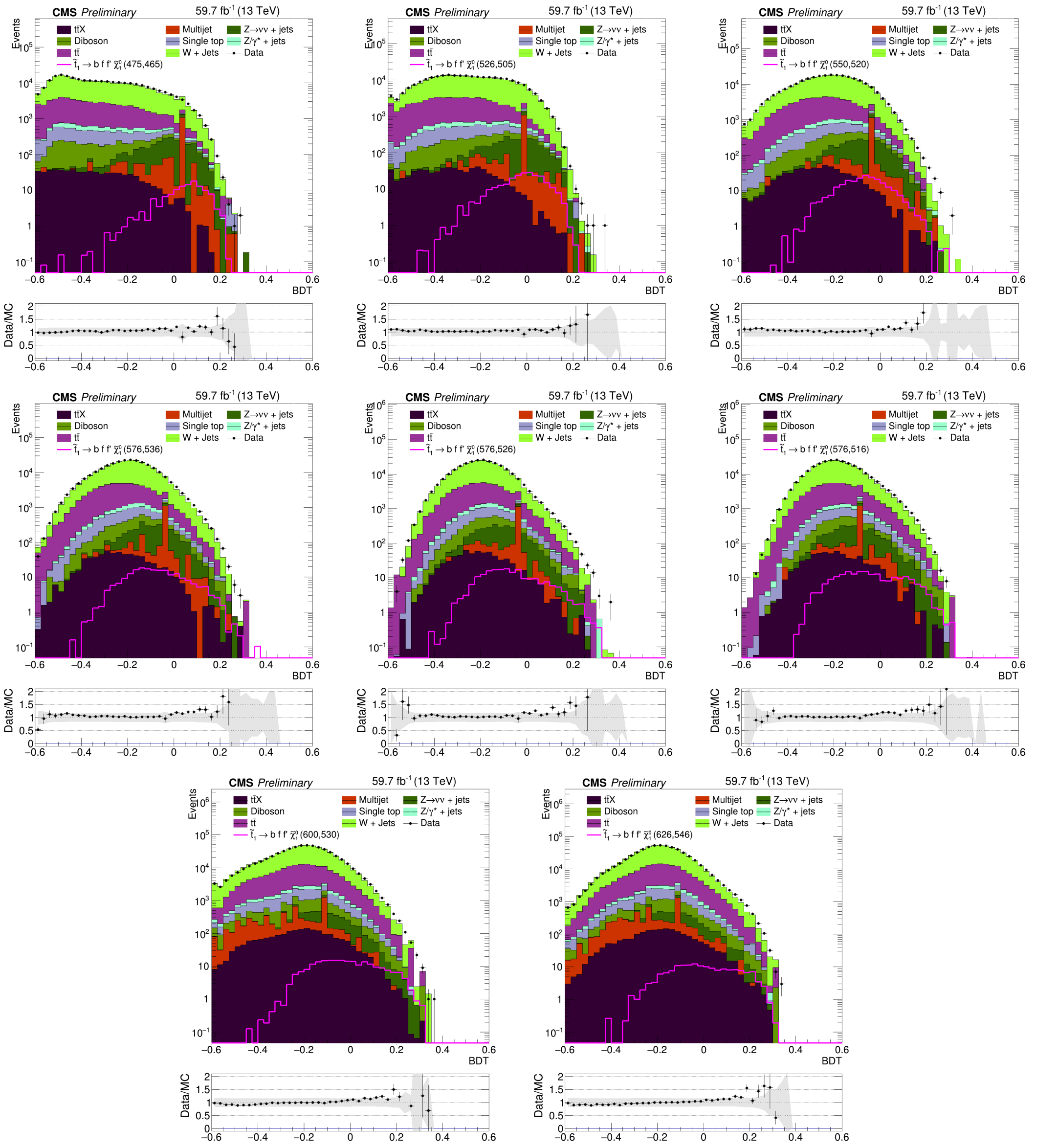

Figure C.13: 2018 Data and expected MC contributions for the BDT output for L=59.7 fb^{-1} at the preselection level, in the VR2 region. From top-left to bottom-right, plots show the BDT output for Δm = 10, 20, 30, 40, 50, 60, 70 and 80 GeV.

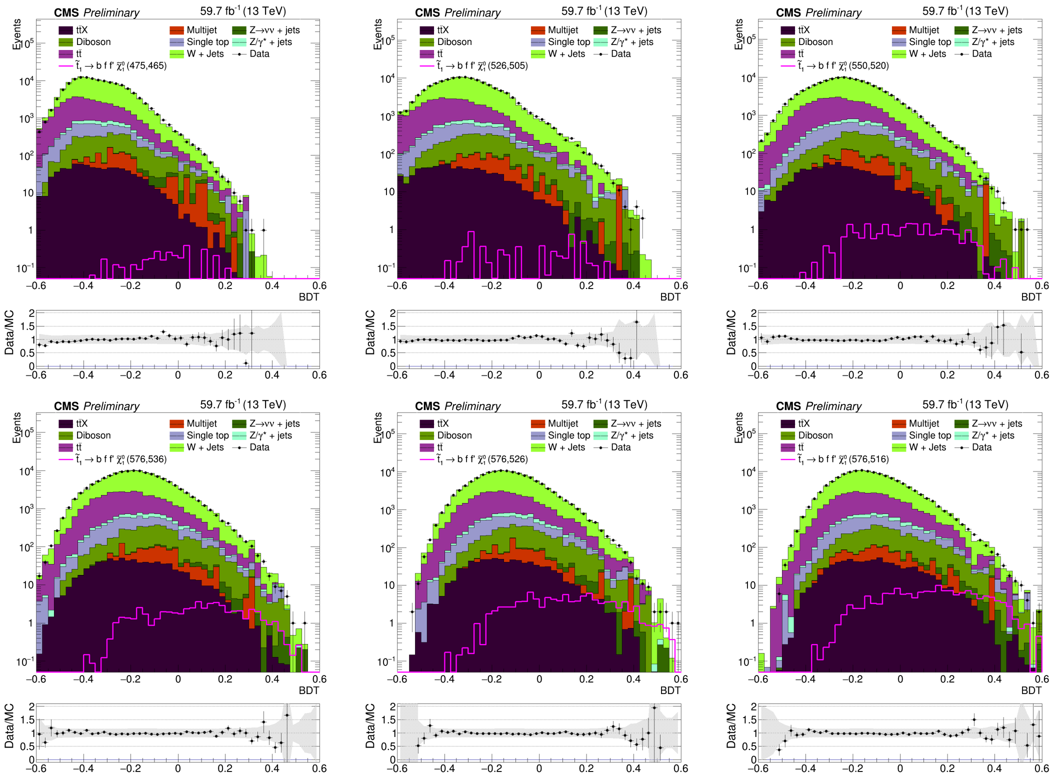

Figure C.14: 2018 Data and expected MC contributions for the BDT output for L=59.7 fb^{-1} at the preselection level, in the VR3 region. From top-left to bottom-right, plots show the BDT output for Δm = 10, 20, 30, 40, 50 and 60 GeV.

C.5 Raw closure test for the prediction of the background with a nonprompt lepton

In order to test the closure of the method and associate a systematic uncertainty to it, the difference $Diff$, between the predicted background contribution with a nonprompt lepton $Y_{\mathrm{np}}^{\mathrm{SR}}$, and the nonprompt leptons that pass the tight requirement, $N_{Tight}^{SR}(np)$, is measured:

$$Diff = \quad Y_{\mathrm{np}}^{\mathrm{SR}} - N_{Tight}^{SR}(np) \tag{C.1}$$

To measure the systematic uncertainty of the closure method, the statistical uncertainty of $Diff$, σ_{Diff}, and the precision of the nonprompt leptons prediction method $\sigma_{Y_{\mathrm{np}}^{\mathrm{SR}}}$ are taken into account. To be conservative, the maximum between both quantities is taken as the systematic uncertainty of the closure method:

$$\delta^2_{RawClosure} = Max(Diff^2 - \sigma^2_{Diff}, \sigma^2_{Y_{\mathrm{np}}^{\mathrm{SR}}}), \tag{C.2}$$

where the term σ^2_{Diff} is subtracted to $Diff^2$ in order to account for the precision associated with the measurement of $Diff$. The term $\sigma_{Y_{\mathrm{np}}^{\mathrm{SR}}}$ is the inherent uncertainty in the nonprompt background prediction method. Tables C.1 and C.2 summarize the relative systematic uncertainty of the closure for all Δm regions for 2017 and 2018 respectively.

Table C.1: 2017: Simulated events for an integrated luminosity of $41.2 fb^{-1}$. In each Δm region, the number $N_{Tight}^{SR}(np)$ of events with a *tight* non-prompt lepton passing the final selection is compared to the number of events predicted by data-driven method in the same SR. The ensuing percentual disagreement is calculated.

Δm (GeV)	$N_{Tight}^{SR}(np)$	$Y_{\mathrm{np}}^{\mathrm{SR}}$	Raw Closure
10	23.84 ± 1.51	23.65 ± 1.09	4.6 %
20	46.38 ± 2.19	46.06 ± 1.63	3.5 %
30	36.91 ± 2.00	39.05 ± 1.62	4.1 %
40	25.90 ± 1.63	30.34 ± 3.42	11.3 %
50	15.78 ± 1.26	18.06 ± 1.09	8.6 %
60	7.54 ± 0.83	8.25 ± 0.70	8.5 %
70	8.95 ± 0.92	10.46 ± 0.76	9.0 %
80	5.13 ± 0.68	6.45 ± 0.62	14.6 %

To compute the relative systematic uncertainty due to the closure of the method, the relative systematic uncertainty of the non-universality of ϵ_{TL} is taken into account as shown in tables 7.1 and 7.2 (in the Lepton universality column). When performing the raw closure test, the central value of ϵ_{TL} is used without taking into account its systematic uncertainty from Table 6.1. Therefore, the precision of the raw closure test is constrained by the relative systematic uncertainty of the ϵ_{TL} due to the lepton non-universality. The latter uncertainty is defined as $\delta_{LeptonUniversality}$, and the uncertainty due to the closure of the method as $\delta_{Closure}$:

$$\delta^2_{Closure} = Max(\delta^2_{RawClosure} - \delta^2_{LeptonUniversality}, 0) \tag{C.3}$$

Table C.2: 2018: Simulated events for an integrated luminosity of $59.7fb^{-1}$. In each Δm region, the number $N^{SR}_{Tight}(np)$ of events with a *tight* non-prompt lepton passing the final selection is compared to the number of events predicted by data-driven method in the same SR. The ensuing percentual disagreement is calculated.

Δm (GeV)	$N^{SR}_{Tight}(np)$	$Y^{\rm SR}_{\rm np}$	Raw Closure
10	47.82 ± 2.94	54.01 ± 2.16	9.26 %
20	39.80 ± 2.23	39.57 ± 1.57	3.96 %
30	67.10 ± 3.26	67.54 ± 2.36	3.49 %
40	31.86 ± 2.29	33.27 ± 1.50	4.51 %
50	21.10 ± 1.63	21.06 ± 1.23	5.84 %
60	25.94 ± 1.77	28.55 ± 1.42	4.96 %
70	23.23 ± 1.98	23.40 ± 1.32	5.62 %
80	9.49 ± 1.16	10.75 ± 0.88	8.18 %

The relative systematic uncertainty from equation C.3 is added to complete the tables 7.1 and 7.2 (in the Closure column).

C.6 Test of the prediction of $W+$jets and $t\bar{t}$ for different Δm

As can be observed, from Tables C.3 to C.58, across different selection tools (i.e. BDT trainings) and different validation regions (with different background composition and kinematics), the number of predicted background events in the SR is most of the time compatible with the number of observed data events in the corresponding VR within one standard deviation. The systematic error ascribed to the prediction of the background $N^{SR}_{DDprompt}(X)$ is based on the difference between the prediction and observed number of data events in the signal region of the VR, and is developed in Chapter 7.

Table C.3: 2017 validation in the VR1 region for the case Δm = 10. Number of observed data events and simulated events in the control region CR(W+jets), within the validation region VR1. Number of simulated events and number of estimated W+jets events in the signal region within the VR1. The number of simulated rare events is also provided to calculate the number of expected total background and compare it with the observed data events. The contribution of the $t\bar{t}$ background is included in $N^{SR}(Other)$. The uncertainty in the estimated yield is statistical only.

	$N^{CR}(W+jets)$		$N^{CR}(Other)$		$N^{CR}(Data)$
CR(W+jets)	91461 ± 423		7202 ± 152		102524 ± 320
	$N^{SR}(W+jets)$	$Y_{\text{p}}^{\text{SR}}(W+jets)$	$N^{SR}(Other)$	$N^{SR}(Predicted)$	$N^{SR}(Data)$
SR(W+jets)	5477.3 ± 103.4	5708.5 ± 112.9	2337.0 ± 1143.3	8045.5 ± 1148.8	7500 ± 87

Table C.4: 2017 validation in the VR1 region for the case Δm = 20. Number of observed data events and simulated events in the control region CR(W+jets), within the validation region VR1. Number of simulated events and number of estimated W+jets events in the signal region within the VR1. The number of simulated rare events is also provided to calculate the number of expected total background and compare it with the observed data events. The contribution of the $t\bar{t}$ background is included in $N^{SR}(Other)$. The uncertainty in the estimated yield is statistical only.

	$N^{CR}(W+jets)$		$N^{CR}(Other)$		$N^{CR}(Data)$
CR(W+jets)	91207 ± 423		8321 ± 1151		102373 ± 320
	$N^{SR}(W+jets)$	$Y_{\text{p}}^{\text{SR}}(W+jets)$	$N^{SR}(Other)$	$N^{SR}(Predicted)$	$N^{SR}(Data)$
SR(W+jets)	5731.1 ± 103.3	5909.9 ± 133.1	1217.8 ± 78.5	7127.7 ± 154.5	7651 ± 87

Table C.5: 2017 validation in the VR1 region for the case Δm = 30. Number of observed data events and simulated events in the control region CR(W+jets), within the validation region VR1. Number of simulated events and number of estimated W+jets events in the signal region within the VR1. The number of simulated rare events is also provided to calculate the number of expected total background and compare it with the observed data events. The contribution of the $t\bar{t}$ background is included in $N^{SR}(Other)$. The uncertainty in the estimated yield is statistical only.

	$N^{CR}(W+jets)$		$N^{CR}(Other)$		$N^{CR}(Data)$
CR(W+jets)	92972 ± 427		8493 ± 1150		104355 ± 323
	$N^{SR}(W+jets)$	$Y_{\text{p}}^{\text{SR}}(W+jets)$	$N^{SR}(Other)$	$N^{SR}(Predicted)$	$N^{SR}(Data)$
SR(W+jets)	3967.1 ± 86.2	4090.4 ± 104.1	1045.6 ± 85.1	5136.0 ± 134.5	5669 ± 75

Table C.6: 2017 validation in the VR1 region for the case Δm = 40. Number of observed data events and simulated events in the control region CR(*W*+jets), within the validation region VR1. Number of simulated events and number of estimated *W*+jets events in the signal region within the VR1. The number of simulated rare events is also provided to calculate the number of expected total background and compare it with the observed data events. The contribution of the $t\bar{t}$ background is included in $N^{SR}(Other)$. The uncertainty in the estimated yield is statistical only.

	$N^{CR}(W + jets)$		$N^{CR}(Other)$		$N^{CR}(Data)$
CR(*W*+jets)	93768 ± 429		8680 ± 1151		105536 ± 325
	$N^{SR}(W + jets)$	$Y_{\text{p}}^{\text{SR}}(W + jets)$	$N^{SR}(Other)$	$N^{SR}(Predicted)$	$N^{SR}(Data)$
SR(*W*+jets)	3170.5 ± 76.4	3274.9 ± 89.9	858.3 ± 78.2	4133.2 ± 119.2	4488 ± 67

Table C.7: 2017 validation in the VR1 region for the case Δm = 50. Number of observed data events and simulated events in the control region CR(*W*+jets), within the validation region VR1. Number of simulated events and number of estimated *W*+jets events in the signal region within the VR1. The number of simulated rare events is also provided to calculate the number of expected total background and compare it with the observed data events. The contribution of the $t\bar{t}$ background is included in $N^{SR}(Other)$. The uncertainty in the estimated yield is statistical only.

	$N^{CR}(W + jets)$		$N^{CR}(Other)$		$N^{CR}(Data)$
CR(*W*+jets)	93790 ± 429		8715 ± 1151		105538 ± 325
	$N^{SR}(W + jets)$	$Y_{\text{p}}^{\text{SR}}(W + jets)$	$N^{SR}(Other)$	$N^{SR}(Predicted)$	$N^{SR}(Data)$
SR(*W*+jets)	3149.1 ± 75.7	3250.9 ± 89.1	824.1 ± 67.3	4075.0 ± 111.7	4486 ± 67

Table C.8: 2017 validation in the VR1 region for the case Δm = 60. Number of observed data events and simulated events in the control region CR(*W*+jets), within the validation region VR1. Number of simulated events and number of estimated *W*+jets events in the signal region within the VR1. The number of simulated rare events is also provided to calculate the number of expected total background and compare it with the observed data events. The contribution of the $t\bar{t}$ background is included in $N^{SR}(Other)$. The uncertainty in the estimated yield is statistical only.

	$N^{CR}(W + jets)$		$N^{CR}(Other)$		$N^{CR}(Data)$
CR(*W*+jets)	93127 ± 427		8632 ± 1151		104731 ± 324
	$N^{SR}(W + jets)$	$Y_{\text{p}}^{\text{SR}}(W + jets)$	$N^{SR}(Other)$	$N^{SR}(Predicted)$	$N^{SR}(Data)$
SR(*W*+jets)	3812.0 ± 86.0	3933.7 ± 102.9	907.2 ± 69.9	4840.9 ± 124.4	5293 ± 73

Table C.9: 2017 validation in the VR1 region for the case Δm = 70. Number of observed data events and simulated events in the control region CR(*W*+jets), within the validation region VR1. Number of simulated events and number of estimated *W*+jets events in the signal region within the VR1. The number of simulated rare events is also provided to calculate the number of expected total background and compare it with the observed data events. The contribution of the $t\bar{t}$ background is included in $N^{SR}(Other)$. The uncertainty in the estimated yield is statistical only.

	$N^{CR}(W + jets)$		$N^{CR}(Other)$		$N^{CR}(Data)$
CR(*W*+jets)	207907 ± 588		20003 ± 1171		230221 ± 480
	$N^{SR}(W + jets)$	$Y_{\text{p}}^{\text{SR}}(W + jets)$	$N^{SR}(Other)$	$N^{SR}(Predicted)$	$N^{SR}(Data)$
SR(*W*+jets)	7548.1 ± 113.3	7632.0 ± 125.3	1841.2 ± 93.3	9473.2 ± 156.2	10553 ± 103

Table C.10: 2017 validation in the VR1 region for the case Δm = 80. Number of observed data events and simulated events in the control region CR(W+jets), within the validation region VR1. Number of simulated events and number of estimated W+jets events in the signal region within the VR1. The number of simulated rare events is also provided to calculate the number of expected total background and compare it with the observed data events. The contribution of the $t\bar{t}$ background is included in $N^{SR}(Other)$. The uncertainty in the estimated yield is statistical only.

	$N^{CR}(W + jets)$		$N^{CR}(Other)$		$N^{CR}(Data)$
CR(W+jets)	206609 ± 586		19708 ± 1170		228182 ± 478
	$N^{SR}(W + jets)$	$Y_{\text{p}}^{\text{SR}}(W + jets)$	$N^{SR}(Other)$	$N^{SR}(Predicted)$	$N^{SR}(Data)$
SR(W+jets)	8845.5 ± 121.9	8925.3 ± 136.7	2136.6 ± 98.4	11061.9 ± 168.5	12592 ± 112

Table C.11: 2017 validation in the VR1 region for the case Δm = 10. Number of observed data events and simulated events in the control region CR($t\bar{t}$), within the validation region VR1. Number of simulated events and number of estimated $t\bar{t}$ events in the signal region within the VR1. The number of simulated rare events is also provided to calculate the number of expected total background and compare it with the observed data events. The contribution of the W+jets background is included in $N^{SR}(Other)$. The uncertainty in the estimated yield is statistical only.

	$N^{CR}(t\bar{t})$		$N^{CR}(Other)$		$N^{CR}(Data)$
CR($t\bar{t}$)	21217 ± 270		5684 ± 562		28750 ± 170
	$N^{SR}(t\bar{t})$	$Y_{\text{p}}^{\text{SR}}(t\bar{t})$	$N^{SR}(Other)$	$N^{SR}(Predicted)$	$N^{SR}(Data)$
SR($t\bar{t}$)	7.1 ± 4.1	7.8 ± 4.5	11.3 ± 4.0	19.0 ± 6.0	13 ± 4

Table C.12: 2017 validation in the VR1 region for the case Δm = 20. Number of observed data events and simulated events in the control region CR($t\bar{t}$), within the validation region VR1. Number of simulated events and number of estimated $t\bar{t}$ events in the signal region within the VR1. The number of simulated rare events is also provided to calculate the number of expected total background and compare it with the observed data events. The contribution of the W+jets background is included in $N^{SR}(Other)$. The uncertainty in the estimated yield is statistical only.

	$N^{CR}(t\bar{t})$		$N^{CR}(Other)$		$N^{CR}(Data)$
CR($t\bar{t}$)	21139 ± 269		5629 ± 562		28605 ± 169
	$N^{SR}(t\bar{t})$	$Y_{\text{p}}^{\text{SR}}(t\bar{t})$	$N^{SR}(Other)$	$N^{SR}(Predicted)$	$N^{SR}(Data)$
SR($t\bar{t}$)	87.7 ± 14.9	95.3 ± 16.5	66.6 ± 11.0	161.9 ± 19.8	158 ± 13

Table C.13: 2017 validation in the VR1 region for the case Δm = 30. Number of observed data events and simulated events in the control region CR($t\bar{t}$), within the validation region VR1. Number of simulated events and number of estimated $t\bar{t}$ events in the signal region within the VR1. The number of simulated rare events is also provided to calculate the number of expected total background and compare it with the observed data events. The contribution of the W+jets background is included in $N^{SR}(Other)$. The uncertainty in the estimated yield is statistical only.

	$N^{CR}(t\bar{t})$		$N^{CR}(Other)$		$N^{CR}(Data)$
CR($t\bar{t}$)	21149 ± 269		5646 ± 562		28653 ± 169
	$N^{SR}(t\bar{t})$	$Y_{\text{p}}^{\text{SR}}(t\bar{t})$	$N^{SR}(Other)$	$N^{SR}(Predicted)$	$N^{SR}(Data)$
SR($t\bar{t}$)	75.4 ± 14.1	82.0 ± 15.5	49.6 ± 7.6	131.7 ± 17.2	110 ± 10

Table C.14: 2017 validation in the VR1 region for the case Δm = 40. Number of observed data events and simulated events in the control region CR($t\bar{t}$), within the validation region VR1. Number of simulated events and number of estimated $t\bar{t}$ events in the signal region within the VR1. The number of simulated rare events is also provided to calculate the number of expected total background and compare it with the observed data events. The contribution of the W+jets background is included in $N^{SR}(Other)$. The uncertainty in the estimated yield is statistical only.

	$N^{CR}(t\bar{t})$		$N^{CR}(Other)$		$N^{CR}(Data)$
CR($t\bar{t}$)	21039 ± 269		5615 ± 562		28563 ± 169
	$N^{SR}(t\bar{t})$	$Y_{\mathrm{p}}^{\mathrm{SR}}(t\bar{t})$	$N^{SR}(Other)$	$N^{SR}(Predicted)$	$N^{SR}(Data)$
SR($t\bar{t}$)	185.1 ± 22.7	201.8 ± 25.4	80.8 ± 10.5	282.7 ± 27.5	200 ± 14

Table C.15: 2017 validation in the VR1 region for the case Δm = 50. Number of observed data events and simulated events in the control region CR($t\bar{t}$), within the validation region VR1. Number of simulated events and number of estimated $t\bar{t}$ events in the signal region within the VR1. The number of simulated rare events is also provided to calculate the number of expected total background and compare it with the observed data events. The contribution of the W+jets background is included in $N^{SR}(Other)$. The uncertainty in the estimated yield is statistical only.

	$N^{CR}(t\bar{t})$		$N^{CR}(Other)$		$N^{CR}(Data)$
CR($t\bar{t}$)	20934 ± 268		5573 ± 562		28372 ± 168
	$N^{SR}(t\bar{t})$	$Y_{\mathrm{p}}^{\mathrm{SR}}(t\bar{t})$	$N^{SR}(Other)$	$N^{SR}(Predicted)$	$N^{SR}(Data)$
SR($t\bar{t}$)	290.6 ± 30.6	316.5 ± 34.5	122.6 ± 12.3	439.1 ± 36.6	391 ± 20

Table C.16: 2017 validation in the VR1 region for the case Δm = 60. Number of observed data events and simulated events in the control region CR($t\bar{t}$), within the validation region VR1. Number of simulated events and number of estimated $t\bar{t}$ events in the signal region within the VR1. The number of simulated rare events is also provided to calculate the number of expected total background and compare it with the observed data events. The contribution of the W+jets background is included in $N^{SR}(Other)$. The uncertainty in the estimated yield is statistical only.

	$N^{CR}(t\bar{t})$		$N^{CR}(Other)$		$N^{CR}(Data)$
CR($t\bar{t}$)	20807 ± 267		5537 ± 562		28236 ± 168
	$N^{SR}(t\bar{t})$	$Y_{\mathrm{p}}^{\mathrm{SR}}(t\bar{t})$	$N^{SR}(Other)$	$N^{SR}(Predicted)$	$N^{SR}(Data)$
SR($t\bar{t}$)	417.3 ± 36.2	455.3 ± 41.6	158.4 ± 14.0	613.7 ± 43.9	527 ± 23

Table C.17: 2017 validation in the VR1 region for the case Δm = 70. Number of observed data events and simulated events in the control region CR($t\bar{t}$), within the validation region VR1. Number of simulated events and number of estimated $t\bar{t}$ events in the signal region within the VR1. The number of simulated rare events is also provided to calculate the number of expected total background and compare it with the observed data events. The contribution of the W+jets background is included in $N^{SR}(Other)$. The uncertainty in the estimated yield is statistical only.

	$N^{CR}(t\bar{t})$		$N^{CR}(Other)$		$N^{CR}(Data)$
CR($t\bar{t}$)	54266 ± 438		13185 ± 571		67446 ± 260
	$N^{SR}(t\bar{t})$	$Y_{\mathrm{p}}^{\mathrm{SR}}(t\bar{t})$	$N^{SR}(Other)$	$N^{SR}(Predicted)$	$N^{SR}(Data)$
SR($t\bar{t}$)	1601.1 ± 78.4	1600.9 ± 81.6	361.9 ± 18.7	1962.9 ± 83.7	2085 ± 46

Table C.18: 2017 validation in the VR1 region for the case Δm = 80. Number of observed data events and simulated events in the control region CR($t\bar{t}$), within the validation region VR1. Number of simulated events and number of estimated $t\bar{t}$ events in the signal region within the VR1. The number of simulated rare events is also provided to calculate the number of expected total background and compare it with the observed data events. The contribution of the W+jets background is included in $N^{SR}(Other)$. The uncertainty in the estimated yield is statistical only.

	$N^{CR}(t\bar{t})$		$N^{CR}(Other)$		$N^{CR}(Data)$
CR($t\bar{t}$)	54006 ± 436		13190 ± 571		67144 ± 259
	$N^{SR}(t\bar{t})$	$Y_p^{SR}(t\bar{t})$	$N^{SR}(Other)$	$N^{SR}(Predicted)$	$N^{SR}(Data)$
SR($t\bar{t}$)	1860.6 ± 84.8	1858.8 ± 88.7	357.0 ± 17.7	2215.8 ± 90.5	2387 ± 49

Table C.19: 2017 validation in the VR2 region for the case Δm = 10. Number of observed data events and simulated events in the control region CR(W+jets), within the validation region VR2. Number of simulated events and number of estimated W+jets events in the signal region within the VR2. The number of simulated rare events is also provided to calculate the number of expected total background and compare it with the observed data events. The contribution of the $t\bar{t}$ background is included in $N^{SR}(Other)$. The uncertainty in the estimated yield is statistical only.

	$N^{CR}(W+jets)$		$N^{CR}(Other)$		$N^{CR}(Data)$
CR(W+jets)	47662 ± 178		4968 ± 143		53205 ± 231
	$N^{SR}(W+jets)$	$Y_p^{SR}(W+jets)$	$N^{SR}(Other)$	$N^{SR}(Predicted)$	$N^{SR}(Data)$
SR(W+jets)	350.5 ± 8.2	354.7 ± 8.6	74.5 ± 10.7	429.2 ± 13.7	500 ± 22

Table C.20: 2017 validation in the VR2 region for the case Δm = 20. Number of observed data events and simulated events in the control region CR(W+jets), within the validation region VR2. Number of simulated events and number of estimated W+jets events in the signal region within the VR2. The number of simulated rare events is also provided to calculate the number of expected total background and compare it with the observed data events. The contribution of the $t\bar{t}$ background is included in $N^{SR}(Other)$. The uncertainty in the estimated yield is statistical only.

	$N^{CR}(W+jets)$		$N^{CR}(Other)$		$N^{CR}(Data)$
CR(W+jets)	46583 ± 178		4750 ± 141		51808 ± 228
	$N^{SR}(W+jets)$	$Y_p^{SR}(W+jets)$	$N^{SR}(Other)$	$N^{SR}(Predicted)$	$N^{SR}(Data)$
SR(W+jets)	1429.9 ± 18.7	1444.5 ± 21.3	292.3 ± 24.0	1736.8 ± 32.1	1897 ± 44

Table C.21: 2017 validation in the VR2 region for the case Δm = 30. Number of observed data events and simulated events in the control region CR(W+jets), within the validation region VR2. Number of simulated events and number of estimated W+jets events in the signal region within the VR2. The number of simulated rare events is also provided to calculate the number of expected total background and compare it with the observed data events. The contribution of the $t\bar{t}$ background is included in $N^{SR}(Other)$. The uncertainty in the estimated yield is statistical only.

	$N^{CR}(W+jets)$		$N^{CR}(Other)$		$N^{CR}(Data)$
CR(W+jets)	44121 ± 175		4209 ± 136		48713 ± 221
	$N^{SR}(W+jets)$	$Y_p^{SR}(W+jets)$	$N^{SR}(Other)$	$N^{SR}(Predicted)$	$N^{SR}(Data)$
SR(W+jets)	3891.1 ± 35.4	3924.8 ± 45.1	832.9 ± 46.9	4757.8 ± 65.1	4992 ± 71

Table C.22: 2017 validation in the VR2 region for the case Δm = 40. Number of observed data events and simulated events in the control region CR(*W*+jets), within the validation region VR2. Number of simulated events and number of estimated *W*+jets events in the signal region within the VR2. The number of simulated rare events is also provided to calculate the number of expected total background and compare it with the observed data events. The contribution of the $t\bar{t}$ background is included in $N^{SR}(Other)$. The uncertainty in the estimated yield is statistical only.

	$N^{CR}(W + jets)$		$N^{CR}(Other)$		$N^{CR}(Data)$
CR(*W*+jets)	39793 ± 171		3475 ± 128		43898 ± 210
	$N^{SR}(W + jets)$	$Y_{\mathrm{p}}^{\mathrm{SR}}(W + jets)$	$N^{SR}(Other)$	$N^{SR}(Predicted)$	$N^{SR}(Data)$
SR(*W*+jets)	8219.3 ± 51.1	8349.5 ± 81.0	1567.5 ± 63.7	9916.9 ± 103.0	9807 ± 99

Table C.23: 2017 validation in the VR2 region for the case Δm = 50. Number of observed data events and simulated events in the control region CR(*W*+jets), within the validation region VR2. Number of simulated events and number of estimated *W*+jets events in the signal region within the VR2. The number of simulated rare events is also provided to calculate the number of expected total background and compare it with the observed data events. The contribution of the $t\bar{t}$ background is included in $N^{SR}(Other)$. The uncertainty in the estimated yield is statistical only.

	$N^{CR}(W + jets)$		$N^{CR}(Other)$		$N^{CR}(Data)$
CR(*W*+jets)	40277 ± 171		3393 ± 127		44216 ± 210
	$N^{SR}(W + jets)$	$Y_{\mathrm{p}}^{\mathrm{SR}}(W + jets)$	$N^{SR}(Other)$	$N^{SR}(Predicted)$	$N^{SR}(Data)$
SR(*W*+jets)	7735.4 ± 51.8	7840.3 ± 78.0	1649.6 ± 65.7	9489.9 ± 102.0	9489 ± 97

Table C.24: 2017 validation in the VR2 region for the case Δm = 60. Number of observed data events and simulated events in the control region CR(*W*+jets), within the validation region VR2. Number of simulated events and number of estimated *W*+jets events in the signal region within the VR2. The number of simulated rare events is also provided to calculate the number of expected total background and compare it with the observed data events. The contribution of the $t\bar{t}$ background is included in $N^{SR}(Other)$. The uncertainty in the estimated yield is statistical only.

	$N^{CR}(W + jets)$		$N^{CR}(Other)$		$N^{CR}(Data)$
CR(*W*+jets)	39081 ± 169		3178 ± 124		42822 ± 207
	$N^{SR}(W + jets)$	$Y_{\mathrm{p}}^{\mathrm{SR}}(W + jets)$	$N^{SR}(Other)$	$N^{SR}(Predicted)$	$N^{SR}(Data)$
SR(*W*+jets)	8932.0 ± 56.4	9060.8 ± 88.6	1864.4 ± 71.7	10925.2 ± 114.0	10883 ± 104

Table C.25: 2017 validation in the VR2 region for the case Δm = 10. Number of observed data events and simulated events in the control region CR($t\bar{t}$), within the validation region VR2. Number of simulated events and number of estimated $t\bar{t}$ events in the signal region within the VR2. The number of simulated rare events is also provided to calculate the number of expected total background and compare it with the observed data events. The contribution of the *W*+jets background is included in $N^{SR}(Other)$. The uncertainty in the estimated yield is statistical only.

	$N^{CR}(t\bar{t})$		$N^{CR}(Other)$		$N^{CR}(Data)$
CR($t\bar{t}$)	11596 ± 224		3701 ± 47		13475 ± 116
	$N^{SR}(t\bar{t})$	$Y_{\mathrm{p}}^{\mathrm{SR}}(t\bar{t})$	$N^{SR}(Other)$	$N^{SR}(Predicted)$	$N^{SR}(Data)$
SR($t\bar{t}$)	14.8 ± 7.6	12.5 ± 6.4	18.8 ± 2.1	31.3 ± 6.8	27 ± 5

Table C.26: 2017 validation in the VR2 region for the case Δm = 20. Number of observed data events and simulated events in the control region CR($t\bar{t}$), within the validation region VR2. Number of simulated events and number of estimated $t\bar{t}$ events in the signal region within the VR2. The number of simulated rare events is also provided to calculate the number of expected total background and compare it with the observed data events. The contribution of the W+jets background is included in $N^{SR}(Other)$. The uncertainty in the estimated yield is statistical only.

	$N^{CR}(t\bar{t})$		$N^{CR}(Other)$		$N^{CR}(Data)$
CR($t\bar{t}$)	11595 ± 224		3698 ± 47		13476 ± 116
	$N^{SR}(t\bar{t})$	$Y_{\mathrm{p}}^{\mathrm{SR}}(t\bar{t})$	$N^{SR}(Other)$	$N^{SR}(Predicted)$	$N^{SR}(Data)$
SR($t\bar{t}$)	16.5 ± 8.0	13.9 ± 6.8	21.8 ± 2.6	35.7 ± 7.3	26 ± 5

Table C.27: 2017 validation in the VR2 region for the case Δm = 30. Number of observed data events and simulated events in the control region CR($t\bar{t}$), within the validation region VR2. Number of simulated events and number of estimated $t\bar{t}$ events in the signal region within the VR2. The number of simulated rare events is also provided to calculate the number of expected total background and compare it with the observed data events. The contribution of the W+jets background is included in $N^{SR}(Other)$. The uncertainty in the estimated yield is statistical only.

	$N^{CR}(t\bar{t})$		$N^{CR}(Other)$		$N^{CR}(Data)$
CR($t\bar{t}$)	11448 ± 222		3574 ± 47		13240 ± 115
	$N^{SR}(t\bar{t})$	$Y_{\mathrm{p}}^{\mathrm{SR}}(t\bar{t})$	$N^{SR}(Other)$	$N^{SR}(Predicted)$	$N^{SR}(Data)$
SR($t\bar{t}$)	163.6 ± 29.5	138.1 ± 25.1	146.0 ± 7.3	284.1 ± 26.2	262 ± 16

Table C.28: 2017 validation in the VR2 region for the case Δm = 40. Number of observed data events and simulated events in the control region CR($t\bar{t}$), within the validation region VR2. Number of simulated events and number of estimated $t\bar{t}$ events in the signal region within the VR2. The number of simulated rare events is also provided to calculate the number of expected total background and compare it with the observed data events. The contribution of the W+jets background is included in $N^{SR}(Other)$. The uncertainty in the estimated yield is statistical only.

	$N^{CR}(t\bar{t})$		$N^{CR}(Other)$		$N^{CR}(Data)$
CR($t\bar{t}$)	11031 ± 218		3331 ± 45		12654 ± 112
	$N^{SR}(t\bar{t})$	$Y_{\mathrm{p}}^{\mathrm{SR}}(t\bar{t})$	$N^{SR}(Other)$	$N^{SR}(Predicted)$	$N^{SR}(Data)$
SR($t\bar{t}$)	579.9 ± 51.7	490.1 ± 45.2	388.9 ± 14.9	879.0 ± 47.6	848 ± 29

Table C.29: 2017 validation in the VR2 region for the case Δm = 50. Number of observed data events and simulated events in the control region CR($t\bar{t}$), within the validation region VR2. Number of simulated events and number of estimated $t\bar{t}$ events in the signal region within the VR2. The number of simulated rare events is also provided to calculate the number of expected total background and compare it with the observed data events. The contribution of the W+jets background is included in $N^{SR}(Other)$. The uncertainty in the estimated yield is statistical only.

	$N^{CR}(t\bar{t})$		$N^{CR}(Other)$		$N^{CR}(Data)$
CR($t\bar{t}$)	10667 ± 214		3207 ± 44		12146 ± 110
	$N^{SR}(t\bar{t})$	$Y_{\mathrm{p}}^{\mathrm{SR}}(t\bar{t})$	$N^{SR}(Other)$	$N^{SR}(Predicted)$	$N^{SR}(Data)$
SR($t\bar{t}$)	944.2 ± 67.6	791.3 ± 59.8	512.9 ± 17.2	1304.2 ± 62.2	1356 ± 37

Table C.30: 2017 validation in the VR2 region for the case Δm = 60. Number of observed data events and simulated events in the control region CR($t\bar{t}$), within the validation region VR2. Number of simulated events and number of estimated $t\bar{t}$ events in the signal region within the VR2. The number of simulated rare events is also provided to calculate the number of expected total background and compare it with the observed data events. The contribution of the *W*+jets background is included in $N^{SR}(Other)$. The uncertainty in the estimated yield is statistical only.

	$N^{CR}(t\bar{t})$		$N^{CR}(Other)$		$N^{CR}(Data)$
CR($t\bar{t}$)	10423 ± 211		3101 ± 43		11745 ± 108
	$N^{SR}(t\bar{t})$	$Y_{\mathrm{p}}^{\mathrm{SR}}(t\bar{t})$	$N^{SR}(Other)$	$N^{SR}(Predicted)$	$N^{SR}(Data)$
SR($t\bar{t}$)	1188.1 ± 76.9	985.4 ± 68.1	619.1 ± 18.5	1604.5 ± 71	1757 ± 42

Table C.31: 2018 validation in the VR1 region for the case Δm = 10. Number of observed data events and simulated events in the control region CR(W+jets), within the validation region VR1. Number of simulated events and number of estimated W+jets events in the signal region within the VR1. The number of simulated rare events is also provided to calculate the number of expected total background and compare it with the observed data events. The contribution of the $t\bar{t}$ background is included in $N^{SR}(Other)$. The uncertainty in the estimated yield is statistical only.

	$N^{CR}(W+jets)$		$N^{CR}(Other)$		$N^{CR}(Data)$
CR(W+jets)	121245 ± 545		9402 ± 167		133594 ± 366
	$N^{SR}(W+jets)$	$Y_{\mathrm{p}}^{\mathrm{SR}}(W+jets)$	$N^{SR}(Other)$	$N^{SR}(Predicted)$	$N^{SR}(Data)$
SR(W+jets)	7240.8 ± 130.0	7416.8 ± 139.4	2539.1 ± 1079.2	9955.9 ± 1088.2	9418 ± 97

Table C.32: 2018 validation in the VR1 region for the case Δm = 20. Number of observed data events and simulated events in the control region CR(W+jets), within the validation region VR1. Number of simulated events and number of estimated W+jets events in the signal region within the VR1. The number of simulated rare events is also provided to calculate the number of expected total background and compare it with the observed data events. The contribution of the $t\bar{t}$ background is included in $N^{SR}(Other)$. The uncertainty in the estimated yield is statistical only.

	$N^{CR}(W+jets)$		$N^{CR}(Other)$		$N^{CR}(Data)$
CR(W+jets)	118128 ± 538		10307 ± 1090		130476 ± 361
	$N^{SR}(W+jets)$	$Y_{\mathrm{p}}^{\mathrm{SR}}(W+jets)$	$N^{SR}(Other)$	$N^{SR}(Predicted)$	$N^{SR}(Data)$
SR(W+jets)	10358.5 ± 156.5	10537.4 ± 194.4	1634.4 ± 68.2	12171.8 ± 206.0	12536 ± 112

Table C.33: 2018 validation in the VR1 region for the case Δm = 30. Number of observed data events and simulated events in the control region CR(W+jets), within the validation region VR1. Number of simulated events and number of estimated W+jets events in the signal region within the VR1. The number of simulated rare events is also provided to calculate the number of expected total background and compare it with the observed data events. The contribution of the $t\bar{t}$ background is included in $N^{SR}(Other)$. The uncertainty in the estimated yield is statistical only.

	$N^{CR}(W+jets)$		$N^{CR}(Other)$		$N^{CR}(Data)$
CR(W+jets)	122667 ± 548		10740 ± 1090		135199 ± 368
	$N^{SR}(W+jets)$	$Y_{\mathrm{p}}^{\mathrm{SR}}(W+jets)$	$N^{SR}(Other)$	$N^{SR}(Predicted)$	$N^{SR}(Data)$
SR(W+jets)	5818.9 ± 116.8	5903.9 ± 133.1	1201.9 ± 62.8	7105.8 ± 147.2	7813 ± 88

Table C.34: 2018 validation in the VR1 region for the case Δm = 40. Number of observed data events and simulated events in the control region CR(W+jets), within the validation region VR1. Number of simulated events and number of estimated W+jets events in the signal region within the VR1. The number of simulated rare events is also provided to calculate the number of expected total background and compare it with the observed data events. The contribution of the $t\bar{t}$ background is included in $N^{SR}(Other)$. The uncertainty in the estimated yield is statistical only.

	$N^{CR}(W+jets)$		$N^{CR}(Other)$		$N^{CR}(Data)$
CR(W+jets)	123330 ± 549		10803 ± 1090		135576 ± 368
	$N^{SR}(W+jets)$	$Y_{\mathrm{p}}^{\mathrm{SR}}(W+jets)$	$N^{SR}(Other)$	$N^{SR}(Predicted)$	$N^{SR}(Data)$
SR(W+jets)	5156.4 ± 109.9	5216.7 ± 123.3	1138.8 ± 64.7	6355.5 ± 139.3	7436 ± 86

Table C.35: 2018 validation in the VR1 region for the case Δm = 50. Number of observed data events and simulated events in the control region CR(*W*+jets), within the validation region VR1. Number of simulated events and number of estimated *W*+jets events in the signal region within the VR1. The number of simulated rare events is also provided to calculate the number of expected total background and compare it with the observed data events. The contribution of the $t\bar{t}$ background is included in $N^{SR}(Other)$. The uncertainty in the estimated yield is statistical only.

	$N^{CR}(W + jets)$		$N^{CR}(Other)$		$N^{CR}(Data)$
CR(*W*+jets)	124630 ± 552		10974 ± 1090		137322 ± 371
	$N^{SR}(W + jets)$	$Y_{\mathrm{p}}^{\mathrm{SR}}(W + jets)$	$N^{SR}(Other)$	$N^{SR}(Predicted)$	$N^{SR}(Data)$
SR(*W*+jets)	3856.5 ± 93.4	3909.7 ± 102.6	967.7 ± 60.9	4877.4 ± 119.3	5690 ± 75

Table C.36: 2018 validation in the VR1 region for the case Δm = 60. Number of observed data events and simulated events in the control region CR(*W*+jets), within the validation region VR1. Number of simulated events and number of estimated *W*+jets events in the signal region within the VR1. The number of simulated rare events is also provided to calculate the number of expected total background and compare it with the observed data events. The contribution of the $t\bar{t}$ background is included in $N^{SR}(Other)$. The uncertainty in the estimated yield is statistical only.

	$N^{CR}(W + jets)$		$N^{CR}(Other)$		$N^{CR}(Data)$
CR(*W*+jets)	122916 ± 548		10698 ± 1090		134841 ± 367.207
	$N^{SR}(W + jets)$	$Y_{\mathrm{p}}^{\mathrm{SR}}(W + jets)$	$N^{SR}(Other)$	$N^{SR}(Predicted)$	$N^{SR}(Data)$
SR(*W*+jets)	5570.3 ± 115.1	5625.9 ± 129.8	1244.1 ± 68.9	6870.0 ± 147.0	8171 ± 90

Table C.37: 2018 validation in the VR1 region for the case Δm = 70. Number of observed data events and simulated events in the control region CR(*W*+jets), within the validation region VR1. Number of simulated events and number of estimated *W*+jets events in the signal region within the VR1. The number of simulated rare events is also provided to calculate the number of expected total background and compare it with the observed data events. The contribution of the $t\bar{t}$ background is included in $N^{SR}(Other)$. The uncertainty in the estimated yield is statistical only.

	$N^{CR}(W + jets)$		$N^{CR}(Other)$		$N^{CR}(Data)$
CR(*W*+jets)	274962 ± 763		25318 ± 1139		296890 ± 545
	$N^{SR}(W + jets)$	$Y_{\mathrm{p}}^{\mathrm{SR}}(W + jets)$	$N^{SR}(Other)$	$N^{SR}(Predicted)$	$N^{SR}(Data)$
SR(*W*+jets)	11844.9 ± 160.8	11698.9 ± 171.0	2523.9 ± 103.2	14222.8 ± 199.7	16153 ± 127

Table C.38: 2018 validation in the VR1 region for the case Δm = 80. Number of observed data events and simulated events in the control region CR(*W*+jets), within the validation region VR1. Number of simulated events and number of estimated *W*+jets events in the signal region within the VR1. The number of simulated rare events is also provided to calculate the number of expected total background and compare it with the observed data events. The contribution of the $t\bar{t}$ background is included in $N^{SR}(Other)$. The uncertainty in the estimated yield is statistical only.

	$N^{CR}(W + jets)$		$N^{CR}(Other)$		$N^{CR}(Data)$
CR(*W*+jets)	275780 ± 765		24864 ± 1138		297245 ± 545
	$N^{SR}(W + jets)$	$Y_{\mathrm{p}}^{\mathrm{SR}}(W + jets)$	$N^{SR}(Other)$	$N^{SR}(Predicted)$	$N^{SR}(Data)$
SR(*W*+jets)	11026.7 ± 151.4	10890.8 ± 160.7	2978.3 ± 112.9	13869.1 ± 196.4	15798 ± 126

Table C.39: 2018 validation in the VR1 region for the case Δm = 10. Number of observed data events and simulated events in the control region CR($t\bar{t}$), within the validation region VR1. Number of simulated events and number of estimated $t\bar{t}$ events in the signal region within the VR1. The number of simulated rare events is also provided to calculate the number of expected total background and compare it with the observed data events. The contribution of the *W*+jets background is included in $N^{SR}(Other)$. The uncertainty in the estimated yield is statistical only.

	$N^{CR}(t\bar{t})$		$N^{CR}(Other)$		$N^{CR}(Data)$
CR($t\bar{t}$)	30947 ± 407		7452 ± 125		40154 ± 200
	$N^{SR}(t\bar{t})$	$Y_p^{SR}(t\bar{t})$	$N^{SR}(Other)$	$N^{SR}(Predicted)$	$N^{SR}(Data)$
SR($t\bar{t}$)	340.3 ± 42.6	359.5 ± 45.3	266.0 ± 19.5	625.6 ± 49.3	866 ± 29

Table C.40: 2018 validation in the VR1 region for the case Δm = 20. Number of observed data events and simulated events in the control region CR($t\bar{t}$), within the validation region VR1. Number of simulated events and number of estimated $t\bar{t}$ events in the signal region within the VR1. The number of simulated rare events is also provided to calculate the number of expected total background and compare it with the observed data events. The contribution of the *W*+jets background is included in $N^{SR}(Other)$. The uncertainty in the estimated yield is statistical only.

	$N^{CR}(t\bar{t})$		$N^{CR}(Other)$		$N^{CR}(Data)$
CR($t\bar{t}$)	31103 ± 408		7522 ± 126		40559 ± 201
	$N^{SR}(t\bar{t})$	$Y_p^{SR}(t\bar{t})$	$N^{SR}(Other)$	$N^{SR}(Predicted)$	$N^{SR}(Data)$
SR($t\bar{t}$)	184.2 ± 28.7	195.6 ± 30.6	196.1 ± 16.4	391.7 ± 34.7	461 ± 21

Table C.41: 2018 validation in the VR1 region for the case Δm = 30. Number of observed data events and simulated events in the control region CR($t\bar{t}$), within the validation region VR1. Number of simulated events and number of estimated $t\bar{t}$ events in the signal region within the VR1. The number of simulated rare events is also provided to calculate the number of expected total background and compare it with the observed data events. The contribution of the *W*+jets background is included in $N^{SR}(Other)$. The uncertainty in the estimated yield is statistical only.

	$N^{CR}(t\bar{t})$		$N^{CR}(Other)$		$N^{CR}(Data)$
CR($t\bar{t}$)	31028 ± 407		7473 ± 125		40374 ± 201
	$N^{SR}(t\bar{t})$	$Y_p^{SR}(t\bar{t})$	$N^{SR}(Other)$	$N^{SR}(Predicted)$	$N^{SR}(Data)$
SR($t\bar{t}$)	259.7 ± 35.9	275.3 ± 38.3	244.6 ± 18.2	520.0 ± 42.4	646 ± 25

Table C.42: 2018 validation in the VR1 region for the case Δm = 40. Number of observed data events and simulated events in the control region CR($t\bar{t}$), within the validation region VR1. Number of simulated events and number of estimated $t\bar{t}$ events in the signal region within the VR1. The number of simulated rare events is also provided to calculate the number of expected total background and compare it with the observed data events. The contribution of the *W*+jets background is included in $N^{SR}(Other)$. The uncertainty in the estimated yield is statistical only.

	$N^{CR}(t\bar{t})$		$N^{CR}(Other)$		$N^{CR}(Data)$
CR($t\bar{t}$)	30769 ± 406		7377 ± 124		39958 ± 200
	$N^{SR}(t\bar{t})$	$Y_p^{SR}(t\bar{t})$	$N^{SR}(Other)$	$N^{SR}(Predicted)$	$N^{SR}(Data)$
SR($t\bar{t}$)	518.6 ± 50.6	549.2 ± 54.2	341.0 ± 24.0	890.2 ± 59.27	1062 ± 33

Table C.43: 2018 validation in the VR1 region for the case Δm = 50. Number of observed data events and simulated events in the control region CR($t\bar{t}$), within the validation region VR1. Number of simulated events and number of estimated $t\bar{t}$ events in the signal region within the VR1. The number of simulated rare events is also provided to calculate the number of expected total background and compare it with the observed data events. The contribution of the W+jets background is included in $N^{SR}(Other)$. The uncertainty in the estimated yield is statistical only.

	$N^{CR}(t\bar{t})$		$N^{CR}(Other)$		$N^{CR}(Data)$
CR($t\bar{t}$)	30587 ± 405		7320 ± 124		39691 ± 199
	$N^{SR}(t\bar{t})$	$Y_{\text{p}}^{\text{SR}}(t\bar{t})$	$N^{SR}(Other)$	$N^{SR}(Predicted)$	$N^{SR}(Data)$
SR($t\bar{t}$)	701.1 ± 59.5	742.0 ± 63.9	398.0 ± 25.9	1140.0 ± 69.0	1329 ± 36

Table C.44: 2018 validation in the VR1 region for the case Δm = 60. Number of observed data events and simulated events in the control region CR($t\bar{t}$), within the validation region VR1. Number of simulated events and number of estimated $t\bar{t}$ events in the signal region within the VR1. The number of simulated rare events is also provided to calculate the number of expected total background and compare it with the observed data events. The contribution of the W+jets background is included in $N^{SR}(Other)$. The uncertainty in the estimated yield is statistical only.

	$N^{CR}(t\bar{t})$		$N^{CR}(Other)$		$N^{CR}(Data)$
CR($t\bar{t}$)	29896 ± 400		7021 ± 121		38536 ± 196
	$N^{SR}(t\bar{t})$	$Y_{\text{p}}^{\text{SR}}(t\bar{t})$	$N^{SR}(Other)$	$N^{SR}(Predicted)$	$N^{SR}(Data)$
SR($t\bar{t}$)	1391.2 ± 84.1	1466.5 ± 91.4	697.3 ± 35.5	2163.7 ± 98.0	2484 ± 50

Table C.45: 2018 validation in the VR1 region for the case Δm = 70. Number of observed data events and simulated events in the control region CR($t\bar{t}$), within the validation region VR1. Number of simulated events and number of estimated $t\bar{t}$ events in the signal region within the VR1. The number of simulated rare events is also provided to calculate the number of expected total background and compare it with the observed data events. The contribution of the W+jets background is included in $N^{SR}(Other)$. The uncertainty in the estimated yield is statistical only.

	$N^{CR}(t\bar{t})$		$N^{CR}(Other)$		$N^{CR}(Data)$
CR($t\bar{t}$)	84352 ± 680		19717 ± 194		99723 ± 316
	$N^{SR}(t\bar{t})$	$Y_{\text{p}}^{\text{SR}}(t\bar{t})$	$N^{SR}(Other)$	$N^{SR}(Predicted)$	$N^{SR}(Data)$
SR($t\bar{t}$)	447.0 ± 47.0	423.9 ± 44.8	152.7 ± 18.2	576.7 ± 48.3	567 ± 24

Table C.46: 2018 validation in the VR1 region for the case Δm = 80. Number of observed data events and simulated events in the control region CR($t\bar{t}$), within the validation region VR1. Number of simulated events and number of estimated $t\bar{t}$ events in the signal region within the VR1. The number of simulated rare events is also provided to calculate the number of expected total background and compare it with the observed data events. The contribution of the W+jets background is included in $N^{SR}(Other)$. The uncertainty in the estimated yield is statistical only.

	$N^{CR}(t\bar{t})$		$N^{CR}(Other)$		$N^{CR}(Data)$
CR($t\bar{t}$)	84356 ± 680		19785 ± 195		99792 ± 316
	$N^{SR}(t\bar{t})$	$Y_{\text{p}}^{\text{SR}}(t\bar{t})$	$N^{SR}(Other)$	$N^{SR}(Predicted)$	$N^{SR}(Data)$
SR($t\bar{t}$)	443.4 ± 47.8	420.5 ± 45.5	84.8 ± 14.1	505.3 ± 47.7	498 ± 22

Table C.47: 2018 validation in the VR2 region for the case Δm = 10. Number of observed data events and simulated events in the control region CR(*W*+jets), within the validation region VR2. Number of simulated events and number of estimated *W*+jets events in the signal region within the VR2. The number of simulated rare events is also provided to calculate the number of expected total background and compare it with the observed data events. The contribution of the $t\bar{t}$ background is included in $N^{SR}(Other)$. The uncertainty in the estimated yield is statistical only.

	$N^{CR}(W + jets)$		$N^{CR}(Other)$		$N^{CR}(Data)$
CR(*W*+jets)	61375 ± 278		6563 ± 153		68652 ± 262
	$N^{SR}(W + jets)$	$Y_p^{SR}(W + jets)$	$N^{SR}(Other)$	$N^{SR}(Predicted)$	$N^{SR}(Data)$
SR(*W*+jets)	100.9 ± 6.6	102.0 ± 6.7	42.1 ± 7.9	144.1 ± 10.4	166 ± 13

Table C.48: 2018 validation in the VR2 region for the case Δm = 20. Number of observed data events and simulated events in the control region CR(*W*+jets), within the validation region VR2. Number of simulated events and number of estimated *W*+jets events in the signal region within the VR2. The number of simulated rare events is also provided to calculate the number of expected total background and compare it with the observed data events. The contribution of the $t\bar{t}$ background is included in $N^{SR}(Other)$. The uncertainty in the estimated yield is statistical only.

	$N^{CR}(W + jets)$		$N^{CR}(Other)$		$N^{CR}(Data)$
CR(*W*+jets)	59906 ± 276		6172 ± 149		66747 ± 258
	$N^{SR}(W + jets)$	$Y_p^{SR}(W + jets)$	$N^{SR}(Other)$	$N^{SR}(Predicted)$	$N^{SR}(Data)$
SR(*W*+jets)	1570.0 ± 34.6	1587.5 ± 36.6	433.3 ± 35.6	2020.8 ± 51.1	2071 ± 46

Table C.49: 2018 validation in the VR2 region for the case Δm = 30. Number of observed data events and simulated events in the control region CR(*W*+jets), within the validation region VR2. Number of simulated events and number of estimated *W*+jets events in the signal region within the VR2. The number of simulated rare events is also provided to calculate the number of expected total background and compare it with the observed data events. The contribution of the $t\bar{t}$ background is included in $N^{SR}(Other)$. The uncertainty in the estimated yield is statistical only.

	$N^{CR}(W + jets)$		$N^{CR}(Other)$		$N^{CR}(Data)$
CR(*W*+jets)	57616 ± 273		5750 ± 144		63782 ± 253
	$N^{SR}(W + jets)$	$Y_p^{SR}(W + jets)$	$N^{SR}(Other)$	$N^{SR}(Predicted)$	$N^{SR}(Data)$
SR(*W*+jets)	3860.1 ± 52.5	3888 ± 59.3	855.2 ± 52.6	4743.2 ± 79.2	5036 ± 71

Table C.50: 2018 validation in the VR2 region for the case Δm = 40. Number of observed data events and simulated events in the control region CR(*W*+jets), within the validation region VR2. Number of simulated events and number of estimated *W*+jets events in the signal region within the VR2. The number of simulated rare events is also provided to calculate the number of expected total background and compare it with the observed data events. The contribution of the $t\bar{t}$ background is included in $N^{SR}(Other)$. The uncertainty in the estimated yield is statistical only.

	$N^{CR}(W + jets)$		$N^{CR}(Other)$		$N^{CR}(Data)$
CR(*W*+jets)	55148 ± 270		5100 ± 136		60522 ± 246
	$N^{SR}(W + jets)$	$Y_p^{SR}(W + jets)$	$N^{SR}(Other)$	$N^{SR}(Predicted)$	$N^{SR}(Data)$
SR(*W*+jets)	6328.1 ± 66.7	6359.5 ± 80.6	1505.1 ± 71.3	7864.6 ± 107.6	8296 ± 91

Table C.51: 2018 validation in the VR2 region for the case Δm = 50. Number of observed data events and simulated events in the control region CR(W+jets), within the validation region VR2. Number of simulated events and number of estimated W+jets events in the signal region within the VR2. The number of simulated rare events is also provided to calculate the number of expected total background and compare it with the observed data events. The contribution of the $t\bar{t}$ background is included in $N^{SR}(Other)$. The uncertainty in the estimated yield is statistical only.

	$N^{CR}(W+jets)$		$N^{CR}(Other)$		$N^{CR}(Data)$
CR(W+jets)	52173 ± 266		4642 ± 130		57121 ± 239
	$N^{SR}(W+jets)$	$Y_{\text{p}}^{\text{SR}}(W+jets)$	$N^{SR}(Other)$	$N^{SR}(Predicted)$	$N^{SR}(Data)$
SR(W+jets)	9303.8 ± 83.3	9358.5 ± 107.9	1963.4 ± 80.4	11321.9 ± 134.6	11697 ± 108

Table C.52: 2018 validation in the VR2 region for the case Δm = 60. Number of observed data events and simulated events in the control region CR(W+jets), within the validation region VR2. Number of simulated events and number of estimated W+jets events in the signal region within the VR2. The number of simulated rare events is also provided to calculate the number of expected total background and compare it with the observed data events. The contribution of the $t\bar{t}$ background is included in $N^{SR}(Other)$. The uncertainty in the estimated yield is statistical only.

	$N^{CR}(W+jets)$		$N^{CR}(Other)$		$N^{CR}(Data)$
CR(W+jets)	51855 ± 265		4439 ± 128		56651 ± 238
	$N^{SR}(W+jets)$	$Y_{\text{p}}^{\text{SR}}(W+jets)$	$N^{SR}(Other)$	$N^{SR}(Predicted)$	$N^{SR}(Data)$
SR(W+jets)	9621.5 ± 85.1	9687.8 ± 110.9	2166.3 ± 85.0	11854.1 ± 139.7	12167 ± 110

Table C.53: 2018 validation in the VR2 region for the case Δm = 10. Number of observed data events and simulated events in the control region CR($t\bar{t}$), within the validation region VR2. Number of simulated events and number of estimated $t\bar{t}$ events in the signal region within the VR2. The number of simulated rare events is also provided to calculate the number of expected total background and compare it with the observed data events. The contribution of the W+jets background is included in $N^{SR}(Other)$. The uncertainty in the estimated yield is statistical only.

	$N^{CR}(t\bar{t})$		$N^{CR}(Other)$		$N^{CR}(Data)$
CR($t\bar{t}$)	18711 ± 349		5606 ± 96		20093 ± 142
	$N^{SR}(t\bar{t})$	$Y_{\text{p}}^{\text{SR}}(t\bar{t})$	$N^{SR}(Other)$	$N^{SR}(Predicted)$	$N^{SR}(Data)$
SR($t\bar{t}$)	20.8 ± 9.4	16.1 ± 7.3	8.7 ± 4.5	24.9 ± 8.6	15 ± 4

Table C.54: 2018 validation in the VR2 region for the case Δm = 20. Number of observed data events and simulated events in the control region CR($t\bar{t}$), within the validation region VR2. Number of simulated events and number of estimated $t\bar{t}$ events in the signal region within the VR2. The number of simulated rare events is also provided to calculate the number of expected total background and compare it with the observed data events. The contribution of the W+jets background is included in $N^{SR}(Other)$. The uncertainty in the estimated yield is statistical only.

	$N^{CR}(t\bar{t})$		$N^{CR}(Other)$		$N^{CR}(Data)$
CR($t\bar{t}$)	18549 ± 348		5506 ± 95		19973 ± 141
	$N^{SR}(t\bar{t})$	$Y_{\text{p}}^{\text{SR}}(t\bar{t})$	$N^{SR}(Other)$	$N^{SR}(Predicted)$	$N^{SR}(Data)$
SR($t\bar{t}$)	183.3 ± 28.1	143.0 ± 22.1	108.5 ± 14.3	251.5 ± 26.3	135 ± 12

Table C.55: 2018 validation in the VR2 region for the case Δm = 30. Number of observed data events and simulated events in the control region CR($t\bar{t}$), within the validation region VR2. Number of simulated events and number of estimated $t\bar{t}$ events in the signal region within the VR2. The number of simulated rare events is also provided to calculate the number of expected total background and compare it with the observed data events. The contribution of the *W*+jets background is included in $N^{SR}(Other)$. The uncertainty in the estimated yield is statistical only.

	$N^{CR}(t\bar{t})$		$N^{CR}(Other)$		$N^{CR}(Data)$
CR($t\bar{t}$)	18196 ± 344		5299 ± 94		19554 ± 140
	$N^{SR}(t\bar{t})$	$Y_{\mathrm{p}}^{\mathrm{SR}}(t\bar{t})$	$N^{SR}(Other)$	$N^{SR}(Predicted)$	$N^{SR}(Data)$
SR($t\bar{t}$)	536.0 ± 54.9	419.9 ± 44.0	315.1 ± 21.8	735.0 ± 49.1	554 ± 24

Table C.56: 2018 validation in the VR2 region for the case Δm = 40. Number of observed data events and simulated events in the control region CR($t\bar{t}$), within the validation region VR2. Number of simulated events and number of estimated $t\bar{t}$ events in the signal region within the VR2. The number of simulated rare events is also provided to calculate the number of expected total background and compare it with the observed data events. The contribution of the *W*+jets background is included in $N^{SR}(Other)$. The uncertainty in the estimated yield is statistical only.

	$N^{CR}(t\bar{t})$		$N^{CR}(Other)$		$N^{CR}(Data)$
CR($t\bar{t}$)	17379 ± 336		4959 ± 91		18653 ± 137
	$N^{SR}(t\bar{t})$	$Y_{\mathrm{p}}^{\mathrm{SR}}(t\bar{t})$	$N^{SR}(Other)$	$N^{SR}(Predicted)$	$N^{SR}(Data)$
SR($t\bar{t}$)	1353.0 ± 92.0	1066.2 ± 76.5	655.8 ± 30.2	1722.0 ± 82.2	1455 ± 38

Table C.57: 2018 validation in the VR2 region for the case Δm = 50. Number of observed data events and simulated events in the control region CR($t\bar{t}$), within the validation region VR2. Number of simulated events and number of estimated $t\bar{t}$ events in the signal region within the VR2. The number of simulated rare events is also provided to calculate the number of expected total background and compare it with the observed data events. The contribution of the *W*+jets background is included in $N^{SR}(Other)$. The uncertainty in the estimated yield is statistical only.

	$N^{CR}(t\bar{t})$		$N^{CR}(Other)$		$N^{CR}(Data)$
CR($t\bar{t}$)	16544 ± 328		4639 ± 89		17622 ± 133
	$N^{SR}(t\bar{t})$	$Y_{\mathrm{p}}^{\mathrm{SR}}(t\bar{t})$	$N^{SR}(Other)$	$N^{SR}(Predicted)$	$N^{SR}(Data)$
SR($t\bar{t}$)	2188.2 ± 118.3	1717.1 ± 101.1	975.2 ± 36.4	2692.3 ± 107.5	2486 ± 50

Table C.58: 2018 validation in the VR2 region for the case Δm = 60. Number of observed data events and simulated events in the control region CR($t\bar{t}$), within the validation region VR2. Number of simulated events and number of estimated $t\bar{t}$ events in the signal region within the VR2. The number of simulated rare events is also provided to calculate the number of expected total background and compare it with the observed data events. The contribution of the *W*+jets background is included in $N^{SR}(Other)$. The uncertainty in the estimated yield is statistical only.

	$N^{CR}(t\bar{t})$		$N^{CR}(Other)$		$N^{CR}(Data)$
CR($t\bar{t}$)	15845 ± 320		4476 ± 88		16795 ± 130
	$N^{SR}(t\bar{t})$	$Y_{\mathrm{p}}^{\mathrm{SR}}(t\bar{t})$	$N^{SR}(Other)$	$N^{SR}(Predicted)$	$N^{SR}(Data)$
SR($t\bar{t}$)	2887.4 ± 139.3	2244.9 ± 120.8	1138.6 ± 39.6	3383.5 ± 127.1	3313 ± 58

C.7 Assessing BDT shape disagreements

To better illustrate the method that assess the disagreement in the BDT shape between the CR and SR of the VR introduced in section 7.3 we now plot the BDT distribution for all Δm for the years of 2017 and 2018 in Figures C.15–C.22. The following Figures show the BDT output distributions for CR(W+jets) and CR($t\bar{t}$) in the validation region VR2 and VR3.

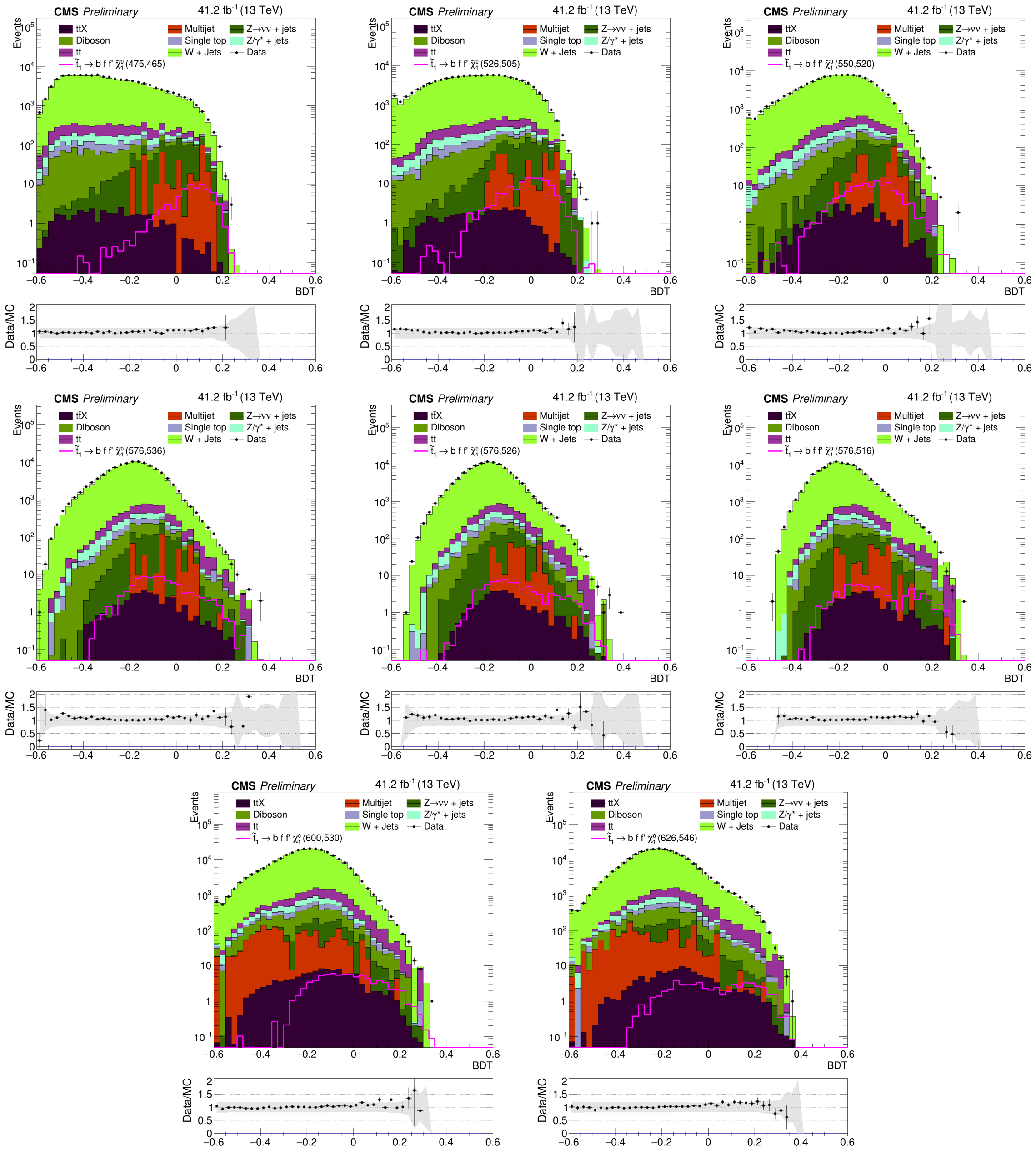

Figure C.15: 2017 BDT output for CR(W+jets) in the validation region VR2. Starting from top-left to bottom-right: Δm = 10 to 80 GeV.

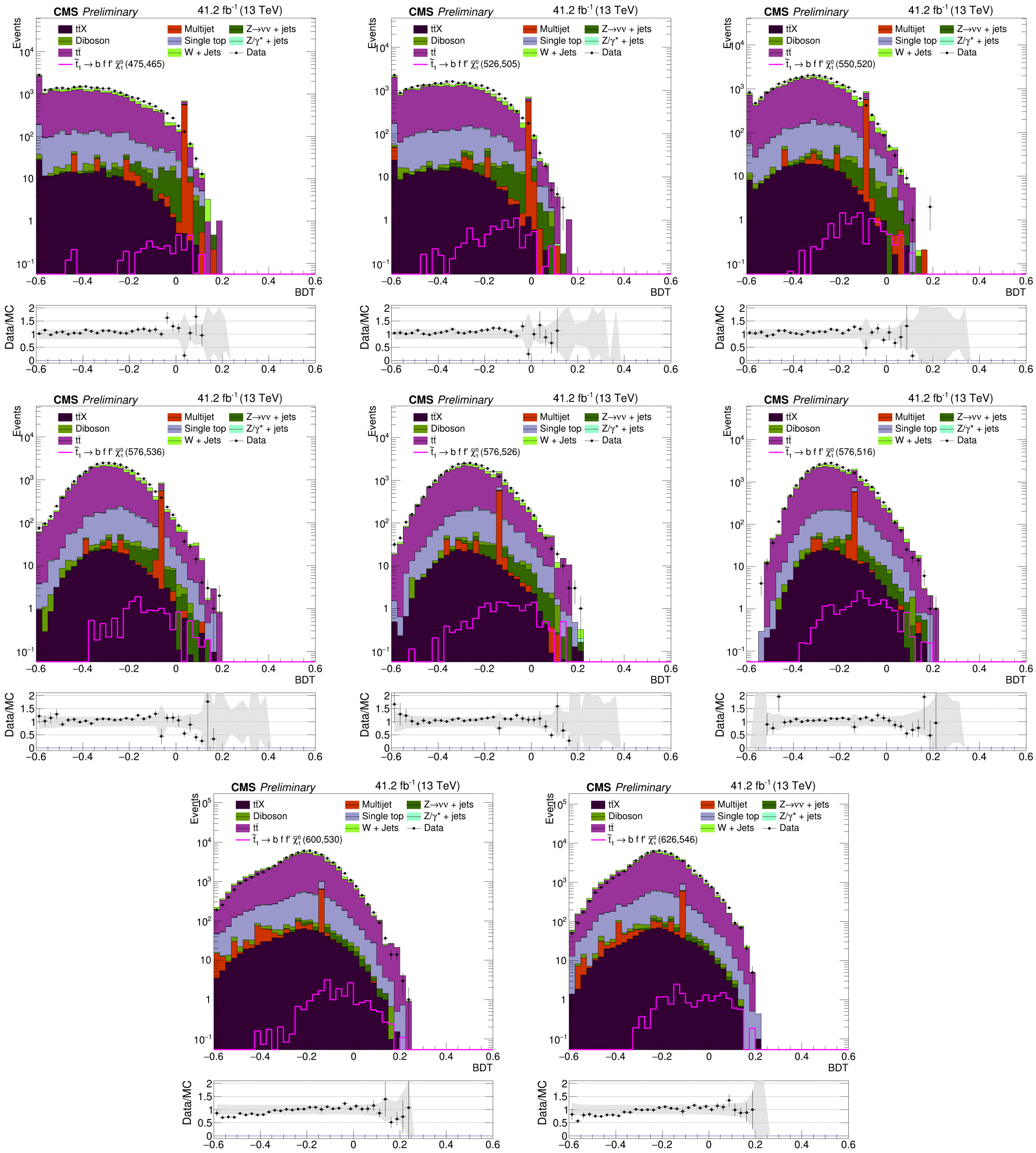

Figure C.16: 2017 BDT output for CR($t\bar{t}$) in the validation region VR2. Starting from top-left to bottom-right: Δm = 10 to 80 GeV.

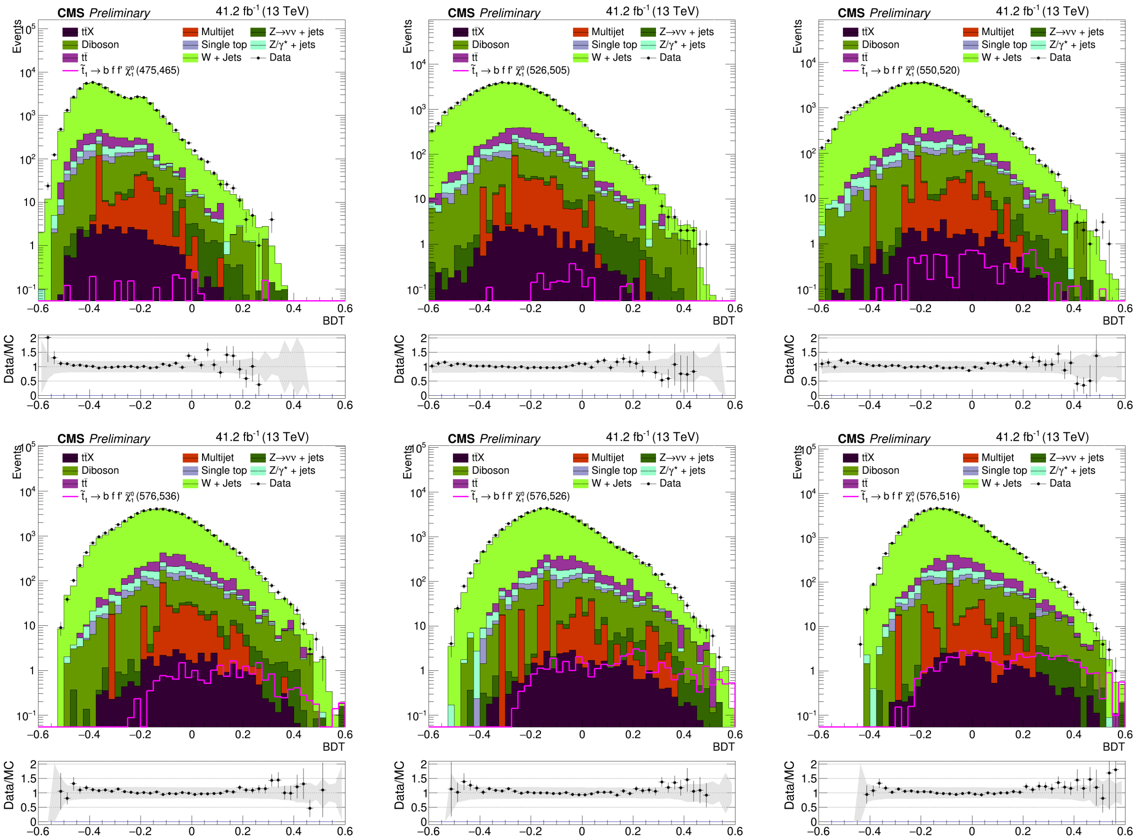

Figure C.17: 2017 BDT output for CR(W+jets) in the validation region VR3. Starting from top-left to bottom-right: Δm = 10 to 60 GeV.

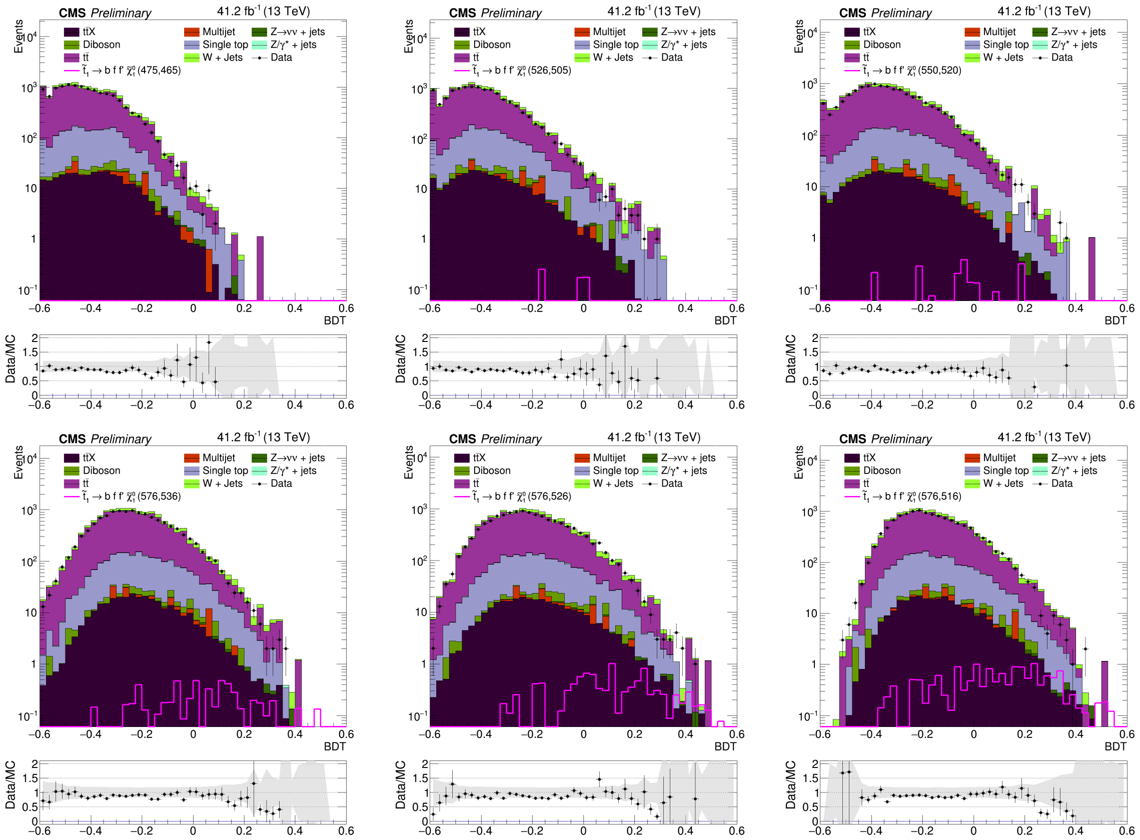

Figure C.18: 2017 BDT output for CR($t\bar{t}$) in the validation region VR3. Starting from top-left to bottom-right: Δm = 10 to 60 GeV.

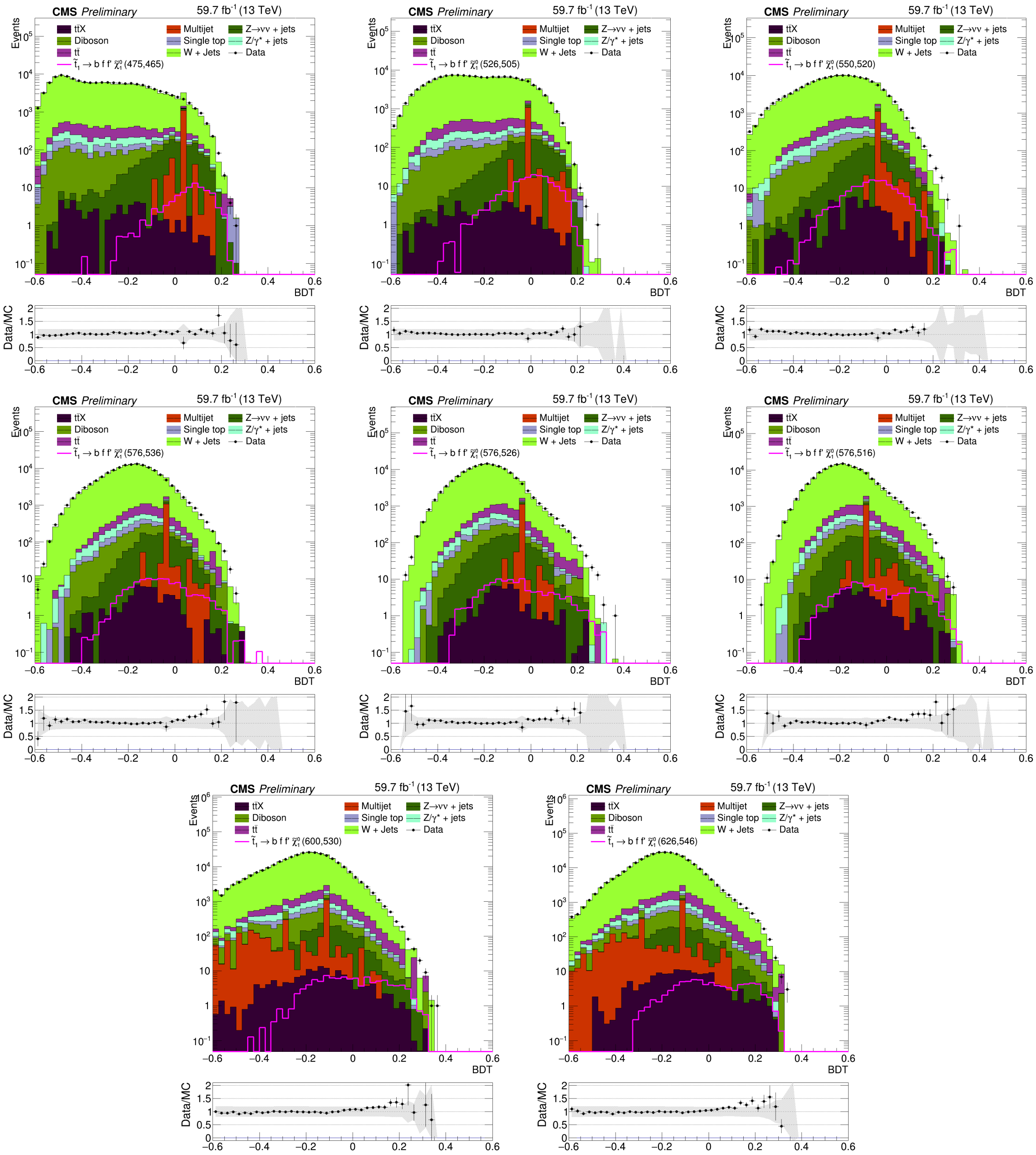

Figure C.19: 2018 BDT output for CR(W+jets) in the validation region VR2. Starting from top-left to bottom-right: Δm = 10 to 80 GeV.

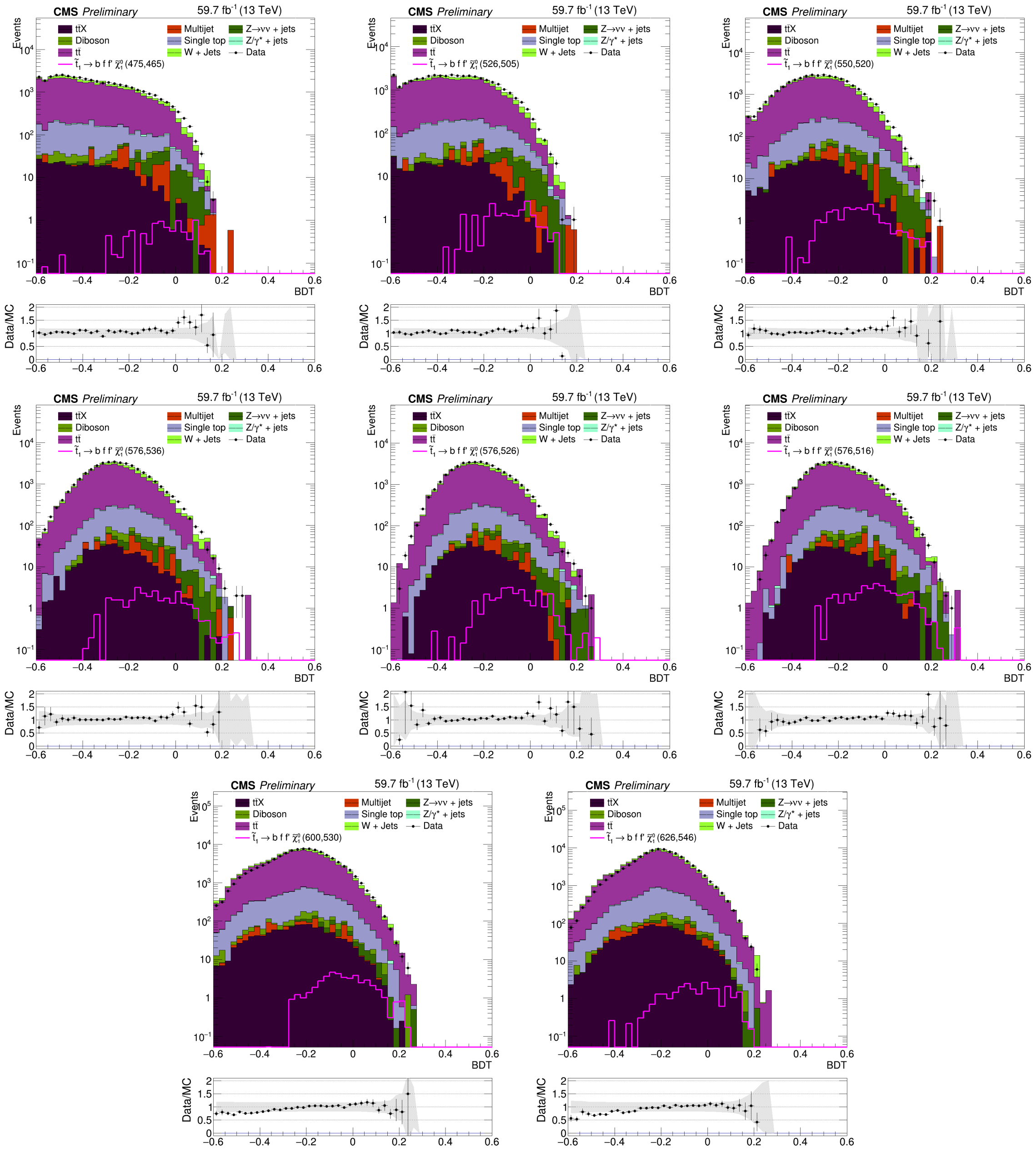

Figure C.20: 2018 BDT output for CR($t\bar{t}$) in the validation region VR2. Starting from top-left to bottom-right: Δm = 10 to 80 GeV.

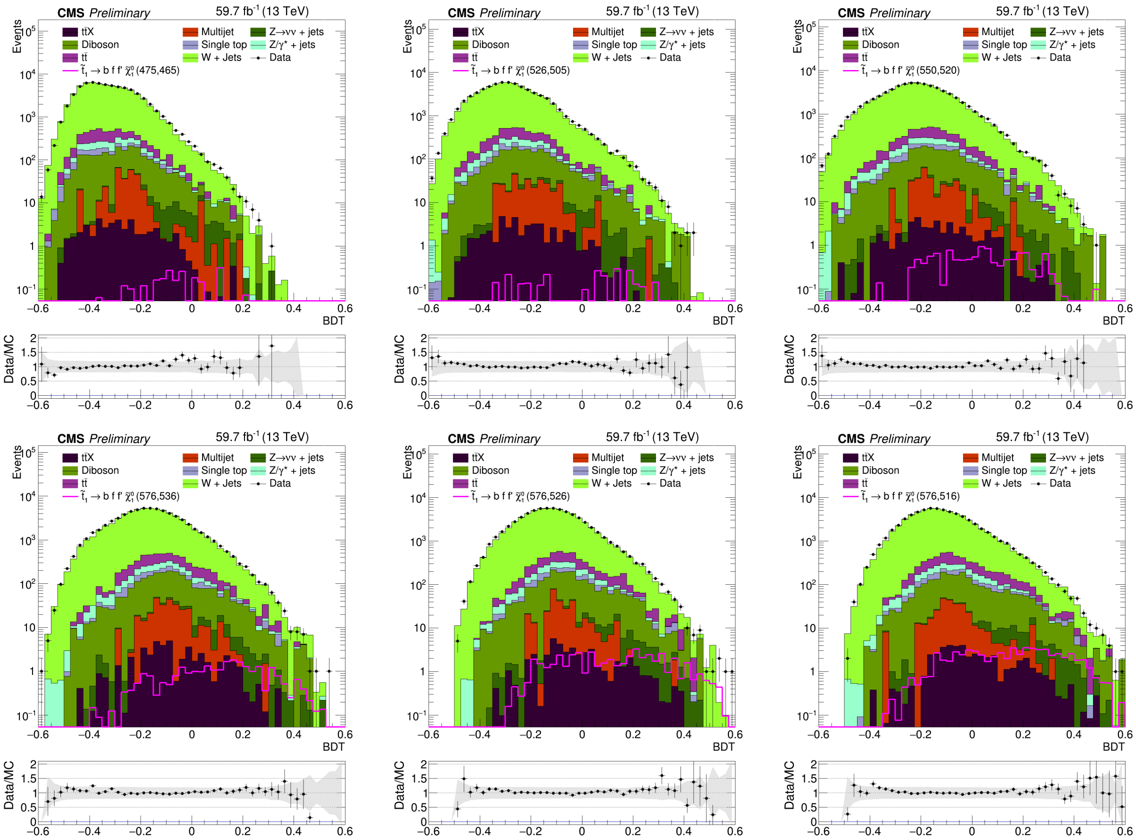

Figure C.21: 2018 BDT output for CR(W+jets) in the validation region VR3. Starting from top-left to bottom-right: Δm = 10 to 60 GeV.

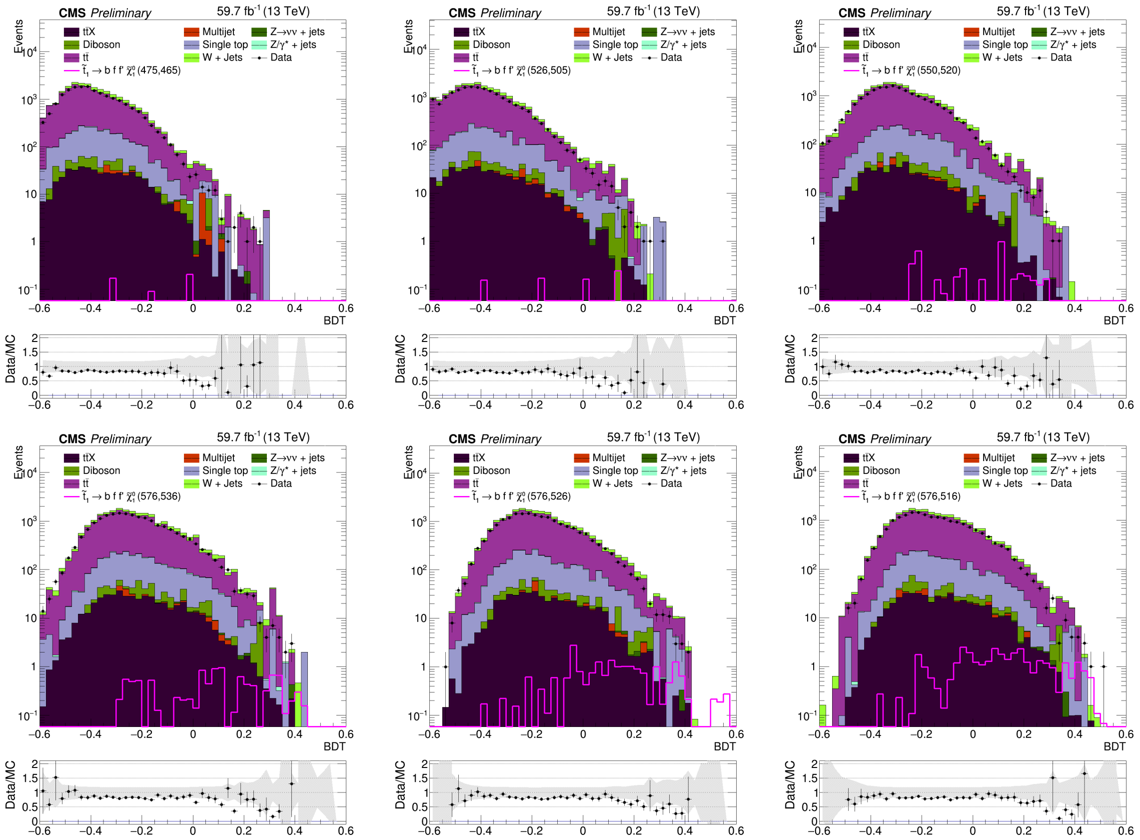

Figure C.22: 2018 BDT output for CR($t\bar{t}$) in the validation region VR3. Starting from top-left to bottom-right: Δm = 10 to 60 GeV.

D

Studies of the excesses at low Δm

Contents

Across the three years of the Run–2 LHC data taking period, where the collected data has increased every year, a deviation of the observed from the expected limit has been observed for $\Delta m = 10$ GeV. In the data of 2016, 2017, and 2018, an excess of 0.7, 1.1, and 2.9 standard deviations were observed, respectively. After combining the 3 years, the excess in the data corresponds to 2.5 standard deviations. Without considering the hypothesis of a signal being present, there are several hypothesis which can possibly explain this excess:

1. There is an obvious MC mismodeling of data
2. The background prediction methods are unstable or have a problem
3. There is an underestimation of the nonprompt background
4. It is a statistical fluctuation

The following sections address the different hypothesis.

D.1 BDT output of data/MC at Δm = 10 GeV

As one can see in Figure D.1, there is a good agreement between data and MC at $\Delta m = 10$ GeV in the SR. The disagreement in the data of 2018 points in the opposite direction, where there is a small excess of MC compared to data. Because of this, MC background modelling is not the reason for explaining the excess.

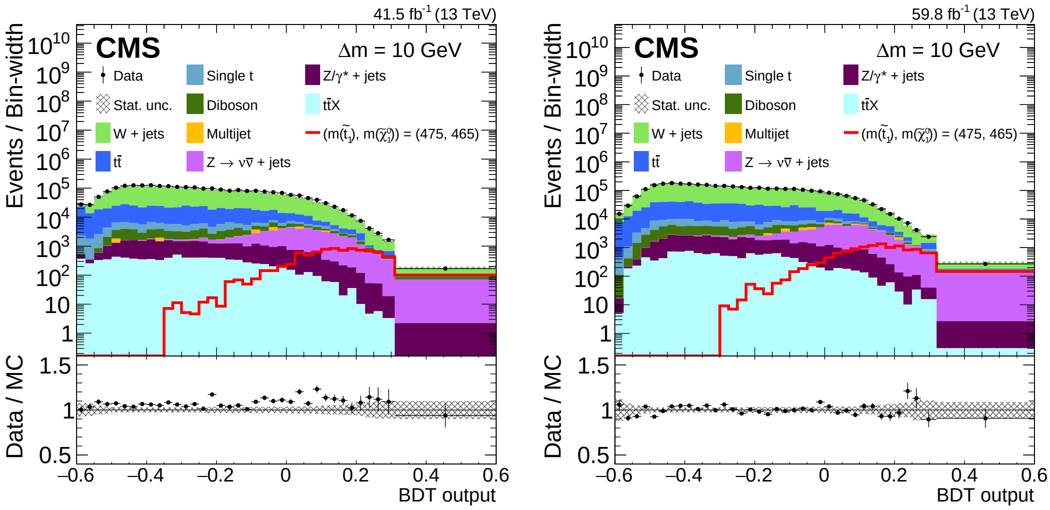

Figure D.1: Distributions of the BDT output at the preselection level in data and simulation for $\Delta m = 10$ GeV for the data of 2017 (left) and 2018 (right). The last bin represents the SR. For each BDT training, a representative $(m(\widetilde{t}_1),\ m(\widetilde{\chi}^0_1))$ signal point is also presented, while not added to the SM background. The shaded area on the Data/MC ratio represents the statistical uncertainty of the simulated background.

D.2 Evaluating the prediction methods as a function of the BDT output

The predicted yields of all backgrounds were studied as function of a selection on the output of the BDT, as reported in Figures D.2 to D.4 for all Δm and for both years. In these Figures, the prediction of three main background processes, namely W+jets, $t\bar{t}$ and nonprompt leptons, is derived from data for each selection value of the BDT output. While for all cases the total background predicts well the data, it is observed that in the specific case of Δm =10 GeV for 2018, the predicted background "underpredicts" the data, to a smaller extent for Δm =20 GeV within the same year, and also to a smaller extent for the same Δm =10 GeV but in 2017. However, the total background matches well the observed data for lower values of the BDT output, which is an expected feature of classification. Therefore, the slight excess in data is not attributed to a possible systematic problem in the background estimation methods.

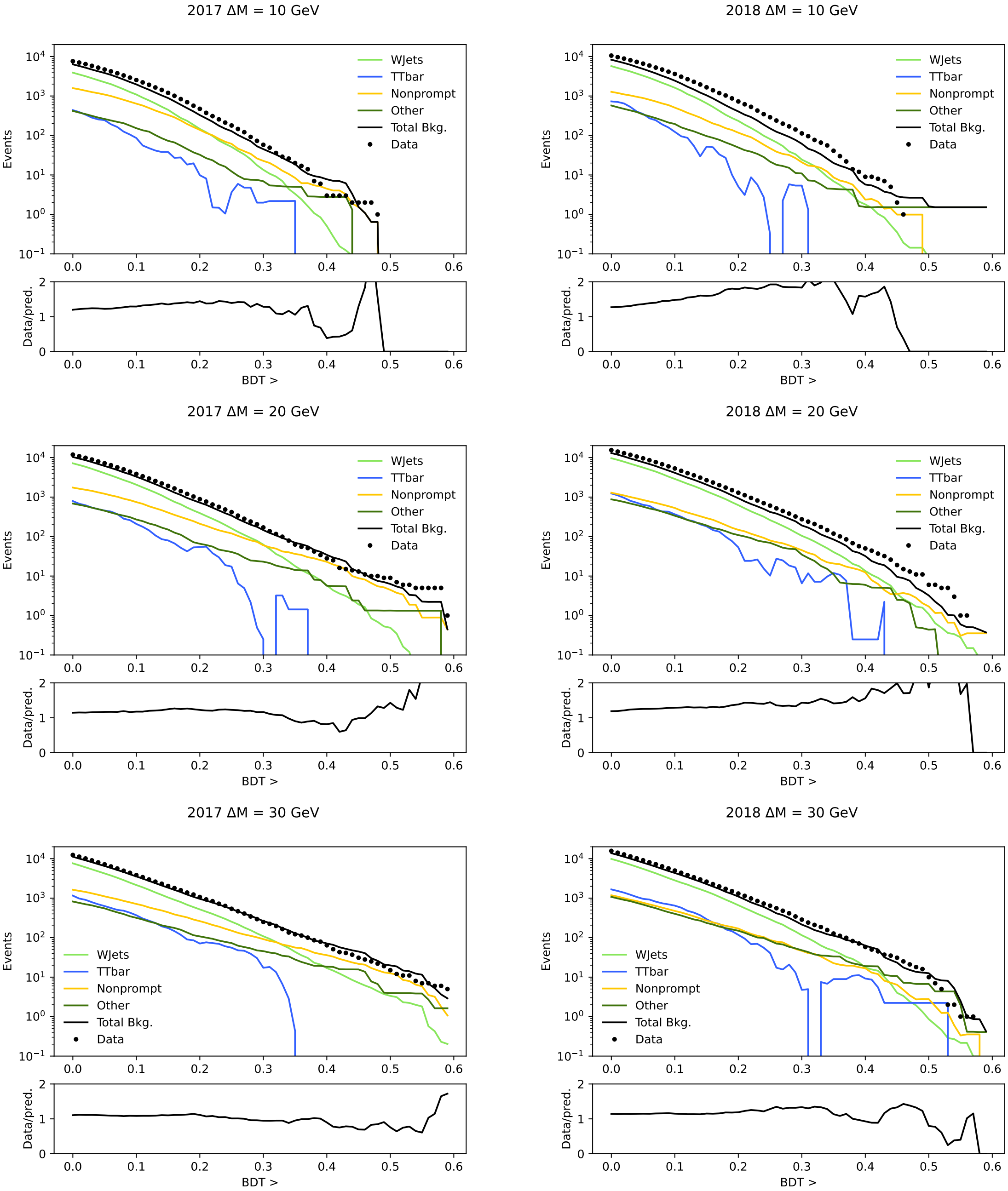

Figure D.2: Predicted background yields and observed data as function of the cut on the BDT output. The predictions of the three main sources of background, namely W+jets $t\bar{t}$ and nonprompt lepton background are data-driven. The results are shown for Δm = 10 (top), 20 (middle), and 30 (bottom) GeV, and for the years 2017 (left) and 2018 (right).

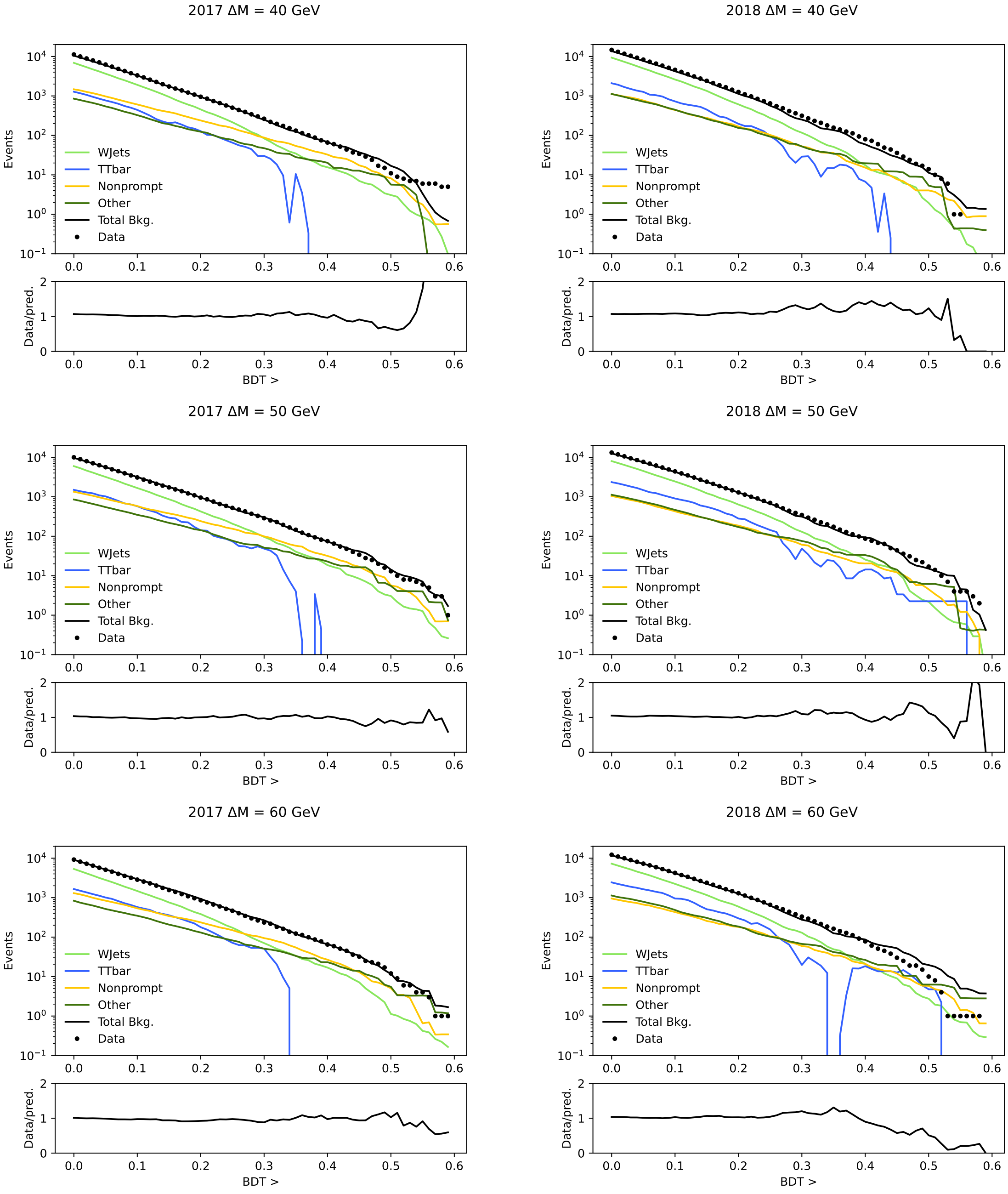

Figure D.3: Predicted background yields and observed data as function of the cut on the BDT output. The predictions of the three main sources of background, namely W+jets $t\bar{t}$ and nonprompt lepton background are data-driven. The results are shown for Δm = 40 (top), 50 (middle), and 60 (bottom) GeV, and for the years 2017 (left) and 2018 (right).

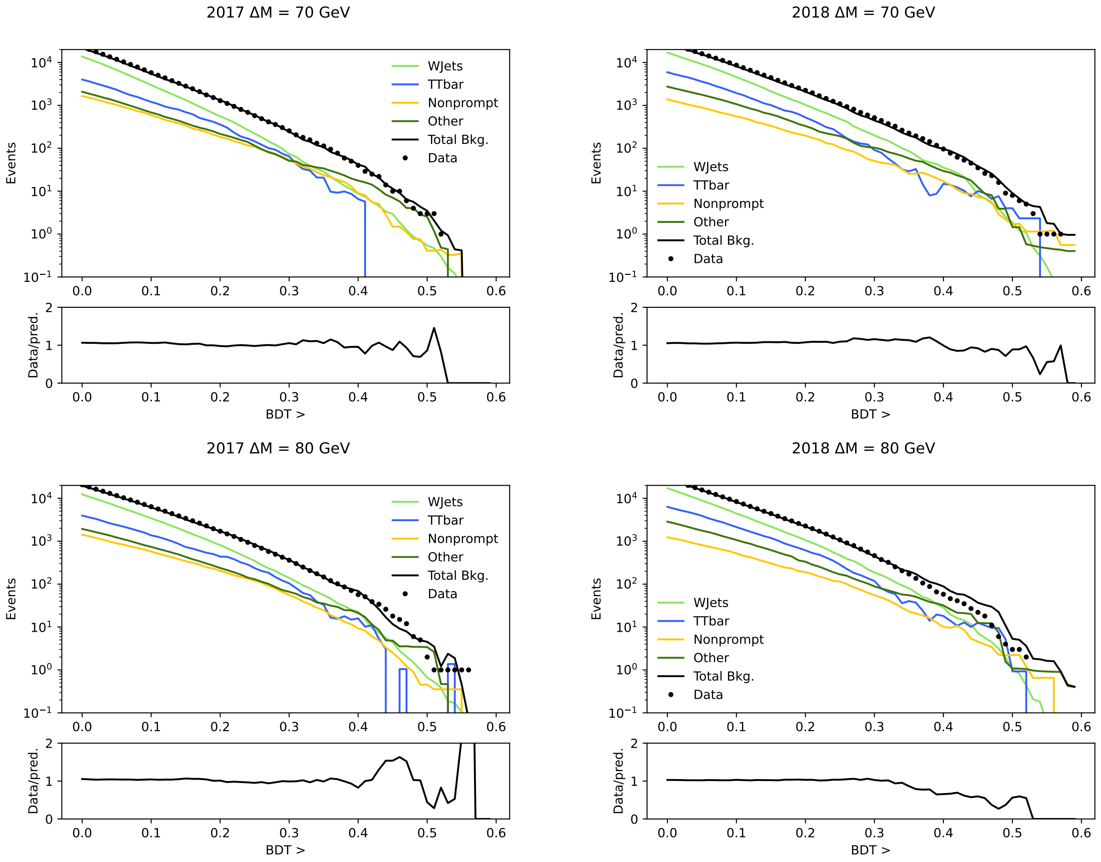

Figure D.4: 2017(Predicted background yields and observed data as function of the cut on the BDT output. The predictions of the three main sources of background, namely W+jets $t\bar{t}$ and nonprompt lepton background are data-driven. The results are shown for Δm = 70 (top), and 80 (bottom) GeV, and for the years 2017 (left) and 2018 (right).

D.3 Comparison of nonprompt leptons in simulation, prediction and data

In the previous sections, Section D.1 and D.2, the MC and the data–driven predictions of the nonprompt background were analyzed. In the present section, the MC and data–driven predictions of the nonprompt leptons are compared.

In the equation predicting the nonprompt background:

$$Y_{\mathrm{np}}^{\mathrm{SR}} = \frac{\epsilon_{\mathrm{TL}}}{1-\epsilon_{\mathrm{TL}}} \cdot [N^{\mathrm{L!T}}(\text{Data}) - N_{\mathrm{p}}^{\mathrm{L!T}}(\text{MC})], \tag{D.1}$$

two terms have the most impact on the prediction of $Y_{\mathrm{np}}^{\mathrm{SR}}$: ϵ_{TL} and $N^{\mathrm{L!T}}(\text{Data})$. The first term, ϵ_{TL}, is very similar for the two years as can be seen in Figures 6.5 and 6.6. If ϵ_{TL} is the cause of the excess, a similar excess should be seen in both years. Therefore, the measurement of ϵ_{TL} is not the cause for the excesses.

To investigate if there is an underestimation of $N^{\mathrm{L!T}}(\text{Data})$, consider the following points:

- $Z \to \nu\overline{\nu}$+jets predicted by MC: this yield should be smaller than $Y_{\mathrm{np}}^{\mathrm{SR}}$, which is the final prediction of the nonprompt background since it accounts for the contributions of $Z \to \nu\overline{\nu}$+jets, multijet and nonprompt leptons from W+jets and $t\bar{t}$
- The ratio of tight-to-loose leptons in data events in the SR. How it compares across different Δm regions in the same year. This ratio is expected to be similar.

Table D.1: $Z \to \nu\overline{\nu}$+jets predicted by MC, $Y_{\mathrm{np}}^{\mathrm{SR}}$ predicted from the nonprompt data–driven prediction method as in Equation D.1, $N^{\mathrm{L!T}}(\text{Data})$ and the ratio of loose-not-tight measured in data, for all the Δm regions in 2017.

Δm (GeV)	**MC $Z \to \nu\overline{\nu}$+jets**	**data–driven $Y_{\mathrm{np}}^{\mathrm{SR}}$**	**data $N^{\mathrm{L!T}}$(Data)**	**data tight/loose ratio**
10	19.6	20.1	21	0.53
20	38.3	49.6	53	0.51
30	31.1	41.7	43	0.47
40	21.9	32.6	34	0.45
50	13.0	22.3	23	0.46
60	6.1	7.6	8	0.55
70	7.3	12.9	14	0.58
80	4.2	8.3	9	0.69

In Table D.1, $Y_{\mathrm{np}}^{\mathrm{SR}} > Z \to \nu\overline{\nu}+jets$ for all Δm regions as expected. While, in Table D.2, the same is not observed. This could suggest that either the MC prediction is overestimating and the data–driven one is the more accurate and vice–versa. Table D.3 reports the cases for $\Delta m = 10$, 30 and 50 GeV where $Y_{\mathrm{np}}^{\mathrm{SR}} < Z \to \nu\overline{\nu} + jets$ for the year of 2018. The ratio of events in the SR for data/MC and data/data–driven is also reported in order to explore if the apparent deficit of $Y_{\mathrm{np}}^{\mathrm{SR}}$ is the cause for the excess observed in the final result.

In summary, in the $\Delta m = 10$ GeV, the MC prediction is compatible to the observed events in data, while $Y_{\mathrm{np}}^{\mathrm{SR}}$ seems too small. Although, in the $\Delta m = 30$ and 50 GeV regions, $Y_{\mathrm{np}}^{\mathrm{SR}}$ is equally too small, when compared to the MC prediction, as in the $\Delta m = 10$ GeV, yet, the final prediction of

Table D.2: $Z \rightarrow \nu\overline{\nu}$+jets predicted by MC, $Y_{\mathrm{np}}^{\mathrm{SR}}$ predicted from the nonprompt data–driven prediction method as in Equation D.1, $N^{\mathrm{L!T}}(\mathrm{Data})$ and the ratio of loose-not-tight measured in data, for all the Δm regions in 2018.

Δm (GeV)	MC $Z \rightarrow \nu\overline{\nu}$+jets	data–driven $Y_{\mathrm{np}}^{\mathrm{SR}}$	data $N^{\mathrm{L!T}}$(Data)	tight/loose ratio
10	40.3	16.7	18	0.69
20	34.2	14.5	17	0.63
30	56.1	22.5	29	0.68
40	26.7	11.7	12	0.65
50	18.3	10.5	11	0.63
60	21.9	17.3	19	0.60
70	19.2	16.9	19	0.71
80	7.7	10.7	11	0.67

Table D.3: $Z \rightarrow \nu\overline{\nu}$+jets predicted by MC, $Y_{\mathrm{np}}^{\mathrm{SR}}$, $N^{\mathrm{L!T}}(\mathrm{Data})$ and the ratio of loose-not-tight for all the Δm regions in 2018.

Δm	Year	MC		data–driven		data		
(GeV)		$Z \rightarrow \nu\overline{\nu}$+jets	$N_{\mathrm{MC}}^{\mathrm{SR}}$(Total)	$Y_{\mathrm{np}}^{\mathrm{SR}}$	$N_{\mathrm{dd}}^{\mathrm{SR}}$(Total)	$N_{\mathrm{data}}^{\mathrm{SR}}$(Total)	data/MC	data/data–driven
10	2017	19.6	51.8	20.1	38.6	49	~ 1	~ 1.3
	2018	40.3	82.5	16.7	42.3	77	~ 1	~ 1.8
30	2017	31.1	67.4	41.7	94.0	86	~ 1.3	~ 1
	2018	56.1	163.0	22.5	121.7	121	~ 0.7	~ 1
50	2017	13.0	34.2	22.3	52.7	48	~ 1.4	~ 1
	2018	18.3	39.8	10.5	34.9	36	~ 1	~ 1

events is compatible with data. Therefore, a systematic underestimation of $Y_{\mathrm{np}}^{\mathrm{SR}}$ is not the cause for the observed excess.

D.4 Final considerations

From these studies, the excess of the final result seem to point to a statistical fluctuation. An excess of 2.5 standard deviations means that such a result is expected to be seen with a probability of 1/160 even in the absence of SUSY.